An alveolar model based on development of ultrathin artificial basement membrane and automatic system for tissue formation derived from human induced pluripotent stem cells

Yong He

PSL
UNIVERSITÉ PARIS

THÈSE DE DOCTORAT
DE L'UNIVERSITÉ PSL

Préparée à [École Normale Supérieure de Paris]

Un modèle alvéolaire basé sur le développement des nouveaux dispositifs et des nouveaux protocoles pour la différenciation des cellules souches pluripotentes humaines induites

Soutenue par
Yong HE
Le 18/12/2020

Ecole doctorale n° 388
Chimie physique et chimie analytique de Paris Centre

Spécialité
Chimie Physique et Chimie Analytique

Composition du jury :

Marie-Claude, POTIER Directeur de recherche CNRS, ICM	*Président*
Anne-Marie, HAGHIRI Directeur de recherche CNRS, C2N	*Rapporteur*
Manuel, THERY Directeur de recherche CEA, IUH	*Rapporteur*
Armelle, BAEZA-SQUIBAN Professeur, BFA, Univ. Paris Diderot	*Examinateur*
Jean- François, BERRET Directeur de recherche CNRS, LMSC Univ. Paris Diderot	*Examinateur*
Yong, CHEN Directeur de recherche CNRS, ENS	*Directeur de thèse*

ENS | PSL

Acknowledgement

Many years ago, when I was a small child in a distant countryside, I couldn't believe that I could finish a Ph.D. degree 20 years later. This is my biggest achievement during my first 29 years and it is my great honor to have this chance to spend three years in the Chemistry Department at the École normale supérieure de Paris which is part of Université PSL (Paris Sciences & Lettres), a prestigious place full of wisdom and philosophy.

First, I would like to present my gratitude to the Chinese Scholarship Council for funding me to study abroad for the whole three years, to the École normale supérieure for providing me an excellent research environment, and to the doctoral school ED388 (Ecole doctorale de Chimie Physique et de Chimie Analytique de Paris Centre) for accepting me as a Ph.D. candidate.

Then, I would like to give my sincerest gratitude to my supervisor, Professor Yong CHEN. His passion and curiosity are always motivating, his knowledge and observation are always inspiring, and finally, his support and help are always encouraging. I cannot say that my results are fruitful, but I believe what I learned from him will be useful for me forever.

Next, I would like to thank the members of my thesis committee: Prof. Armelle Baeza-Squiban of the University Paris Diderot, Dr. Anne-Marie Haghiri, CNRS research director at the Centre de Nanosciences et de Nanotechnologies (C2N), University Paris-Saclay, Dr. Jean-François Berret, CNRS research director at the Laboratory de Matière et Systèmes Complexes (LMSC), Université Paris Diderot, Dr. Marie-Claude POTIER, CNRS research director at the Institut du Cerveau et de la Moelle Epinière (ICM), Hôpital Pitié-Salpêtrière, Sorbonne University, and Dr. Manuel Théry, CEA research director at the Institut Universitaire d'Hématologie de l'Hôpital Saint-Louis, for their suggestions and insightful comments.

A special thanks to Dr. Juan Peng, Boxin Huang and Xiaochen Huang and Elrade Rofaani of the laboratory, Dr. Li Wang and Jian Shi of Mesobiotech SAS, and Dr. Milad Radiom of the University Paris Diderot, for their close and fruitful collaborations. My gratitude also goes to Dr. Carole Aimé, Damien Baigl, Changchong Chen, Vadim Dilhas, Feng Liang, Dr. Gabriele Pintingolo, Dr. Bin Wang, Dr. Xiaolong Tu, and Dr. Ayako Yamada of ENS for their daily help. I would also like to thank Prof. Rodolphe Vuilleumier, director of UMR 8640, for his

support and encouragement, and my friends, Dr. Na Pan, Dr. Meiling Tian, Dr. Panhui Huang, Dr. Lihui Hu, Dr. Ruikang Zhang, Haoran Geng, Linjie Lu for their sympathy and helpfulness.

My thanks also go to Mme Anne Halloppe of ENS, Mme Armelle Ringuede, Mr. Auguste Filippi, Mr. Stéphane Emery, and Mme Soobrayen Koonavadee of UPMC, who were always so kind to help me in student affairs management.

Thanks to my family, my parents, grandparents, and my sister for their selfless and unconditional support, also to my parents in law for their endless encouragement and care.

To my love Yan Liu, thanks for waiting and supporting me to pursue a Ph.D. degree abroad, for encouraging me when I failed in my experiment, for sharing her feelings, for planning our future, and for missing me.

Yong HE

November 2020

Contents

Outline

The adult human lung consists of millions of tiny sacs (alveoli) where gas exchange takes place. The inner layer of the sac, the alveolar epithelium, is composed of two types of cells: Alveolar Type 1 (AT1) and Alveolar Type 2 (AT2). Together with the specific supporting extracellular matrix, the alveolar basement membrane, they form a tight air-blood barrier with respect to the blood capillary networks on the outer layer of the sac. It is known that AT1 cells cover 95% of the alveolar surface while AT2 cells secrete surfactant to coat the inner layer of the sac. AT2 cells can also produce AT1 cells to repair the injured alveoli. There are also immune cells such as alveolar macrophages in the alveoli sacs to help the alveoli functioning. Many diseases are due to the dysfunction of alveoli caused by infection, pollution, aging, etc. Although a huge number of studies are performed, there are only a few in-vitro models and none of them is capable of recapitulating the human in-vivo specification by taking into account, for example, the immunity of all constituent cells and the molecular and morphology feature of the supporting basement membrane.

The purpose of this thesis work is to develop an alveolar model by differentiating human induced pluripotent stem cells to AT1 and AT2 cells and cultivating them on an artificial basement membrane. This thesis was initially planned for alveolar tissue fabrication but the outbreak of new coronavirus suddenly appeared, which obliged additional works toward immunological studies involving both viral infection and immune microenvironment.

Human-induced pluripotent stem cells (hiPSCs) are obtained by reprogramming somatic tissue cells. They are embryonic-like stem cells and capable of self-renewing for many generations and differentiating into different types of cells, including alveolar, endothelial, and immune cells. This allows developing a sophisticated in-vitro model for alveolar tissue and viral-host interaction studies. Since the tissue and immune cells are both derived from the same hiPSCs, they have human-cells specific receptors and they are intrinsically immune tolerant, which makes the sense to put forward this approach. In order to recapitulate the epithelium specification, ultrathin artificial basement membranes are produced using type 4 collagen and laminin. Furthermore, an automatic culture system has been developed for either multi-source differentiation of hiPSCs or long-term control of different cell maturation.

The thesis is organized as follows:

The objective of this thesis work is to develop a method for automatic hiPSC differentiation towards functional alveolar epithelium that can be used for immunology studies.

The thesis is organized into five chapters, followed by a general conclusion and four appendixes.

Chapter 2 introduces the different fabrication methods and microfluidic techniques used in this work. Photolithography, vacuum assisted molding and electrospinning which are necessary for the patch (culture device) fabrication are described. The microfluidic device configuration for the patch or tissue integration is discussed. Other fabrication techniques such as micro-milling and cutting plotters that are used for the improvement of cell seeding and differentiation processing are also presented.

Chapter 3 is dedicated to the development of an automatic culture system for hiPSC differentiation. This system is composed of a unit for culture medium selection, a unit for incubation, and a central unit for process control. By using such a system, static and dynamic cultures are compared and differentiation of hiPSCs to cardiomyocytes is studied to show the high potential of this approach for different applications.

Chapter 4 focuses on the production of alveolar epithelium by differentiation of hiPSCs. Alveolar organoids are firstly generated in a gel layer, which can be freezed, defreezed, and dissociated into single cells. This greatly facilitates the whole tissue engineering processes since the generated organoids contain both type 1 and type 2 alveolar cells and they are readily useful once produced. By replating the disassociated cells on a patch or an artificial basement membrane, the alveolar epithelium can be achieved and studied by both immunostaining observation and transepithelial electrical resistance measurements.

Chapter 5 describes a preliminary study on virus-host interaction by using the fabricated S-proteins of the new coronavirus (SARS-CoV-2) and alveolar or cardiac cells. The cell responses of the alveoli to S-proteins are monitored by ROS measurement in the presence of angiotensin II (Ang II) based on the hypothesis that coupling of S-proteins and the receptor Angiotensin-converting enzyme 2 (ACE2) of the cells increases the activation of angiotensin type 1 receptor (AT1R) and decreases the production of angiotensin (1-7) so that the activation of the G-protein coupled receptor Mas receptor (MASR). Knowing that AT1R and MASR play opposite rule in host cell homeostasis, the S-protein of SARS-CoV-2 itself can be highly cytotoxic. In addition, hiPSC derived cardiomyocytes are also used to show the toxicity of the S-proteins.

Chapter 6 is the summary and perspective of the thesis.

In the appendix, several works related to the present thesis are given, which respectively describe the studies of i) response of alveolar cells to S-protein of SARS-CoV-2, ii) fabrication of micro-cage devices for spheroid handling, iii) fabrication of ultrathin artificial basement

membrane, iv) effect of periodic deformation of alveolar cell layer on nanofibers, and v) realization of a bioreactor for patch-based hiPSC differentiation.

Chapter 1
Introduction

Introduction

This chapter gives a general introduction to this work. We firstly present basic concepts of cells and stem cells, especially induced pluripotent stem cells (iPSCs). Then, we recall the fundamental notions of the cellular microenvironment with a particular focus on extracellular matrix and cell culture substrate for in-vitro studies. Physiological systems and more specifically the lung and alveoli are also described. Finally, we discuss the main characteristics of commonly used biomaterials and culture devices, including microfluidic devices and organ-on-a-chip systems.

1.1 Cells and stem cells

1.1.1 Cells

Cells are the smallest units of living organisms and they share some common features. For example, most cells have one nucleus which contains the chromosomes of the cell's gene, and the nucleoli that produce ribosomes. The cell membrane is on the cell surface which controls the entry and exit of substances. The cytoplasm of the cell is composed of liquid substances and organelles. The ribosome produced in the nucleus can produce proteins, which can work inside the cell or leave the cell. The endoplasmic reticulum is for substance transport inside cells. Mitochondria is for energy production for cell activity. Lysosomes are for enzymatic breakdown of particles that enter cells. The centrioles play essential roles in cell division.

The human body is composed of many different types of cells, including neurons, cardiomyocytes, alveolar, airway, muscle, skin and cells, etc. As shown in Figure 1.1, they have different forms and different functions. Some cells such as blood cells can move in the blood vessels without sticking to each other and some others such as muscle cells are tightly connected to each other. Some cells such as skin cells can divide and proliferate quickly and some others such as neurons will not divide or proliferate. A variety of cells are dedicated to producing hormones, enzymes, milk, insulin, etc. Some alveolar cells secrete mucus, and some cells in the mouth produce saliva. Muscle cells do not produce substances but produce movement. Neurons produce both electrical impulses and neurotransmitters to ensure connections to the nervous system in the brain and the rest of the body.

In addition to the cells, a huge number of microorganisms live in different parts of the human body to help the food digestion or to prevent the growth of more dangerous bacteria, for example [1, 2].

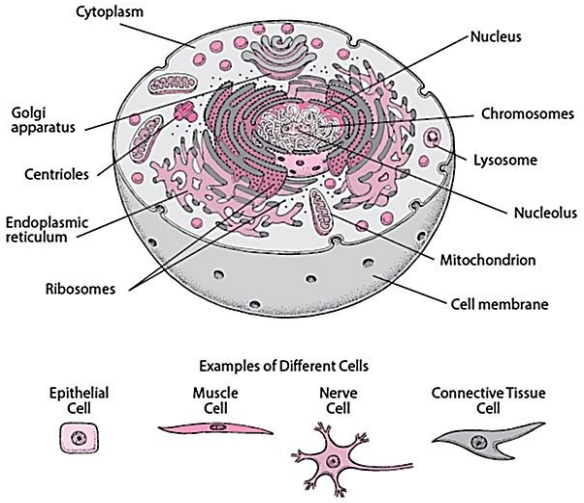

Figure 1.1 Schematic of cellular structure, showing cell membrane, organelles, cytoplasm, nucleolus, and epithelial cells, nerve cells, muscle cells and connective tissue cells [3]

1.1.2 Stem cells

In the human body, most cells are "professional" to suit their specific functions, but the stem cells are not. They can be renewed and differentiated to a particular type of professional cells as shown in Fig 1.2 [4-7]. In particular, they can repair damaged tissue by replacing damaged cells or stimulate the regeneration function of native cells [8-14].

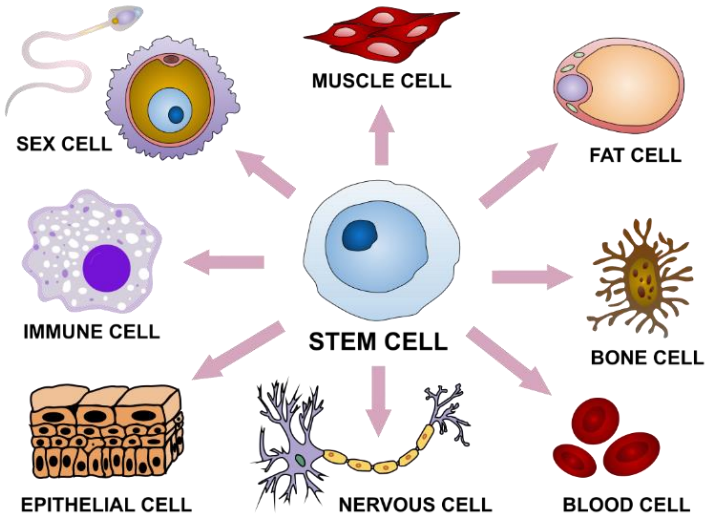

Figure 1.2 Stem cells and examples of stem cell-derived adult cells, including immune cells, epithelial cells, nerve cells, blood cells, etc.

Embryonic stem cells (ESC) can be differentiated to adult stem cells (ASC) and then specific adult cells [15-17]. ESCs can be self-renewed many times and differentiated into all tissue cells, including germ cells. ASCs such as umbilical cord stem cells and bone marrow stem cells are located in specific tissues of adults, which can be differentiated into cells with specific functions.

Depending on their differentiation ability, stem cells are called totipotent, pluripotent or unipotent. Totipotent stem cells are capable to generate fertilized eggs so a complete individual, pluripotent stem cells (PSC), including both embryonic stem cells (ESC) or induced pluripotent stem cells (iPSC), can be used to produce various tissues and blood cells, and finally, unipotent stem cells such as neural stem cells and hematopoietic stem cells are restricted to differentiate to only limited cell types.

1.1.3 Induced pluripotent stem cell

Induced pluripotent stem cells (iPSCs) are obtained by reprogramming somatic cells and they are capable, quite like ESCs, of self-renewing for many generations and deafferenting into many cell types. The iPSCs were obtained from mouse fibroblast then form human fibroblast by the team of Professor Yamanaka of Kyoto University in Japan in 2006 [18], for which he was awarded the 2012 Nobel Prize [19, 20] The reprogramming factors used by his team (also called Yamanaka factors) are four transcription factors (Oct4, Sox2, cMyc, and Klf4). Many studies have shown that a set of small molecules can be used for reprogramming and that many types of adult stem cells and matured adult cells, including umbilical cord blood cells, bone marrow cells, peripheral blood cells, fibroblasts, keratinocytes, etc. can be reprogrammed and then turned into other types of adult stem cells and matured adult cells. Similar to ESCs, iPSCs can be used to generate all three primary germ layers (ectoderm, mesoderm, and endoderm) and all of their derivatives (Figure 1.3).

Compared to ESCs, the use of iPSCs does not pose any ethical problem and iPSCs can be derived from cells of either a healthy donor or a patient, thereby also reducing the risk of immune rejection [21-23]. The emergence of iPSCs has stimulated a strong response in research fields such as stem cells, epigenetics, and biomedicine, giving people a new understanding of the regulatory mechanism of pluripotency, and reducing the distance between stem cells and clinical diseases. iPSCs have great potential in cell replacement therapy and pathogenesis research, screening of new drugs, and treatment of clinical diseases such as neurological diseases and cardiovascular diseases [24-29].

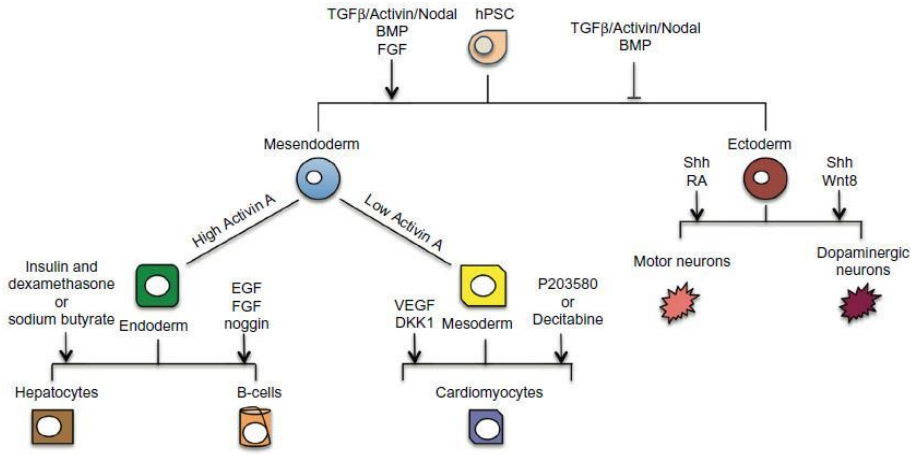

Figure 1.3 Schematic of differentiation of human PSCs to all three embryonic germ layers and adult cells by using different sets of cell factors.

1.2 Cellular microenvironment

Cell behaviors are largely influenced by the cellular microenvironment, includes the extracellular matrix (ECM), soluble factors and cell-cell contacts.

1.2.1 ECM

The extracellular matrix (ECM) is a complex network out of the cell and composed of a variety of specific molecules synthesized and secreted by cells as shown in Fig 1.4 [30-33]. These molecules such as collagen, fibronectin, and laminin are mostly glycoproteins and account for 1.0% to 1.5% of proteins in mammalian proteomes.

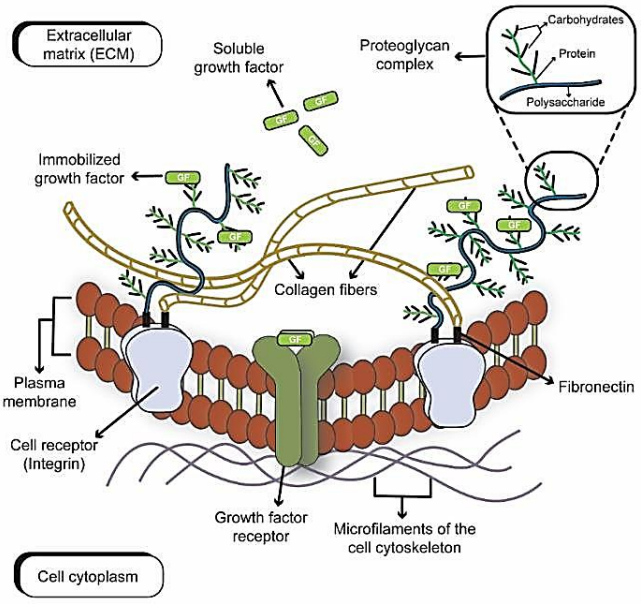

Figure 1.4 Interaction of extracellular matrix (growth factors, collagen fibers, proteoglycan, fibronectin) and cell membrane proteins (receptors, plasma membrane).

The animal extracellular matrices are divided into two categories, i.e., the interstitial matrix and the basement membrane. The interstitial matrix is located in the intercellular spaces and largely composed of polysaccharides and fibrous proteins, acting as a compression buffer against the stress. Basement membranes (BMs) are sheet-like ECM composed of specific ECM proteins, supporting as substrate the formation of epithelial or endothelial cell layers. Each type of connective tissue in animals has a type of ECM: collagen fibers and bone mineral comprise the ECM of bone tissue; reticular fibers and ground substances comprise the ECM of loose connective tissue; and blood plasma is the ECM of blood.

ECM provides not only a physical support for cells but also important signaling through interactions between αβ integrin heterodimer and ECM peptide motifs. Therefore, cell migration, proliferation, differentiation and survival are all ECM dependent [34-37] (Figure 1.5A).

BMs are also important and found underneath all epithelial and endothelial cell layers [38-41]. They support and help the organization of cell layers and act as a barrier, together with the attached cell layer, to protect the organ, limit the loss of large molecules but allow selectively small molecules. BMs are made principally by type IV collagen [42, 43], laminin [43, 44], nidogen (previously called entactin) [45, 46] and perlecan [45, 47, 48]. Each of them plays a role in the structural assembly, which is characterized by two distinct but tightly linked polymer networks, one made of type IV collagen and another of laminin to ensure the BM's stability. Different from other types of collagen which are all fibrous, type IV collagen cannot form fibrous with its triple helix composed of three α-chains. Laminin is characterized by a heterotrimeric three-pronged fork made of α-, β-, and γ-chains. More than two laminin isoforms were found with different combinations of five α-chains, three β-chains, and three γ-chains. Laminin isoforms also provide different structural variations, which contribute to a functional diversity of BMs. Type IV collagen and laminin networks are connected by nidogen and perlecan, which are secreted by cells and cannot self-assemble into a network (Figure 1.5B). Finally, epithelial and endothelial cells adhere to a BM surface by forming integrin-containing focal adhesion and hemidesmosomes.

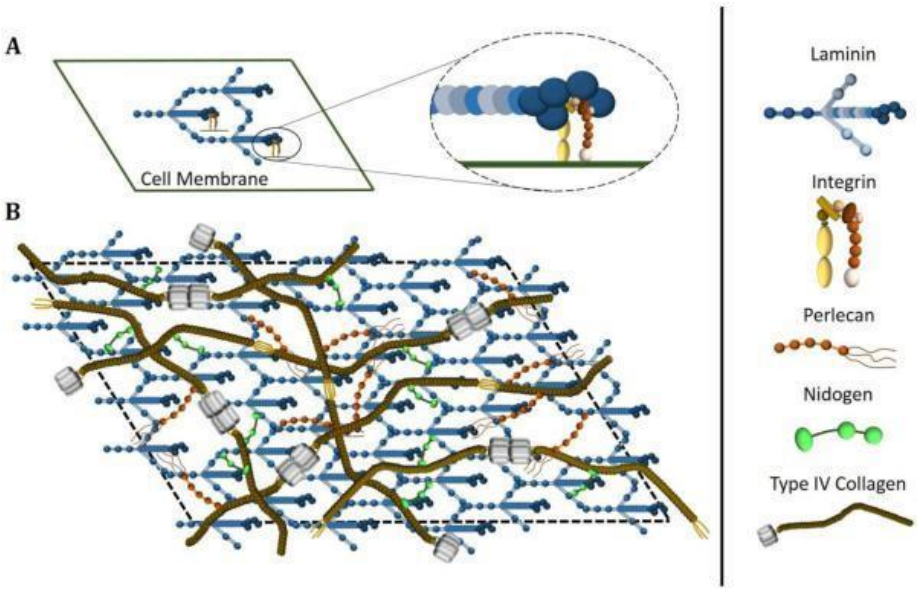

Figure 1.5 Illustration of basement membrane (laminin, type IV collagen, perlecan, nidogen) and cell-basement membrane interaction via integrin-laminin coupling.

1.2.2 Soluble factors

In the cell and extracellular matrix, there are many different types of soluble factors [49, 50] including growth factors for the development, cytokines for immune-modulating, hormones for transferring signals.

Growth factors refer to the natural protein which can stimulate cell proliferation and cell differentiation [51-57]. They regulate various activities and functions of cells. As signaling molecules, growth factors can activate specific receptors on the surface of target cells. These factors usually promote cell differentiation and maturation. Different growth factors have diverse functions, for example, bone morphogenetic protein stimulates the differentiation of bone cells; while vascular endothelial growth factor stimulates the proliferation of vascular endothelial cells.

Cytokines comprise interleukins, interferons, tumor necrosis factors, chemokines, and lymphokines [51, 58-62]. They are produced by macrophages, mast cells and B and T lymphocytes, endothelial cells, fibroblasts and a large variety of stromal cells.

Some growth factors may cause apoptosis of target cells and some cytokines may have inhibitory effects on cell growth and proliferation.

Hormones are chemical messengers that pass from one cell to another and change the cell's metabolism with a small dose. They are produced by cells, glands, or organs that can affect the activities of other cells in the body [63-69]. They are usually transported to designated locations in the body through the blood, and cells respond to hormones through their special receptors.

After the hormone molecule binds to a receptor protein, it opens a signaling pathway for signal transduction and eventually causes the cell to respond specifically. Hormone molecules secreted by the endocrine system are usually released directly into the blood, mainly into blood capillaries. Although the amount of hormones in the human body is quite small, it has a huge impact on health [70-73]. Lack of or excessive secretion causes various diseases, for example too much growth hormone secretion will cause gigantism, too little secretion will cause dwarfism; and excessive secretion of thyroid hormone will cause palpitations, hand sweats and fast metabolism, too little secretion will easily lead to obesity, drowsiness, etc.; insufficient insulin secretion will lead to diabetes.

1.2.3 Cell-cell contact

Cell-cell contact is critical to multicellular organisms. Some cell-cell interactions are stable such as cells in the epithelium and some others are transient such as the interactions between immune cells and that between immune cells and infected cells in a host tissue. Three types of cell-cell junctions are critical to the maintenance and function of an epithelium:

Tight junction is a protein complex that seals neighboring cells together in an epithelial sheet to prevent leakage of water and water-soluble molecules between them [74-76].

Desmosomes (Anchoring junction) is a cluster of proteins associating the intermediate filaments in one cell to those in a neighbor [77-79].

Gap junction (Communicating junction) is composed of transmembrane proteins called connexins and allows the passage of small water-soluble ions and molecules [80-83].

1.3 Physiological systems

1.3.1 General notions

The human body is composed of trillions of physiological systems, from intracellular systems that operate at the molecular level to the highly developed central nervous system (CNS). In terms of complexity and scale, these systems range from systems contained within cells to systems responsible for coordinating the activities of millions of cells. However, every physiological system has a common purpose, which is to regulate all aspects of body functions to maintain homeostasis.

From the perspective of macroscopic human organs, the human body is made of ten physiological systems [84, 85], i.e., the cardiovascular, digestive, endocrine, immune, muscular system, nervous, renal, reproductive, respiratory, and skeletal systems. Their functions and related organs and cells are listed in Table 1.

Table 1 Physiological systems and their functions

Physiological sys.	Related organs and cells	Functions
Cardiovascular system [86-89]	Heart, blood vessels, and the blood	● Circulates O2 and removes CO2. ● Provides cells with nutrients. ● Removes the waste products of metabolism to the excretory organs for disposal. ● Protects the body against disease and infection. ● Clotting stops bleeding after an injury. ● Transports hormones to target cells and organs. ● Helps regulate body temperature.
Digestive system [90, 91]	The gastrointestinal tract, the liver, pancreas, and gallbladder	● Proteins break into amino acids ● Fats break into fatty acids and glycerol ● Carbohydrates break into simple sugars
Endocrine system [92, 93]	Hypothalamus, Pituitary, Thyroid, Parathyroids, Adrenals, Pineal body, The ovaries, The testes,	● Makes hormones that control your moods, growth and development, metabolism, organs, and reproduction. ● Controls how your hormones are released. ● Send those hormones into the bloodstream so they can travel to other body parts.
Immune system [94-96]	Bone marrow. Thymus. Lymph nodes. Spleen. Tonsils. Mucous membranes.	● Fights disease-causing germs (pathogens) like bacteria, viruses, parasites, or fungi, and to remove them from the body, ● Recognizes and neutralizes harmful substances from the environment, and. ● Fights disease-causing changes in the body, such as cancer cells.
Muscular system [97, 98]	Skeletal muscle. Smooth muscle. Cardiac muscle.	● Mobility, Stability, Circulation, Respiration, Digestion, Urination, Organ protection, Temperature regulation
Nervous system [99, 100]	The brain, Spinal cord, Sensory organs, All of the nerves	● Control of the body's internal environment to maintain 'homeostasis' ● Programming of spinal cord reflexes. ● Memory and learning. ● Voluntary control of movement.

Renal system [101-103]	The kidneys, Renal pelvis, Ureters, Bladder, Urethra.	● Eliminates waste from the body. ● Regulates blood volume and blood pressure. ● Controls levels of electrolytes and metabolites. ● Regulates blood pH.
Reproductive system [104-106]	Male: the penis, scrotum, testes, epididymis, vas deferens, prostate, seminal vesicles, and the urethra. Female: the ovaries, Fallopian tubes, uterus, vagina, accessory glands, and external genital organs	● Produce egg and sperm cells. ● Transport and sustain these cells. ● Nurture the developing offspring. ● Produce hormones.
Respiratory system [107]	Nose. Mouth. Throat (pharynx) Voicebox (larynx) Windpipe (trachea) Airways (bronchi) Lungs.	● Gas Exchange – oxygen and carbon dioxide. ● Breathing – movement of air. ● Sound Production. ● Olfactory Assistance – sense of smell. ● Protection – from dust and microbes entering the body through mucus production, cilia, and coughing.
Skeletal system [108-110]	Bones, Ligaments, Tendons, Joints	● Support, movement, protection, production of blood cells, storage of ions, and endocrine regulation.

1.3.2 Lung and alveoli

. The lungs contain approximately 300 to 500 million alveoli, connected to the alveolar ducts and respiratory airway bronchioles [111, 112]. The alveoli are the elementary units of the lungs that ensure respiration, i.e., the gas exchange or extracting oxygen from the atmosphere and transferring it into the bloodstream, and reversely, releasing carbon dioxide from the bloodstream into the atmosphere. Each alveolus is surrounded by a blood capillary network to ensure receiving deoxygenated blood from the heart for a maximum release of carbon dioxide and sending oxygenated blood with a maximum absorbed oxygen to the body [113, 114].

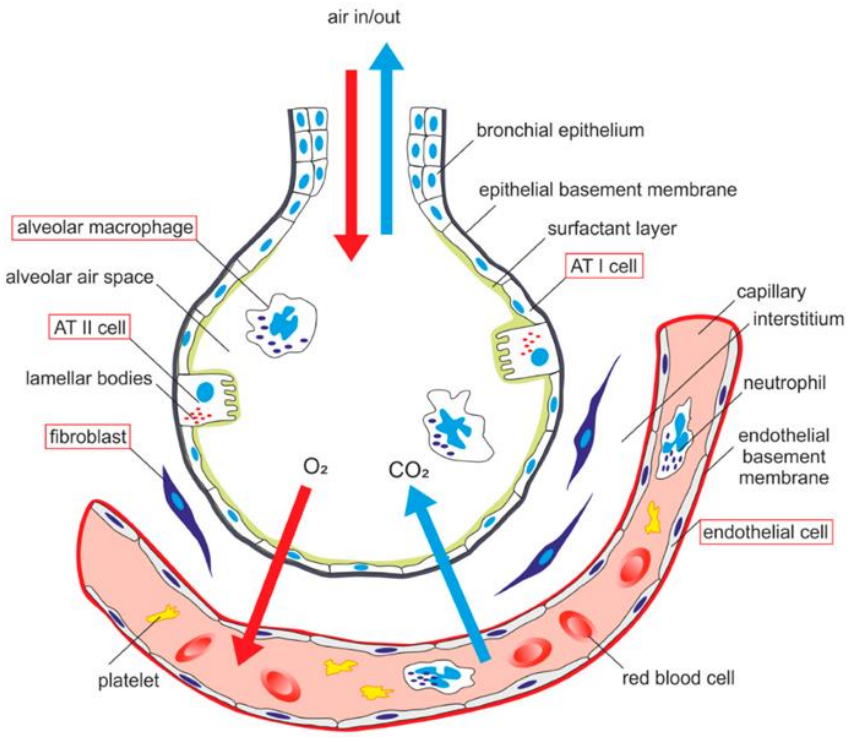

Figure 1.6 Illustration of alveolus made of an alveolar sac, a blood capillary, alveolar macrophages, fibroblasts, and associated basement membranes, and gas exchange function.

Microscopically, the lung alveoli are constructed with two types of alveolar epithelial cells, capillary endothelial cells, macrophages, and fibroblasts (Fig 1.6).

Alveolar epithelial type I cells (AT1) are thin squamous cells for oxygen diffusion from air sac to capillaries across the basement membranes which cover ~96% of the total lung surface area [115]. Alveolar epithelial type II cells (AT2) are cuboidal cells for producing surfactant proteins and lipids, which are important for keeping a low surface tension of the alveoli and preventing the collapse of the alveoli upon breathing [116, 117].

AT2 cells are also capable of responding to innate immune stimuli, thus having the functions in the immune response. AT1 and AT2 cells are both derived from alveolar progenitor cells [118]but AT2 cells themselves can also be self-renewed and become AT1 cells [119, 120].

Alveolar macrophages (AMs) are tissue-specific immune cells that are found on the luminal epithelial surface of the alveoli [121-123]. They are the first protective line against invading pathogens. AMs are heterogeneous in disease environments where a subset of monocyte-derived AMs express profibrotic genes [124]. It is known that many acute and chronic lung diseases are associated with inflammation of alveoli but many questions remain to be answered.

1.4 Cell culture substrate

Conventionally, culture dishes, flasks, multi-well plates, etc., are used for cell culture and cell-based assays. To get a better performance, a variety of cell adhesion molecules are used to coat the cell culture surface. However, these coatings may not be sufficient to achieve particular functionalities because of 2D characteristics of the culture substrate.

The problem emerged for culture and differentiation of pluripotent stem cells, co-culture of more than two types of cells, tumor spheroids, organoids, etc. In such cases, cells may not be always organized in 2D and more sophisticated ECM proteins organizations have to be introduced to achieve tissue or organ-like higher functions. In the following, we discuss cell culture-related material properties.

1.4.1 Hydrogels

A hydrogel is a network of cross-linked polymer chains which is intrinsically hydrophilic and water permeable. Due to their flexibility in synthesis, high biocompatibility, large range of constituents, and unique physical characteristics, hydrogels became one of the best choices for biomaterial engineering and tissue engineering [125-127]. Hydrogels can also be used for drug and protein delivery as well as adhesives or barriers between tissue and material surfaces [128, 129].

Poly (ethylene glycol) (PEG) and derivatives: PEG is a synthetic polymer largely used in biomedical and biotechnological fields [130]. The molecular weight of PEG covers a broad range between 10^2 and 10^7 g/mol. The chemical structures of PEG such as linear, branched, or combined chains are available. The synthetic procedure determines the polymer's end groups which allow the introduction of different specific or functional groups as well as linkage to other polymers. Nevertheless, PEG-based biomaterials are resistant to hydrolytic or enzymatic degradation which causes concern about accumulation effects. Cell-binding sites like integrin need to be incorporated into the polymeric matrix to enable cell adhesion. The formation of PEG-based hydrogels is usually based on various mechanisms including ionic, physical, or covalent crosslinking. PEG-based hydrogels, however, hold the highest mechanical stability by covalent crosslinking, for example, by introducing diacrylate units into PEG chains which results in poly (ethylene glycol) diacrylate (PEGDA). In contrast to classic polyesters, these materials do not release acidic by-products during their degradation and also are reported capable of cell adhesion [131].

Agarose: Agarose is a linear polysaccharide extracted from seaweed. Most commonly known as a component of agar, it is formed by a disaccharide of β-D-galactose and 3,6-

anhydro-α-L-galactopyranose [132]. Agarose can be dissolved in hot water using a water bath or simply a microwave oven. Agarose gel can be formed upon cooling. The gelation process is thermoreversible at gelation temperatures, which are specific depending on different types of agarose or the methoxyl content. Agarose can form strong gels at concentrations even below 1%. As for suspension culture, agarose can form a thin gel layer on the surface coating. Agarose gel also offers a high diffusion rate and is commonly used as filters, or purification, due to its porous structure and adjustable pore sizes (100-500 nm) which are determined by agarose concentration.

Gelatin: Gelatin is produced by acidic, alkaline, or hydrolysis of collagen from bovine or porcine skin, thus it is a biodegradable protein [133]. By hydrolysis, random gelatin chains can be produced by breaking up the collagen's triple helix structure. Gelatin can be also classified into two types depending on the origin and extraction reaction.

Gelatin Type A is processed by acid, generally with a low viscosity but high bloom.

Gelatin Type B is processed by alkali, generally with a high viscosity but low bloom.

Upon cooling, a three-dimensional hydrogel network can be formed by reassembling random gelatin chains into a triple helix structure. Both in vivo and in vitro, gelatin is enzymatically degraded without producing harmful species. Moreover, gelatin still contains integrin-binding sites which promote cell adhesion [134].

Gelatin methacrylate (GelMA): Gelatin's gelation is a temperature-dependent, reversible process. However, the use of gelatin hydrogels as scaffold materials is limited due to their rapid degradation property [135-137]. Thus, the vinyl methacrylate groups in the gelatin polymeric backbone can result in stable and covalent crosslinking networks, since they can react between themselves or with vinyl groups of other small molecules, oligomers, or polymers through photo- or temperature-initiated radical polymerization.

Matrigel: a commercial hydrogel containing protein mixture isolated from the Engelbreth-Holm-Swarm (EHS) mouse sarcoma, an ECM-protein rich tumor [138]. Matrigel is thereby composed of several ECM proteins like laminin and collagen, making it an excellent substrate or hydrogel for both two-dimensional cell adhesion and three-dimensional cell culture or organoid culture. Some growth factors and proteins are also included in Matrigel. It polymerizes rapidly into a 3D network at temperatures between 22 and 35 ℃. At 4 ℃, Matrigel starts to thaw. Consequently, the preparation and processing of Matrigel-based samples need to be performed under cold conditions.

Collagen: the most abundant protein in mammals (up to 25% to 35% of the whole-body protein content), the main structural protein in ECM of different connective tissues, and the

most prominent biopolymers for tissue engineering and biomedical applications [139-142]. Collagen is made of amino acids that bind together to form a triple helix of elongated fibril known as a collagen helix. It is mostly found in fibrous tissues such as tendons, ligaments, and skin. It is highly organized with an extraordinary tensile strength but can be degraded by enzymatic reactions. Finally, it offers many integrin-binding sites for cell adhesion.

Collagen has five most common types found in different tissues or organs:

Type I: mostly in skin, tendon, vasculature, organs, bone;

Type II: mostly in cartilage;

Type III: mostly in reticulate, commonly alongside type I;

Type IV: forms basal lamina and epithelium-secreted basement membrane);

Type V: mostly on cell surfaces, in hair and placenta.

In practice, collagen has a large number of applications, including tissue regeneration, wound healing, cosmetic surgery, bone grafts, and cardiac imaging [139].

1.4.2 Nanofibers

Nanofibers are fibers with diameters in the nanometer range. Nanofibers can be generated from different polymers and thereby have different physical properties and application potentials. The most commonly used natural polymers include collagen [143], gelatin [144], silk fibroin [145], keratin [146] and polysaccharides such as chitosan [147]and alginate [148]. Synthetic polymers include poly(lactic acid) (PLA) [149], polycaprolactone (PCL) [150], poly(lactic-co-glycolic acid) (PLGA) [151], etc. also hold excellent mechanical properties and biocompatibility. Polymer chains are connected with covalent bonds. The diameters of nanofibers vary depending on the type of polymer and the method of fabrication. Every type of nanofibers is unique in terms of surface-to-volume ratio, porosity, mechanical strength, and flexibility in functionalization compared to their microfiber counterparts.

To fabricate nanofibers, many different methods have emerged, including electrospinning [152], drawing, self-assembly, template synthesis, and thermal-induced phase separation [153]. Among all methods, electrospinning is the most commonly used method to produce nanofibers due to the straightforward setup, the compatibility to mass-produce nanofibers from different polymers, and the capability to fabricate ultrathin fibers with controllable diameters, orientations, and different blend compositions. This technique (including coaxial electrospinning) allows controlling the shape and organization of the fibers so that different

structures (i.e., hollow, flat, and ribbon-shaped) can be produced, depending on application purposes.

Nanofibers have many applications such as tissue engineering, drug delivery, cancer diagnosis, optical sensors, and air filtration.

1.4.3 Surface treatment

For more than 100 years, glass flasks and Petri dishes were used for cell culture. Many cells, however, especially primary cell cultures, had difficulty attaching to glass. In 1956, George Gey coated glass using collagen from rat tail to improve cell attachment and growth [154]. Besides, glass Petri dishes require very careful cleaning procedures to ensure that detergent residues do not interfere with cellular processes. As a result, the researchers began to use disposable plastic Petri dishes (including the first microplate) for experiments. By the 1960s, plastic flasks, Petri dishes, and 96-well plates were all available on the market. Most of these containers are made of polystyrene, which is a long carbon chain polymer with benzene rings connected to other carbon atoms. Polystyrene was chosen because it has excellent optical transparency, is easy to mold, and can be sterilized by radiation. However, it also has a significant disadvantage because it is a hydrophobic (non-wettable) polymer, and it is difficult for cells to attach. In general, a hydrophilic surface is required to allow the deposition of cell attachment proteins (vitronectin and fibronectin) which are found in serum-containing medium. Using corona discharge under atmospheric conditions or gas plasma under vacuum is the common method to treat freshly molded polystyrene surfaces. These processes all produce high-energy oxygen ions, which are oxidized and grafted onto the surface polystyrene chains (Figure 1.7), so once the medium is added, the surface becomes hydrophilic and negatively charged [155-158] By the mid-1970s, most researchers were culturing cells in treated polystyrene containers instead of glass containers.

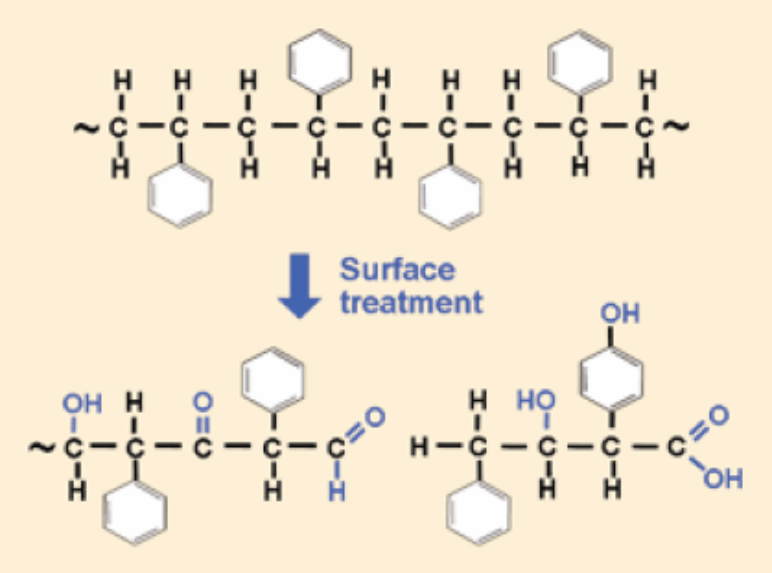

Figure 1.7 Molecule structure of polystyrene before and after surface treatment by oxidizing and grafting. After the treatment, polystyrene becomes suitable for cell culture.

In recent years, nanofiber meshes mainly fabricated by electrospinning using biocompatible polymers have shown remarkable cell culture advantages, such as good cell attachment, biodegradation, easy-manipulation, and also low cost [134, 159-162]. Combined with hydrogels like PEGDA, elegant cell scaffolds or microcarriers can be formed depending on different applications [163].

1.4.3.1 Cell-attachment treatment

When serum-free media are used for cell culture, even treated polystyrene cannot be used since there is no more serum protein deposition. Then, BM proteins were considered for surface coating of the substrate to improve the cell attachment, migration, and function [164]. In addition, mucopolysaccharides such as heparin sulfate, hyaluronic acid, and chondroitin sulfate, and synthetic polymers such as poly-D-lysine (PDL) are used for coatings to generate a positively charged surface of polystyrene. For certain cell types, it can enhance cell attachment, growth, and differentiation, especially in serum-free and low serum conditions. PDL coating can generally improve the attachment and growth of primary neurons, glial cells, neuroblastoma, and various transfected cell lines [165]. Inspired by this, nanofiber substrates using these coatings are more suitable for growing cells under serum-free conditions and maintaining primary cell cultures.

1.4.3.2 Ultra-Low attachment treatment

Sometimes there is a need to prevent the cell from attaching to a surface. Although untreated polystyrene surfaces are hydrophobic, certain cell types can still attach to it, due partially to their sterilization by irradiation. In order to minimize cell adhesion, Corning® introduced ultra-low adhesion surface coating containers in the 1990s. These containers have a very hydrophilic and neutrally charged hydrogel layer that is directly covalently attached to the polystyrene surface to prevent peeling. Because cell attachment proteins and other biological molecules are passively adsorbed to the polystyrene surface through hydrophobic or ionic interactions, the hydrogel surface naturally inhibits non-specific immobilization through these interactions, thereby inhibiting subsequent cell attachment. The surface is very stable, non-cytotoxic, and biologically inert.

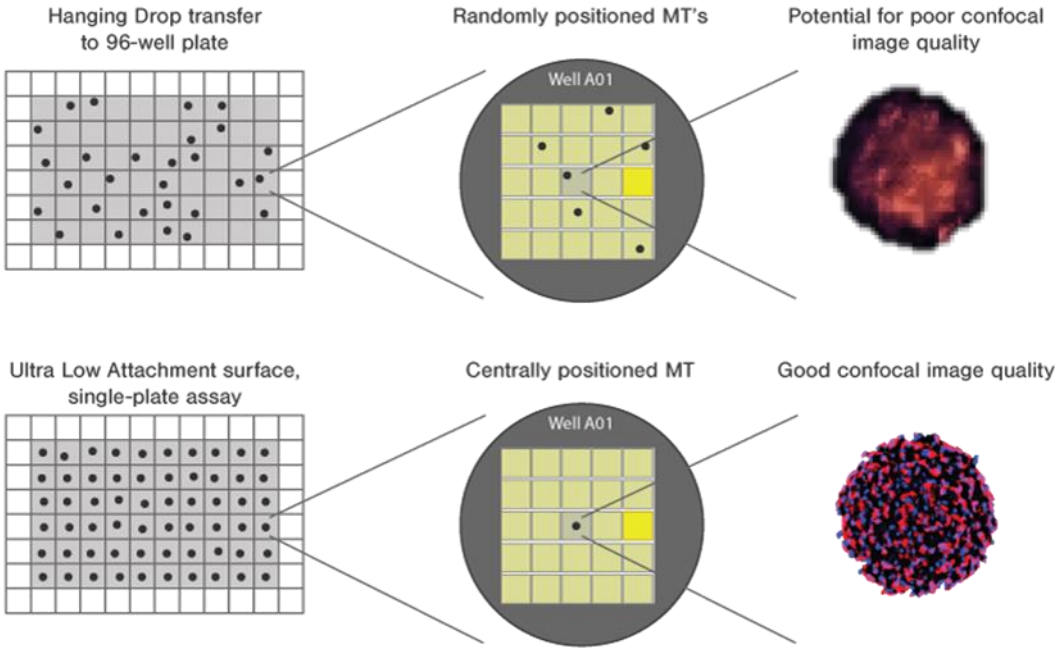

Figure 1.8 Formation of 3D microtissues on ultra-low attachment plate or after hanging drop transfer. Better image quality can be achieved for those on ultra-low attachment plates.

The ultra-low attachment surface can be used to prevent attachment and activation of macrophages and neutrophils [166]. It can also be used for spheroid and tumoroid formation (see Fig 1.8), which in turn allows isolating both primary tumor and stem cell spheroids from the brain and mammary tissues [167-171], and can help avoid overgrowth by normal cells which will undergo apoptosis. The ultra-low attachment surface is also recommended for easy-to-harvest embryoid bodies derived from embryonic stem cells or induced pluripotent stem cells [172].

Besides, lab-made ultra-low attachment substrates also hold good quality based on commercial Petri dishes and multi-well plates or the formation of hydrogel multiwells. Agarose is an ideal polysaccharide which inhibits cell attachment and promotes cell aggregation due to the linear molecule structure. In laboratory studies, low attachment surfaces are usually formed by applying a thin layer of agarose gel on Petri dishes or multi-well plates. Uniform tumor spheroids and embryoid bodies can be also easily harvested via cell seeding on this hydrogel surface [173, 174]. Moreover, nanofiber-based bioscaffolds can be also coated with a thin layer of gel to form a low-attachment 3D culture substrate.

1.4.4 From 2D to 3D culture substrate

For many years, culturing cells in Petri dishes and tissue culture flasks (i.e. in vitro) has experienced a completely different microenvironment compared with the natural tissues in the complex three-dimensional extracellular matrix (in vivo), resulting in the various cell morphology and functions. Compared with the current in vivo research, the miniaturized microfluidic culture system (in vitro) can have more advanced tissue functions [175, 176]. Compared to any current in vitro models, this allows for more precise studies of the complex mechanisms of tissue growth, renewal and disease without the difficulties inherent in in vivo studies.

Nowadays, there are many models available for cell culture, namely: 2D or 3D static cell culture and 2D or 3D perfusion microfluidic cell culture. From 2D to 3D culture, cell growth behavior has undergone many changes, from cell shape and structure to cell-cell adhesion tissue, mainly due to differences in cell microenvironment. Clearly, in vitro 3D culture can better simulate the in vivo condition of cells in organs and tissues. Compared with 3D static culture, microfluidic-assisted 3D culture can better deal with related topics, such as multi-cell complex environments, cell vascularization, and continuous medium exchange instead of discrete exchange [177-179]. Besides, several parameters of the sample (such as pH, oxygen, CO2, temperature, osmotic pressure, shear stress) need to be monitored for further downstream studies. All these issues make the 3D culture as close as possible to the internal organs. Recently, many efforts in microfluidic 3D cell culture have targeted lung, vessel, brain, and liver models, or improved cancer models [180-182]. These studies have a crucial impact on understanding the basis of cell activity, which plays a key role in determining physiological and pathological cell states (such as disease characteristics and response to stimuli). The main goal of the cell culture platform is to closely simulate the cell microenvironment in the body and maintain simplicity to obtain reproducible results.

1.4.5 Air-liquid interface

Many cells can be used to model the human respiratory system, including immortalized respiratory cell lines (i.e., A549 cells), primary cells from animals or human donors, and alveolar or airway epithelial cells derived from hiPSCs [183-186]. Although immortalized cell lines and primary cells from animals are widely used, data generated using these cells are not applicable to humans. Submerged culture of primary human alveolar or airway epithelial cells is possible; however, cells in this system fail to undergo further differentiation. In order to recapitulate the phenotype observed in vivo, primary human alveolar or airway epithelial cells must be cultured at an air-liquid interface (ALI) as shown in Fig 1.9.

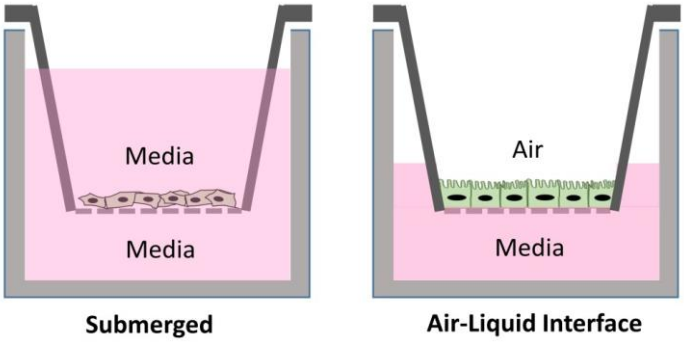

Figure 1.9 Submerged (left) and air-liquid interface (right) culture with a transwell insert

Cell culture at the air-liquid interface (ALI) is necessary for respiratory research since submerge culture is not applicable. ALI culture of alveolar epithelial cells can be used, for instance to:

A. Study the cell biology of the respiratory epithelium, since it is most physiologically relevant for in vitro modeling of the respiratory epithelium [187-189].
B. Study respiratory diseases. Alveolar epithelial cells from patients with chronic respiratory diseases such as cystic fibrosis, chronic obstructive pulmonary disease (COPD) and asthma, can be cultured using ALI techniques, enabling disease mechanisms to be studied in vitro.
C. Study infection of the respiratory epithelium. Some respiratory viruses selectively target cell types present only in fully differentiated alveolar cell cultures, such as the novel coronavirus SARS-CoV-2 binding to the angiotensin-converting enzyme 2 (ACE2) on alveolar epithelial cells [190-192].

D. Test drugs for inhalation delivery. Aerosol particles can be directly deposited onto the semi-dry apical cell surface, mimicking the deposition of powders onto the lung surface in vivo.
E. Test toxicity of inhaled substances. Responses of ALI-differentiated primary epithelial cells to insults such as tobacco smoke components closely mimic reported changes in the human alveoli [193, 194].

1.5 Microfluidic technologies

Microfluidic technologies can control a small volume of fluids (from microliters to picoliters) inside micrometer-level channels, which are increasingly used in various tissue engineering applications, such as bioreactor perfusion, cell patterning, and droplet-based fabrication of biomaterials.

1.5.1 Introduction of microfluidic device

At the sub-macro level, microfluidic technology is a rapidly developing field, and the key dimensions identified in this field are usually less than 1 mm. At such scale, microfluidic technology holds advantages of different physical laws and employ, for example, laminar flows, and dean flow, rapid diffusion and thermal transport, large surface area relative to its volume, and it is also related to surface and interfacial tension, capillary forces. According to these, microfluidic devices have found applications in many aspects, such as analytical chemistry, generation of energy, cell sorting, infectious disease detection molecular biology, and integration within microelectronic devices [195-197].

There are various controlling methods for generating fluid flow. Around 90% of microfluidic devices are driven by either electrokinetic flow or pressure-driven flow, making them the mainstream approaches for flow control in microfluidic devices. During the recent several years, various flow control methods have emerged out, including surface tension driven flow, shear flow, squeeze-film flow, and biologically driven flow. With the more precise flow control requirement, the fabrication methods of microfluidic devices have emerged in recent decades.

1.5.2 Fabrication methods of microfluidic device

1.5.2.1 Lamination

Here we describe a lamination method to fabricate microfluidic devices [198-200]. These are usually created as a stack to form microscale channels and structures by certain bonding

techniques using independently cut layers. Each cut layer can be considered as a 2D flow geometry in these devices and is closed by other layers below and above them. Then, the thickness of the channel layer is determined by the thickness of the material used to form the layer.

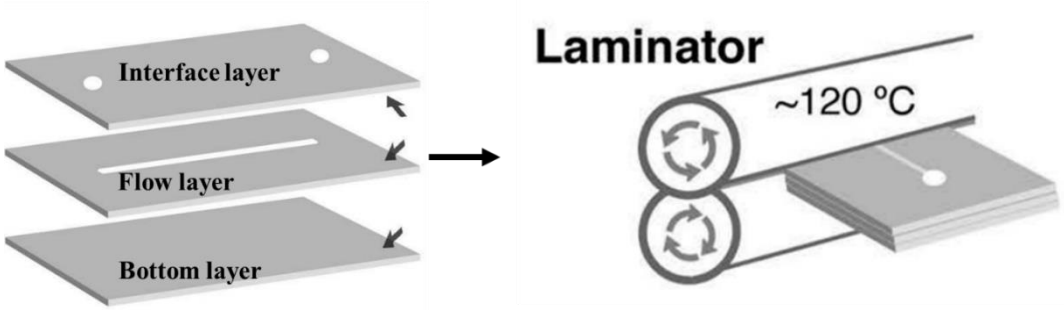

Figure 1.10 Schematic of a fabrication process of a microfluidic device made of an interface layer, a flow layer, and a bottom layer (left), by using a laminator working at 120℃ (right).

The simplistic laminate microfluidic device consists of three layers: a flow layer, an interface layer, and a bottom layer, as shown in Figure 1.10. For example, the interface layer and a flow layer can be cut by a cutting plotter, and the bottom layer uses a glass slide. After a lamination process, this assembled device can be used for microfluidic applications, for example, polymerase chain reaction (PCR) [201]., Polymers (including polycarbonate and acrylic) and glass slides are commonly used materials for a lot of reasons: solvent compatibility, optically clear, and low cost. Besides, simple bonding by double-sided adhesive could be compatible with a large variety of materials.

1.5.2.2 Molding

In terms of molding, microfluidic fabrication can be classified into three well-defined techniques: hot embossing molding, injection molding, and soft lithography (see Fig 1.11).

1.5.2.2.1 Soft lithography

Soft lithography [202, 203] also known as replica molding refers to a technique used to produce microdevices or three-dimensional structures by molding and curing elastomers on a mold. The most common devices made by this technology are microfluidics, which is widely used in cell biology. PDMS (polydimethylsiloxane) is the most commonly used elastomer in this technology due to its biocompatibility, high thermal stability, high chemical stability, low toxicity, chemical inertness, and insulation [204]. It also is transparent to ultraviolet and visible light, low cost, easy to process, good mechanical flexibility, and durability. This is why the

term "soft" is addressed. Silicon, a photoresist (the most commonly used is SU-8) or metal molds processed by lithography or reactive-ion etching (RIE) are currently commonly used materials. Soft lithography is also very suitable for other polymers, gels and organic monolayers. It is a simple, reliable, and low-cost process to replicate three-dimensional structures (from centimeters to micrometers). Microfluidic devices can be finally assembled using plasma bonding which eradicates the contaminants and raises the surface energy.

1.5.2.2.2 Injection molding

As a robust, simple, and standard technique, injection molding can be used for the manufacturing of microfluidic devices. This technique enables mass production of devices (thousands to millions) at a relatively low cost per device while at the same time maintains strict tolerances and desired reproducibility [205-207]. Besides, injection molding can use thermoplastic materials such as polycarbonate (PC, a temperature-stable material for PCR), polystyrene (PS, a classical material for culture vessel), cyclic olefin copolymers (COC, a superior material for microscopic observation), and polypropylene (PP, an inertia material to organic solvents). During the injection molding process, thermoplastic is injected in molten form into a closed cavity, where it may be equipped with contact pressure or water cooler. The disadvantages of this process include high mold cost, longer mold manufacturing time, and possible geometric limitations on certain micro features. Microfluidic devices using this technology may need numerical flow simulation to help to make design decisions.

1.5.2.2.3 Hot embossing

As a quite versatile method of replication, hot embossing can transfer the macro- and microstructures from the master to the polymer by using high pressure and high temperature [208, 209]. It provides a variety of applications, for example, microfluidics. Molds with features in microns can be produced, and then the parts can be stamped with materials such as PS, COC, PMMA, polyethylene (PE), etc. For microfluidics and other applications, this method has advantages including being capable of quickly and cost-effectively producing very clean and precise features from materials that could not normally be processed by other technologies. After hot embossing, drilling, overlay bonding, and even integration of wires and sensors into the device are all possible.

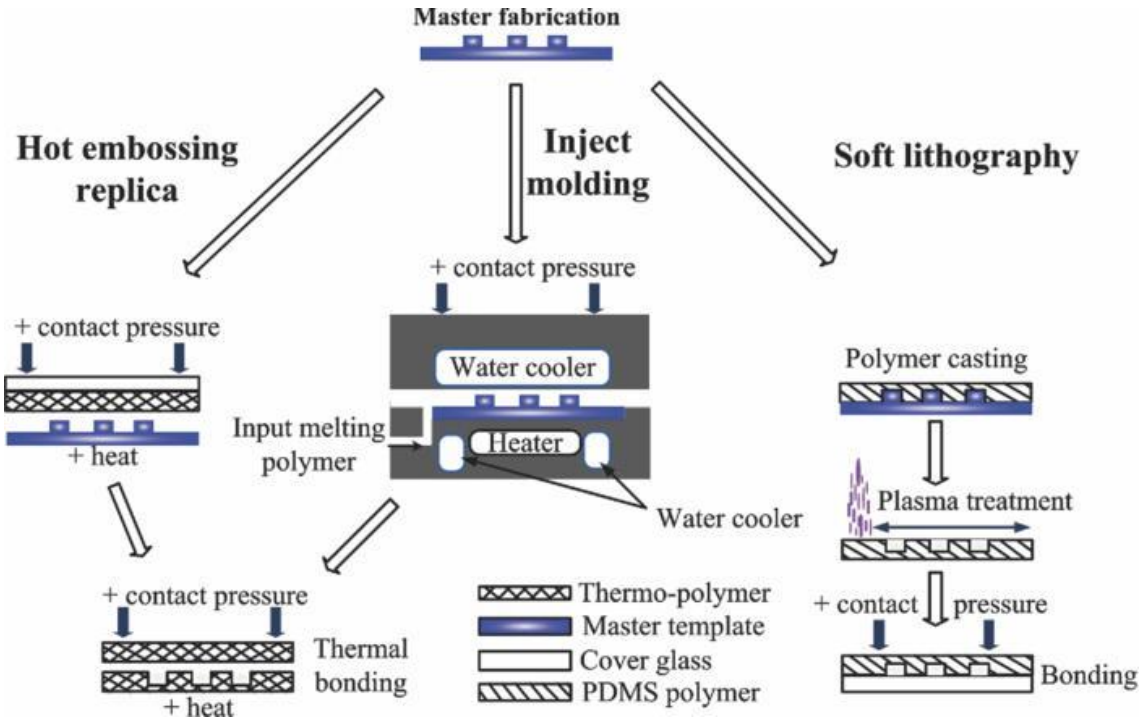

Figure 1.11 Schematic of typical fabrication procedures of microfluidic devices: (left) hot embossing, (middle) inject molding, and (right) soft lithography. [210]

1.5.2.3 3D printing

3D printing is a manufacturing technique formed layer-by-layer, namely a layer of new material is stacked on top of the previous layer. 3D printing technology has fascinating potential in the field of microfluidics and can be easily used for prototyping. In this section, we mainly focus on fused deposition modeling (FDM) and stereolithography (SL).

1.5.2.3.1 Fused Deposition Molding (FDM)

Fused deposition molding is the most commonly used 3D printing process in the world, simple and efficient [211, 212]. It provides great potential and flexibility for creating complex 3D structures and prototypes of parts of any geometry for microfluidic devices. Briefly, the process of FDM includes the melting of polymer filaments and extrusion of polymer lines(see Fig 1.12). The filament starts by being fed and melting in a metal cylinder with heating, and ends at the nozzle. When fresh filaments are continuously supplied into the assembly, the molten polymer is extruded out of the nozzle, and then forms a line, which is approximately the same diameter as the nozzle. In order to form a plastic part based on these lines, the nozzle is placed at a distance above the metal plate (printing bed) according to the required resolution. After the filament leaves the nozzle, it is then deposited on the printing bed and can be heated to promote adhesion. When the printing bed and nozzles move in a controllable manner in the vertical direction, we can draw a two-dimensional graph with the thickness of the polymer line

on the printing bed. The thickness (depends on the resolution of the equipment, usually between 100 μm and 300 μm) is affected by (i) the distance between the printing bed and the nozzle ; (ii) the ratio between the printing speed and the extruding flow rate through the nozzle. After finishing the first layer, the print bed steps lower a certain distance (that is, the thickness of the single layer), and then print a second layer on top of the previous layer. Thus, three-dimensional parts can be accumulated by repeating the above steps. Together with the CAD software package, it is possible to realize the "what you see is what you get" concept. Another advantage is that various biocompatible thermoplastics, such as PLA, acrylonitrile butadiene styrene (ABS), PC, polyamide, and PS can be used for printing. This method also has potential in the development of packaging and enclosures for microfluidic components and electronic parts (such as microelectrode array (MEA) printing).

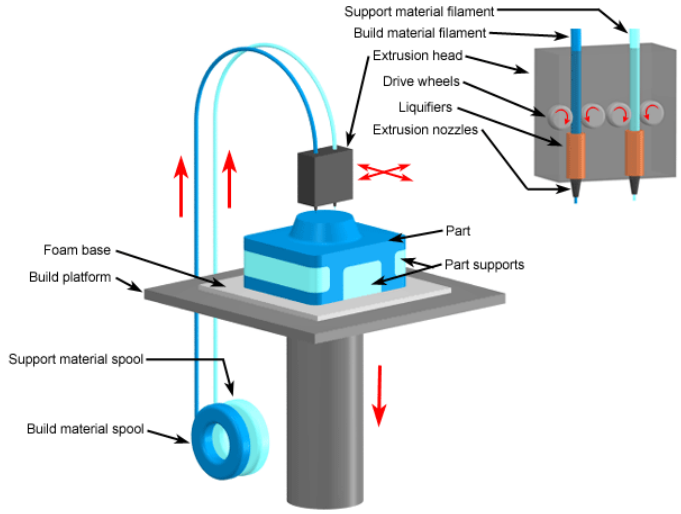

Figure 1.12 A model system for Fused Deposition Molding (FDM), including an extrusion head, a foam base, a build platform and materials. [213]

1.5.2.3.2 Stereolithography (SL)

Stereolithography forms parts using ultraviolet curing [214]. The photopolymer is used for manufacturing as the basic material. Before manufacturing, the photopolymer is usually a liquid, after scanned with an ultraviolet laser, and then a low-power, highly focused laser is used to solidify it. Fig 1.13 shows the printing schematic, the platform steps lower by the same distance to the layer thickness (usually 50 μm – 150 μm), and the laser beam continues to advance to the next layer. By repeating the process, the desired product is finally completed. Each layer still has excess polymer that remains liquid and is washed away from the platform. The final product should be cured under ultraviolet light again. The main advantage of SL

manufacturing is the very high surface resolution accuracy, which offers great potential for microfluidic applications.

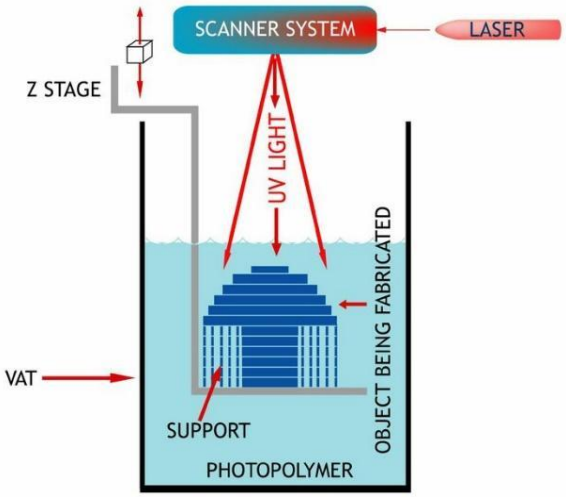

Figure 1.13 A model system for Stereolithography (SL), including a laser scanner system, a Z stage, and a type of photopolymer.

1.6 Cell-based assays

The challenge of understanding the biology of living organisms, including disease processes, lies in its incredible complexity. Scientists have long realized the value of using cells, the most basic unit of life. According to the research, the cell signal transduction, proliferation, apoptosis, cellular genetics/morphology, neurobiology, cancer, etc. of living organisms are analyzed.

The term "cell-based assay", in the pharmaceutical industry and academic research, is generally used to represent a certain measurement on living cells [215]. The needs of the pharmaceutical industry to effectively commercialize drugs are the driving force for innovation in cell-based assays. The industry hopes to use cell-based detection methods to solve the expensive cost and long cycle of drug development. Because the failure of an Investigational New Drug (IND) in the third phase of clinical trials will often cost pharmaceutical companies hundreds of millions of dollars, which is an unacceptable level for most companies.

Many scientific resources are invested in cell-based assays. Unfortunately, the promise of these technologies is daunting, and failure seems to happen at any time. There are many reasons for drug failure. Although animal models are commonly used in IND toxicity and metabolism studies, they are still too expensive and low-throughput, which usually limits their use in the later stages of preclinical testing. In addition, animal models may not always replicate human

metabolism, leading to late failure due to unforeseen toxicity issues. Idiopathic adverse drug reaction (ADR) is another cause of late-stage drug failure due to differences between people. For example, due to a few cases of hepatitis caused by drugs, type II diabetes Troglitazone was withdrawn from the market three years after it was released to the market. ADR caused by heterogeneous differences is often rare. Even large-scale clinical Phase III trials may not be able to detect the low incidence of typical idiosyncratic liver failure (about 1 in 10,000).

Therefore, a fast cell-based method is needed to predict IND with high accuracy. Considering this point, but so far, there is no single technology or group of technologies that can decrease the failure rate in the later stage. An important consideration is the influence of cell types in the study of toxicity testing and metabolism. It is generally believed that long-established cell lines are not superior to primary cells because they are believed to more closely replicate "real cells". However, Primary cells are unstable and can only be cultured for a few generations, cells then begin to age and even undergo undesirable phenotypic changes.

Established cells have the advantages of easy culture stable and phenotypic, and are commonly used in cell-based assays. For example, the cell line HepG2 and NIH/3T3 have anaerobic metabolism, so they are ideal for testing mitochondrial toxicity. However, studies on liver toxicity indicate that the established liver cell lines are not ideal because they only weakly express cytochrome P450 enzymes, which is a protein for oxidizing steroids, fatty acids, and heterologous organisms and is important for the elimination of various compounds and the synthesis and decomposition of hormones.

The utilization of induced pluripotent stem cells (iPSC) is currently being studied to create better in vitro models for drug research [216]. For example, drug-induced liver damage on the differentiated liver model maintains functions longer than primary hepatocytes. ADR caused by idiosyncratic events is usually due to changes caused by patient-specific susceptibility factors (such as genetic factors). One solution to solve this problem is to create a large iPSC library that can be differentiated into hepatocytes as the basis for the automated determination.

Another limitation of traditional cell-based assays is geometric issues. Most cell culture assays are performed in two dimensions, while the real environment of in vivo cells is three-dimensional. 3D cell culture can better create or mimic the extracellular environment (geometry, scaffolds, forces acting on the cells) so that the cells respond to stimuli, toxins, etc. more like in the body.

1.6.1 Organ-on-a-chip

During the process of drug discovery, although animal experiments are essential for preclinical screening, we are still facing the issues such as species differences and even ethical considerations. In order to bypass these problems, cell-based assays have been fastly and actively performed by using human-source cells. However, since cells cultured in conventional cell culture systems generally cannot maintain their original organ functions and morphology, it is still hard to accurately predict the toxicity, efficiency, and organ interactions of drugs. As a new type of in vitro organ model, organ-on-a-chip technology based on microfluidic devices manufactured by micromachining has been extensively studied. As the microfluidic device technology can be used to simulate the in vitro physical and chemical environment, the on-chip organ device can be used to maintain cell function and morphology and replicate the interaction of organs. Currently, the functionalities of different organs or tissues including lung, liver, kidney, and intestine, have been replicated as various in vitro models. In addition, integrating multiple-organ functionalities on a microfluidic device is also a promising method to predict interactions between organs.

1.6.1.1 Lung-on-a-chip

The breathing area of the lungs is mainly for gas exchange by filling with air and maximizing the available surface area. When it refers to the alveoli (in which a basement membrane is used to separate the vascular endothelium and lung epithelium), the smallest functional unit of the lung can be monitored by applying cyclic mechanical stretching to the gas exchange interface. The resulting lung-on-a-chip model has led the development of our biologically inspired organ-on-a-chip today. One side of the porous membrane is plated with human-source alveolar or airway epithelial cells and exposed to air, and the layer of endothelial cells on the other side are perfused with vascular medium. The epithelial-endothelial cell membrane is then inserted into a chip that can be mechanically stretched to recapitulate the respiratory action experienced by the alveoli. The final lung-on-a-chip model (see Fig 1.14) is the first and has succeeded in demonstrating its organ-level behavior [217]. Moreover, numerical modeling was also used to inspire and optimize the design of the lung-on-a-chip chamber using a liquid flow, thereby controlling the gas concentration on both sides of the air-liquid interface and meantime giving a method for measuring gas changes between epithelial-endothelial chambers [218].

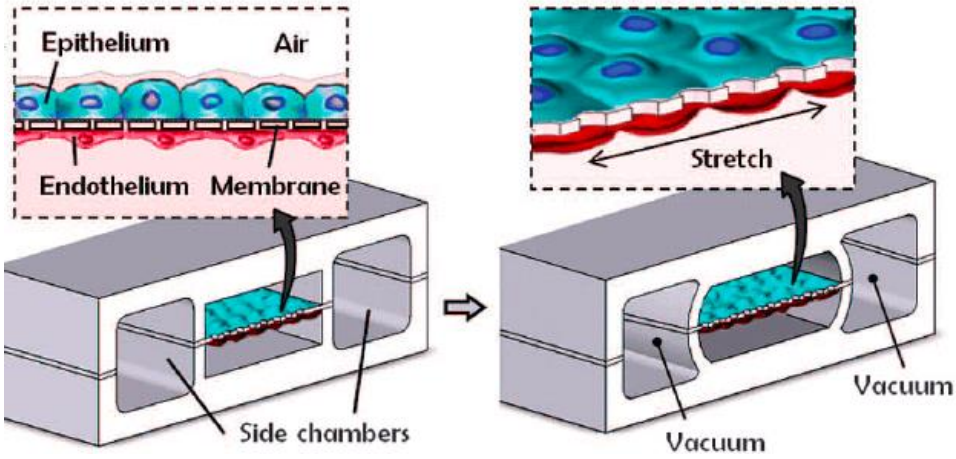

Figure 1.14 An example of the lung-on-a-chip, composed of an epithelium and an endothelium on both sides of a membrane which is continuously and mechanically stretched by applying of vacuum.

1.6.1.2 Liver-on-a-chip

The liver has the functions of glycogen storage, drug metabolism, detoxification, and synthesis of plasma protein. The smallest functional unit is composed of liver lobules or sinusoids and contains hepatocytes that are responsible for drug metabolism. Hepatocyte cultures show reduced function over time, this problem can be resolved by co-cultures (including supporting cells such as fibroblasts, and perfusion). The liver on-a-chip contains hepatocytes and fibroblasts, which are patterned or aggregated to form meaningful arrangements. The micropillar array is used to reconstruct the microstructure of liver lobules so that polarized cells form bile canalicular structures. The liver sinusoids on-a-chip are constructed by incorporating microchannels in which densely packed hepatocytes are connected to an endothelium layer, or membrane co-cultures supported by fluid flow. Human primary hepatocytes are usually used to construct liver on-a-chip models, but due to limited life and availability or cell lines with limited functions, their applications are heavily restricted [219]. Future researches using iPSC-derived hepatocyte models show high promise and can be studied in various patient situations.

1.6.1.3 Kidney-on-a-chip

The kidneys in vertebrates are organs the shape of two beans. They are on the left and right sides of the retroperitoneal space, with a length of about 12 cm for an adult kidney. Nephron is the smallest functional unit of the kidney, it is composed of the Henle loop, the proximal tubule, and the glomerulus. With the responsibilities for filtration and reabsorption, the kidneys frequently undergo toxic reactions during drug development. In each of the three compartments,

the various cell types have helped the development of a nephron on-a-chip to show functional urea concentration within the Henle loop, glomerular filtration, and proximal tubule reabsorption. The use of fluid flow in the proximal tubule on-a-chip containing primary cells can achieve functions, showing in vivo drug toxicity and pathophysiology. Microfluidic technology can also be suitable for mimicking the mechanism of drug delivery and its subsequent toxicity, for example when comparing the effects of continuous and bolus doses of the kidney on-a-chip[220].

1.6.1.4 Gut-on-a-chip

The development of the gut-on-a-chip allows us to study the transport, absorption and metabolism of oral drugs. Similar to a lung-on-a-chip platform, the gut-on-a-chip can be designed to model a large surface area which is provided by the microvilli in the gut. and a cyclic mechanical strain can be also used to mimic peristalsis [221]. The gut-on-a-chip was also used for the symbiotic microbial flora in some studies. 3D structure for villi formation has also been applied on the membrane-based gut-on-a-chip, which can also provide an intestinal epithelium with both the apical and basolateral perfusion. Other gut-on-a-chip models has tried to construct intestinal villi and catch functionality superior to the static Transwell system by inducing human Caco-2 cells through peristalsis and fluid flow, thus approaching the functionality of the human intestine. The method of using iPSCs to create an intestine model includes the use of inherent principles of 3D self-assembly, morphogenesis and differentiation to develop gastric organoids. The organoid-based method can realize the generation of multicellular 3D organoids based on the principles of developmental biology, and therefore can accelerate the application of iPSCs in organ systems.

1.6.1.5 Heart-on-a-chip

The frequent occurrence of human heart disease promotes the development of the human heart on-a-chip. The heart contracts in response to the excitatory electrical signals from the cardiac conduction system, thereby attracting blood. Because a bundle of contractile myocardial fibers can contract and generate force in response to depolarized electrical signals, these fibers can be considered as the basic functional unit of the heart. In a heart-on-a-chip, the function of pace-making sinoatrial nodes is always mimicked by electrical stimulation. The synchronized cell contraction triggered by electrical stimulation leads to the construction of a relevant cardiac on-a-chip model in a physiological aspect.

To design a cardiac on-a-chip, factors to consider include the anisotropic arrangement of human iPSC-derived cardiomyocytes, electromechanical stimulation, co-culture with cell types

(fibroblasts, alveolar cells, neurons, and endothelial cells), and real-time recordings of cardiac electrophysiology and contractility. Methods to obtain cardiomyocytes via hiPSCs have become highly effective with emerging protocols. Combining electrical stimulation with mechanical stimulation, we can enhance the maturation of cardiomyocytes and achieve physiological drug response. The perfusion of medium increases the functions of cardiac on-a-chip, this is developed by plating cardiomyocytes on the cantilevers which showed a deflection during cardiac contraction and demonstrated the positive inotropic effect of isoproterenol on the myocardial thin film[222]. Perfusion can also extend the long-term culture of the myocardium stretched on a nanofiber patch which supports stimulation and readouts of electrical signals through MEA, as well as a drug toxicity screening [134]. Finally, the vascularization using bio-printed aligned cardiomyocytes and endothelial cells can also be achieved by perfusion [223].

1.6.1.6 Multi-organ-on-a-chip

Within the circulatory system, cells and organ systems communicate through the secretion of extracellular vesicles and soluble factors with functions of mediating crosstalk. Therefore, the biomimetic integration method is very important for establishing the interaction between physiological organs in the organ-on-a-chip platform. Fig 1.15 shows that through microfluidic technology, each organ-on-a-chip model is connected to one another, thereby mimicking the in vivo effects of vascular perfusion and controlling the culture environment with respect to homeostasis[224]. These multi-connections can facilitate drug delivery and absorption between organs of interest.

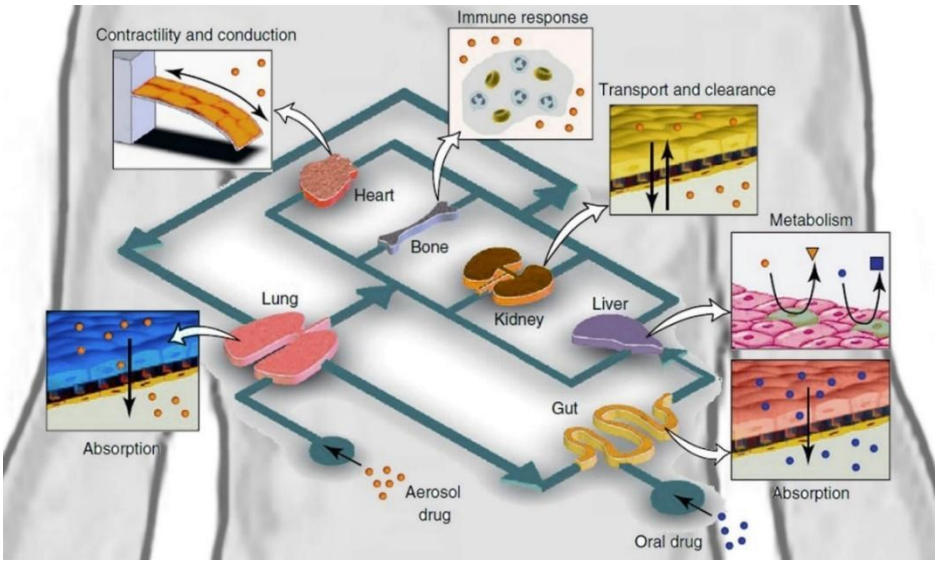

Figure 1.15 Schematic of a multi-organ on-a-chip, including heart, bone, kidney, liver, gut and lung, which are placed to have specific microfluidic compartments.

References

[1] Hoffmann, AR, et al. (2016). "The microbiome: the trillions of microorganisms that maintain health and cause disease in humans and companion animals." Veterinary pathology **53**(1): 10-21.

[2] Lin, Z, et al. (2016). "Research progress in mechanism of intestinal microorganisms in human diseases." Yao Xue Xue Bao **51**(6): 843-852.

[3] Karp, G (2009). Cell and molecular biology: concepts and experiments, John Wiley & Sons.

[4] Keller, G (2005). "Embryonic stem cell differentiation: emergence of a new era in biology and medicine." Genes & development **19**(10): 1129-1155.

[5] Dang, SM, et al. (2004). "Controlled, scalable embryonic stem cell differentiation culture." Stem Cells **22**(3): 275-282.

[6] Puri, MC and Nagy, A (2012). "Concise review: embryonic stem cells versus induced pluripotent stem cells: the game is on." Stem Cells **30**(1): 10-14.

[7] Ying, QL, et al. (2008). "The ground state of embryonic stem cell self-renewal." Nature **453**(7194): 519-523.

[8] Beachy, PA, et al. (2004). "Tissue repair and stem cell renewal in carcinogenesis." Nature **432**(7015): 324-331.

[9] Cao, Q, et al. (2002). "Stem cell repair of central nervous system injury." Journal of neuroscience research **68**(5): 501-510.

[10] Fu, X, et al. (2019). "Mesenchymal Stem Cell Migration and Tissue Repair." Cells **8**(8): 784.

[11] Ge, Y, et al. (2017). "Stem Cell Lineage Infidelity Drives Wound Repair and Cancer." Cell **169**(4): 636-650 e614.

[12] Johnson, K, et al. (2012). "A stem cell–based approach to cartilage repair." Science **336**(6082): 717-721.

[13] Neuringer, IP and SH Randell (2004). "Stem cells and repair of lung injuries." Respiratory research **5**(1): 6.

[14] Sasaki, M, et al. (2008). "Mesenchymal stem cells are recruited into wounded skin and contribute to wound repair by transdifferentiation into multiple skin cell type." The Journal of immunology **180**(4): 2581-2587.

[15] Bang, OY, et al. (2016). "Adult Stem Cell Therapy for Stroke: Challenges and Progress." Journal of Stroke **18**(3): 256-266.

[16] Dulak, J, et al. (2015). "Adult stem cells: hopes and hypes of regenerative medicine." Acta Biochimica Polonica **62**(3): 329-337.

[17] Li, L and H Clevers (2010). "Coexistence of quiescent and active adult stem cells in mammals." Science **327**(5965): 542-545.

[18] Takahashi, K and S Yamanaka (2006). "Induction of pluripotent stem cells from mouse embryonic and adult fibroblast cultures by defined factors." Cell **126**(4): 663-676.

[19] Holmes, D (2012). "Stem cell scientists share 2012 Nobel Prize for medicine." Lancet **380**(9850): 1295.

[20] Takahashi, K, et al. (2007). "Induction of pluripotent stem cells from adult human fibroblasts by defined factors." Cell **131**(5): 861-872.

[21] Kaneko, S and S Yamanaka (2013). "To be immunogenic, or not to be: that's the iPSC question." Cell stem cell **12**(4): 385-386.

[22] Suchy, F, et al. (2018). "iPSC-Derived Organs In Vivo: Challenges and Promise." Cell stem cell **22**(1): 21-24.

[23] Yoshida, S, et al. (2020). "Syngeneic mesenchymal stem cells reduce immune rejection after induced pluripotent stem cell-derived allogeneic cardiomyocyte transplantation." Scientific reports **10**(1): 1-11.

[24] Csöbönyeiová, M, et al. (2016). "Toxicity testing and drug screening using iPSC-derived hepatocytes, cardiomyocytes, and neural cells." Canadian journal of physiology & pharmacology **94**(7): 687-694.

[25] Ebert, AD, et al. (2012). "Induced pluripotent stem cells as a disease modeling and drug screening platform." Journal of cardiovascular pharmacology **60**(4): 408.

[26] Elitt, MS, et al. (2018). "Drug screening for human genetic diseases using iPSC models." Human molecular genetics **27**(R2): R89-R98.

[27] Mo, SJ, et al. (2020). "A microfluidic gradient device for drug screening with human iPSC-derived motoneurons." Analyst **145**(8): 3081-3089.

[28] Ortiz-Vitali, JL and R Darabi (2019). "iPSCs as a platform for disease modeling, drug screening, and personalized therapy in muscular dystrophies." Cells **8**(1): 20.

[29] Smith, AS, et al. (2017). "Human iPSC-derived cardiomyocytes and tissue engineering strategies for disease modeling and drug screening." Biotechnology advances **35**(1): 77-94.

[30] Frantz, C, et al. (2010). "The extracellular matrix at a glance." Journal of cell science **123**(24): 4195-4200.

[31] Geiger, B, et al. (2001). "Transmembrane crosstalk between the extracellular matrix and the cytoskeleton." Nature reviews **2**(11): 793-805.

[32] Hay, ED (2013). Cell biology of extracellular matrix, Springer Science & Business Media.

[33] Hynes, RO (2009). "The extracellular matrix: not just pretty fibrils." Science **326**(5957): 1216-1219.

[34] Dityatev, A, et al. (2010). "The dual role of the extracellular matrix in synaptic plasticity and homeostasis." Nature Reviews Neuroscience **11**(11): 735-746.

[35] Faulk, DM, et al. (2014). "Role of the extracellular matrix in whole organ engineering." Journal of cellular physiology **229**(8): 984-989.

[36] Tzanakakis, G, et al. (2018). "Role of the extracellular matrix in cancer-associated epithelial to mesenchymal transition phenomenon." Developmental Dynamics **247**(3): 368-381.

[37] Watt, FM and WT Huck (2013). "Role of the extracellular matrix in regulating stem cell fate." Nature reviews Molecular cell biology **14**(8): 467-473.

[38] Jayadev, R and DR Sherwood (2017). "Basement membranes." Current Biology **27**(6): R207-R211.

[39] Paulsson, M (1992). "Basement membrane proteins: structure, assembly, and cellular interactions." Critical reviews in biochemistry and molecular biology **27**(1-2): 93-127.

[40] Pozzi, A, et al. (2017). "The nature and biology of basement membranes." Matrix Biology **57-58**: 1-11.

[41] Timpl, R (1989). "Structure and biological activity of basement membrane proteins." European Journal of Biochemistry **180**(3): 487-502.

[42] Pöschl, E, et al. (2004). "Collagen IV is essential for basement membrane stability but dispensable for initiation of its assembly during early development." Development **131**(7): 1619-1628.

[43] Mak, KM and R Mei (2017). "Basement membrane type IV collagen and laminin: an overview of their biology and value as fibrosis biomarkers of liver disease." The Anatomical Record **300**(8): 1371-1390.

[44] Hohenester, E and PD Yurchenco (2013). "Laminins in basement membrane assembly." Cell adhesion & migration **7**(1): 56-63.

[45] Santhanam, A, et al. (2015). "Differential expression of epithelial basement membrane components nidogens and perlecan in corneal stromal cells in vitro." Molecular vision **21**: 1318-1327.

[46] Wolfstetter, G, et al. (2019). "Characterization of Drosophila Nidogen/entactin reveals roles in basement membrane stability, barrier function and nervous system patterning." Development **146**(2).

[47] Kefalides, NA and JP Borel (2005). "Structural macromolecules: laminins, entactin/nidogen, and proteoglycans (Perlecan, Agrin)." Current Topics in Membranes **56**: 147-197.

[48] Escalante, T, et al. (2011). "Role of collagens and perlecan in microvascular stability: exploring the mechanism of capillary vessel damage by snake venom metalloproteinases." PLoS One **6**(12): e28017.

[49] Bassi, EJ, et al. (2012). "Exploring the role of soluble factors associated with immune regulatory properties of mesenchymal stem cells." Stem Cell Reviews and Reports **8**(2): 329-342.

[50] Dingal, PC and DE Discher (2014). "Combining insoluble and soluble factors to steer stem cell fate." Nature Materials **13**(6): 532-537.

[51] Barrientos, S, et al. (2008). "Growth factors and cytokines in wound healing." Wound Repair and Regeneration **16**(5): 585-601.

[52] Hagberg, CE, et al. (2010). "Vascular endothelial growth factor B controls endothelial fatty acid uptake." Nature **464**(7290): 917-921.

[53] Koch, S, et al. (2011). "Signal transduction by vascular endothelial growth factor receptors." Biochemical journal **437**(2): 169-183.

[54] Masuda, H, et al. (2012). "Role of epidermal growth factor receptor in breast cancer." Breast cancer research and treatment **136**(2): 331-345.

[55] Ornitz, DM and N Itoh (2001). "Fibroblast growth factors." Genome Biology **2**(3): REVIEWS 3005.

[56] Turner, N and R Grose (2010). "Fibroblast growth factor signalling: from development to cancer." Nature Reviews Cancer **10**(2): 116-129.

[57] Wee, P and Z Wang (2017). "Epidermal Growth Factor Receptor Cell Proliferation Signaling Pathways." Cancers (Basel) **9**(5): 52.

[58] Hanada, T and A Yoshimura (2002). "Regulation of cytokine signaling and inflammation." Cytokine & Growth Factor Reviews **13**(4-5): 413-421.

[59] Huse, M, et al. (2006). "T cells use two directionally distinct pathways for cytokine secretion." Nature immunology **7**(3): 247-255.

[60] Kelley, KW, et al. (2003). "Cytokine-induced sickness behavior." Brain Behavior & Immunity **17 Suppl 1**(1): S112-118.

[61] Naik, E and VM Dixit (2011). "Mitochondrial reactive oxygen species drive proinflammatory cytokine production." Journal of Experimental Medicine **208**(3): 417-420.

[62] O'Shea, JJ and PJ Murray (2008). "Cytokine signaling modules in inflammatory responses." Immunity **28**(4): 477-487.

[63] Beato, M and J Klug (2000). "Steroid hormone receptors: an update." Hum Reprod Update **6**(3): 225-236.

[64] Casadesus, G, et al. (2006). "Luteinizing hormone modulates cognition and amyloid-beta deposition in Alzheimer APP transgenic mice." Biochim Biophys Acta **1762**(4): 447-452.

[65] Giustina, A, et al. (2008). "Growth hormone, insulin-like growth factors, and the skeleton." Endocrine Reviews **29**(5): 535-559.

[66] Klein, I and K Ojamaa (2001). "Thyroid hormone and the cardiovascular system." The New England Journal of Medicine **344**(7): 501-509.

[67] Lupu, F, et al. (2001). "Roles of growth hormone and insulin-like growth factor 1 in mouse postnatal growth." Developmental biology **229**(1): 141-162.

[68] Mullur, R, et al. (2014). "Thyroid hormone regulation of metabolism." Physiological Reviews **94**(2): 355-382.

[69] Wren, AM, et al. (2000). "The novel hypothalamic peptide ghrelin stimulates food intake and growth hormone secretion." Endocrinology **141**(11): 4325-4328.

[70] Flyvbjerg, A, et al. (2004). "The involvement of growth hormone (GH), insulin-like growth factors (IGFs) and vascular endothelial growth factor (VEGF) in diabetic kidney disease." Current Pharmaceutical Design **10**(27): 3385-3394.

[71] Katznelson, L, et al. (2003). "Effects of growth hormone secretion on body composition in patients with Crohn's disease." The Journal of Clinical Endocrinology & Metabolism **88**(11): 5468-5472.

[72] Kopchick, J, et al. (2002). "Growth hormone receptor antagonists: discovery, development, and use in patients with acromegaly." Endocrine reviews **23**(5): 623-646.

[73] Toogood, AA, et al. (1994). "The severity of growth hormone deficiency in adults with pituitary disease is related to the degree of hypopituitarism." Clinical Endocrinology **41**(4): 511-516.

[74] Anderson, JM and CM Van Itallie (2009). "Physiology and function of the tight junction." Cold Spring Harb Perspect Biol **1**(2): a002584.

[75] Gonzalez-Mariscal, L, et al. (2003). "Tight junction proteins." Progress In Biophysics & Molecular Biology **81**(1): 1-44.

[76] Schneeberger, EE and RD Lynch (2004). "The tight junction: a multifunctional complex." American Journal of Physiology. Cell Physiology **286**(6): C1213-1228.

[77] Green, KJ and CL Simpson (2007). "Desmosomes: new perspectives on a classic." Journal of Investigative Dermatology **127**(11): 2499-2515.

[78] Lie, PP, et al. (2011). The biology of the desmosome-like junction: a versatile anchoring junction and signal transducer in the seminiferous epithelium. International review of cell and molecular biology, Elsevier. **286:** 223-269.

[79] Yin, T and KJ Green (2004). Regulation of desmosome assembly and adhesion. Seminars in cell & developmental biology, Elsevier.

[80] Elias, LA, et al. (2007). "Gap junction adhesion is necessary for radial migration in the neocortex." Nature **448**(7156): 901-907.

[81] Hervé, J-C and M Derangeon (2013). "Gap-junction-mediated cell-to-cell communication." Cell tissue research **352**(1): 21-31.

[82] Krutovskikh, VA, et al. (2002). "Gap junction intercellular communication propagates cell death in cancerous cells." Oncogene **21**(13): 1989-1999.

[83] Kumar, NM and NB Gilula (1996). "The gap junction communication channel." Cell **84**(3): 381-388.

[84] Klowden, MJ (2013). Physiological systems in insects, Academic press.

[85] Marmarelis, V (2012). Analysis of physiological systems: The white-noise approach, Springer Science & Business Media.

[86] Berntson, GG, et al. (2017). "Cardiovascular psychophysiology."

[87] Levick, JR (2013). An introduction to cardiovascular physiology, Butterworth-Heinemann.

[88] Opie, LH (2004). Heart physiology: from cell to circulation, Lippincott Williams & Wilkins.

[89] Rychik, J (2004). "Fetal cardiovascular physiology." Pediatric Cardiology **25**(3): 201-209.

[90] Kay, RN and AG Davies (1994). "Digestive physiology." Colobine monkeys: Their ecology, behaviour evolution 229-249.

[91] Stevens, CE and ID Hume (2004). Comparative physiology of the vertebrate digestive system, Cambridge University Press.

[92] Chahal, HS and WM Drake (2007). "The endocrine system and ageing." Journal of Pathology **211**(2): 173-180.

[93] Kohrle, J, et al. (2005). "Selenium, the thyroid, and the endocrine system." Endocrine Reviews **26**(7): 944-984.

[94] Chandra, RK (1997). "Nutrition and the immune system: an introduction." American Journal of Clinical Nutrition **66**(2): 460S-463S.

[95] Parham, P (2014). The immune system, Garland Science.

[96] Parkin, J and B Cohen (2001). "An overview of the immune system." Lancet **357**(9270): 1777-1789.

[97] Liem, KF and AP Summers (1999). Muscular system, Johns Hopkins University Press, Baltimore.

[98] Vaughan, TA (1970). "The muscular system." Biology of bats **1**: 140-194.

[99] Mai, JK and G Paxinos (2011). The human nervous system, Academic press.

[100] Nieuwenhuys, R, et al. (2014). The central nervous system of vertebrates, Springer.

[101] Holz, PH (2020). "Anatomy and Physiology of the Reptile Renal System." Vet Clin North Am Exot Anim Pract **23**(1): 103-114.

[102] Koushanpour, E and W Kriz (2013). Renal physiology: principles, structure, and function, Springer Science & Business media.

[103] Preuss, HG (1993). "Basics of renal anatomy and physiology." Clinics in Laboratory Medicine **13**(1): 1-11.

[104] Creasy, DM and RE Chapin (2013). Male reproductive system. Haschek and Rousseaux's handbook of Toxicologic pathology, Elsevier**:** 2493-2598.

[105] Heffner, LJ and DJ Schust (2010). The reproductive system at a glance, John Wiley & Sons.

[106] Roberts, KP and JL Pryor (1997). Anatomy and physiology of the male reproductive system. Male Infertility and Sexual Dysfunction, Springer**:** 1-21.

[107] Levitzky, MG (2018). Pulmonary physiology, McGraw-Hill Education.

[108] Huysseune, A (2000). Skeletal system. The laboratory fish, Elsevier**:** 307-317.

[109] Markings, B (1995). "The skeletal system."

[110] Watson, EC and RH Adams (2018). "Biology of Bone: The Vasculature of the Skeletal System." Cold Spring Harb Perspect Med **8**(7): a031559.

[111] McKleroy, W and K Lyn-Kew (2018). 500 Million Alveoli from 30,000 Feet: A Brief Primer on Lung Anatomy. Lung Innate Immunity and Inflammation, Springer**:** 3-15.

[112] Ochs, M, et al. (2004). "The number of alveoli in the human lung." American Journal Of Respiratory And Critical Care Medicine **169**(1): 120-124.

[113] Knudsen, L and M Ochs (2018). "The micromechanics of lung alveoli: structure and function of surfactant and tissue components." Histochemistry And Cell Biology **150**(6): 661-676.

[114] Weibel, ER (2017). "Lung morphometry: the link between structure and function." Cell Tissue Research **367**(3): 413-426.

[115] Williams, MC (2003). "Alveolar type I cells: molecular phenotype and development." Annual Review of Physiology **65**(1): 669-695.

[116] Herzog, EL, et al. (2008). "Knowns and unknowns of the alveolus." Proc Am Thorac Soc **5**(7): 778-782.

[117] Weibel, ER (2015). "On the tricks alveolar epithelial cells play to make a good lung." American Journal Of Respiratory Critical Care Medicine **191**(5): 504-513.

[118] Evans, KV and JH Lee (2020). "Alveolar wars: The rise of in vitro models to understand human lung alveolar maintenance, regeneration, and disease." Stem Cells Transl Med **9**(8): 867-881.

[119] Barkauskas, CE, et al. (2013). "Type 2 alveolar cells are stem cells in adult lung." J Clin Invest **123**(7): 3025-3036.

[120] Desai, TJ, et al. (2014). "Alveolar progenitor and stem cells in lung development, renewal and cancer." Nature **507**(7491): 190-194.

[121] Fels, AO and ZA Cohn (1986). "The alveolar macrophage." J Appl Physiol (1985) **60**(2): 353-369.

[122] Peters-Golden, M (2004). "The alveolar macrophage: the forgotten cell in asthma." Am J Respir Cell Mol Biol **31**(1): 3-7.

[123] Wang, C, et al. (2020). "Alveolar macrophage dysfunction and cytokine storm in the pathogenesis of two severe COVID-19 patients." EBioMedicine **57**: 102833.

[124] Aran, D, et al. (2019). "Reference-based analysis of lung single-cell sequencing reveals a transitional profibrotic macrophage." Nat Immunol **20**(2): 163-172.

[125] Billiet, T, et al. (2012). "A review of trends and limitations in hydrogel-rapid prototyping for tissue engineering." Biomaterials **33**(26): 6020-6041.

[126] Drury, JL and DJ Mooney (2003). "Hydrogels for tissue engineering: scaffold design variables and applications." Biomaterials **24**(24): 4337-4351.

[127] Van Vlierberghe, S, et al. (2011). "Biopolymer-based hydrogels as scaffolds for tissue engineering applications: a review." **12**(5): 1387-1408.

[128] Harrison, RH, et al. (2014). "Tissue engineering and regenerative medicine: a year in review." Tissue Eng Part B Rev **20**(1): 1-16.

[129] Slaughter, BV, et al. (2009). "Hydrogels in regenerative medicine." Adv Mater **21**(32-33): 3307-3329.

[130] Lin, CC and KS Anseth (2009). "PEG hydrogels for the controlled release of biomolecules in regenerative medicine." Pharm Res **26**(3): 631-643.

[131] Raeber, GP, et al. (2005). "Molecularly engineered PEG hydrogels: a novel model system for proteolytically mediated cell migration." Biophys J **89**(2): 1374-1388.

[132] Armisen, R and F Gaiatas (2009). Agar. Handbook of hydrocolloids, Elsevier**:** 82-107.

[133] Su, K and C Wang (2015). "Recent advances in the use of gelatin in biomedical research." Biotechnology letters **37**(11): 2139-2145.

[134] Tang, Y, et al. (2016). "Induction and differentiation of human induced pluripotent stem cells into functional cardiomyocytes on a compartmented monolayer of gelatin nanofibers." Nanoscale **8**(30): 14530-14540.

[135] Chen, YC, et al. (2012). "Functional Human Vascular Network Generated in Photocrosslinkable Gelatin Methacrylate Hydrogels." Adv Funct Mater **22**(10): 2027-2039.

[136] Nichol, JW, et al. (2010). "Cell-laden microengineered gelatin methacrylate hydrogels." Biomaterials **31**(21): 5536-5544.

[137] Xiao, S, et al. (2019). "Gelatin Methacrylate (GelMA)-Based Hydrogels for Cell Transplantation: an Effective Strategy for Tissue Engineering." Stem Cell Rev Rep **15**(5): 664-679.

[138] Hughes, CS, et al. (2010). "Matrigel: a complex protein mixture required for optimal growth of cell culture." Proteomics **10**(9): 1886-1890.

[139] Gu, L, et al. (2019). "Novel Biomedical Applications of Crosslinked Collagen." Trends Biotechnol **37**(5): 464-491.

[140] Lee, CH, et al. (2001). "Biomedical applications of collagen." Int J Pharm **221**(1-2): 1-22.

[141] Pawelec, KM, et al. (2016). "Collagen: a network for regenerative medicine." J Mater Chem B **4**(40): 6484-6496.

[142] Shoulders, MD and RT Raines (2009). "Collagen structure and stability." Annu Rev Biochem **78**: 929-958.

[143] Matthews, JA, et al. (2002). "Electrospinning of collagen nanofibers." Biomacromolecules **3**(2): 232-238.

[144] Song, JH, et al. (2008). "Production of electrospun gelatin nanofiber by water-based co-solvent approach." J Mater Sci Mater Med **19**(1): 95-102.

[145] Kim, SH, et al. (2003). "Silk fibroin nanofiber. Electrospinning, properties, and structure." Polymer Journal **35**(2): 185-190.

[146] Xing, Z-C, et al. (2011). Keratin nanofibers as a biomaterial. Int Conf Nanotechnology and Biosensors, Singapore.

[147] Ohkawa, K, et al. (2006). "Chitosan nanofiber." Biomacromolecules **7**(11): 3291-3294.

[148] Bonino, CA, et al. (2012). "Three-dimensional electrospun alginate nanofiber mats via tailored charge repulsions." Small **8**(12): 1928-1936.

[149] Abdal-Hay, A, et al. (2016). "Fabrication of novel high performance ductile poly (lactic acid) nanofiber scaffold coated with poly(vinyl alcohol) for tissue engineering applications." Mater Sci Eng C Mater Biol Appl **60**: 143-150.

[150] Ko, YM, et al. (2015). "Characteristics of Plasma Treated Electrospun Polycaprolactone (PCL) Nanofiber Scaffold for Bone Tissue Engineering." J Nanosci Nanotechnol **15**(1): 192-195.

[151] Shin, HJ, et al. (2006). "Electrospun PLGA nanofiber scaffolds for articular cartilage reconstruction: mechanical stability, degradation and cellular responses under mechanical stimulation in vitro." J Biomater Sci Polym Ed **17**(1-2): 103-119.

[152] Bhardwaj, N and SC Kundu (2010). "Electrospinning: a fascinating fiber fabrication technique." Biotechnol Adv **28**(3): 325-347.

[153] Beachley, V and X Wen (2010). "Polymer nanofibrous structures: Fabrication, biofunctionalization, and cell interactions." Prog Polym Sci **35**(7): 868-892.

[154] Ehrmann, RL and GO Gey (1956). "The growth of cells on a transparent gel of reconstituted rat-tail collagen." J Natl Cancer Inst **16**(6): 1375-1403.

[155] Amstein, CF and PA Hartman (1975). "Adaptation of plastic surfaces for tissue culture by glow discharge." J Clin Microbiol **2**(1): 46-54.

[156] Curtis, AS, et al. (1983). "Adhesion of cells to polystyrene surfaces." J Cell Biol **97**(5 Pt 1): 1500-1506.

[157] Hollahan, JR and AT Bell (1974). "Techniques and applications of plasma chemistry."

[158] Ramsey, WS, et al. (1984). "Surface treatments and cell attachment." In Vitro **20**(10): 802-808.

[159] Cho, SJ, et al. (2015). "Preparation of hydrophilic PCL nanofiber scaffolds via electrospinning of PCL/PVP-b-PCL block copolymers for enhanced cell biocompatibility." Polymer **69**: 95-102.

[160] Lee, KH, et al. (2009). "Hydrophilic electrospun polyurethane nanofiber matrices for hMSC culture in a microfluidic cell chip." J Biomed Mater Res A **90**(2): 619-628.

[161] Shi, J, et al. (2010). "Incorporating protein gradient into electrospun nanofibers as scaffolds for tissue engineering." ACS applied materials interfaces **2**(4): 1025-1030.

[162] Zhang, Y, et al. (2006). "Crosslinking of the electrospun gelatin nanofibers." Polymer **47**(8): 2911-2917.

[163] Wang, B, et al. (2018). "Fabrication of spaced monolayers of electrospun nanofibers for three-dimensional cell infiltration and proliferation." Microelectronic Engineering **198**: 73-77.
[164] Reid, LM and M Rojkind (1979). [21] New Techniques for Culturing Differential Cells: Reconstituted basement membrane rafts. Methods in enzymology, Elsevier. **58:** 263-278.
[165] Ryan, JA (2008). "Evolution of cell culture surfaces." BioFiles **3**(8): 21.
[166] Shen, M and TA Horbett (2001). "The effects of surface chemistry and adsorbed proteins on monocyte/macrophage adhesion to chemically modified polystyrene surfaces." J Biomed Mater Res **57**(3): 336-345.
[167] Dontu, G, et al. (2003). "In vitro propagation and transcriptional profiling of human mammary stem/progenitor cells." **17**(10): 1253-1270.
[168] Dontu, G, et al. (2003). "In vitro propagation and transcriptional profiling of human mammary stem/progenitor cells." Genes Dev **17**(10): 1253-1270.
[169] Li, S, et al. (2005). "Bystander effect-mediated gene therapy of gliomas using genetically engineered neural stem cells." Cancer Gene Therapy **12**(7): 600-607.
[170] Liu, S, et al. (2006). "Hedgehog signaling and Bmi-1 regulate self-renewal of normal and malignant human mammary stem cells." Cancer Res **66**(12): 6063-6071.
[171] Ohtsuka, T, et al. (2001). "Roles of the basic helix-loop-helix genes Hes1 and Hes5 in expansion of neural stem cells of the developing brain." J Biol Chem **276**(32): 30467-30474.
[172] Chiao, E, et al. (2008). "Derivation of human embryonic stem cells in standard and chemically defined conditions." Methods Cell Biol **86**: 1-14.
[173] He, Y, et al. (2020). "Fabrication of micro-cages and caged tumor spheroids for microfluidic chip-based assays." Microelectronic Engineering **225**: 111256.
[174] Tang, Y, et al. (2016). "Agarose multi-wells for tumour spheroid formation and anti-cancer drug test." Microelectronic Engineering **158**: 41-45.
[175] van Duinen, V, et al. (2015). "Microfluidic 3D cell culture: from tools to tissue models." Curr Opin Biotechnol **35**: 118-126.
[176] Rothbauer, M, et al. (2018). "Recent advances in microfluidic technologies for cell-to-cell interaction studies." Lab Chip **18**(2): 249-270.
[177] Gupta, N, et al. (2016). "Microfluidics-based 3D cell culture models: Utility in novel drug discovery and delivery research." Bioeng Transl Med **1**(1): 63-81.
[178] van Duinen, V, et al. (2019). "Perfused 3D angiogenic sprouting in a high-throughput in vitro platform." Angiogenesis **22**(1): 157-165.
[179] Zhang, K and A Manninen (2019). 3D Cell Culture Models of Epithelial Tissues. Kidney Organogenesis, Springer**:** 77-84.

[180] Ma, J, et al. (2018). "Bioprinting of 3D tissues/organs combined with microfluidics." RSC advances **8**(39): 21712-21727.

[181] Sontheimer-Phelps, A, et al. (2019). "Modelling cancer in microfluidic human organs-on-chips." Nat Rev Cancer **19**(2): 65-81.

[182] Yu, F and D Choudhury (2019). "Microfluidic bioprinting for organ-on-a-chip models." Drug Discov Today **24**(6): 1248-1257.

[183] Chen, S and J Schoen (2019). "Air-liquid interface cell culture: From airway epithelium to the female reproductive tract." Reprod Domest Anim **54 Suppl 3**: 38-45.

[184] Wu, J, et al. (2018). "Characterization of air-liquid interface culture of A549 alveolar epithelial cells." Brazilian Journal of Medical Biological Research **51**(2).

[185] Van Riet, S, et al. (2020). "In vitro modelling of alveolar repair at the air-liquid interface using alveolar epithelial cells derived from human induced pluripotent stem cells." Scientific reports **10**(1): 1-12.

[186] Yamashiro, C, et al. (2020). "Generation of human oogonia from induced pluripotent stem cells in culture." Nat Protoc **15**(4): 1560-1583.

[187] Fulcher, ML and SH Randell (2012). Human nasal and tracheo-bronchial respiratory epithelial cell culture. Epithelial Cell Culture Protocols, Springer**:** 109-121.

[188] Kuehn, A, et al. (2016). "Human alveolar epithelial cells expressing tight junctions to model the air-blood barrier." ALTEX **33**(3): 251-260.

[189] Lin, H, et al. (2007). "Air-liquid interface (ALI) culture of human bronchial epithelial cell monolayers as an in vitro model for airway drug transport studies." Journal of pharmaceutical sciences **96**(2): 341-350.

[190] Huang, J, et al. (2020). "SARS-CoV-2 infection of pluripotent stem cell-derived human lung alveolar type 2 cells elicits a rapid epithelial-intrinsic inflammatory response." Cell stem cell.

[191] Jackson, DJ, et al. (2020). "Association of respiratory allergy, asthma, and expression of the SARS-CoV-2 receptor ACE2." J Allergy Clin Immunol **146**(1): 203-206 e203.

[192] Mulay, A, et al. (2020). "SARS-CoV-2 infection of primary human lung epithelium for COVID-19 modeling and drug discovery." bioRxiv.

[193] Li, X (2016). "In vitro toxicity testing of cigarette smoke based on the air-liquid interface exposure: A review." Toxicol In Vitro **36**: 105-113.

[194] Schamberger, AC, et al. (2015). "Cigarette smoke alters primary human bronchial epithelial cell differentiation at the air-liquid interface." Scientific reports **5**: 8163.

[195] Kumar, CS (2010). Microfluidic devices in nanotechnology: applications, John Wiley & Sons.

[196] Liu, D, et al. (2018). "Current developments and applications of microfluidic technology toward clinical translation of nanomedicines." Adv Drug Deliv Rev **128**: 54-83.

[197] Mairhofer, J, et al. (2009). "Microfluidic systems for pathogen sensing: a review." Sensors (Basel) **9**(6): 4804-4823.

[198] Abgrall, P, et al. (2005). "A novel fabrication method of flexible and monolithic 3D microfluidic structures using lamination of SU-8 films." Journal of micromechanics & microengineering **16**(1): 113.

[199] Paul, D, et al. (2007). "Lamination-based rapid prototyping of microfluidic devices using flexible thermoplastic substrates." Electrophoresis **28**(7): 1115-1122.

[200] Weigl, BH, et al. (2001). "Design and rapid prototyping of thin-film laminate-based microfluidic devices." Biomedical Microdevices **3**(4): 267-274.

[201] Ouyang, Y, et al. (2015). "A disposable laser print-cut-laminate polyester microchip for multiplexed PCR via infra-red-mediated thermal control." **901**: 59-67.

[202] Kim, P, et al. (2008). "Soft lithography for microfluidics: a review."

[203] Whitesides, GM, et al. (2001). "Soft lithography in biology and biochemistry." Annu Rev Biomed Eng **3**(1): 335-373.

[204] Jo, B-H, et al. (2000). "Three-dimensional micro-channel fabrication in polydimethylsiloxane (PDMS) elastomer." Journal of microelectromechanical systems **9**(1): 76-81.

[205] Bryce, DM (1996). Plastic injection molding: manufacturing process fundamentals, Society of Manufacturing Engineers.

[206] Malloy, RA (1994). Plastic part design for injection molding, Hanser Publishers New York.

[207] Rosato, DV and MG Rosato (2012). Injection molding handbook, Springer Science & Business Media.

[208] Becker, H and U Heim (2000). "Hot embossing as a method for the fabrication of polymer high aspect ratio structures." Sensors & Actuators A: Physical **83**(1-3): 130-135.

[209] Worgull, M (2009). Hot embossing: theory and technology of microreplication, William Andrew.

[210] Wu, J and M Gu (2011). "Microfluidic sensing: state of the art fabrication and detection techniques." J Biomed Opt **16**(8): 080901.

[211] Carneiro, OS, et al. (2015). "Fused deposition modeling with polypropylene." Materials Design **83**: 768-776.

[212] Ning, F, et al. (2015). "Additive manufacturing of carbon fiber reinforced thermoplastic composites using fused deposition modeling." Composites Part B: Engineering **80**: 369-378.

[213] Lee, KY, et al. (2015). "Accuracy of three-dimensional printing for manufacturing replica teeth." Korean J Orthod **45**(5): 217-225.

[214] Melchels, FP, et al. (2010). "A review on stereolithography and its applications in biomedical engineering." Biomaterials **31**(24): 6121-6130.

[215] An, WF and N Tolliday (2010). "Cell-based assays for high-throughput screening." Mol Biotechnol **45**(2): 180-186.

[216] Ebert, AD, et al. (2012). "Induced pluripotent stem cells as a disease modeling and drug screening platform." **60**(4): 408.

[217] Huh, D, et al. (2010). "Reconstituting organ-level lung functions on a chip." Science **328**(5986): 1662-1668.

[218] Long, C, et al. (2012). "Design optimization of liquid-phase flow patterns for microfabricated lung on a chip." Ann Biomed Eng **40**(6): 1255-1267.

[219] Bhise, NS, et al. (2016). "A liver-on-a-chip platform with bioprinted hepatic spheroids." Biofabrication **8**(1): 014101.

[220] Wilmer, MJ, et al. (2016). "Kidney-on-a-Chip Technology for Drug-Induced Nephrotoxicity Screening." Trends Biotechnol **34**(2): 156-170.

[221] Kim, HJ, et al. (2016). "Contributions of microbiome and mechanical deformation to intestinal bacterial overgrowth and inflammation in a human gut-on-a-chip." Proc Natl Acad Sci U S A **113**(1): E7-15.

[222] Agarwal, A, et al. (2013). "Microfluidic heart on a chip for higher throughput pharmacological studies." Lab on a Chip **13**(18): 3599-3608.

[223] Zhang, YS, et al. (2016). "Bioprinting 3D microfibrous scaffolds for engineering endothelialized myocardium and heart-on-a-chip." Biomaterials **110**: 45-59.

[224] Kimura, H, et al. (2018). "Organ/body-on-a-chip based on microfluidic technology for drug discovery." Drug Metab Pharmacokinet **33**(1): 43-48.

Chapter 2
Device fabrication and microfluidic techniques

Device fabrication and microfluidic techniques

In this chapter, we describe device fabrication and microfluidic techniques. Firstly, we introduce photolithography, vacuum assisted molding, and electrospinning techniques, which are used for the fabrication of our culture devices. Basically, these devices are made of a monolayer of crosslinked gelatin nanofibers on a thin frame. They can be used directly as a substrate for off-ground cell culture or as a backbone of the artificial basement membrane (Appendix A). We describe several other fabrication techniques, including micro-milling, cutting plotter, and Parylene deposition, which are also used in this work. Secondly, we present the culture device accessories which facilitate cell seeding and air-liquid interface culture. Finally, we show a microfluidic device configuration for the patch integration.

2.1 Photolithography

Photolithography, also known as optical lithography, is a microfabrication process that can use ultraviolet (UV)light to transfer the geometric pattern from a photomask to a photoresist layer [1-4]. This process also depends on the photoresist materials, either exposed or unexposed areas are removed in a developer. As a simple and universal method, it allows a pattern replication with minimum feature size down to 1 µm under conventional lab conditions.

In this work, we used software L-Edit (Tanner research, USA) to define the device pattern and a micropattern generator (µPG 101 from Heidelberg Instruments) to produce the pattern on a blank photomask (Fig 2.1). Here, the photomask is a glass plate pre-deposited with a chrome layer and a photoresist layer. A focused UV laser beam is scanning on the surface of the photomask to write directly the pattern on the photoresist layer (AZ1518, Microchem). Then, the resist pattern is developed in AZ726 MIF (Microchem) for ~ 1 min with gentle agitation and rinsed in DI water. Afterward, the photomask is merged in a Chrome-Etch solution to remove the unprotected area of the chrome layer. Finally, the photoresist residual is removed in acetone.

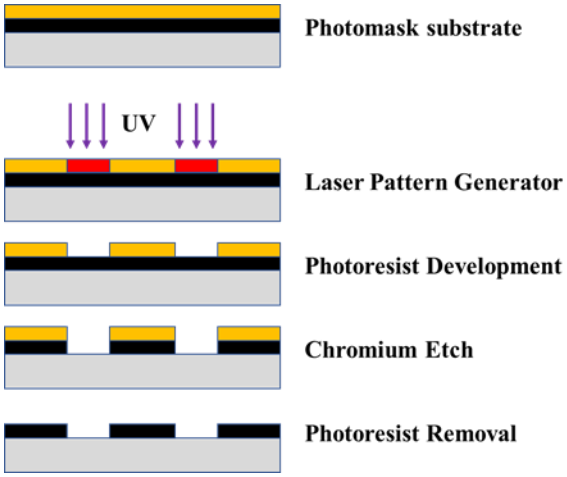

Figure 2.1 Schematic of a fabrication process of photomask: pattern generation with a laser writer, photoresist developing, chromium etching, and photoresist removal.

To fabricate the frame of our culture devices, we used a vacuum assisted molding technique that replicates a pattern of relatively large thickness from a mold. This mold, generally made of polydimethylsiloxane (PDMS) [5], can be obtained by soft-lithography from a master defined by photolithography.

The fabrication of the master is as follows (Fig 2.2):

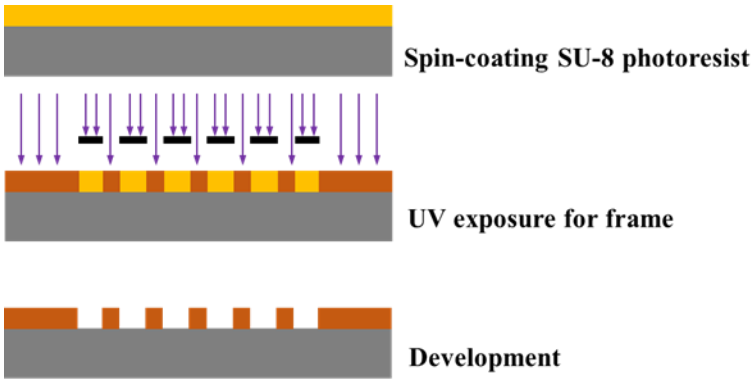

Figure 2.2 Schematic of a fabrication process of honeycomb frame master: spin-coating, UV exposure and development.

a) Silicon wafer cleaning
   - Piranha Clean (96% H_2SO_4 : 30% H_2O_2, 1:1) : 10~20 min.
   - DI water rinse: 15 min (3 times in baths, 5 min each one)
   - Sample dry: N2 gun
   - Hotplate Bake (200℃ for 5 min)

b) Photoresist deposition

The photoresist is spin-coated on a silicon wafer, and the thickness is controlled by spinning speed.

After spin coating, the photoresist is baked to evaporate the solvent and cure the film. With a typical temperature range from 90 to 110 °C, soft baking is usually carried out on a hot plate. This process must completely remove the solvent at the interface of photoresist-substrate. However, the control of the evaporation rate must be relatively precise, especially when baking thick photoresist (approximately more than 4-5 μm). If the solvent evaporates too quickly, bubbles may be caused, and circular voids will be observed in the film after baking. If the photoresist film is thick, it usually requires multiple-step baking processes with graded increasing temperatures to achieve appropriate evaporation rates and avoid bubbles. On the contrary, if the evaporation rate is too slow, a "skin" layer may form on the film surface, thereby inhibiting the further evaporation of the solvent. For example, a 50 μm thickness of SU-8 photoresist needs a 15 min soft baking process at 95 °C.

c) Exposure and developing

After cooling down to room temperature, the photoresist coated wafer is exposed under a UV light with a photomask closely in contact to the photoresist layer. Here, the distance between the photomask and the photoresist layer affects the final precision. The closer contact between mask and photoresist, the higher precision of the pattern will be transferred. For the negative photoresist, e.g., SU-8, UV light results in a crosslinking reaction of resist polymer, making it hard to be dissolved in the developer, while unexposed resist will be dissolved in the developer. While on the contrary, UV light breaks long-chain polymers in positive photoresist to become more soluble, resulting in exposed areas dissolving in the developing process. Note that for negative photoresist, a post bake after exposure is mandatory to improve the crosslinking efficacy.

d) Anti-sticking treatment

The frame mold is then exposed in trimethylchlorosilane (TMCS, Sigma, France) vapor for 10 min for anti-sticking surface treatment based on the silanization mechanism.

2.2 Vacuum-assisted molding

Vacuum-assisted molding is based on the capillary force in a closed mold. The procedure of vacuum-assisted molding starts with punching holes in the PDMS mold and then the PEGDA solution is injected into the cavity of the pattern, followed by UV crosslinking.

2.2.1 PDMS mold fabrication

PDMS mold fabrication is based on soft lithography, which usually creates an elastic stamp first, and then enables the transfer of patterns onto glass, silicon, or polymer surfaces [6-8]. Polydimethylsiloxane (PDMS) is optically clear, and, in general, inert, non-toxic, and non-flammable. It also has an optical transparency of about ~300 nm and thermal stability to 150 °C. Especially the low surface energy (21.6×10^{-3} J m^{-2}) of PDMS allows easy release from templates and surfaces. The most widely used two commercial PDMS products for soft lithography are RTV 615 from GE Toshiba Silicones Co., Ltd, and Sylgard 184 from Dow Corning. In this thesis work, an RTV 615 mixture of part A (pre-polymer) and part B (curing agent) is used. The normal ratio of A and B is 10:1 (w/w) and after mixing completely, cured PDMS can be obtained after two hours at 75°C, Fig 2.3 reveals the sketch of the crosslinking process between the PDMS chains.

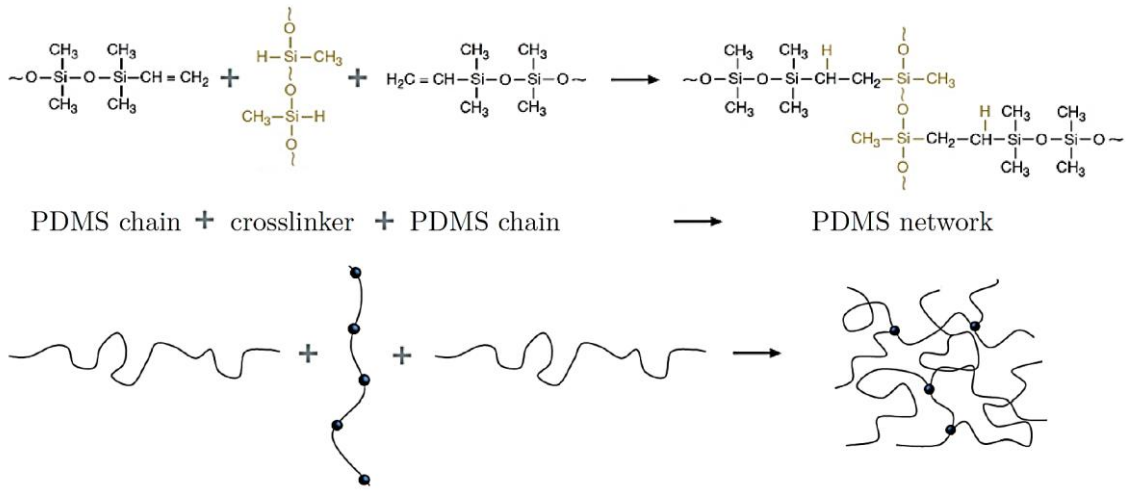

Figure 2.3 Sketch of the crosslinking reaction between the two PDMS components. One of them contains the prepolymer chains and the other one a crosslinking material [9]

Basically, the PDMS mold is replicated from the above frame mold. Briefly, mixed PDMS is cast on the top of the frame mold which is on a silicon wafer. During this casting, the bubbles are not possible to avoid, so it is necessary to degas the PDMS, we transfer the PDMS mixture into a vacuum chamber. The vacuum will let bubbles rise and gather on the top surface of the PDMS mixture. Then we take out the PDMS mixture and use a N2 gun to remove the air bubbles by gently blowing. Afterward, the PDMS mixture can be placed into a hot oven at a constant 75°C. The curing time should normally be at least 2 hours. After curing, the solid PDMS mold can be taken out from the hot oven. After several minutes of cooling down to room temperature, the PDMS mold is easier to peel off. Finally, a scalpel is used to cut out the

desired pattern. Fig 2.4 shows the simplified PDMS replica molding (also known as soft lithography) process.

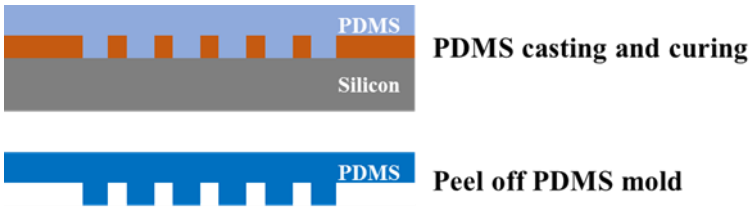

Figure 2.4 Schematic of a fabrication process of PDMS mold. After anti-sticking surface treatment, a prepolymer PDMS is casted on the mold and cured, before peeling off.

2.2.2 PEGDA molding

To ensure a better molding, a material of poly (ethylene glycol) diacrylates (PEGDA, Fig 2.5) is used. This material is a subfamily of PEG-based hydrogels. The synthesis by photo-crosslinking the PEG-based hydrogels is the most common way to convert PEG prepolymer into a crosslinked and stable structure or insoluble hydrogels. In recent years, PEGDA has been widely used in various applications, such as cell encapsulating [10, 11], cartilage tissue regeneration [12-14], tissue resurfacing [15]and wound healing [16-18]. Hence, it's a safe and stable material for cell and cell differentiation in this thesis work.

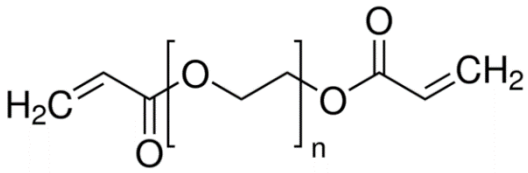

Figure 2.5 Molecular structure of polyethylene glycol diacrylate

The PDMS mold is attached on a glass substrate with gentle pressing. To ensure good PDMS-glass assembling and enhance the capillary effect, we first placed it in the vacuum chamber for 3 minutes under 300 mbar. Afterward, the PDMS-glass assembly was taken out, and a solution of polyethylene glycol diacrylate mixed with a photoinitiator (e.g. 1 % v/v Irgacure 2959) was injected by a pipette tip (p200) in the free space of the PDMS-glass assembly, as shown in Fig 2.6. The solution can usually not fill the free space of pattern immediately, but it would fill completely under 15 minutes assisted by capillary force. After full filling, a UV exposure was processed for 2 min. The PEGDA frame can be obtained on the glass substrate after peeling off PDMS mold. To release the PEGDA frame, we can either use a scalpel to scratch off or directly merge the glass in DI water for auto detaching.

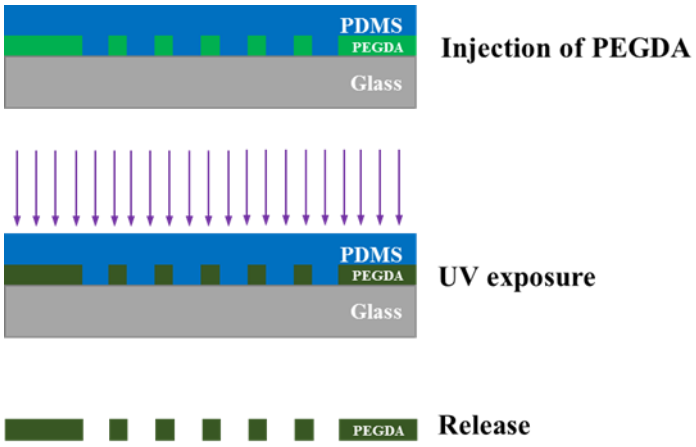

Figure 2.6 Schematic of a fabrication process of PEGDA frame. The PDMS mold is placed on a glass slide and the assembly is treated in a desiccator for air evacuation. Then, liquid PEGDA is placed around the mold cavity and then absorbed inside the cavity, before UV exposure and mold and substrate release.

2.3 Electrospinning

Electrospinning is a commonly used processing method for preparing nanoscale and ultrafine micro/nano fibers by jetting polymer solutions (or melts) under an electric field. Electrospinning technology is fast, efficient, simple equipment, easy to operate, and easy to control the chemical composition and physical properties of products. Non-woven fabrics made from electrospun fibers have the advantages of high porosity, large specific surface area, high fiber fineness and uniformity, and large length-to-diameter ratio, which gives electrospinning fibers a wide range of applications. In addition, the non-woven fabric made by electrospinning has good biocompatibility, so it can be used as biomimetic scaffolds and is particularly suitable for preparing tissue engineering scaffolds.

2.3.1 Electrospinning

Electrospinning is based on an electrohydrodynamic process, during which a liquid droplet is electrified to generate a jet, followed by stretching and elongation to generate micro/nanofibers [19]. As illustrated in Fig 2.7, the setup contains a syringe driver, a high voltage supply, a needle (e.g. a hypodermic needle), and a conductive collector. Before electrospinning, a polymer solution is first prepared by completely dissolving the polymer in a certain solvent and keeping stirring until homogenous. A syringe is fed with a polymer solution and mounted on a syringe driver. The syringe needle is connected with a positive electrode,

while the collector connects the negative electrode. During electrospinning, the polymer solution in the syringe is extruded by the syringe driver to form a droplet as a result of surface tension. Upon electrification, the same positive charges among the droplet surface deform the droplet into a Taylor cone, a charged jet is then ejected beyond surface tension and keeps continuous. To obtain a better quality of fibers, several parameters have to be optimized before the electrospinning, such as humidity, the temperature of environment, as well as the solution composition, the flow rate, the voltage, and the distance between the needle and the collector.

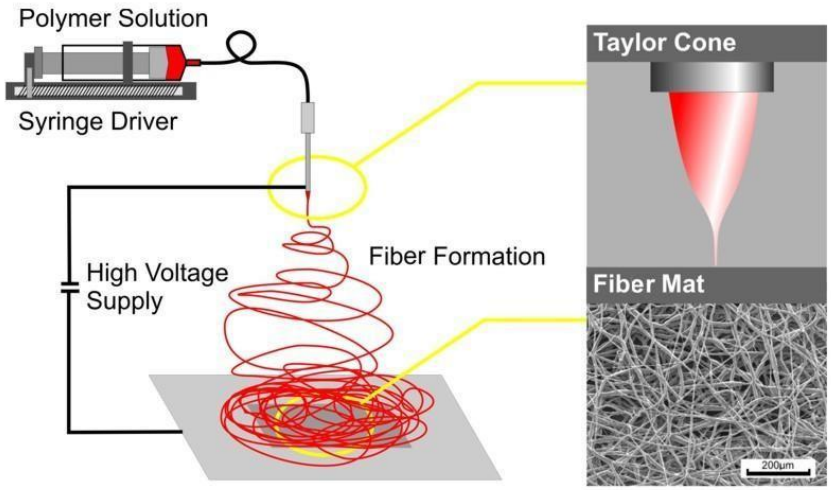

Figure 2.7 Schematic and principle of electrospinning setup, including a syringe driver, a high voltage supply and fiber formation in the presence of Taylor cone.

Various materials, such as biocompatible natural or synthetic polymers can be used to fabricate micro/nanofibers. For adhesive cell culture, the fibers can be surface-modified with plasma, wet chemical etch, protein deposition (e.g. fibronectin, vitronectin), or co-electrospinning with surface agents and other polymers. For suspension culture, the fiber mat can be also incorporated with ultra-low attachment materials such as agarose, sodium alginate, PEG-PLL, etc. Methods of modification include dip coating, spray coating, deposition coating (e.g. formation of protein film).

However, the application of electrospun nanofibers still faces severe challenges. Due to relatively poor mechanical properties, scaffolds made of nanofiber are usually fragile, and they cannot provide sufficient strength for further in vitro cell culture and in vivo implantation or long-term culture. These explain why most scaffolds made of nanofiber have relatively low porosity and large thickness, which inhibits cell sprouting and penetration into the fiber mat and also prevents effective diffusion of nutrients. In this thesis work, we use a biocompatible

frame to support the electrospun monolayer nanofiber. Crosslinking is another necessary modification to enhance the stability of nanofiber scaffolds, there are two main fiber-crosslinking methods: thermal crosslinking and chemical crosslinking.

2.3.2 Chemical crosslinking

Chemical cross-linking is a universal method to improve and enhance the chemical and thermal stability of polymer films. Among the methods of cross-linking, many current researches focus on chemical cross-linking, in which the polymer reacts with a cross-linking agent in the presence of a catalyst to form a network structure. For example, Beppu [20] and Shenvi [21] used glutaraldehyde and sodium tripolyphosphate as the crosslinking agents to prepare crosslinked chitosan films. Rhim [22]and Heydari [23]use different cross-linking agents (such as sulfosuccinate acid or fumaric acid) to make crosslinked polyvinyl alcohol films. Our previous research work [24]used N-hydroxysuccinimide (NHS, Sigma) and 1ethyl-3-(3-dimethylaminopropyl) carbodiimide hydrochloride (EDC, Sigma) to produce a crosslinked monolayer of gelatin nanofibers. Chemical crosslinking mainly optimized the properties of polymer membranes, such as hydrophilicity and separation performance. In addition, after chemical crosslinking and washing, there are almost no residual crosslinkers in final crosslinked polymer films or fiber mats, achieving non-toxicity substrates for cell culture. However, the thermal and chemical stability of the film has not been greatly improved, especially for thermal stability.

2.3.3 Thermal crosslinking

Compared with chemical crosslinking, thermal and chemical stability of polymer films can be significantly improved by thermal crosslinking, because the thermal rearrangement and crosslinking occur in the polymer segments to form a stable 3D network structure. Tsuru and Albo [25-27]used different methods to pretreat several polyamide-derived composite membranes, and discussed changes induced by temperature in the structure of polymers and the transmission performance of composite membranes. Hou [28] and Guo [29]improved the mechanical and thermal stability as well as the hydrothermal property of SPEEK membranes used in fuel cells through thermal crosslinking. Wind [30]and Qiu [31]prepared a thermally crosslinked membrane derived from polyimide to solve the problem of CO2 plasticization in natural gas separation. Our previous research work used citric acid and gelatin blend solution for electrospinning and obtained thermally crosslinked fibers at a temperature of 140 ℃ for 4 hours [32]. As for cell culture, according to our experience, the thermal crosslinking may have a risk of existing cell toxic crosslinkers (i.e., citric acid) inside the polymer fibers after the

crosslinking process. Thus, in this thesis work, we use chemical crosslinking for the monolayer nanofiber formation.

2.4 Micro-milling

Milling is a material-removal process that uses rotating tools to remove material from the raw material of the workpiece. Usually a complete milling system includes (i) a cutting tool (for example, an endmill); (ii) a spindle for fixing and rotating the cutting tool (Fig 2.8); (iii) a worktable for placing the workpiece. The origin of these methods can be traced back to 1818 [33], has made considerable progress, and now it has become the main tool in the work of machinists. Traditionally, the positions of the worktable (X and Y-axis) and spindle (Z-axis) are manually adjusted with mechanical levers and cranks, but modern factories now use computer numerical control (CNC) to automate the process, and further the repeatability and precision can be improved, human error can be reduced, and advanced capabilities are also added (e.g., the direct converting from computer-aided design (CAD) into finished parts).

Micro-milling can be highly useful in the microfluidic field for two main functions (i) machining a mold which can be used in subsequent fabrication processes (e.g., hot embossing or injection molding) [34, 35]or (ii) milling microchannels or micro features into the final work part directly. For the latter case, micro-milling has a key advantage: plastic or metal workpieces can be milled into usable parts in less than 30 minutes, which greatly reduces the process time from design to part production.

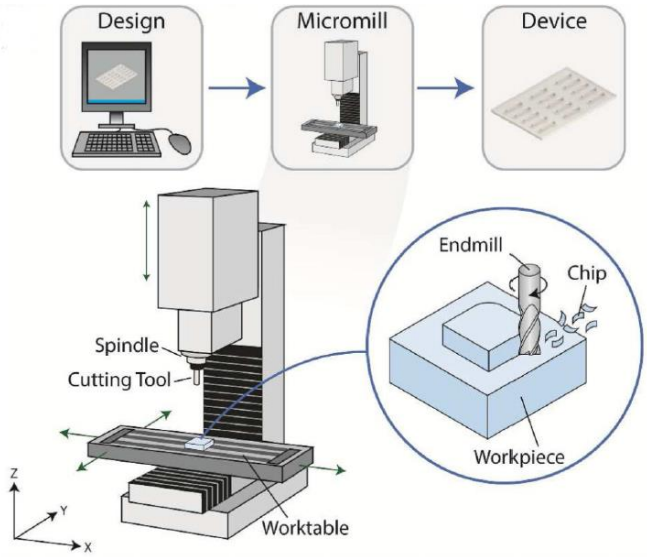

Figure 2.8 Components of a CNC system, including computer design, a worktable, cutting tools, and the schematic of producing microfluidic devices

2.5 Cutting plotter

A cutting plotter is an equipment that uses a blade to cut a piece of material (such as paper, polyester film, or vinyl film) into a pattern, which lies on the cut area of the plotter. In detail, this method is achieved by connecting the cutting plotter to a computer, which contains a specialized pattern design or a software used for pattern design. These computer softwares also send the size information to the cutting plotter to control and command the cutter head to produce a predetermined trajectory, and finally form the originally designed pattern [36]. The cutting plotter has the following advantages:

a) Reliable performance: the cutting plotter can withstand a lot of uses and the service life is more than several years. Various materials, such as PDMS film, thin plastic sheets, and paper can be cut on this equipment, providing a relatively versatile function. .

b) Faster and higher quality: the cutting plotter is just simple CNC blades that help to cut thin materials accurately, thus providing ultimate quality. In addition, it can complete work quickly, achieving a perfect balance between speed and quality.

c) Low operating costs: another wonderful thing about these machines is their low operating costs. They come with everything needed to run them, including self-adhesive sheets, blades, and specialized software.

In recent years the use of cutting plotters has become popular in the microfluidic field such as sealing membrane cutting and microfluidic channel cutting due to the above reasons. Such tools allow the desired membrane and channel shapes to be cut out very precisely and repeated perfectly and identically. Fig 2.9 is a desktop version cutting plotter.

Figure 2.9 A cutting plotter (Graphtec Corporation, Japan) used in this work.

2.6 Parylene deposition

A substrate or a device can be coated by Parylene using a chemical vapor deposition (CVD) system. The Parylene deposition is simply processed at ambient temperature under normal vacuum conditions [37]. The deposition of Parylene polymers occurs at the molecular level, at which the film basically "grows" one molecule at a time. As shown in Fig 2.10, the process stages are:

Stage 1: Samples are placed inside a vacuum chamber, where they are used for coating. The Parylene dimer, in solid powder form, is heated and turns from a solid to a gas in the vaporizer.

Stage 2: The dimer vapor is transferred into the pyrolysis furnace, which breaks the dimer gas into monomer gas by means of additional heating.

Stage 3: The monomer vapor in the highly excited state then enters the room temperature deposition chamber. Because all samples are in the chamber and are fixed, here, a single monomer will be combined with other monomers and deposited on all objects in the chamber. This deposition process finally produces a thin, transparent and highly uniform coating.

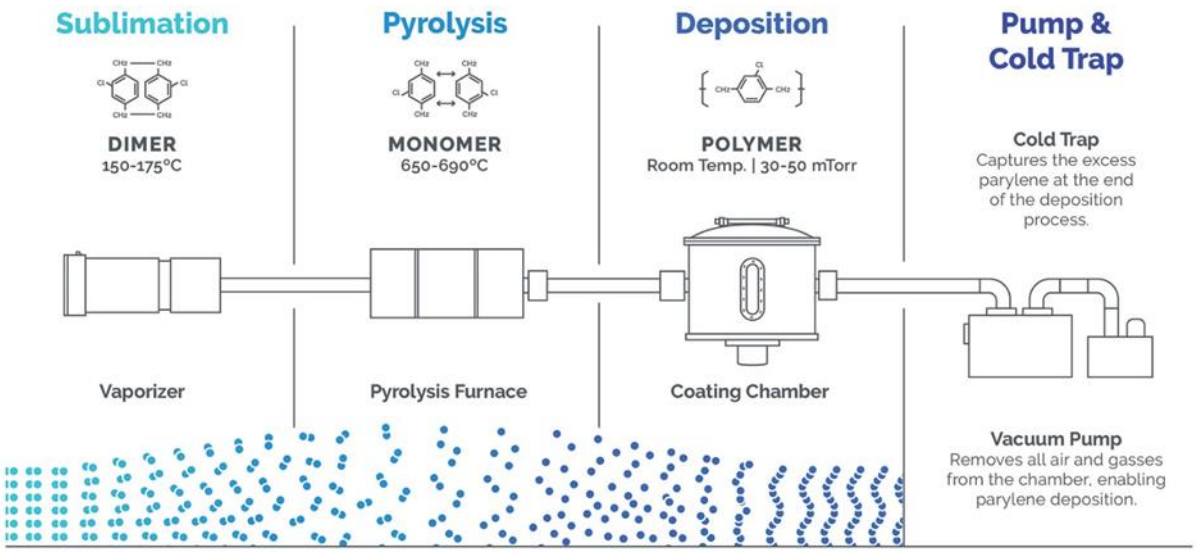

Figure 2.10 Schematic diaphragm of Parylene deposition process, including sublimation of dimmers, pyrolysis into monomers, deposition for forming polymer.

Since Parylene is applied as a gas, the coating can easily penetrate the gaps and narrow areas on the multilayer component, thereby providing a complete and uniform encapsulation. The optimal thickness of the polymer deposition depends on the application and the required coating properties. Although the thickness of the Parylene deposition can be between hundreds of angstroms to a few mils, a typical thickness is in the micrometer range.

Previously, Parylene deposition was often applied to electronic circuits and other equipment as electrical insulation, moisture barriers, or protection against corrosion and chemical attack. They are also used to reduce friction, and in medicine to prevent adverse reactions to implanted devices. In the biological field, Parylene is also non-toxic material, thereby can be used for cell culture due to its inert surface [38]; Parylene deposition also has broadened the applications of other materials which are not previously appropriate for biological applications.

2.7 Culture patch, basement membrane mimics and accessories

2.7.1 Culture patch

The fabrication of the culture patch has already been detailed in [30]. Briefly, photolithography and vacuum assisted molding techniques have been used to fabricate the honeycomb microframes. Gelatin nanofibers were deposited and crosslinked on the microframe by electrospinning and chemical crosslinking. The dimension and thickness of the honeycomb microframe can be changed for different applications. For example, the formation of organoids or spheroids often requests a frame of larger and deeper honeycomb compartments with respect to that of normal cell layers. The geometric parameters of the culture patch for different uses are given in the following chapters and appendices.

2.7.2 Ultrathin artificial basement membrane

Details of the fabrication process of the ultrathin artificial basement membrane (uABM) can be found in Appendix 1. Briefly, a honeycomb microframe is used as a carrier and the monolayer of crosslinked gelatin nanofibers deposited on the frame is used as the backbone for the formation of ultrathin ABM. Here, the electrospinning was performed with a gelatin solution of 12 wt% gelatin powder (G2625, Sigma) in DI water, ethyl acetate, and acetic acid at a volume ratio of 10: 14: 21. The ejection of the gelatin solution through a needle (23-gauge) to the collector (cage) was controlled at a speed of 0.2 mL/h, a distance of 10 cm, a bias voltage of 11 kV, and an electrospinning time of 3 min, respectively. After deposition of nanofibers on the honeycomb frame, the sample was then dried overnight in a desiccator and the gelatin nanofibers were soaked in an ethanol solution containing 2 M N-hydroxysuccinimide (NHS, Sigma) and 0.2 M 1ethyl-3-(3-dimethylaminopropyl) carbodiimide hydrochloride (EDC, Sigma) for 4 h. The sample was then washed three times in ethanol and the nanofiber patch was obtained after drying in a vacuum chamber overnight. Before cell culture, the nanofiber patch was sterilized by submerging into a 70% ethanol solution and placing it under UV light. Finally, the nanofiber patch was treated by uniform covering of 50 µL solution of laminin (20

μg/mL) and collagen type IV (1 mg/ml) in DI water, and ABM patch was formed after dehydration in an incubator at 37 ºC for 4 hours or overnight.

2.7.3 Chamber for improved cell seeding on patch

Cell seeding can be easily done with a patch by dropping a cell containing culture medium in the patch area. However, the resulting cell distribution is often non-uniform due to the surface tension of cell suspension. To solve this problem, a PDMS well was fabricated. Fig 2.11 depicts the whole process of fabrication and implementation. 3D printing or micro-milling was used to make a mold of the cell seeding cavity. Then Parylene deposition on the mold was used for anti-sticking treatment. The next step was to put the mold into a dish and pour liquid PDMS and cure at least 2 h. This step ensures that the PDMS does not flood over the mold. After that, we removed the mold and cut out the PDMS piece. After the necessary sterile process (e.g. 70% Ethanol immersion), a culture patch is placed under the cavity and sticks well with the dish, and the cell suspension can be added finally. We usually wait for 10 minutes for the cells to settle down before we can move the dish into the incubator.

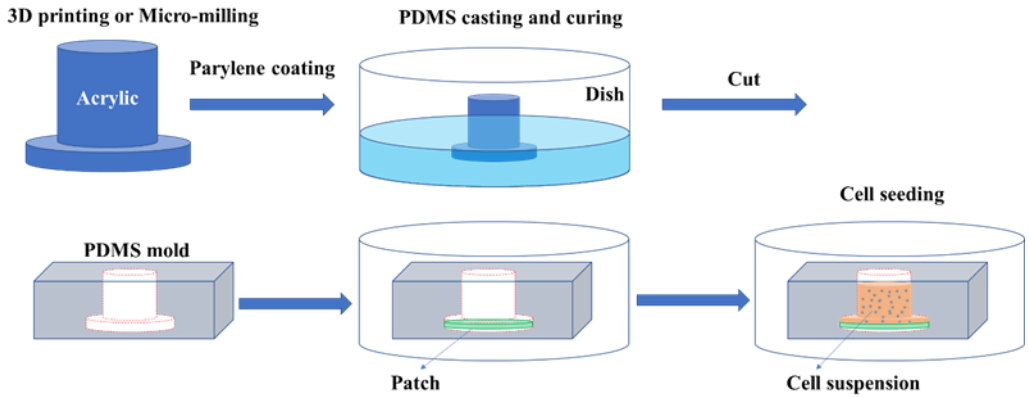

Figure 2.11 Schematic process fabrication of PDMS chamber, including micro-milling, Parylene coating and PDMS casting & curing; and schematic process of cell seeding. Note: PDMS mold is detached from an acrylic mold after curing.

This method of planting cells on a smaller surface is a new solution for the cell seeding problem. It saves the number of cells and the volume of the culture medium. In addition, without necessary bonding, the PDMS material used also has good adhesion to the culture dish and there is no leakage. Therefore, it is very suitable for mass production of samples, with good repeatability, and is an excellent method for drug screening and dose control.

2.7.4 Patch handler for Air-liquid interface (ALI) culture

ALI culture is known to be necessary for cultivation and studies of respiratory cells. Compared with conventional Transwell membrane made of polycarbonate, our culture patch

with a monolayer of nanofiber film which is relatively thinner, more biocompatible, and more permeable, is a better candidate for basement membrane mimicking. Hence, we integrated our culture patch into an ALI culture device for handling, as shown in Fig 2.12. This patch handler for ALI culture is composed of an apical part, two PDMS O-rings, a culture patch, and a basal part. The apical part and the basal part can be connected by a threaded connection, the culture patch insert is clamped by two PDMS O-rings to avoid the medium leakage from the basal side, providing a robust assembling and easy handling for the ALI culture and further processing.

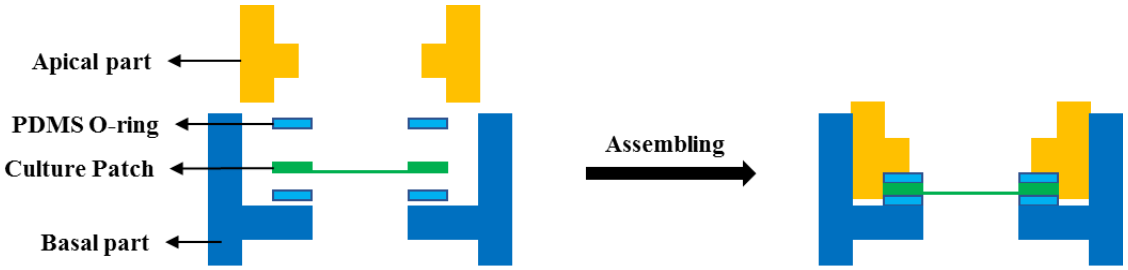

Figure 2.12 Schematic of ALI parts (left) and assembled ALI culture device (right) for human epithelial cells grown using culture patch inserts.

Fig 2.13a shows the different parts and an assembled patch handler for ALI culture, the apical and basal parts were made of PTFE, a material with high insulation and non-toxicity to cells. In addition, the basal part has 4 grooves on its bottom surface to form an open cavity and ensure medium diffusion from nearby. This assembled and tiny patch handler fits very well in a well of 6-well plate. With our culture patch insert, the basal side only needs to fill 1.2 ~ 1.5 mL medium to maintain and differentiate cells under the ALI culture condition. Fig2.13b is an ongoing ALI culture with our patch handler. Moreover, Transepithelial electrical resistance (TEER) measurement is always an important method to evaluate the growth of the cell layer under ALI culture. Our patch handler is also compatible with the electrode intervention with its separated apical and basal compartments. (See Chapter 4)

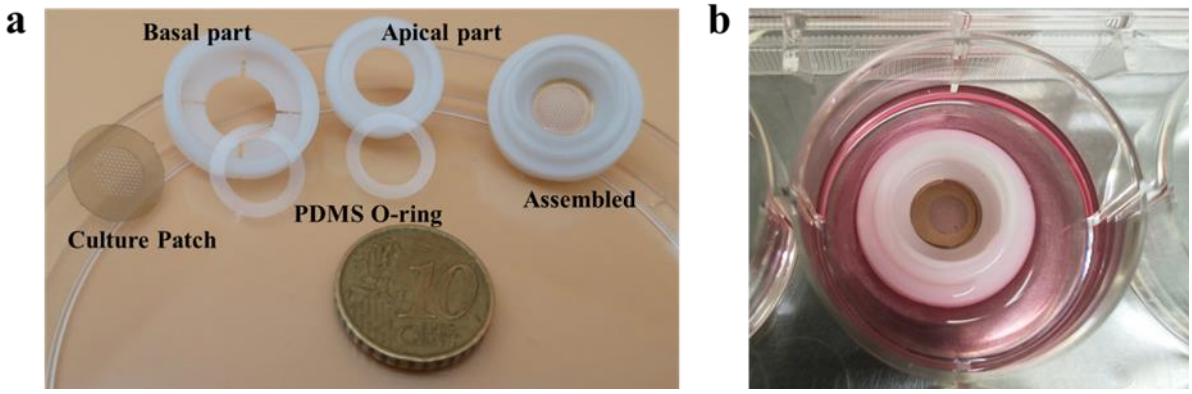

Figure 2.13 Images of patch handler for ALI culture. (a) Different parts (culture patch, basal part, apical part, PDMS O-ring) and assembled patch handler for ALI culture; (b) A patch handler for an ongoing ALI culture in a 6-well plate

2.8 Microfluidic devices

All microfluidic devices used in this work are based on the standard device configuration proposed by Mesobiotech (www.mesoiotech.www), a spinoff startup company of the ENS laboratory for microfluidics. This configuration relies on mechanical clamping of two plastic plates with a cell patch or a tissue construct as a removable insert. Such a device configuration has clear advantages of easy integration and easy removal of a cell patch or a tissue construct, prepared before and characterized after with more conventional techniques.

2.8.1 Device configuration

A microfluidic chip is a set of microchannels etched or molded into materials (glass, silicon or polymers such as PDMS, silicone). The microchannels forming the microfluidic chip are connected together to achieve the desired function (mixing, pumping, sorting or controlling the biochemical environment).

The device configuration we adopted from Mesobiotech is a modular assembly with two plastic plates in polycarbonate manufactured by injection molding, as shown in Figure 2.14. Here, small magnets are embedded in the four corners of the upper and the lower plates, which ensure a self-aligned and reversible device assembling. A thin film of PDMS is bonded on the contacting surface of two plastic plates to a good sealing after clamping. Moreover, standard Luer connectors are molded on the upper plastic plate, allowing easy fluidic connection of the device with the out world. Micro-chambers and micro-channels are pre-patterned in both plastic plates. Once assembled with a patch insert, two independent microfluidic working spaces are created. These two microfluidic chambers can be perfused with different culture

media. Thus, a tissue interface can be formed to simulate alveolar, stomach, intestine, kidney, liver, brain-blood, skin functions, etc. Thus, a cell layer or a tissue construct can be characterized in situ or removed for downstream analysis.

By using the micro-milling technique, we can easily modify the channel structure of the plastic plate. By using the cutter plotter technique, we can easily create new structures in PDMS thin layers of the device. Thus, we could be able to easily fabricate new patterns within the framework of the standard device configuration.

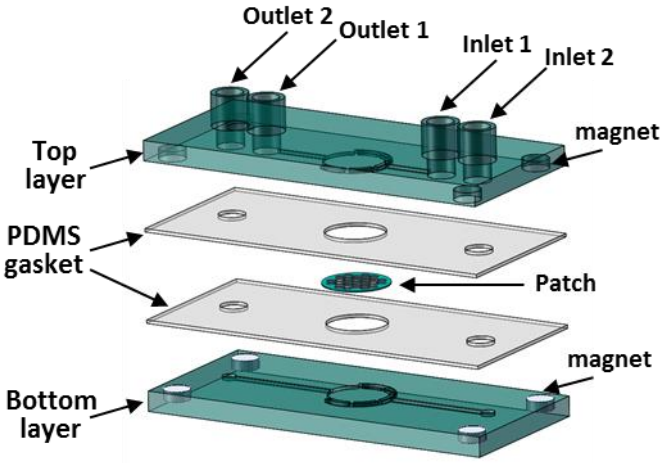

Figure 2.14 Schematic diagram of the Mesobiotech device configuration. A thin layer of PDMS with channel access holes is chemically bonded on the upper and lower plastic plate with microchannels. The patch is then sandwiched between the two plastic plates with the help of four pairs of embedded magnets.

2.8.2 Mechanical clamping

Traditionally, chemical and thermal bonding techniques are used to assemble a microfluidic device from a patterned layer and a substrate. This assembling is irreversible and the resulting device cannot be reused because it is difficult to clean enclosed channels and micro-chambers. In contrast, mechanical assembling of a microfluidic device is reversible, which allows reusing the device except for the insert such as culture patch or microfilter. More importantly, the cell layer can be prepared before placing inside the microfluidic device and it can then be removed for subsequent studies after microfluidic operations. By using a substrate with a cover glass window, high-resolution imaging can be performed. Mesobiotech has also proposed a clamp with 4 hand screws for easy and rapid assembling of their devices. This clamp is made of anodized aluminum which is compatible with the cell culture environment in terms of stability in humidity, temperature, and chemical resistance.

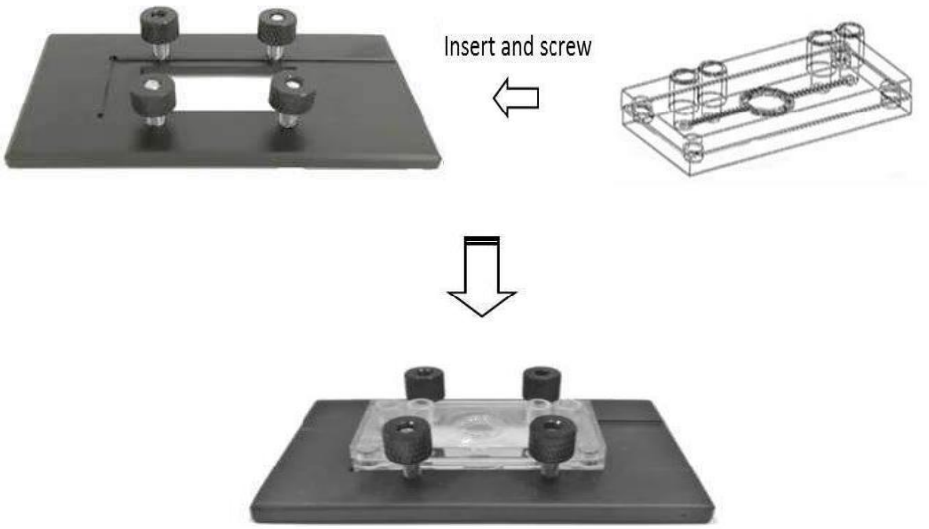

Figure 2.15 Clamping of a patch integrated microfluidic device for enhanced sealing, with the help of 4 hand screws for fast assembly and release.

2.8.3 Concluding remarks

A large variety of fabrication techniques are available for microfluidic device prototyping and manufacturing. We have presented a few of them used in this work. We have also presented more specific the patch holder and patch integration devices, which are now manufactured by Mesobiotech. Accordingly, we will pay more attentions on the suitability of these devices in the development of new systems (Chapter 3 and appendices) and new protocols (Chapters 4 and 5 and appendices).

References

[1] Levenson, MD, et al. (1982). "Improving resolution in photolithography with a phase-shifting mask." Trends in pharmacological sciences **29**(12): 1828-1836.

[2] Dumon, P, et al. (2004). "Low-loss SOI photonic wires and ring resonators fabricated with deep UV lithography." IEEE Photonics Technology Letters **16**(5): 1328-1330.

[3] Braat, JJ (1999). Extreme-UV lithography: a candidate for next-generation lithography. Photonics, Devices, and Systems, International Society for Optics and Photonics.

[4] Lin, BJ (1975). "Deep UV lithography." Journal of vacuum science technology **12**(6): 1317-1320.

[5] Rogers, JA and RG Nuzzo (2005). "Recent progress in soft lithography." Materials today **8**(2): 50-56.

[6] Gitlin, L, et al. (2009). "Rapid replication of master structures by double casting with PDMS." Lab on a Chip **9**(20): 3000-3002.

[7] Rolland, JP, et al. (2004). "High-resolution soft lithography: enabling materials for nanotechnologies." Angewandte Chemie International Edition **43**(43): 5796-5799.

[8] Xia, Y and GM Whitesides (1998). "Soft lithography." Annual review of materials science **28**(1): 153-184.

[9] Madsen, F, et al. (2014). "Visualisation and characterisation of heterogeneous bimodal PDMS networks." RSC Advances **4**(14): 6939-6945.

[10] Durst, CA, et al. (2011). "Flexural characterization of cell encapsulated PEGDA hydrogels with applications for tissue engineered heart valves." Acta biomaterialia **7**(6): 2467-2476.

[11] Nachlas, AL, et al. (2018). "Human iPSC-derived mesenchymal stem cells encapsulated in PEGDA hydrogels mature into valve interstitial-like cells." Acta biomaterialia **71**: 235-246.

[12] Kim, HD, et al. (2017). "Biomimetically reinforced polyvinyl alcohol-based hybrid scaffolds for cartilage tissue engineering." Polymers **9**(12): 655.

[13] Uttayarat, P, et al. (2015). Photopolymerization of hydrogels for cartilage tissue engineering. 2015 8th Biomedical Engineering International Conference (BMEiCON), IEEE.

[14] Zhu, W, et al. (2018). "3D bioprinting mesenchymal stem cell-laden construct with core–shell nanospheres for cartilage tissue engineering." Nanotechnology **29**(18): 185101.

[15] Nemir, S, et al. (2010). "PEGDA hydrogels with patterned elasticity: Novel tools for the study of cell response to substrate rigidity." Biotechnology and bioengineering **105**(3): 636-644.

[16] Kim, S, et al. (2014). "Fabrication of poly (ethylene oxide) hydrogels for wound dressing application using E-beam." Macromolecular Research **22**(2): 131-138.

[17] Sokic, S and G Papavasiliou (2012). "FGF-1 and proteolytically mediated cleavage site presentation influence three-dimensional fibroblast invasion in biomimetic PEGDA hydrogels." Acta biomaterialia **8**(6): 2213-2222.

[18] Wang, Y, et al. (2019). "Fabrication of bi-layer photocrosslinked GelMA/PEGDA fibrous membrane for guided bone regeneration materials." Materials Letters **249**: 112-115.

[19] Ding, B, et al. (2018). Electrospinning: nanofabrication and applications, William Andrew.

[20] Beppu, M, et al. (2007). "Crosslinking of chitosan membranes using glutaraldehyde: Effect on ion permeability and water absorption." Journal of membrane science **301**(1-2): 126-130.

[21] Shenvi, S, et al. (2014). "Preparation and characterization study of PPEES/chitosan composite membrane crosslinked with tripolyphosphate." Desalination **344**: 90-96.

[22] Rhim, J-W, et al. (2004). "Crosslinked poly (vinyl alcohol) membranes containing sulfonic acid group: proton and methanol transport through membranes." Journal of membrane science **238**(1-2): 143-151.

[23] Heydari, M, et al. (2013). "Effect of cross-linking time on the thermal and mechanical properties and pervaporation performance of poly (vinyl alcohol) membrane cross-linked with fumaric acid used for dehydration of isopropanol." Journal of applied polymer science **128**(3): 1640-1651.

[24] Tang, Y, et al. (2016). "Induction and differentiation of human induced pluripotent stem cells into functional cardiomyocytes on a compartmented monolayer of gelatin nanofibers." Nanoscale **8**(30): 14530-14540.

[25] Albo, J, et al. (2014). "Structural characterization of thin-film polyamide reverse osmosis membranes." Industrial Engineering Chemistry Research **53**(4): 1442-1451.

[26] Albo, J, et al. (2014). "Gas transport properties of interfacially polymerized polyamide composite membranes under different pre-treatments and temperatures." Journal of membrane science **449**: 109-118.

[27] Albo, J, et al. (2014). "Application of interfacially polymerized polyamide composite membranes to isopropanol dehydration: Effect of membrane pre-treatment and temperature." Journal of membrane science **453**: 384-393.

[28] Hou, H, et al. (2012). "Crosslinked SPEEK membranes: Mechanical, thermal, and hydrothermal properties." 1950-1957.

[29] Guo, M, et al. (2010). "Preparation of sulfonated poly (ether ether ketone) s containing amino groups/epoxy resin composite membranes and their in situ crosslinking for application in fuel cells." Journal of Power Sources **195**(1): 11-20.

[30] Wind, JD, et al. (2002). "The effects of crosslinking chemistry on CO2 plasticization of polyimide gas separation membranes." Industrial engineering chemistry research **41**(24): 6139-6148.

[31] Qiu, W, et al. (2011). "Sub-T g cross-linking of a polyimide membrane for enhanced CO2 plasticization resistance for natural gas separation." Macromolecules **44**(15): 6046-6056.

[32] Nagura, M, et al. (2002). "Structures and physical properties of cross-linked gelatin fibers." Polymer Journal **34**(10): 761-766.

[33] Woodbury, RS and S Kobayashi (1974). "Studies in the History of Machine Tools."

[34] Wilson, ME, et al. (2011). "Fabrication of circular microfluidic channels by combining mechanical micromilling and soft lithography." Lab on a Chip **11**(8): 1550-1555.

[35] Okagbare, PI, et al. (2010). "Fabrication of a cyclic olefin copolymer planar waveguide embedded in a multi-channel poly (methyl methacrylate) fluidic chip for evanescence excitation." Lab on a Chip **10**(1): 66-73.

[36] Shibata, T, et al. (2012). Cutting plotter, cutting plotter driving control device, cut target medium supporting sheet, cut target medium, cutting pen, method of manufacturing paper product, and method of generating cut data, Google Patents.

[37] Song, JS, et al. (2009). "Improved biocompatibility of parylene-C films prepared by chemical vapor deposition and the subsequent plasma treatment." Journal of applied polymer science **112**(6): 3677-3685.

[38] Staufert, S, et al. (2019). "Highly Adherent Parylene-C Coatings With Nanostructuring for Enhanced Cell Adhesion and Growth." IEEE transactions on nanobioscience **18**(2): 230-233.

Chapter 3
Automatic stem cell differentiation

Automatic stem cell differentiation

In this chapter, we present the development of an automatic culture system for human pluripotent stem cell differentiation. Firstly, we provide a brief introduction to the previous approaches in emphasizing the necessity of the new system for research and development of hiPSCs at a laboratory scale. Then, we describe in detail the system we developed in this work, followed by three validation examples: i) a dynamic culture under a perfusion-diffusion regime which increases the cell proliferation rate, ii) a multi-source culture for hiPSC differentiation to cardiomyocytes, and iii) a long-term culture for neural network maturation. Finally, we discuss the application potential of the system in stem cell studies.

3.1 Introduction

Cell proliferation and stem cell differentiation are essential for many cell-based assays and organ-on-a-chip applications [1, 2]. In particular, differentiation of human induced pluripotent stem cells (hiPSC) can give rise to different types of cells that can be used for regenerative medicine, drug discovery, or cell therapies [3-8]. Despite their high potential, it is still challenging to control the quality of hiPSCs and their derivatives. One of the possible reasons is that the proposed protocols have been mostly established by using conventional tools and techniques. Differentiation of hiPSCs requires sequential operations over a long period for culture medium preparation and exchange, substrate replacement, and cell passages that are often laborious and cumbersome [9]. Automatic differentiation of hiPSCs has been demonstrated using commercial bioreactors for different target cell types, including cardiomyocytes [10], macrophages [11], alveolar epithelium [12], and neurons [13]. However, most bioreactors are limited to suspension culture, in which cells are in an agitated growth medium with or without micro-carriers, and cells are subjected to constant perturbations, including shear stress and gravitational force changes. Large platforms for automatic hiPSC self-renewing [14] and differentiation [15, 16] have also been reported, which were essentially based on large-scale machinery for robotic manipulation of culture wares. These platforms are generally expensive and difficult to change cultural conditions. For example, the system proposed by Sartorius allows standard operations with large batches for which the medium change relies on serious processes, including retrieving T-flask from the incubator, removing T-flask cap, pouring media into a waste funnel, adding the new medium, and replacing T-flask

in the flask carousel incubator, with the help of a robot, shaking machine and pumps [16]. This system can be used in highly specialized research centers or industries but not suited for common laboratory uses. As in the current stage of hiPSCs development, there are still many challenges requiring flexible and quick access to process automation, a laboratory platform is desirable.

To begin with, we designed a system at a low cost but autonomic and polyvalent for different assays. The following aspects have to be considered. First of all, the culture media should be stored in a refrigerator and each of them can be loaded automatically upon request. Secondly, the culture platform should be compatible with conventional culture wares such as Petri dishes and multiwell plates as well as microfluidic devices. Thirdly, the system can be used for a dynamic culture where the culture medium is exchanged permanently or at a high-frequency rate. Finally, when the system is used for hiPSC differentiation, functional tissue constructs have to be obtained after automatic processing involving multi-sources over a few weeks and, if necessary, a maturation stage over a few months.

In the following, we first present the development of a prototype and then demonstrate its usefulness in dynamic culture, hiPSCs differentiation to cardiomyocytes and neural network maturation. We show that this prototype is compact and flexible. It does not only reduce the manpower and reagent consumption but also minimizes risks of operation error and contamination. It should be applicable to the recapitulation of the in-vivo cellular microenvironment, to optimize new differentiation protocols, and to develop more sophisticated organ-on-a-chip systems.

3.2 Development of the system

As the first generation of the platform, we have chosen to work with an ATmega 2560 based microcontroller, Arduino boards, to automatically control the culture and differentiation processes (https://www.arduino.cc/). The Arduino boards are commercially available, which are equipped with sets of digital and analog input/output (I/O) pins that may be interfaced with the electronic and pneumatic components as well as additional circuits involved in an automatic system. The boards also provide serial communications interfaces to a PC using a USB cable, which allows loading a program with an easy application programming interface.

Figure 3.1 shows a typical platform configuration in three parts: i) Storage unit, ii) Control unit, and iii) Cell culture unit. The storage unit was designed to keep the culture media at low temperature in standard falcon tubes (M1-M6) and to distribute them upon request. The cap of

each tube has an inlet connected to the rotating valve Ra and an outlet connected to rotating valve Rm. The cell culture unit consists of two peristaltic pumps (3, 4), two falcon tubes (R, W), and a culture dish plate where a metallic handling plate is fixed above the dish cover. The control unit is based on an Arduino board Mega 2560. In addition, it is also equipped with two peristaltic pumps (1, 2), a keyboard, an OLED display, RS485 communication ports, etc. The four pumps (1-4) and two valves (Ra, Rm) are all controlled by the microcontroller and silicone tubing with standard Luer connectors are used for as pipelines of the culture media.

During cell cultivation, the storage unit is kept at 4°C in a refrigerator and the cell culture unit is placed in an incubator at 37°C with 5% humidified CO_2. When a culture medium is selected, the two rotating valves are simultaneously switched to the positions where filtered air can come in the tube and the medium can be pumped out. The medium is firstly injected into tube R by pump 1. When tube R is filled, the medium is injected into the culture dish by pump 3 for incubation. Afterward, the medium is transported into tube W by pump 4.

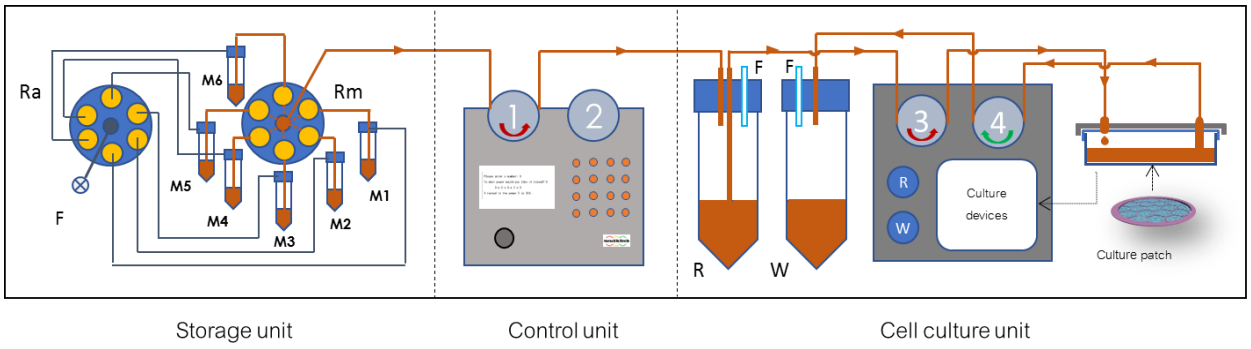

Figure 3.1 Schematic presentation of the laboratory platform designed for automated cell culture and differentiation of stem cells. Here, the storage unit is placed in a refrigerator (left), the cell culture unit is placed in an incubator (right), and the control unit is used to pump the media from the storage unit to the cell culture unit and to control fluidic motion of all pipelines (middle).

Figure 3.2 shows photographs of the three units of the laboratory platform with fluidic pipelines (a), a dish cover handling plate (b), a culture patch (c), and a patch mounting device (d). Here, two female Luer locks to panel mount with barb are fixed on the cover handling plate for injection and aspiration of the culture medium (b). The culture patch is made of a monolayer of gelatin nanofibers deposited on a honeycomb micro-frame (see below). The patch mounting device in polytetrafluoroethylene (PTFE) is used to localize 6 patches and place them together in the culture dish.

Cell culture and stem cell differentiation sequences are programmed in Arduino C with a PC and then transferred to the memory of the Arduino board through a USB cable. The processing parameters and sequences are shown on the OLED display of the control unit, which can be modified or chosen with the keyboard. During automatic processes, a sequence can be stopped or paused for manual intervention. In addition, the control unit integrated a Wireless or Bluetooth module for eventual remote control.

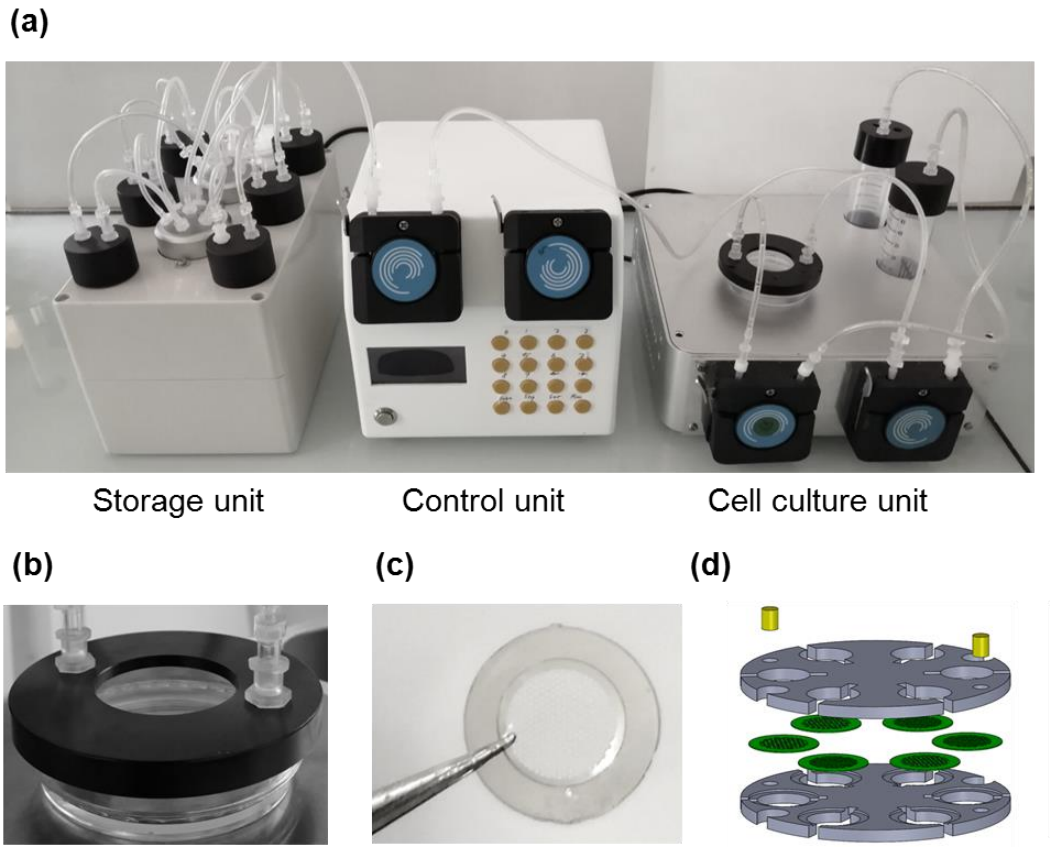

Figure 3.2 (a) Photographs of the platform, showing a media-distribution unit (left), a control unit (center) and a culture unit (right) with fluidic pipelines according to Figure 3.1. (b) Photograph of a metallic holder with inlet and outlet mounted on a normal dish cover. (c) Photograph of a culture patch made of monolayer nanofibers and a ring for handling. (d) Schematic diagram of mounting device for six patches.

Before cell cultivation, tubing and connectors were sterilized (falcon tubes are commercial and sterile products). All fluidic connections and cell seeding were performed in a laminar airflow hood. After assembling the three units of the platform, a washing sequence was launched to sterilize all pipelines and liquid passages (silicon tubing, rotating valves, and dish cover handling plate) with a 70% ethanol solution. This washing cycle was repeated two times and the ethanol solution was recovered in falcon tube W. Thereafter, the same sequence was

applied with pen-strep solution (1%) and culture medium to stabilize the system before cell cultivation. A flow rate of 3 mL/min was set for all washing cycles.

3.3 Dynamic cell culture

HeLa S3 cells were used for culture test with DMEM medium supplemented with 10 % fetal bovine serum (FBS), 1 % Penicillin-Streptomycin (pen-strep) and 1 % L-Glutamine. They were seeded on a 60 mm culture dish with a cell number of 2×10^5. Then, the dish was placed in the cell culture unit and cells were incubated in a 5% humidified CO2 incubator at 37°C. After static incubation for 2 h, an automatic culture sequence was launched. Pump 1 and valves Ra and Rm then were used to fill the falcon tube R every two days, while pumps 3 and 4 were used to circulate culture medium inside the incubator: the medium of falcon tube R was firstly pumped out and injected into the dish by pump 3, it was then pumped from the dish to the falcon tube W by pump 4. Since pump 3 and 4 could operate simultaneously, a perfusion culture regime could be created when the medium pumped from the dish was injected into the falcon tube R instead of W. In such a case, a perfusion-diffusion culture regime could also be achieved by applying a run-rest sequence with a small duty cycle. Here, a sequence of 4 s run – 1 min rest was tested.

A control experiment was performed by manually exchanging the same amount of culture medium every 2 days. Cell growth was monitored, using an inverted light microscope, for several days. Pictures were taken after 1, 24, 48, 72 and 96 hours. Quantitative analysis of proliferation rate and confluence were performed using free software ImageJ (NIH USA). Here, a threshold function was used to calculate the cell covered area at day 1, 2 and 3 and a confluence state was obtained once the whole dish area was fully covered.

Figure 3.3a shows microphotographs of Hela cells after incubation for 1, 24, 48, 72 and 96 hours in both cases of automatic and manual culture, respectively. Here, automatic culture means not only automatically renew the culture medium in falcon tube R every two days but also perfuse the culture medium in the dish quasi-continuously over the whole period of culture. Clearly, the HeLa cells cultivated under perfusion-diffusion regime grew more rapidly than static culture and they reached confluence after 72 h, in contrast that after 96 h with manual renewal of the culture medium. Figure 3.3b shows a comparison between the two types of culture after incubation for 96 h, the empty spaces indicated by white arrows suggested a lower confluence quantity of static culture. The microphotographs of both automatic and manual culture were further analyzed by ImageJ, showing remarkable differences in proliferation

(Figure 3.3c). This is due probably to the enhanced uptake of nutrients and enhanced clearance of the metabolites, thanks to the quasi-continuous renewing of the culture medium.

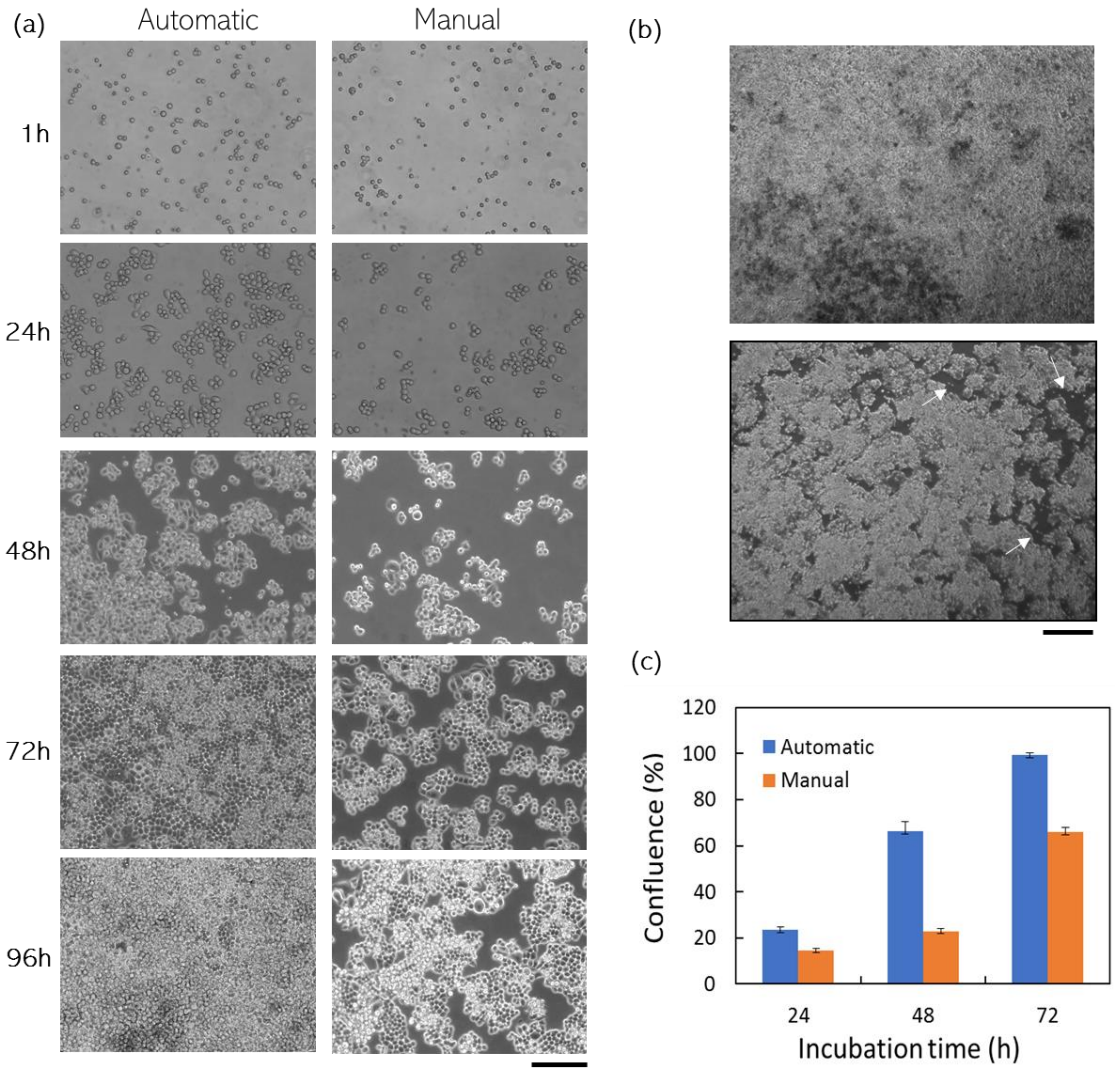

Figure 3.3 Phase contrast images (10 x objectives) of HeLa cells under automatic (left column) and manual (right column) culture conditions (a). The percentages of the cell layer confluence under the two types of culture conditions are compared (b, c), showing significant differences due to different growth rates. Scale bars: 50 µm.

The software COMSOL Multiphysics was used to simulate the gradient concentration in a tissue culture dish of 60 mm diameter under both static and dynamic culture conditions. Firstly, we established the fluid domain by SolidWorks and imported it to COMSOL Multiphysics. Then, we chose simulation modules “Creeping flow” and “Transport of Diluted Species” for numerical simulation based on the Finite-Element Method (FEM). The simulation results are reported as a pattern of solute concentration in the culture dish after reaching a steady state.

Numerical simulation has been performed with the fluid domain as shown in Figure 3.4a and a solute of a diffusion coefficient of 6×10^{-10} m²/s. Under static culture conditions (diffusion dominant), cells grow on the surface of the dish and the solute concentration should be highest on the top level of the medium surface and lowest on the cell layer. With a homogenous solute concentration of 25 mol/m^3 and a medium height of 2 mm. A steady stage could be reached in 1 h. As can be seen in Figure 3.4b by the color ribbons, the concentration varies from bottom to upper surface in a range of 12~25 mol/m^3, which means that in the proximity of the cell layer the concentration of nutrients is only half of that of the top surface. On the contrary, the concentration of cellular metabolites in the proximity of the cell layer is larger than that of the top surface. Under dynamic culture conditions (perfusion dominant), we assumed an initial concentration of 25 mol/m^3 at the inlet and 0 solute at the outlet. After one minute with a flow rate of 20 µl/s for both inlet and outlet, a steady state could be reached. As shown in Figure 3.4c by the color ribbons, the simulation suggests a quite uniform solute concentration over the whole medium layer, due to continuous renewal of the medium in the dish. Similarly, the concentration of the metabolites should also be homogenous. Thus, we can conclude that dynamic culture may enhance both nutrient uptake and metabolite clearance of the cells which gives rise to an increased cell proliferation rate. More generally, a perfusion-diffusion regime can be reached by alternating static and dynamic culture conditions.

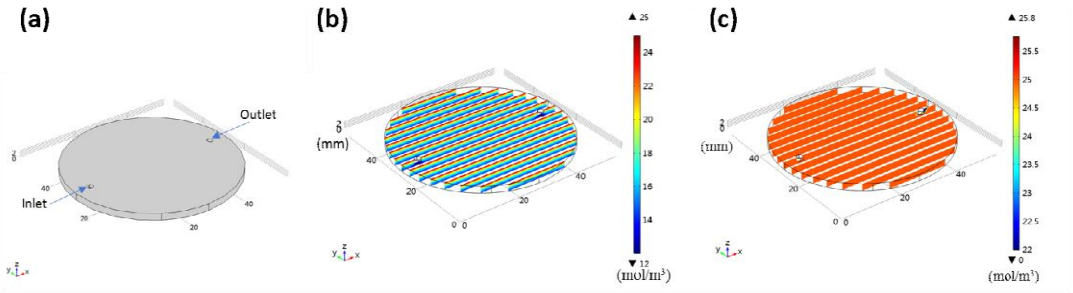

Figure 3.4 Numerical simulation based on COMSOL-Multiphysics: (a) Fluid domain with a culture dish of 60 mm diameter and a pair of well-separated inlet and outlet; (b) Solute concentration in the dish under static culture condition; (c) Solute concentration in the dish under dynamic culture condition.

3.4 Cardiac differentiation

To evaluate the performance of the platform for hiPSCs differentiation, we have been working with a known protocol toward functional cardiomyocytes. This differentiation protocol involves six types of culture media and needs regular medium replacements at a low

exchange rate over two weeks. With our culture patch technique, we show the formation of homogeneous hiPSC colonies and regular beating of the resulting cardiomyocytes. We also demonstrated that our platform is highly feasible for those differentiations with multi phases, such as cardiac differentiation.

3.4.1 Fabrication of the culture patch

The same protocol of our previous work has been employed for the fabrication of the culture patch for the proposed automated platform [17]. Briefly, the patch consists of a monolayer of crosslinked gelatin nanofibers supported by a polyethylene glycol diacrylate (PEGDA Mw=250, Sigma) honeycomb frame (Figure 3.2c). The PEGDA frame was fabricated with a UV based molding method, the gelatin nanofibers were obtained by electrospinning. A pattern of honeycomb frame was produced on a chromium mask with a micropattern generator (µPG 101, Heidelberg Instruments, Germany). A photoresist layer of 50 µm thickness (SU 8, MicroChem, France) was then spin-coated on a silicon wafer with the chromium mask and exposed with UV light. After development, for anti-sticking treatment the mask was placed in trimethylchlorosilane (TMCS) vapor for 1 min. A Polydimethylsiloxane (PDMS) solution composed of a pre-polymer and cross-linker (GE RTV 615, GE, France) at a weight ratio of 10:1 was prepared and poured onto the photoresist mold. After curing (75 °C for 2 h), the PDMS layer was peeled off and placed on a glass slide. After degassing of the mold for 15 min, PEGDA with 1 v/v% photo-initiator (Irgacure 2959, Sigma) was introduced to fill the PDMS-glass cavity, followed by 2 min UV exposure (23 mW/cm2). Finally, the solidified PEGDA honeycomb was separated from the PDMS mold and gelatin nanofibers were electrospun on the PEGDA frame.

3.4.2 Preparation of the culture media with different factors

The following culture media were prepared for cardiac differentiation:

M1: Complete Essential 8™ Medium Add Essential 8™ Supplement (50X) 10 mL (thawing at RT ~1h) to Essential 8™ Basal Medium 490 mL. Complete Essential 8™ Medium can be stored at 2–8°C for up to 2 weeks.

5 mM ROCK inhibitor (Y27632) In a sterile environment, add 6.24 ml PBS to 10 mg Y27632. Aliquot 100 µl samples into 1.5 ml tubes and store at −20 °C for up to 1 year.

M2: Complete Essential 8™ Medium + 10 µM Y-27632

CHIR99021(36mM) Add 1.49ml DMSO to 25mg CHIR99021. Aliquot and store at -20℃ for up to 1 year.

IWP2 (5 mM) Add 4.28 ml DMSO to 10 mg IWP2. Incubate the mixture at 37 °C for 10 minutes to dissolve the IWP2. Aliquot 100 µl samples into 1.5 ml tubes and store at −20 °C for up to 1 year.

M3: RPMI/B27-insulin + 12 µM CHIR99021 (10ml) Add 3.33 µl of 36 mM CHIR99021 into 10 ml RPMI/B27-insulin. It's not recommended to store this medium.

M4: RPMI/B27-insulin In a sterile environment, mix 500 ml of RPMI and 10 ml B27 supplement minus Insulin. The medium can be stored at 4 °C for up to 1 month.

M5: RPMI/B27-insulin + 5 µM IWP-2 (15ml) Add 15 µl of 5 mM IWP-2 into 15 ml RPMI/B27-insulin. It's not recommended to store this medium.

M6: RPMI/B27 In a sterile environment, mix 500 ml of RPMI and 10 ml of B27 supplement. The medium can be stored at 4 °C for up to 1 month.

They were then respectively placed in six 50 ml tubes for centrifuge of the storage unit at 4°C.

3.4.3 Protocol implementation

HiPSCs of cell line 253G1 were cultured with complete E8 medium (M1) in a culture dish coated with 1:100 diluted vitronectin (Thermo Fisher, France) at 37 °C in 5% CO2. The medium was renewed every day until the cells reached about 80% confluence. Cells were then collected by dissociation using a 0.5 mM EDTA solution. To promote the adhesion of hiPSCs on gelatin fibers, the culture patch was coated with vitronectin diluted in DPBS at a ratio of 1:500 and then placed in a culture dish. 2×10^5 hiPSCs in 50 µl E8 medium containing 10 µM Y-27632 (M2) (ROCK inhibitor, Hello Bio, UK) were dropped on the culture patch and then incubated for 1 h. Thereafter, the culture dish was connected to the circuit of the automated culture platform and the mediums and factors were changed automatically. Briefly, the M2 medium was automatically replaced by RPMI 1640 medium containing B27 minus insulin supplement and 12 µM of CHIR99021 (STEMCELL Technology) (M3). After 24 h incubation, the M3 was replaced with RPMI 1640/B27 without insulin (M4). After another 48 h, the M4 was replaced by RPMI 1640/B27 without insulin but containing 5 µM IWP2 (Hello Bio) (M5). After 48 h in the incubator, the M5 was replaced with M4. After 48 h, the M4 was replaced by RPMI 1640/B27 (M6) and changed every three days.

3.4.4 Results

The automated differentiation of hiPSCs toward functional cardiomyocytes has been tested with several culture patches using a PTFE patch mounting device. Once patches were fixed, the device was placed in a conventional 60 mm culture dish. This mounting device is

particularly useful which guarantees a uniform iPSCs culture and optimum cardiac differentiation. To illustrate the high potential of the system, we adopted a differentiated protocol previously developed for cardiac differentiation [18]. The process flow is in Figure 3.5, which consists of three parts: i) system preparation, ii) hiPSCs culture and embryoids (EBs) formation and iii) cardiac differentiation. Particular attention has to be paid to the system preparation since this part involves both manual and machine-controlled operation and any contamination has to be avoided.

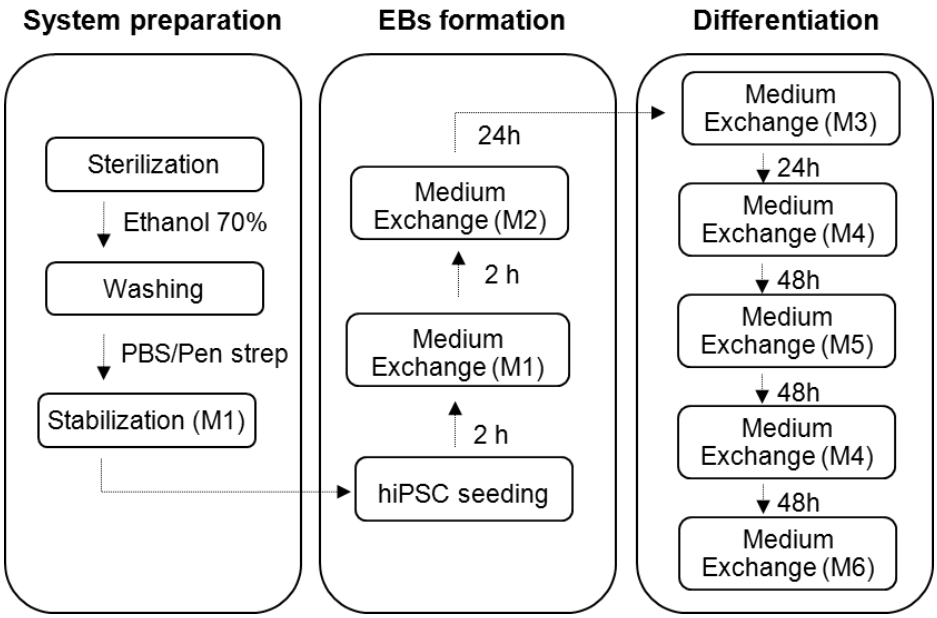

Figure 3.5 Automated media change pipeline for cardiac differentiation and preparation steps. M1: E8+10 µMY27632, M2 = E8, M3: RPMI 1640 + B27 without insulin + 12 µm CHIR 99021, M4: RPMI 1640 + B27 without insulin, M5: RPMI 1640 + B27 without insulin + 5µM IWP, M6: RPMI 1640 + B27.

By using our laboratory platform with a hiPSC differentiation protocol previously defined [19], we could be able to produce automatically functional cardiomyocytes on a patch (Figure 3.6). During the early stage of the process, cells migrated progressively away from the hemisphere colonies to form a cell sheet at day 4 and then showed up and started irregular beating around day 9. At day 14, the cardiac contraction became robust and homogeneous over the whole patch area. Here, the contraction profiles were plotted by simply measuring the time course of the image intensity change in a small ROI of the movies (Figure 3.6b and 3.6c). As can be seen in Figure 3.6d, the beating rate of automatically processed cells is slightly higher than that by manual operations. Since the same differentiation protocol was used in both cases, this difference in beating frequency may be attributed to the difference in off-ground distance

of the patches: it was simply placed in the dish in the case of manual culture (short distance) but mounted in a supporting device in the case of automatic processing (Figure 3.2d) (large distance). It is known that the beating rate of cardiomyocytes increases with time during the maturation phase, suggesting that the cardiomyocytes obtained by automatic processing have improved maturation than that of manual one, due probably to the enhanced uptake of nutrient and the enhanced clearance of metabolites.

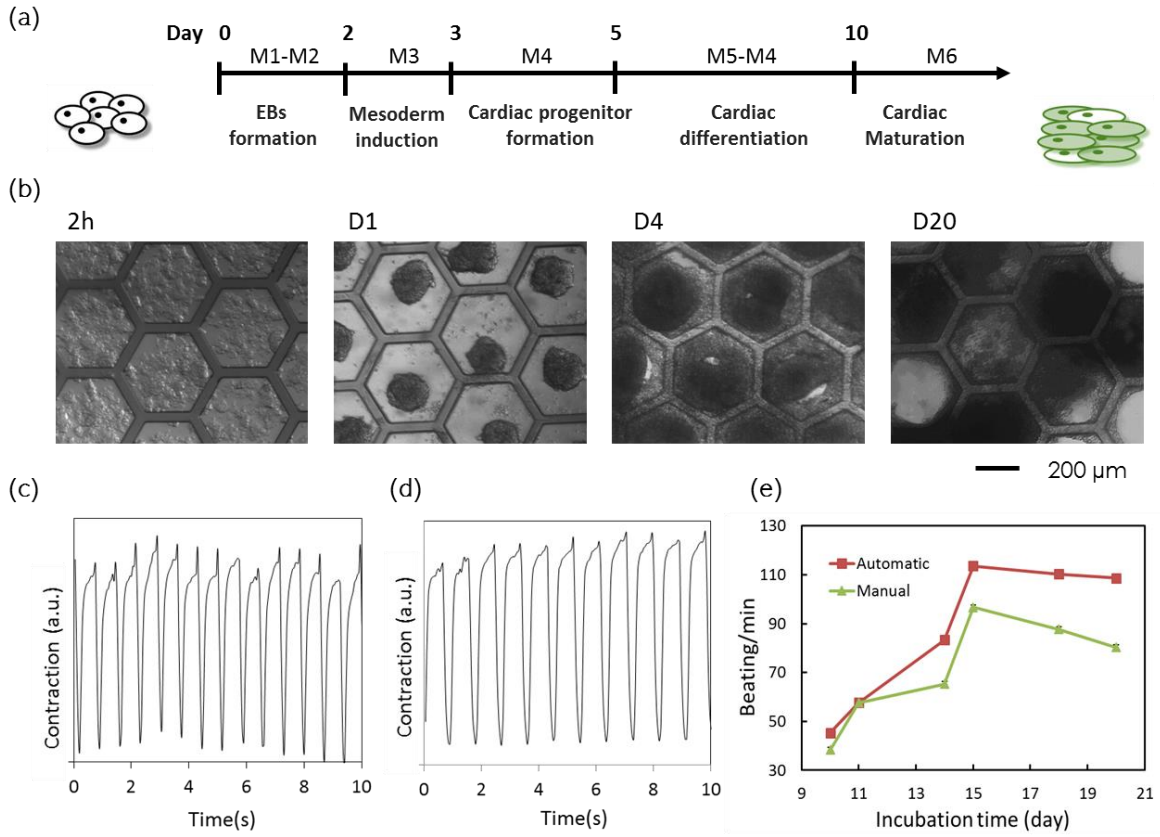

Figure 3.6 On-patch cardiac differentiation of hiPSCs under different culture conditions. (a) Differentiation protocol; (b) Phase contrast images of differentiating hiPSCs after incubation for 2 h and 1, 4, and 20 days. Cardiac beating profiles of differentiating hiPSCs at day 14 under automatic (c) and manual (d) culture conditions. (e) Variation of the beating rate as function of operation time.

3.5 Neuron network maturation

To evaluate the performance of the system, we also worked on hiPSCs differentiation toward functional neural networks. Previously, a large number of investigations have been performed to obtain cell-type specific neurons such as dopaminergic neurons, interneurons,

motor neurons, pyramidal neurons, etc. In general, a cell-type specific differentiation requires a more accurate control of the differentiation steps in order to achieve a high purity specification. To obtain a functional neural network, however, the cell-type specific neurons have to be co-cultivated with other cells such as astrocytes, making the whole process more laborious.

Recently, brain organoids have been obtained from hiPSCs by differentiation within a gel, showing multiple cell-specific types as well as distinctive zones of cortical layers. Obvious, this approach is highly interesting for brain development studies. However, this approach is limited to immature neurons and lack of inner accessibility for such as electrophysiological interrogation. We therefore developed an alternative approach by using a differentiation protocol of hiPSCs to neurons without cell-type specification [20], which allowed us to generate a functional 2D neural network on a patch, containing both neurons and astrocytes.

3.5.1 Protocol implementation

Figure 3.7 shows a typical operation sequence for hiPSC differentiation toward 2D neural networks. Only three types of culture media are used but the neuron maturation stage may last over months. Briefly, hiPSCs are firstly directed to the formation of neuron pre-progenitors and then to neuron progenitors, before going to the final stage for neural network maturation. Here, the produced NPCs are capable of generating a diversity of neural lineages, including both neurons and astrocytes [20]. NPCs were cultured in NPC medium on Geltrex (1:100 dilution) coated petri dish. The medium was changed every other day. Once confluent, cells were passed at a 1:4 production rate for at least 10 generations and the produced NPCs can be cryopreserved in liquid nitrogen for later use. Such NPCs can then be used to achieve functional neural networks after maturation over a long period. During this period, culture medium is simply renewed each day or each other day so that it is highly desirable to automate this process and to have a multi-run system for a continuous generation of the end product.

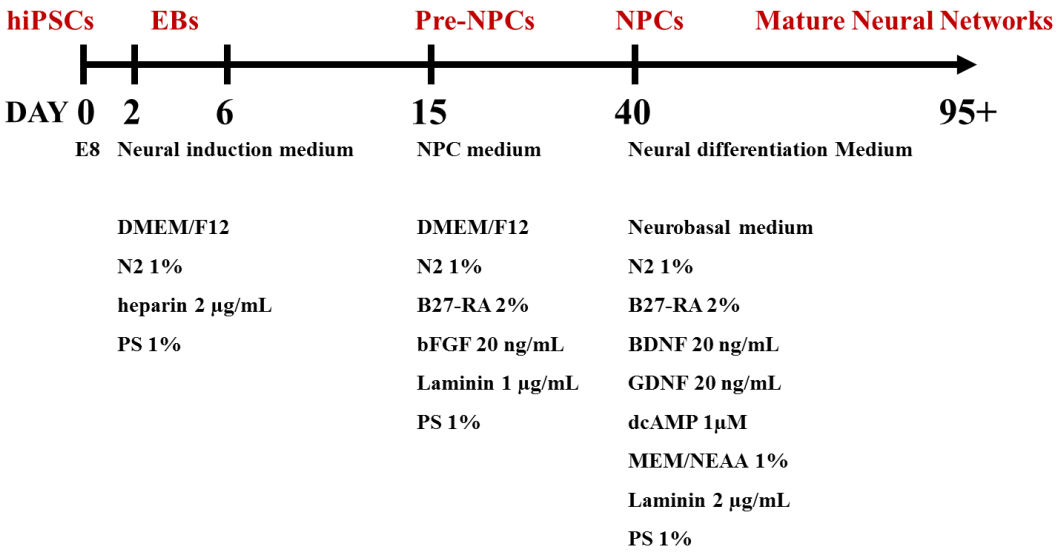

Figure 3.7 Differentiation process of hiPSCs to neural networks. The culture medium and cell factors used in different stages are also listed. Note that three types of culture media are used to reach neuron progenitors cells over 40 days and only one type of culture medium is used for formation of nature neural network over almost two months.

The following culture media were used:

E8: Complete Essential 8™ Medium.

Neuron induction medium: DMEM/F12 supplemented with 1% N2 supplement, 2µg/mL heparin, and 1% penicillin/streptomycin.

Neuron progenitor cells (NPC) medium: DMEM/F12 supplemented with 1% N2 supplement, 2% B27 supplement minus vitamin A (-RA), 20 ng/mL bFGF, 1 µg/mL laminin and 1% penicillin/streptomycin.

Neural differentiation medium: Neurobasal medium supple 1% N2 supplement, 2% B27-RA supplement, 1% minimum essential medium/non-essential amino acid (MEM/NEAA), 20 ng/mL brain-derived neurotrophic factor (BDGF), 20 ng/ml glial cell-derived neurotrophic factor (GDNF), 1 µM dibutyryl cyclic adenosine monophosphate (dcAMP), 200 µM ascorbic acid (AA), 2 µg/mL laminin and 1% penicillin/streptomycin.

3.5.2 Operation details

The culture patch was exposed with plasma and sterilized by UV and 70% ethanol solution for 5 min. After washing by PBS three times, the patch was coated by poly-L-ornithine at 4 ℃ overnight and washed by PBS three times again then dried for 30 min. Next, 50 µL Geltrex (1:100 dilution) was added on top of the fiber side to coat the patch for 1h at 37 ℃. 50 µL cell

suspension contained 2 × 10^5 NPCs derived from iPSCs were seeded on culture patch and incubated for 2 h for cell attachment. Then patches were mounted on the PTFE mounting device and placed in a culture dish. After 4 mL fresh neural differentiation medium was added to the cell culture dish. Thereafter, the culture dish was finally connected to the circuit of the automated culture platform and the media were changed automatically and regularly. Neuron differentiation medium was fully changed every other day from day 40 to day 70. Only half of the medium was replaced from day 70 onwards.

Cells on the culture patch were fixed using 4% formaldehyde in PBS for 15 min. Then cells were treated with 0.5% Triton X-100 in PBS for 10 min at room temperature for permeabilization and then incubated in a blocking solution containing 3% v/v bovine serum albumin, 0.1% Triton X-100 and 0.1% v/v Tween 20 in PBS for 30 min to block out nonspecific bindings. Primary antibodies containing Anti-Synapsin I (1: 200 dilution, Abcam), Anti-Tau (1: 300 dilution, Sigma) in blocking solution were used to incubate the blocked samples at 4°C overnight. Afterward, cells were incubated with the appropriate secondary antibody, Alexa Fluor 488 Donkey anti-rabbit IgG (1:500 dilution, Invitrogen) and Alexa Fluor 633 goat anti-rabbit IgG (1:500 dilution, Invitrogen) in blocking buffer at room temperature for 1 h. Then, cells were incubated with 4'-6-diamidino-2-phenylindole (DAPI, 1:100 dilution) for 30 min for nuclear staining, and finally washed three times with PBS. Then stained cells were observed with confocal microscopy (Zeiss, LSM710).

3.5.3 Results

The neuron maturation step which lasts at least two months, has been controlled with our automatic culture system without human intervention, except the fresh medium filling in the storage unit every two weeks. This obviously reduced manpower and risks of contamination.

Figure 3.8 shows bright-field images of the maturating neural networks on week 2, week 6, and 8 in the same honeycomb of a culture patch. In the beginning, single NPCs adhered to the substrate and showed initial aggregation. Due to the cell proliferation and migration, neuron clusters and extension of neurites were observed. Then, elongated axons (up to several hundred micrometers) appeared on week 6. Neurons are likely to form large clusters when they spread

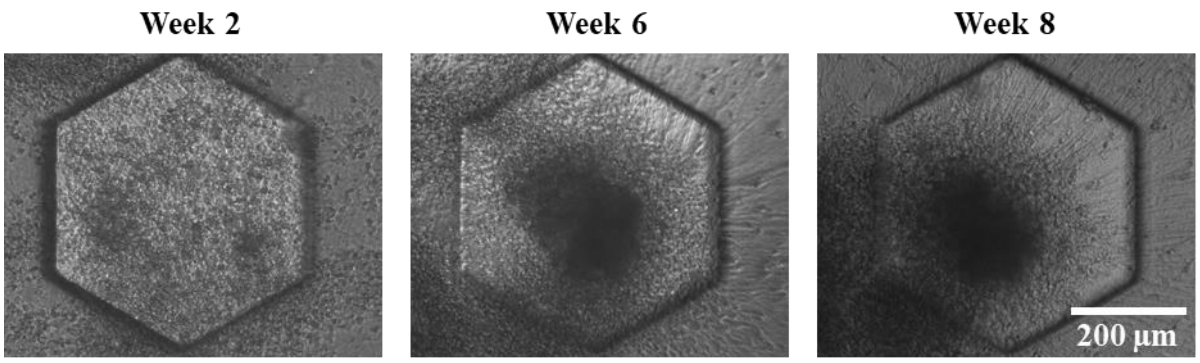

Figure 3.8 Bright-field images of maturating neurons in a honeycomb compartment of culture patch after 2, 6, and 8 weeks incubation, controlled with an automatic culture system.

on the culture patch due to the size limitation and the nanofibers stiffness of the honeycomb compartment. Indeed, neurons are found in the relatively soft tissues of the nervous system, and they are also more active on softer materials in vitro [21, 22]. Compared with the microenvironment of the nervous system in the body, glass and MEA are too rigid for neuron culture because of the poor attachment [23], while the culture patch composed of cross-linked single-layer gelatin nanofibers can provide in vivo ECM-like environment for neuron proliferation and neurite expansion. In addition, with the perfusion of an automated culture platform, the regular feeding every other day was easily achieved for standardization and interference-free cell culture.

Confocal imaging was performed in week 8 after the plating of NPCs. Cells on the culture patch were stained with neuron-specific synaptic marker Synapsin I and tubulin marker Tau as shown in Figure 3.9. Most of the neurons were Synapsin I positive neurons, showing bright points. We also observed microtubule Tau positive neuron networks, demonstrating that the automatic processing is suitable for the maturation of neural networks.

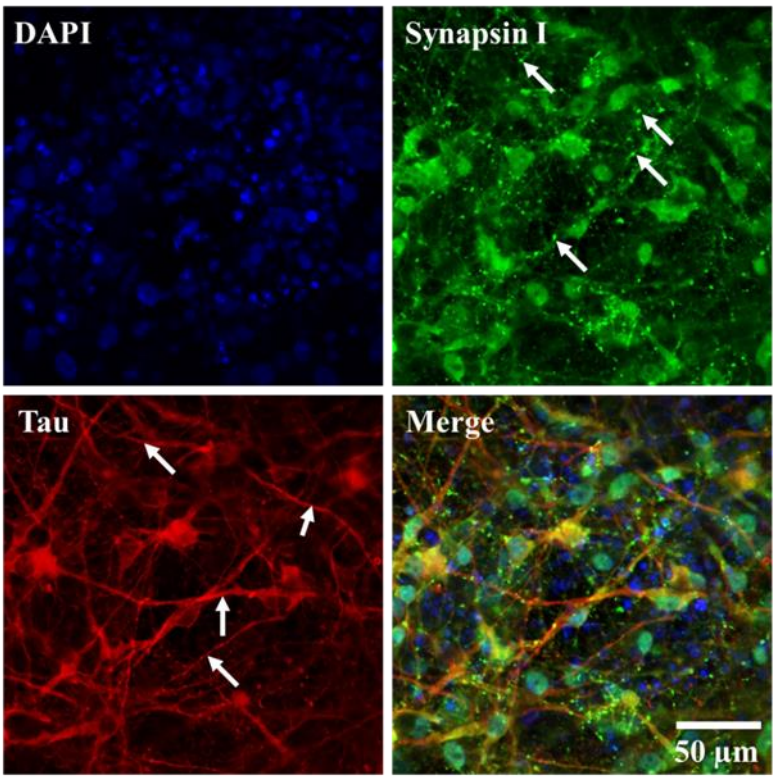

Figure 3.9 Immunostaining images of neurons during maturation in week 8. DAPI: nuclear (blue); Synapsin I: neuron synaptic proteins (green); Tau: neural microtubule (red).

3.6 Conclusion and discussions

In this chapter, a cost-effective, modular, and compact platform for automated cell culture and hiPSC differentiation has been developed. This platform has then been validated with a perfusion-diffusion based culture of Hela cells which showed a higher growth rate compared to the static culture. Furthermore, it has been used for two types of hiPSC differentiation, one with multisource processing toward functional cardiomyocytes and another for a long-term operation toward mature neural networks. The results of hiPSC differentiation toward alveolar cells will be presented in the next chapters. Finally, this platform is compatible with conventional culture wares (dish, flask, and multiwell plate) as well as culture patches and microfluidic devices. Therefore, it is a valuable alternative to large-scale robotic systems and should be applicable to a large variety of cell-based assays, including organ-on-a-chip and microphysiological systems.

References

[1] Astashkina, A, et al. (2012). "A critical evaluation of in vitro cell culture models for high-throughput drug screening and toxicity." Pharmacology & Therapeutics **134**(1): 82-106.

[2] Langhans, SA (2018). "Three-Dimensional in Vitro Cell Culture Models in Drug Discovery and Drug Repositioning." Frontiers in Pharmacology **9**: 6-.

[3] Daniszewski, M, et al. (2017). "Automated Cell Culture Systems and Their Applications to Human Pluripotent Stem Cell Studies." Slas Technology: 2472630317712220.

[4] Yu, J, et al. (2007). "Induced Pluripotent Stem Cell Lines Derived from Human Somatic Cells." **318**(5858): 1917-1920.

[5] Grskovic, M, et al. "Induced pluripotent stem cells — opportunities for disease modelling and drug discovery." Nature Reviews Drug Discovery.

[6] Limor, et al. (2012). "Derivation and cardiomyocyte differentiation of induced pluripotent stem cells from heart failure patients." European Heart Journal.

[7] Takeda, M, et al. (2018). "Development of In Vitro Drug-Induced Cardiotoxicity Assay by Using Three-Dimensional Cardiac Tissues Derived from Human Induced Pluripotent Stem Cells." Tissue Engineering Part C Methods: ten.TEC.2017.0247.

[8] Tukker, AM, et al. (2018). "Human iPSC-derived neuronal models for in vitro neurotoxicity assessment." Neurotoxicology **67**: 215-225.

[9] Elizabeth, et al. (2011). "Current understanding and challenges in bioprocessing of stem cell-based therapies for regenerative medicine." British Medical Bulletin.

[10] Schroeder, M, et al. (2010). "Differentiation and lineage selection of mouse embryonic stem cells in a stirred bench scale bioreactor with automated process control." Biotechnology & Bioengineering **92**(7): 920-933.

[11] Ackermann, M, et al. (2018). "Bioreactor-based mass production of human iPSC-derived macrophages enables immunotherapies against bacterial airway infections." Nature Communications **9**(1).

[12] Ghaedi, M, et al. (2014). "Alveolar epithelial differentiation of human induced pluripotent stem cells in a rotating bioreactor." Biomaterials **35**(2): 699-710.

[13] Serra, M, et al. (2009). "Integrating human stem cell expansion and neuronal differentiation in bioreactors." Bmc Biotechnology **9**(1): 82.

[14] Konagaya, S, et al. (2015). "Long-term maintenance of human induced pluripotent stem cells by automated cell culture system." Scientific Reports **5**(1): 16647.

[15] Kane, KIW, et al. (2019). "Automated microfluidic cell culture of stem cell derived dopaminergic neurons." Scientific Reports **9**(1).

[16] Regent, F, et al. (2019). "Automation of human pluripotent stem cell differentiation toward retinal pigment epithelial cells for large-scale productions." Scientific Reports **9**(1): 10646.

[17] Tang, Y, et al. (2016). "Effective motor neuron differentiation of hiPSCs on a patch made of crosslinked monolayer gelatin nanofibers." Journal of Materials Chemistry B: 3305-3312.

[18] Tang, Y, et al. (2016). "Induction and differentiation of human induced pluripotent stem cells into functional cardiomyocytes on a compartmented monolayer of gelatin nanofibers." Nanoscale **8**(30): 14530-14540.

[19] Lian, X, et al. (2013). "Directed cardiomyocyte differentiation from human pluripotent stem cells by modulating Wnt/β-catenin signaling under fully defined conditions." Nature Protocols **8**(1): 162-175.

[20] Shi, Y, et al. (2012). "Directed differentiation of human pluripotent stem cells to cerebral cortex neurons and neural networks." Nature Protocol **7**(10): 1836-1846.

[21] Balgude, AP, et al. (2001). "Agarose gel stiffness determines rate of DRG neurite extension in 3D cultures." Biomaterials **22**(10): 1077-1084.

[22] M., et al. (1996). "The Molecular Biology of Axon Guidance." Science **274**(5290): 1123-1133.

[23] Gunhanlar, N, et al. (2017). "A simplified protocol for differentiation of electrophysiologically mature neuronal networks from human induced pluripotent stem cells." Molecular Psychiatry **23**(5).

Chapter 4
Fabrication of alveolar tissue constructs

Fabrication of alveolar tissue constructs

In this chapter, we present a fabrication method of functional alveolar tissue constructs. We aim at the manufacturing of alveolar epithelium which is composed of alveolar type I (AT1) and type II (AT2) pneumocytes. After a brief introduction, we define the strategy of this approach which is firstly the generation of alveolar organoids and then replating the dissociated alveolar cells on an artificial basement membrane (ABM) for further maturation and culture on air-liquid interface (ALI) as described previously. We show that the alveolar organoids composed of both AT1 and AT2 cells can be derived from hiPSCs by automatic differentiation system. Moreover, the produced organoids can be freezed for later use and the replated alveolar cells, together with the underneath basement membrane, form a tight barrier. Finally, we also identified by immunostaining the expression of angiotensin-converting enzyme II (ACE2) as well as TMPRSS2 in the derived alveolar cells, which can be used for SARS-CoV-2 infection studies.

4.1 Introduction

Previous in-vitro alveolar models were mostly based on the immortalized cell line A549 [1], which was derived from a type II pneumocyte lung tumor. Typically, this cell line is used for cancer modeling, anti-cancer drug assays, and gene transfection studies [2-4]. When cultured in vitro, the cells can grow as a monolayer on the surface of the culture dish or flask and may become type I alveolar cells after a long-period culture [5, 6]. The drawback of using such a tumor cell line is the lack of interaction with other non-tumor components (stromal, vascular, inflammatory), in addition to the genetic instability during long-term passage and selective growth of subpopulations on initial culture or during long term passage [7].

More recently, hiPSCs have been used to differentiate alveolar cells and the formation of the alveolar epithelium [8-11]. These cells expressed native AT1 and AT2 markers and contained squamous shape and lamellar bodies, respectively. Since hiPSCs derived cells are more consistent with primary cells and can be derived from different donors, they showed distinct responses depending on patient age, genetic background, and the type of tissue source [12, 13]. Compared to the A549 cells which respond to toxins differently than primary cells and vary in phenotypes and functions under different culture conditions [14], hiPSCs derived alveolar cells can be more stable. However, directed differentiation of hiPSCs into AT1 or AT2

usually needs a long-term culture, an automatic differentiation method as presented in the previous chapter is desirable to reduce the lot-to-lot variation as well as labor costs.

Interestingly, the 3D culture of alveolar or lung organoids can be achieved by using either isolated lung epithelial cells from adult lung tissues [15, 16] or pluripotent stem cells [17-19]. These engineered miniature lungs can more accurately replicate the histology and functions of tissues in vivo so that they can more easily mimic the physiological or pathological environment of the human body, though they are micro-scaled in size. In general, organoids are composed of a variety of cell types and the main extracellular matrix (ECM) components, which makes this approach plausible for in-vitro studies of organ functions. However, the 2D culture of alveolar epithelium is still necessary not only for the requirement of air-liquid interfaces and mechanical deformation in lung modeling but also for the high throughput cell-based assays [20, 21].

Our objective is to fabricate functional alveolar tissue constructs containing both AT1 and AT2 cells by using hiPSCs and artificial basement membrane techniques. Therefore, we firstly fabricate hiPSC derived alveolar organoids. Then, we disassociate the alveolar organoids into single cells and replat them on an artificial basement membrane for maturation and epithelium formation. Fig 4.1 shows the strategy of this approach, which begins with a mesoderm generation from hiPSCs and then the formation of ventral-anterior foregut [11, 22]. Afterward, differentiation factors are introduced to derive the foregut spheroids into bud tip progenitor organoids [22, 23]. Given that bud tip progenitors are a precursor cell to all epithelial cell types during development, bud tip progenitor organoids are uniquely suited for studying mechanisms involved in epithelial cell fate decisions in the developing human lung [23]. Therefore, after maturation, bud tip organoids were directed into alveolar organoids which were then characterized and dissociated to single cells for replating and alveolar epithelium formation. In order to model efficiently, an ultrathin artificial basement-membrane (ABM, thickness <0.2 μm) patch was produced to mimic in vivo microenvironment and support the cell adhesion. The expression of alveolar epithelial type I (AT1) and type II (AT2) cells were specified by related antibodies which binds to Podoplanin (PDPN) or Aquaporin 5 (AQP5) (AT1), SFTPC (AT2), ACE2 (both). After 2 days of stabilization culture, this alveolar epithelium model was mounted on the ALI culture device for another 3~7 days. TEER measurements were also carried out during culture and after culture.

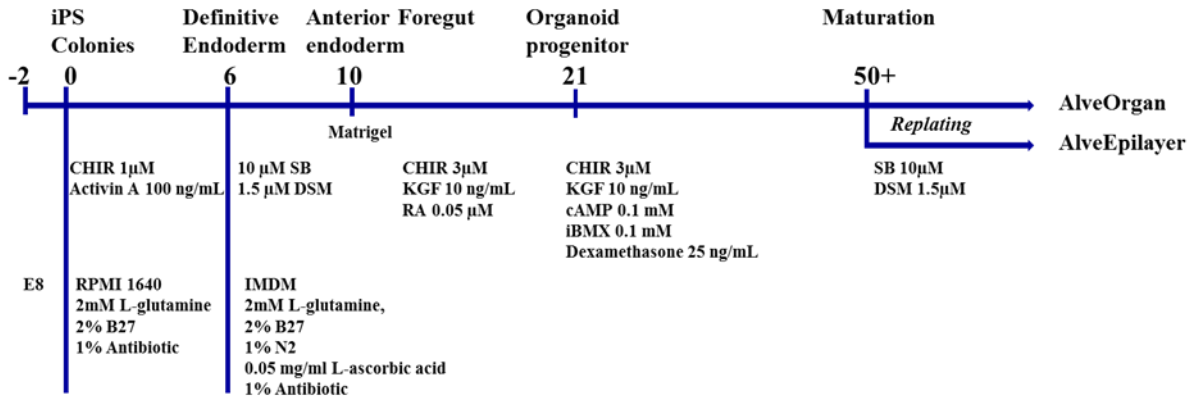

Figure 4.1 Schematic of a differentiation protocol for the formation of alveolar organoids and alveolar epithelial layer. Once the organoid progenitors are reached around day 50, they can be either cultivated for organoid maturation or replated on an artificial basement membrane for the epithelial layer formation.

4.2 Fabrication of alveolar organoids

4.2.1 Preparation of medium and soluble factors

The following culture media were used:

Essential 8 (E8): Essential 8™ Basal Medium (Gibco) supplemented with 2% Essential 8™ Supplement.

Definitive Endoderm induction medium: RPMI 1640 (Gibco) supplemented with 2mM L-glutamine, 2% B27 supplement (Gibco), 1% penicillin/streptomycin (Thermo Fisher Scientific), and induction factors, 1 µM CHIR 99021 (Sigma) and 100 ng/mL Activin A (Stemcell Technologies).

Serum-free differentiation (SFD) medium: IMDM (Gibco) supplemented with GlutaMAX, 2% B27 supplement (Gibco), 1% N2 supplement (Gibco), 0.05 mg/mL L-ascorbic acid (Sigma), 1% penicillin/streptomycin.

4.2.2 HiPSCs maintenance

Human iPSCs (cell line 253G1) were cultured in complete E8 (Gibco), in a vitronectin (Gibco, 1:100 diluted in PBS) coated 60 mm culture dish at 37 ºC with 5% CO_2. The medium was changed every day until 70%~80% of confluency. For iPSCs resuspension, cells were incubated with 0.5 mM EDTA in PBS solution for 5 min at 37 ºC.

4.2.3 Definitive endoderm

We used a simplified protocol for endodermal differentiation in which hiPSCs are differentiated into definitive endoderm in a base medium supplemented with CHIR 99021 and Activin A. HiPSCs were treated with 0.5mM EDTA in PBS for 5 min at 37°C, cells were passaged in a split ratio of 1:4 or 1:5. After maintenance for 24 ~ 48 h in E8, homogeneous hiPSCs colonies were formed. After reaching 60 % ~ 70 % of confluency, the medium was changed to a definite endoderm induction medium. Cells were fed every 36–48 h (depending on the density) by adding fresh media until day 6 after the introduction of the induction medium (day 0).

4.2.4 Anterior foregut endoderm

On day 6, the medium was changed to a serum-free differentiation (SFD) medium supplemented with 1.5 μM Dorsomorphin dihydrochloride (DSM, Tocris, R&D Systems) and 10 μM SB431542 (SB, Tocris, R&D Systems) and then incubated for 96 h (from day 6 to day 10).

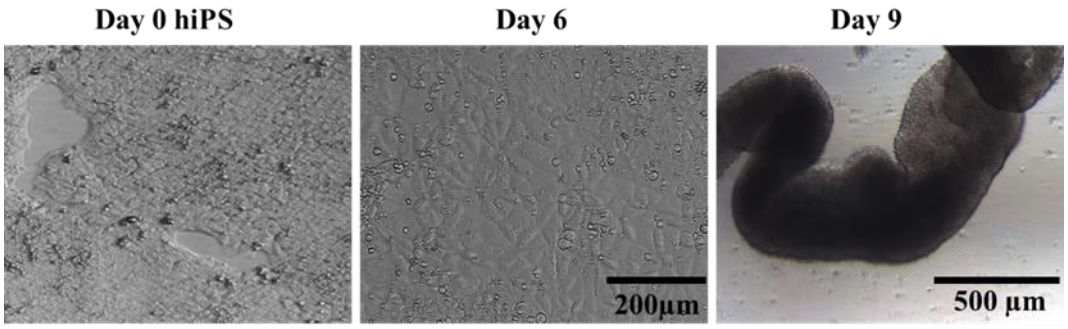

Figure 4.2 Optical images of differentiation from hiPSCs (day 0) into Definite Endoderm (day 6) and Anterior Foregut Endoderm (day 9).

4.2.5 Bud tip progenitor organoids

On day 8 or 9, detached and floating foregut clumps began to form (see Fig 4.2). On day 10, Matrigel (Corning) and SFD medium were mixed at a 1:1 volume ratio on ice. The floating foregut clumps were collected by a cut p1000 pipette tip and transferred to a 1.5-mL conical tube. Although these clumps should settle down by gravity, they could also be gently spun down with a microcentrifuge (VWR) for ~30 s if necessary. Then, the medium was gently removed as much as possible from the tube. Afterward, these foregut clumps were mixed in the Matrigel solution on ice, forming a Matrigel-foregut mixture. A culture patch with

nanofibers or 24-well plate was used as substrate on which up to 25 µL mixture was placed on each patch or well for organoid formation. For the formation of bud tip progenitor organoids, the SFD medium was supplemented with 3 µM CHIR 99021, 10 ng/mL Keratinocyte Growth Factor (KGF, Sigma-Aldrich) and 50 nM all-trans-retinoic acid (ATRA, Sigma-Aldrich). After gelling for 15 min ~ 30 min in an incubator, the Matrigel-foregut droplets on the patch or a well bottom surface were overlaid by 1 mL organoid formation medium in a 24-well plate.

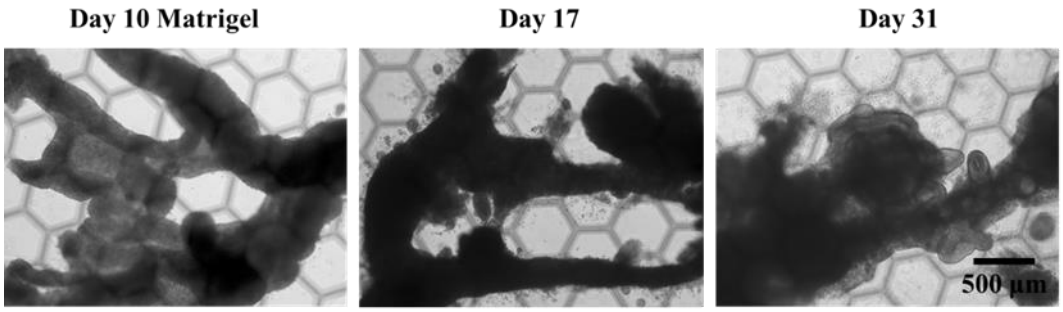

Figure 4.3 Optical images of the development of bud tip progenitor organoids in Matrigel culture on a culture patch, bud tips were observed after 1-week culture (day 17), more bud tips branching were observed after 3 weeks (day 31).

In a serum-free and well-defined medium containing FGF7, CHIR 99021, and all-trans retinoic acid (ATRA), bud tip progenitor organoids could be derived from foregut spheroids. After 3 weeks of culture (see Fig 4.3) of the progenitor organoids, a highly enriched and proliferating cell population appeared with a transcription feature highly similar to that of human fetal alveolar progenitor cells. These cells could then be expanded for more than 16 weeks.

4.2.6 Maturation of alveolar organoids

The expanded bud tip progenitor organoids could be passed every 2 weeks. They could also be placed for gel culture with a maturation medium at least 3 week later. The maturation medium was prepared from SFD medium supplemented with 50 nM dexamethasone (Sigma), 0.1 µM 8-Br-cAMP (cAMP, Sigma), 0.1 µM 3-isobutyl-1-methylxanthine (iBMX, Wako), 10 ng/ml KGF, 3 µM CHIR 99021. Alveolar organoids in this maturation stage could proliferate more rapidly and should be passed every 2 week and, accordingly, the culture medium refreshed every 3 days. After 2-weeks of maturation, more confluent organoids were observed, as shown in Fig 4.4.

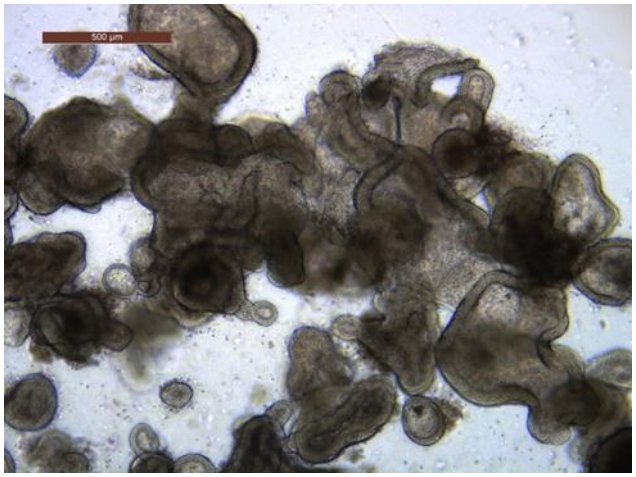

Figure 4.4 Optical image of alveolar organoids after 2-week maturation, showing clear edge and organoid overlay.

4.3 Manipulation of alveolar organoid

Usually, bud tip progenitor organoids were formed after 2 or 3 weeks, longer expansion and maintenance led to more bud tips branching out. Therefore, a passage of organoids should be done every two weeks. Organoids cryopreservation and thawing were also successful, using an optimized protocol. In this thesis work, the manipulation of alveolar progenitor organoids and mature organoids all follow the same protocol of passage, cryopreservation, and thawing.

4.3.1 Passage of alveolar organoids

The passage of either bud tip progenitor or maturated organoids was performed by mechanical splitting and replating. In short, organoids were resuspended from the basement membrane matrix (Matrigel) and broken mechanically into smaller fragments. The fragments were then resuspended in a fresh Matrigel mixture and replated. They were then self-assembled into new organoids. Due to the proliferation and differentiation of the stem cells therein, the transit-amplifying cell activities led to a continuous growth of the organoids. For alveolar (or progenitor) organoids, the passage cycle is 2 weeks. More precisely, we first removed the medium from one well of a 12- or 24-well plate containing the established organoids with a p1000 pipette (precoated with 0.1% BSA solution for anti-sticking) to flush the organoids with 1 ml ice-cold PBS, disrupting the Matrigel droplets. Afterward, the organoids were collected and transferred to a 1.5 ml tube. After a gentle centrifugation in a mini centrifuge (VWR) for ~30 s, PBS supernatant was removed and added fresh ice-cold PBS, this washing step was

repeated 3 times. During this washing, organoids were mechanically split into small fragments via p200 (precoated with 0.1% BSA solution for anti-sticking) repetitive pipetting (~100 times). After final washing, fragments were resuspended in a 1:1 v/v Matrigel/medium solution on ice. Then, a 50 µL fragment-droplet was dispensed into each well of a 12-well plate or 25 µL into each well of a 24-well plate. Next, the plate was reverted, as shown in Fig 4.5 and incubated at 37 ℃ for 30 min to solidify using a hanging-drop method [24], followed by adding 1 mL fresh organoid formation medium as mentioned above. The medium was refreshed every 3 days.

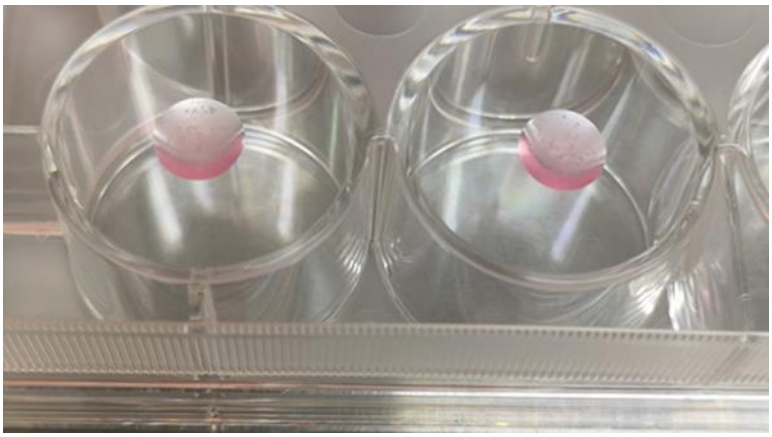

Figure 4.5 Image of alveolar organoids passaged by the hanging-drop method, the 12-well plate is reverted and incubated for 30 min before adding fresh medium.

4.3.2 Cryopreservation of alveolar organoids

Cryopreservation with liquid nitrogen is advisable when long term storing organoids while cryopreservation on dry ice is preferable for organoids shipment. In both cases, organoids were firstly freed from Matrigel and then resuspended in a freezing medium. Briefly, the cryopreservation process was quite similar to the passage process for the first few steps. After washing and mechanically repetitive pipetting, fragments were resuspended in an organoid formation medium containing (10% DMSO + 10 µM Y-27632) and transferred to a cryopreservation vial. Then the vial was placed in a freezing container (Mr. Frosty™), followed by moving the container at -20 ℃ for 10 min, at -80 ℃ for overnight, in liquid nitrogen for long-term storage.

4.3.3 Thawing of alveolar organoids

To restart the cultures, organoids were carefully thawed, washed, and plated in Matrigel domes. After one passage, organoids should have normal growth characteristics and could be used for any downstream assay.

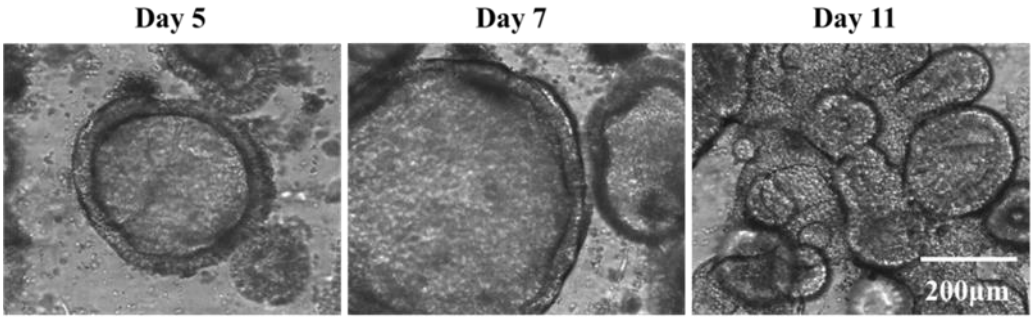

Figure 4.6 Optical images of alveolar organoids recovered from liquid nitrogen on day 5, 7, 11, showing fast proliferation and bud tips branching.

More precisely, the cryopreservation vial was taken out from liquid nitrogen and placed immediately in a 37 ℃ water bath for ~ 2 min until a small piece of ice floating. Then the thawed fragments were transferred into a 15 mL tube containing 5 mL pre-warmed organoid formation medium and resuspended by gentle pipetting. After centrifuging at 1000 rpm for 5 min, the supernatant was removed and fragments were resuspended in a 1:1 v/v Matrigel/medium solution on ice. Then, a 50 µL fragment-droplet was dispensed into each well of a 12-well plate or 25 µL into each well of a 24-well plate. Next, the plate was reverted and incubated at 37 ℃ for 30 min to solidify, followed by adding 1 mL organoid formation medium. The next day, 1 mL fresh medium was used to replace the spent medium containing residual cytotoxic DMSO. Finally, the medium was refreshed every 3 days. From Fig 4.6, recovered alveolar organoids showed high proliferation and branching structures on day 11.

4.3.4 Dissociation and replating

The main objective of this work is to produce alveolar epithelium based on ultrathin artificial basement membrane (uABM) and hiPSCs. By immunostaining observation, we confirmed the expression of AT1 and AT2 cells specific markers in our hiPSCs-derived alveolar organoids. We then need to dissociate them and replate them on uABM, as described below.

Maturated alveolar organoids were firstly collected in a 1.5 mL tube, after washing by ice-cold DPBS two times with gentle microcentrifuge. They were resuspended by adding 1 mL Dispase (2 mg/ml), transferred to a 15 mL conical tube, and then placed in a 37 ºC water bath for 30 min. Alveolar organoids in this step tended to settle down due to gravity, a gentle disturbance was needed to resuspend them in a Dispase solution by hand agitation every 3 min. Afterward, Dispase solution was removed as much as possible without disturbing the pellets. 2 mL TrypLE was added into the 15 mL tube to resuspend organoids again, followed by placing in the 37 ºC water bath for a total of 15 min. Repetitive pipetting using a p1000 tip was done every 3 minutes. The dissociation process is shown in Fig 4.7, showing homogeneous cell suspension. 2 mL stop medium (IMDM + 10 % FBS) was added into the conical tube to stop the dissociation, cells were then filtered using a 40 µm cell strainer and centrifuged at 1000 rpm for 5 min. Finally, cells were resuspended at a density of 1.0×10^6/mL in the replating medium (SFD + 1.5µM DSM + 10 µM SB + 50 nM Dexamethasone + 10 µM Y-27632).

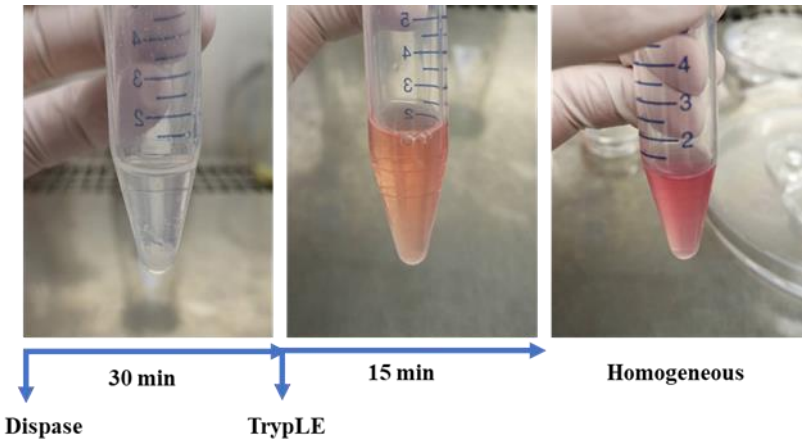

Figure.4.7 Images of the dissociation progress of organoids into single cells in first Dispase (2 mg/mL, 30 min, 37℃) and then TrypLE (15 min, 37℃)

To uniformly deposit the disassociated alveolar cells on the surface of uABM, a PDMS cylindrical chamber was used to confine cells in the patch area. a 200 µL cell-resuspended solution (2×10^5 cells) was placed in the chamber. After 24 h in a 37 ºC incubator, the PDMS cylindrical chamber was removed, the uABM patch was transferred to a 24-well plate and covered by 1 mL fresh medium for submerge culture.

4.3.5 Air-liquid interface (ALI) culture

ALI culture is necessary for mimicking the alveolar environment. After submerge-culture for cell expansion and stability during first 48 h [25], the alveolar patch was placed in replating

medium (SFD+DSM/SB+D+Y). At the end of day 2, the patch was mounted in an ALI culture device for the further maturation of the epithelial layer, as shown in Figure 4.8(a). Then, the device was placed in one chamber of a 6-well plate in which the basolateral space was immediately filled with 1.3 mL ALI culture medium (maturation medium with 5% FBS) and the medium in the apical side, if any, was removed to ensure a good ALI culture.

Figure 4.8 (b) and (c) show one example of the alveolar cell layer formed in a honeycomb compartment during the first 2 days. Due to cell proliferation, the alveolar cells could reach a confluency of around 80%. After more than 3 days under ALI conditions, continuous cell proliferation was observed, as shown in Figure 4.8(c). However, a hole was found on the cell layer, due probably to the imperfection of the ABM layer.

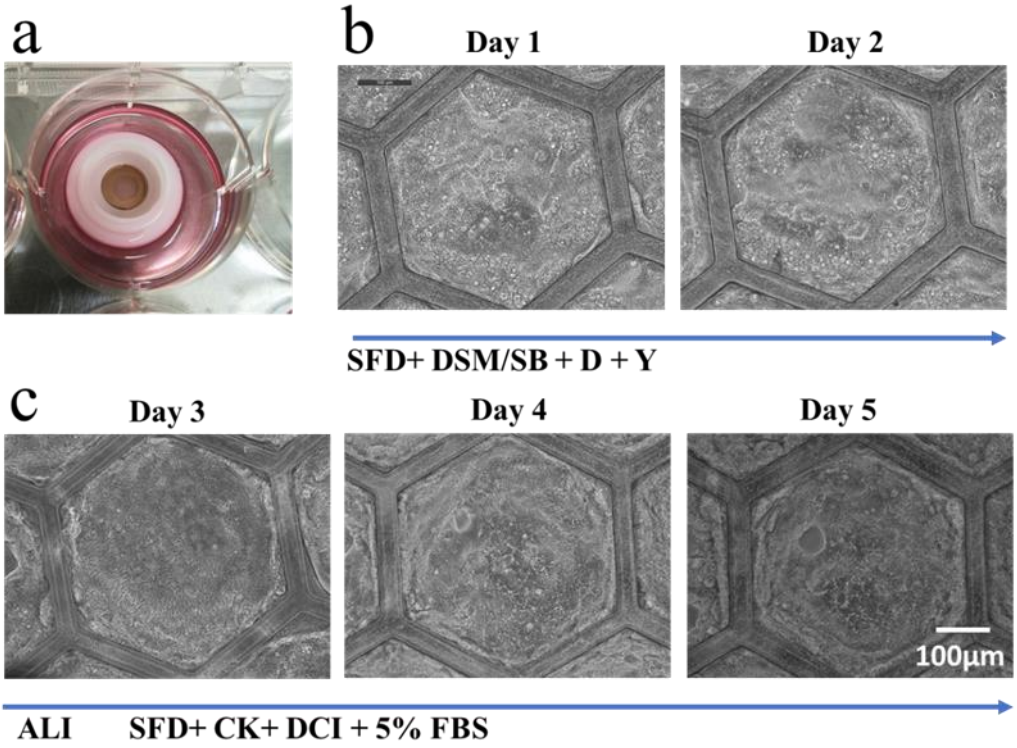

Figure 4.8 (a) A culture patch in the Air-liquid culture device, (b) Replated cells in submerged culture on day 1 and day 2 in the culture medium (SFD + DSM/SB + Y), and (c) in ALI culture from day 3- day 5 in the culture medium (SFD+ CK+ DCI + 5% FBS). SFD: serum-free differentiation; DSM/SB: Dorsomorphin dihydrochloride/ SB431542; D: Dexamethasone; Y: Y-27632 rock inhibitor; CK: CHIR 99021 + KGF; DCI: Dexamethasone +cAMP+ iBMX; FBS: fetal bovine serum.

4.4 Characterization of alveolar organoids and derived epithelium

General speaking, an organoid contains multiple organ-specific cell types as well as organ-specific progenitors. To confirm the expression of cell-specific proteins in the bud tip organoids after maturation for at least 2-weeks, several markers, e.g. PDPN or AQP5, SFTPC, were used for immunostaining observation.

4.4.1 Immunocytochemistry

The organoids after 2-week maturation were labeled with AT1 and AT2 cell markers as well as actin filaments markers. Organoids were first fixed using 4% formaldehyde in PBS for 30 min. Then, samples were treated with 0.5% Triton X-100 in PBS for 30 min at room temperature for permeabilization and then incubated in a blocking solution containing 3% v/v bovine serum albumin, 0.1% Triton X-100 and 0.1% v/v Tween 20 in PBS overnight to block out nonspecific bindings. Primary antibody solutions containing podoplanin (PDPN, 1: 50 dilution, Santa Cruz Biotechnology) and surfactant protein C (SFTPC, 1: 25 dilution, Invitrogen) respectively, were diluted in a blocking solution and then used for incubation at 4°C overnight. Afterward, the organoids were incubated in a blocking buffer containing appropriate secondary antibody, Alexa Fluor 488 Donkey anti-rabbit (1:250 dilution, Invitrogen), at room temperature for 2 h. Afterward, samples were incubated in a PBS buffer solution containing 4’-6-diamidino-2-phenylindole (DAPI, 1:100 dilution) and actin (ActinRed^{TM} 555, Invitrogen) during 30 min for nuclear and actin staining, respectively and finally washed three times with PBS, each time for 15 min.

As shown in Figure 4.9, small alveolar organoid cysts were nicely labeled with AT1 marker PDPN and AT2 marker SFTPC, while actin filaments were also labeled to clarify the cell structure. Clearly, AT1 cells are dominant in the cyst (see Fig 4.9a) and AT2 cells secreted specific surfactant in the inner side of the cyst (see Fig 4.9b). Furthermore, the distribution of the actin filaments in the cyst shows undoubtedly a strong cell polarization, indicating at least a partial maturation of the constituent cells.

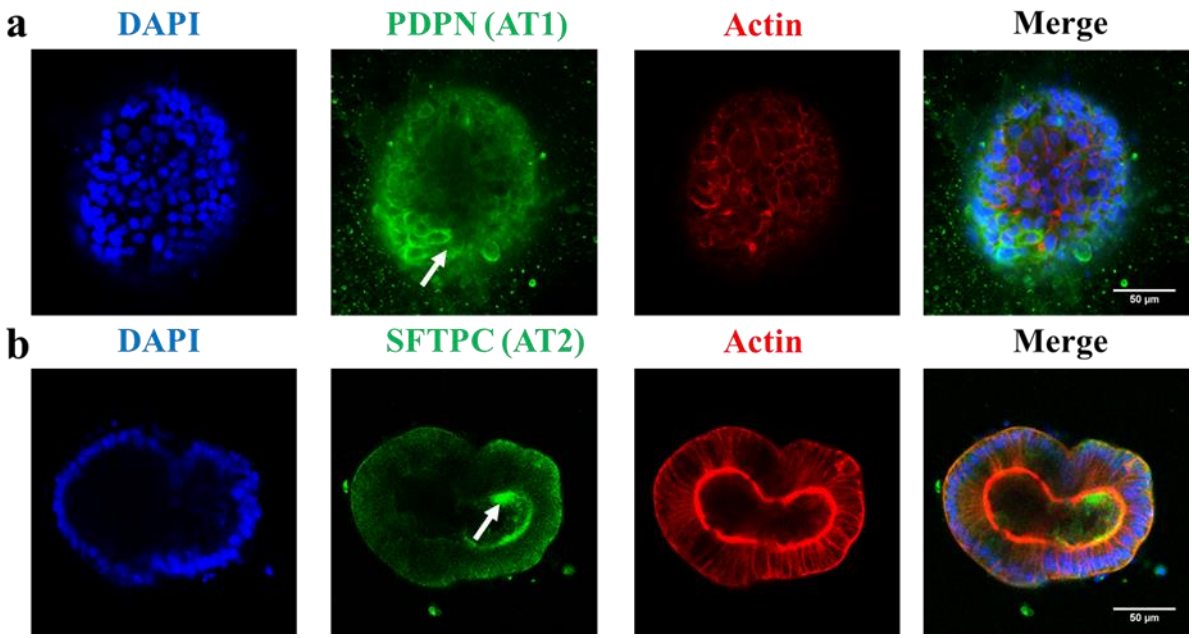

Figure 4.9 Immunofluorescence images of alveolar organoid after 2-week maturation. (a) AT1 labeled with PDPN, (b) AT2 labeled with SFTPC. Common labelings are DAPI for nuclei and actin for filaments (cytoskeleton). Scale bar: 50 μm

In order to investigate the immune responses of hiPSCs derived alveolar organoids, ACE2 and TMPRSS2 proteins were also marked for immunofluorescence imaging. ACE2, angiotensin-converting enzyme 2, generally plays a central role in the renin-angiotensin system, a hormone system that regulates blood pressure and fluid and electrolyte balance, as well as systemic vascular resistance. Recent studies have shown that ACE2 is also the entry point or acceptor of severe acute respiratory syndrome coronavirus 2 (SARS-CoV-2), while TMPRSS2, i.e., transmembrane protease serine 2, is a serine protease to prime the SARS-CoV-2 spike (S) protein. Thus, ACE2 and TMPRSS2 positive-expressing organs are believed to have a high risk of infection. A more detailed study of host-virus interaction will be described in the next chapter. Here, we simply marked our hiPSC derived alveolar organoids with ACE2 and TMPRSS2 after maturation for three weeks. The same protocols of permeabilization and blocking were applied to ACE2 (1:1000 dilution, Invitrogen) and TMPRSS2 (1:100 dilution, Invitrogen) and incubated at 4°C overnight. Then, second antibodies were applied to the incubated organoids by using diluted Alexa Fluor 488 Goat anti-Mouse (1:250 dilution, Invitrogen) and Alexa Fluor 555 Donkey anti-Rabbit (1:250 dilution, Invitrogen) in blocking solution (1:250). Finally, the organoids were incubated with DAPI for 30 min at room temperature and then washed three times with PBS, each time for 15 min. The stained organoids were then observed with confocal microscopy (Zeiss, LSM710).

As result, Fig 4.10 shows immunofluorescence images of ACE2 and TMPRSS2 marked alveolar organoids after 3-week maturation, suggesting the usefulness of the hiPSC derived alveolar organoids in immunological studies including SARS-CoV-2 infection.

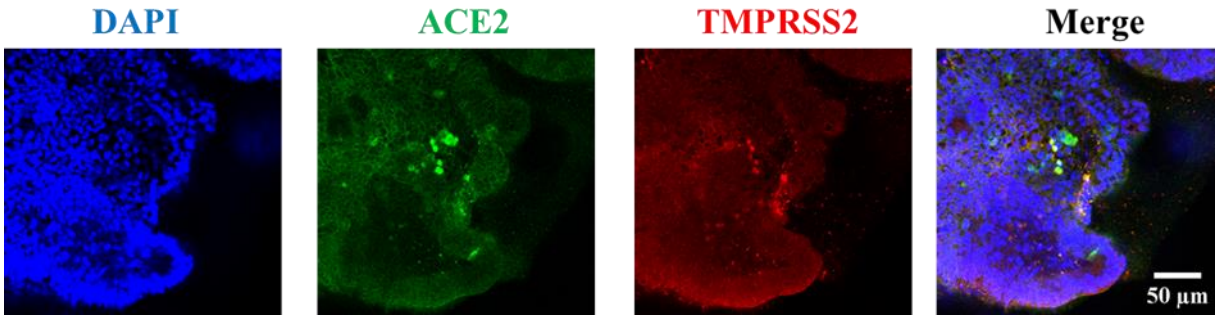

Figure 4.10 Immunofluorescence images of alveolar organoid by antibodies of ACE2 and TMPRSS2 labeling after 3-week maturation. DAPI is for nuclei labeling.

After, we first replated single cells from the dissociated alveolar organoids on a nanofiber patch. 24 h after seeding, cells can form a thin layer of alveolar epithelial cell tissue on the nanofiber membrane with unattached single cells on the surface. It is found that these unattached cells can be removed by slightly washing using the fresh medium (see Figure 4.11a). After 2 days culture, alveolar epithelial cells were fixed using 4% formaldehyde in PBS for 15 min. Then cells were treated with 0.5% Triton X-100 in PBS for 10 min at room temperature for permeabilization and then incubated in a blocking solution containing 3% v/v bovine serum albumin, 0.1% Triton X-100 and 0.1% v/v Tween 20 in PBS for 1 h to block out nonspecific bindings. Primary antibody SFTPC was used to incubate the blocked samples at 4°C overnight. Afterward, secondary antibodies, Alexa Fluor 488 Donkey anti-rabbit, were used for incubation at room temperature for 2 h. Similarly, the samples were incubated with DAPI and actin for 30 min for nuclei and actin staining, respectively and finally washed three times with PBS, each time for 5 min.

As shown in Figure 4.11b, the highly expressed SFTPC marker indicated the existence of AT2 cells, and interestingly we found that the position of this expression is mainly on the nanofiber area without cells, this is partially due to the fluid property of surfactant proteins, which can deposit on the nanofiber membrane made of animal source gelatin. In addition, we also found the SFTPC expression on the cell surface from the cross-sectional view (green arrow). The expressions of action filament and nuclei showed a continuous cell layer and give a high potential of alveolar epithelium constructs.

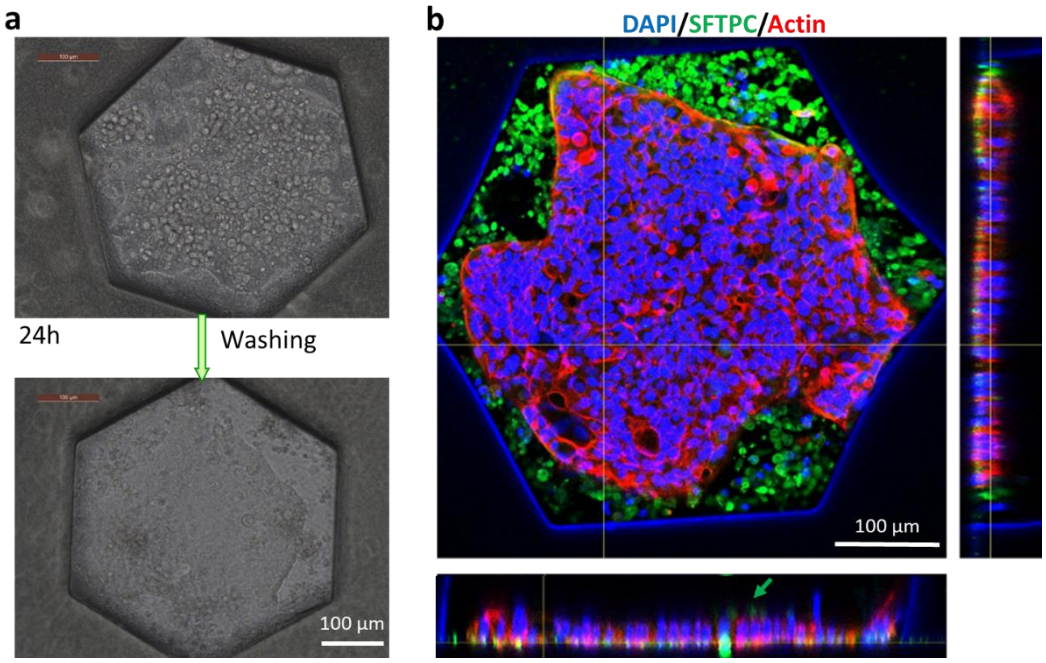

Figure 4.11 (a) Optical images of replated epithelial cells on the nanofiber patch, showing thin layer formation and removable unattached single cells. (b) Immunofluorescence images of replated epithelial cells with SFTPC marker and actin filament marker, DAPI is for nuclei labeling, after 2 days of culture.

Similarly, the hiPSCs derived alveolar epithelium was also studied by immunocytochemistry 5 days after replating. After the same fixing, permeabilization and blocking, primary antibodies containing aquaporin-5 (AQP5, 1: 80 dilution, Santa Cruz Biotechnology), SFTPC, Zonula occludens-1 (ZO-1, 1:100 dilution, Invitrogen), E-Cadherin (1:100 dilution, Invitrogen) and ACE2 (1:1000 dilution, Invitrogen) in blocking solution were used to incubate the blocked samples at 4°C overnight, respectively. The samples were later incubated with the appropriate secondary antibodies, such as Alexa Fluor 568 Donkey anti-goat (1:250 dilution, Invitrogen), Alexa Fluor 633 Donkey anti-rabbit (1:250 dilution, Invitrogen), Alexa Fluor 555 goat anti-rat (1:250 dilution, Invitrogen), Alexa Fluor 633 goat anti-rabbit (1:250 dilution, Invitrogen), Alexa Fluor 488 goat anti-mouse (1:250 dilution, Invitrogen) in blocking buffer at room temperature for 2 h. Then, cells were incubated with DAPI for 30 min for nuclei staining and next washed three times with PBS, each time for 5 min.

Fig 4.12 shows that replated cells were labeled with AT1 marker (AQP5) and AT2 marker (SFTPC), and more importantly ACE2 marker, respectively, with ZO-1 and E-cadherin to depict the cell junctions. From Fig 4.12a, AT1 cells are expressed both with AQP5 marker and

tight junction. Surfactant protein secretion cells, namely AT2 cells, as well as adheres junctions by E-Cadherin, were observed in Fig 4.12b. Importantly, ACE2 positives cells were observed in Fig 4.12c, showing the integrity of alveolar epithelium constructs.

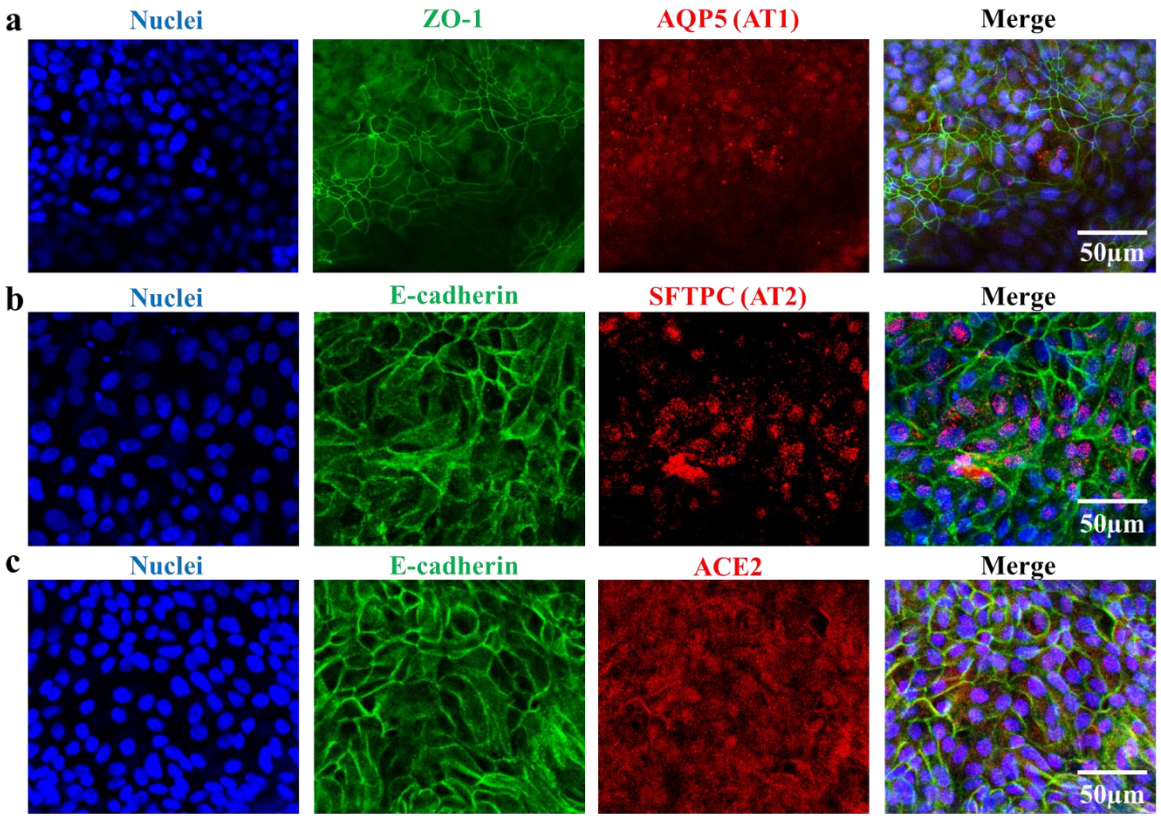

Figure 4.12 Immunofluorescence images of replated epithelial cells on ABM patches after 2 days of submerged culture and 3 days of ALI culture. (a) AT1 labeled with AQP5 antibody, tight junction labeled with ZO-1 antibody, (b) AT2 labeled with SFTPC antibody, adheres junction labeled with E-cadherin antibody, (c) ACE2 receptor labeled with ACE2 antibody, adheres junction labeled with E-cadherin antibody. DAPI is for nuclei labeling.

4.4.2 TEER monitoring

The electrical resistance of a cellular layer, measured in ohms, is a quantitative measure of the barrier integrity [26]. The classic setup for measuring the transepithelial electrical resistance (TEER) consists of a layer of cells cultured on a permeable filter insert that defines dividers of the apical (or upper) and basolateral (or lower) compartments. During a measurement process, two electrodes are used, one electrode is placed on the apical side and the other in the basolateral side so that the electrodes are separated by the cellular layer. According to Ohm's Law, the ohmic resistance can be determined by applying a direct current (DC) voltage to the

electrodes and measuring the current. However, the direct current will damage the cells and electrodes. To overcome this problem, a square-wave alternating current (AC) voltage signal is applied. For example, the widely used TEER measurement system, Millicell-ERS system [27, 28] (Millipore Corp., Bedford, USA), uses an AC square wave at a frequency of 12.5 Hz to avoid any charging effects on the electrodes and the cell layer (see Figure 4.13b). This system is equipped with two electrodes known as "chopstick" electrodes, each electrode contains a silver/silver chloride pellet for measuring voltage and resistance.

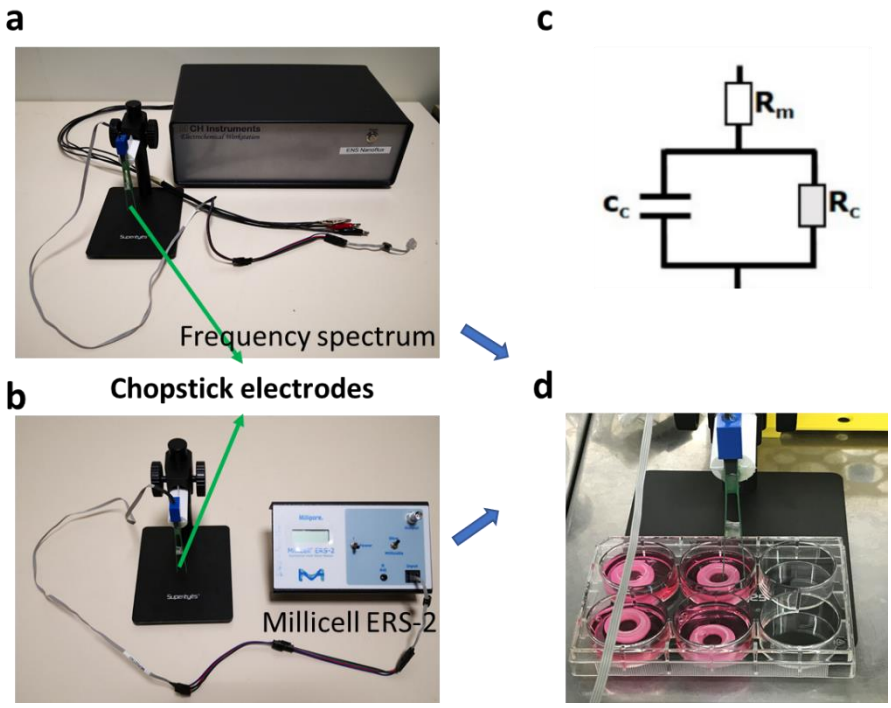

Figure 4.13 Two methods for TEER measurement: (a) impedance spectroscopy (0.1~1000,000 Hz) of resistance measurement using chopstick electrodes combined with a electrochemical workstation (CH Instruments); (b) resistance measurement using chopstick electrodes combined with Millicell ERS-2. (c) a typical equivalent circuit diagram of impedance measurement. (d) chopstick electrodes were merged in the medium with the presence of ALI culture devices.

In our work, TEER of the replated alveolar epithelium was measured during the culture. Our measurement is based on the ALI culture device as shown in Fig 4.13d. Figure 4.13a shows a workstation for impedance measurement, which can provide additional information about the capacitance of the cell layer across a wide spectrum of frequencies instead of a DC/single frequency AC TEER measurement. Figure 4.13c shows a typical equivalent circuit diagram that can be applied to analyze the impedance spectrum of cellular systems. In this circuit, the current can flow through the junctions between cells (paracellular route) or through the cell

membrane of the cells (transcellular route). The resistance of the cell culture medium contributes to an ohmic resistance (R_m) in the equivalent circuit. The tight junction proteins in the paracellular route and each lipid bilayer in the transcellular route contribute to a parallel circuit consisting of ohmic resistance (R_C) and an electrical capacitance (C_C).

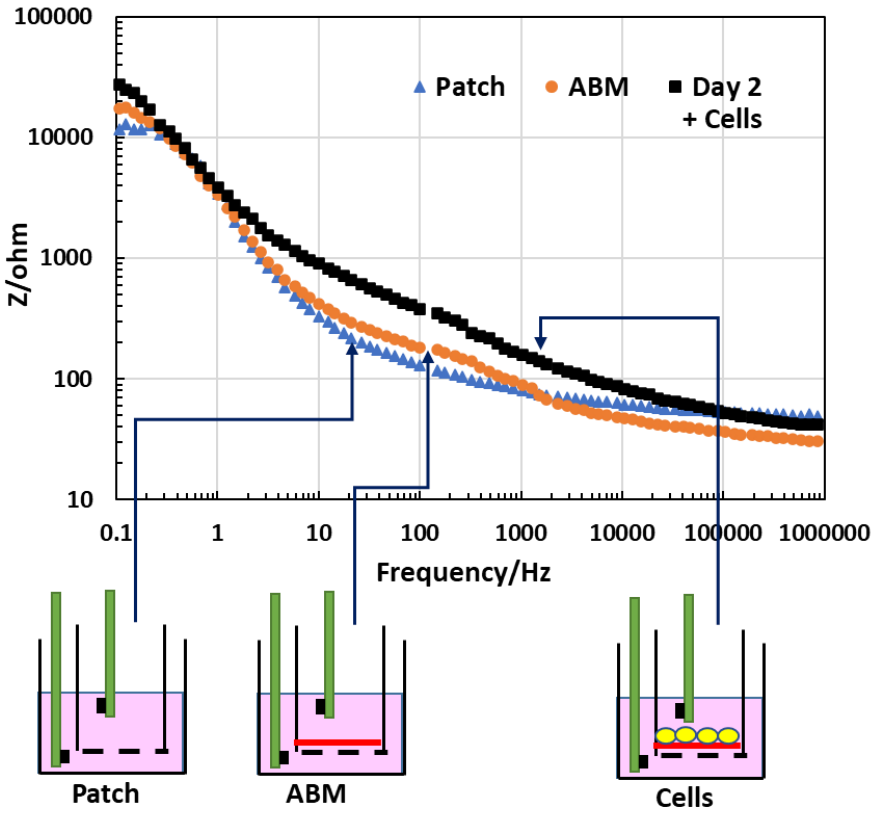

Figure 4.14 Frequency spectrums of impedance measurement using a frequency sweeping equipment (electrochemical workstation), patch, ABM patch and cells on ABM patch after 2 days culture were measured, respectively.

After cell replating and attachment to the ABM patch, we mounted the cell patch on the ALI culture device, with the basolateral side filled with 2 mL and the apical side filled with 200 µL replating medium. During the submerged culture and ALI culture, TEER measurements were applied by inserting the electrodes with one on the apical side and the other on the basal side. We first sterilized the electrodes by merging them into 70% ethanol for 15min and equilibrated the electrodes by soaking them into PBS and subsequently, IMDM medium. Before the measurement, the culture medium in the well was removed and a fresh IMDM medium was added to both sides, with 5 mL in the basolateral side and 600 µL in the apical side. The electrical resistance was measured five times for comparison and average values. After the

measurement, IMDM medium was exchanged with the replating medium or maturation medium to maintain the cell culture.

Figure 4.14 shows cures of total impedance in a wide frequency range. Typically, in the low frequency range, the impedance signal is dominated by the capacitance of the measurement electrodes. In the mid frequency range, the impedance signal is dominated by circuit elements related to the cells, namely R_C and C_C. In the high frequency range, C_C provide a more conductive path and the impedance signal is dominated by R_m. Therefore, in the range of 10 ~ 1000 Hz, we can find that the impedance of the sample with cells is higher than that of both empty patch and ABM patch, and patch with ABM has higher impedance than empty patch. This result demonstrated the feasibility of impedance measurement on our cell sample using our ALI device.

We also measured the resistance by single frequency AC TEER measurement using the commercial widely used Millicell ERS-2. This measurement process includes measuring the blank resistance (R_{blank}) of permeable membrane (without cells) and measuring the resistance (R_{total}) of the cell layer on the permeable membrane. Thus, the resistance of the cell layer (R_{cell}) can be defined as:

$$R_{cell} = R_{total} - R_{blank}$$

Fig 4.15 shows the electrical resistance of alveolar tissue formation during a totally 7 days culture. Comparing the first day (1S) and the third day (3S) in submerged culture, cell culture showed increasing electrical resistance due to cell proliferation. However, the resistance decreased after another two days (3S2A) ALI culture, this may be due to the tightening of cell tissues caused by changing to the maturation medium and adapting to the new air-liquid environment. Subsequently, cells were cultured for another two days (3S4A) under ALI condition, the electrical resistance increased gradually because of stable proliferation, which revealed the differentiation and development of the alveolar epithelium under ALI culture.

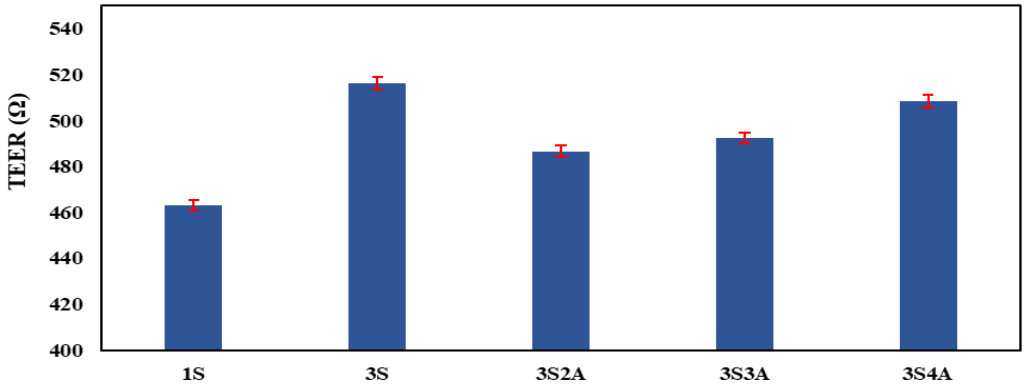

Figure 4.15 Absolute resistance of replated epithelium on different days and in different culture conditions. 1S: 1 day in submerged culture on ABM patch; 3S2A: 3 days in submerged culture and 2 days in ALI on ABM patch.

In addition, we performed TEER measurement or the fabricated alveolar epithelium after ALI culture. This has been done for cell layers for different culture periods and in different culture conditions. They were firstly fixed by 4% formaldehyde in PBS for 15 min and then washed in PBS 3 times. 5 mL fresh IMDM medium was filled into the basolateral side and 600 µL on the apical side. Before inserting the cell layer, TEER values were obtained for IMDM medium and ABM patch alone, respectively. Then, cell patches were mounted and TEER values were obtained by statistical averaging of several measurements. As shown in Fig 4.16, the resistance of the cell patch in submerged-culture for 5 days (5S + ABM) is lower than that for 10 days (10S + ABM), due to cell proliferation under submerged-culture conditions. The resistance of the cell patch after 3 days submerge-culture and then 7 days ALI culture (3S7A + ABM) is lower than that of 10S + ABM, due to the change of culture condition as discussed above. Finally, the TEER value of the cell layer after 10 days submerge culture on 1% Matrigel-coated patch (10S + Matrigel) is smaller than that of 10S + ABM, indicating a better culture performance of the ABM patch comparing to the Matrigel-coated patch.

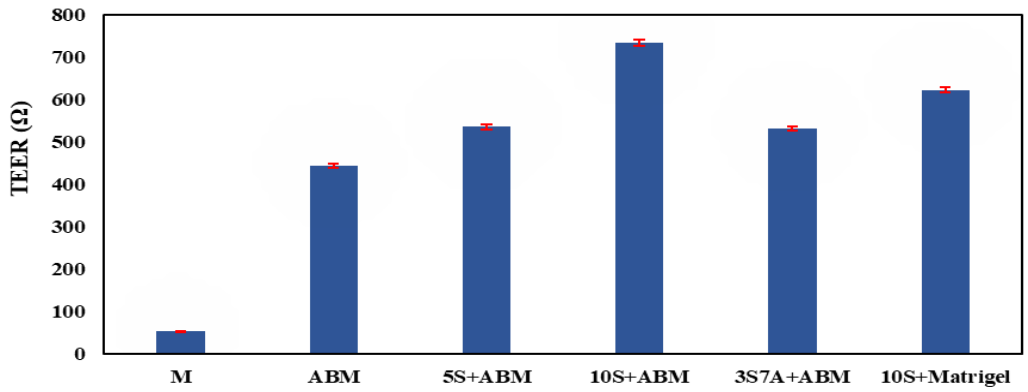

Figure 4.16 Absolute resistance of replated epithelium for different culture days and in different culture conditions. M: empty medium; ABM: ABM patch; 5S + ABM: 5 days in submerged culture on ABM patch; 3S7A + ABM: 3 days in submerged culture and 7 days in ALI on ABM patch; 10S + Matrigel: 10 days in submerged culture on 1% Matrigel-coated patch.

To conclude, based on the absolute resistance of the ABM patch, our alveolar epithelium was measured in a range of 100 ~ 300 Ω on a surface of 10 mm diameter, which is similar to previous works [29-31] and the cell layer has primary barrier function.

4.5 Conclusion

In this chapter, we succeeded in constructing a functional alveolar tissue from hiPSCs. We firstly differentiated hiPSCs into alveolar organoids which were made by AT1 and AT2 cells. The derived alveolar organoids could be maintained in Matrigel domes for long-term culture, showing characteristic maturation, growth, and bud tip formation. We also demonstrated a multi-passage of the alveolar organoids in a 2-week cycle. Cryopreservation and thawing of organoids were both implemented and successful, giving a potential of mass fabrication of the alveolar organoid lineage. By disassociation of maturated alveolar organoids into single cells and replating them on an artificial basement membrane, alveolar epithelium could be formed for both ALI culture and TEER measurement. To apply the above techniques to the immunoassays, we also checked and confirmed the ACE2 expression of the derived alveolar cells. Altogether, our epithelium model is readily useful for a variety of assays, such as drug screening, viral infection, co-culture with endothelial cells and immune cells.

References

[1] Giard, DJ, et al. (1973). "In vitro cultivation of human tumors: establishment of cell lines derived from a series of solid tumors." Journal of the National Cancer Institute **51**(5): 1417-1423.

[2] Akunuru, S, et al. (2012). "Non-small cell lung cancer stem/progenitor cells are enriched in multiple distinct phenotypic subpopulations and exhibit plasticity." Cell Death & Disease **3**(7): e352.

[3] Foster, KA, et al. (1998). "Characterization of the A549 cell line as a type II pulmonary epithelial cell model for drug metabolism." Experimental cell research **243**(2): 359-366.

[4] Zhou, R, et al. (2007). "Electroporation-mediated transfer of plasmids to the lung results in reduced TLR9 signaling and inflammation." Gene Therapy **14**(9): 775-780.

[5] Whitsett, JA and TE Weaver (2015). "Alveolar development and disease." American Journal of Respiratory Cell & Molecular Biology **53**(1): 1-7.

[6] Herriges, M and EE Morrisey (2014). "Lung development: orchestrating the generation and regeneration of a complex organ." Development **141**(3): 502-513.

[7] Gazdar, AF, et al. (2010). "Lung cancer cell lines: Useless artifacts or invaluable tools for medical science?" Lung Cancer **68**(3): 309-318.

[8] Ghaedi, M, et al. (2014). "Alveolar epithelial differentiation of human induced pluripotent stem cells in a rotating bioreactor." Biomaterials **35**(2): 699-710.

[9] Huang, SX, et al. (2015). "The in vitro generation of lung and airway progenitor cells from human pluripotent stem cells." Nature Protocols **10**(3): 413-425.

[10] Jacob, A, et al. (2017). "Differentiation of human pluripotent stem cells into functional lung alveolar epithelial cells." Cell stem cell **21**(4): 472-488. e410.

[11] Yamamoto, Y, et al. (2017). "Long-term expansion of alveolar stem cells derived from human iPS cells in organoids." Nature Methods **14**(11): 1097-1106.

[12] Lorsch, JR, et al. (2014). "Cell Biology. Fixing problems with cell lines." Science **346**(6216): 1452-1453.

[13] Pan, C, et al. (2009). "Comparative proteomic phenotyping of cell lines and primary cells to assess preservation of cell type-specific functions." Molecular & cellular proteomics **8**(3): 443-450.

[14] Heijink, IH, et al. (2010). "Characterisation of cell adhesion in airway epithelial cell types using electric cell–substrate impedance sensing." European Respiratory Journal **35**(4): 894-903.

[15] Evans, KV and JH Lee (2020). "Alveolar wars: The rise of in vitro models to understand human lung alveolar maintenance, regeneration, and disease." STEM CELLS Translational Medicine **9**(8): 867-881.

[16] Tan, Q, et al. (2017). "Human airway organoid engineering as a step toward lung regeneration and disease modeling." Biomaterials **113**: 118-132.

[17] Chen, YW, et al. (2017). "A three-dimensional model of human lung development and disease from pluripotent stem cells." Nature Cell Biology **19**(5): 542-549.

[18] Magro-Lopez, E, et al. (2018). "Effects of lung and airway epithelial maturation cocktail on the structure of lung bud organoids." Stem Cell Research & Therapy **9**(1): 186.

[19] Dye, BR, et al. (2020). "Human lung organoids develop into adult airway-like structures directed by physico-chemical biomaterial properties." Biomaterials **234**: 119757.

[20] Van Riet, S, et al. (2020). "In vitro modelling of alveolar repair at the air-liquid interface using alveolar epithelial cells derived from human induced pluripotent stem cells." Scientific reports **10**(1): 1-12.

[21] Upadhyay, S and L Palmberg (2018). "Air-Liquid Interface: Relevant In Vitro Models for Investigating Air Pollutant-Induced Pulmonary Toxicity." Toxicological Sciences **164**(1): 21-30.

[22] Miller, AJ, et al. (2018). "In Vitro Induction and In Vivo Engraftment of Lung Bud Tip Progenitor Cells Derived from Human Pluripotent Stem Cells." Stem Cell Reports **10**(1): 101-119.

[23] Miller, AJ, et al. (2019). "Generation of lung organoids from human pluripotent stem cells in vitro." Nature Protocols **14**(2): 518-540.

[24] Panek, M, et al. (2018). "The formation of intestinal organoids in a hanging drop culture." Cytotechnology **70**(3): 1085-1095.

[25] Mou, H, et al. (2016). "Dual SMAD Signaling Inhibition Enables Long-Term Expansion of Diverse Epithelial Basal Cells." Cell stem cell **19**(2): 217-231.

[26] Benson, K, et al. (2013). "Impedance-based cell monitoring: barrier properties and beyond." Cerebrospinal Fluid Research **10**(1): 5.

[27] Zucco, F, et al. (2005). "An inter-laboratory study to evaluate the effects of medium composition on the differentiation and barrier function of Caco-2 cell lines." Altern Lab Anim **33**(6): 603-618.

[28] Ferruzza, S, et al. (2013). "Serum-reduced and serum-free media for differentiation of Caco-2 cells." Altex **30**(2): 159-168.

[29] Theile, M, et al. (2019). "A simple approach to perform TEER measurements using a self-made volt-amperemeter with programmable output frequency." JoVE (152): e60087.
[30] Kuehn, A, et al. (2016). "Human alveolar epithelial cells expressing tight junctions to model the air-blood barrier." Altex **33**(3): 251-260.
[31] Ruan, T, et al. (2020). "H1N1 Influenza Virus Cross-Activates Gli1 to Disrupt the Intercellular Junctions of Alveolar Epithelial Cells." Cell Reports **31**(13): 107801.

Chapter 5
Response of hiPSC derived cells to S-proteins of SARS-CoV-2

Response of hiPSC derived cells to S-proteins of SARS-CoV-2

In this chapter, we present preliminary results of virus-host interaction by using hiPSC derived cells, including both alveolar and cardiac cells, with S-proteins of SARS-CoV-2. The physiological aspects and in particular the virus-host interaction of SARS-CoV-2 are firstly introduced. The ACE2 receptor and renin-angiotensin system are briefly discussed, giving rise to a hypothesis that S-protein can be used to study the SARS-CoV-2 related virus-host interaction due to S-ACE2 coupling and regulated AT1R activation as well as resulted oxidative stress to the host cells. ROS levels of alveolar samples after incubation with S-proteins and angiotensin II, with and without Losartan (AT1R blocker) treatment, are studied. hiPSC derived cardiac tissues are also used to study their responses to the S-proteins by observing the variation of the cardiac beatings.

5.1 SARS-CoV-2: Physiological aspects

In the actual context, we are mostly interested in in-vitro alveolar models for studies of severe acute respiratory syndrome-coronavirus 2 (SARS-CoV-2), since the coronavirus mainly infects the human lung alveoli and may cause diffuse alveolar damage with high morbidity and high mortality. Figure 5.1 schematically shows an alveolus before and after injured (acute phase) [1]. In a normal alveolus, the alveolar epithelium is made of alveolar type 1 (AT1) and type 2 (AT2) cells and alveolar basement membrane and shaped like a tiny sac for air filling. This tiny sac is surrounded by a blood capillary network for gas exchange and coated at the air interface with a thin layer of surfactant secreted by AT2 cells. AT2 cells are identified as the main targeting host cells of the coronavirus but they are 10 times less than flat AT1 cells which can be more damaged. In the acute phase, both bronchial and alveolar epithelial cells can slough. In the air sac space, pro-inflammatory cytokines, including interleukin-1®, 6, 8, and 10, (IL-1, 6, 8, and 10) and tumor necrosis factor α (TNFα), and chemokines are secreted by alveolar macrophages to stimulate chemotaxis and activate neutrophils. Once activated, neutrophils come massively in the air sac and release various biochemical reagents, including oxidants, proteases, leukotrienes, and platelet-activating factor (PAF) for further attracting

immune cells to the site of inflammation. Anti-inflammatory mediators are also present in the alveolar milieu and the protein-rich edema fluid can flow into the alveolus, which can inactivate the surfactant. Therefore, the acute phase of lung injury is a consequence of damage to the alveolar-capillary barrier. More importantly, such a loss in epithelial integrity can give rise to alveolar flooding, disruption of normal epithelial fluid transport, reduction of surfactant, septic shock and finally fibrosis.

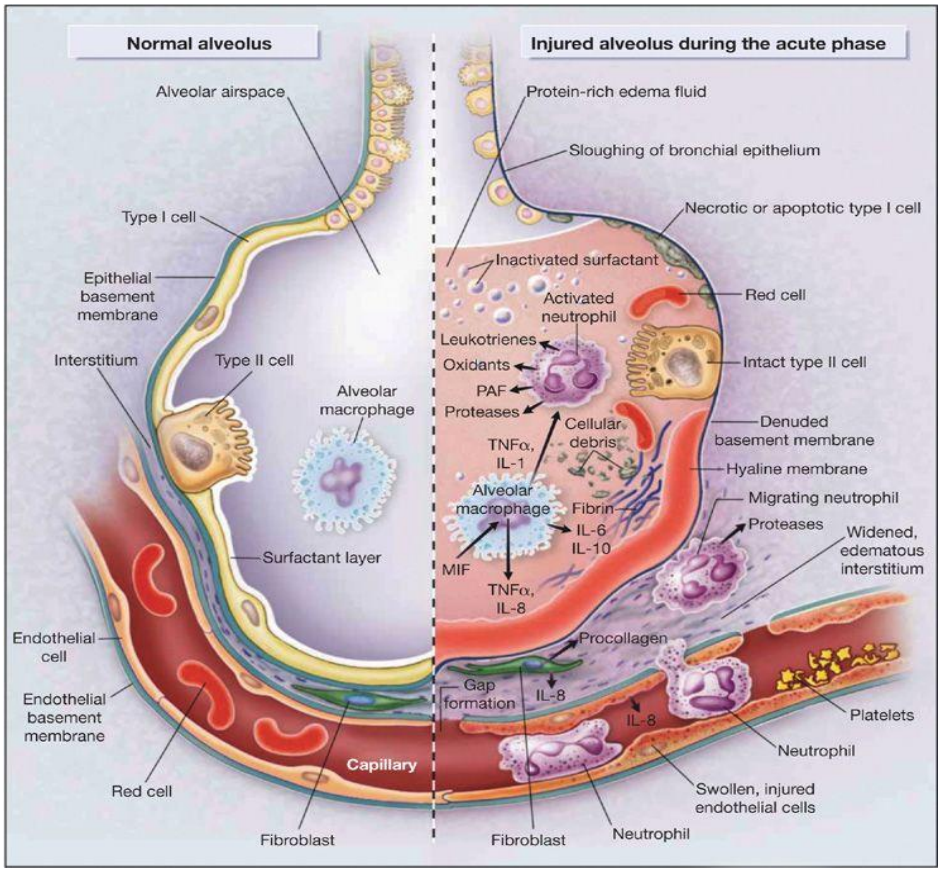

Figure 5.1 Normal alveolus (Left) and injured alveolus in an acute phase (Right).

Human ciliated bronchial epithelial cells (airway) are also the targeting host cells of the coronavirus and other respiratory viruses. Figure 5.2 shows schematically a normal airway epithelium and a virus-induced disruption of the airway barrier. This illustration is adapted from [2] which describes the effect of human rhinovirus. Although SARS-CoV-2 is much more cytopathic than rhinovirus, their barrier disruption mechanisms might be comparable. In a normal airway, cells adhere to the basement membrane by forming hemidesmosomes and focal contacts and connecting each other with tight, adherens and gap junctions. Such an epithelium, together with the airway surface liquid, forms a physical barrier to protect against infection which is also regulated to filter essential molecules, ions, and proteins.

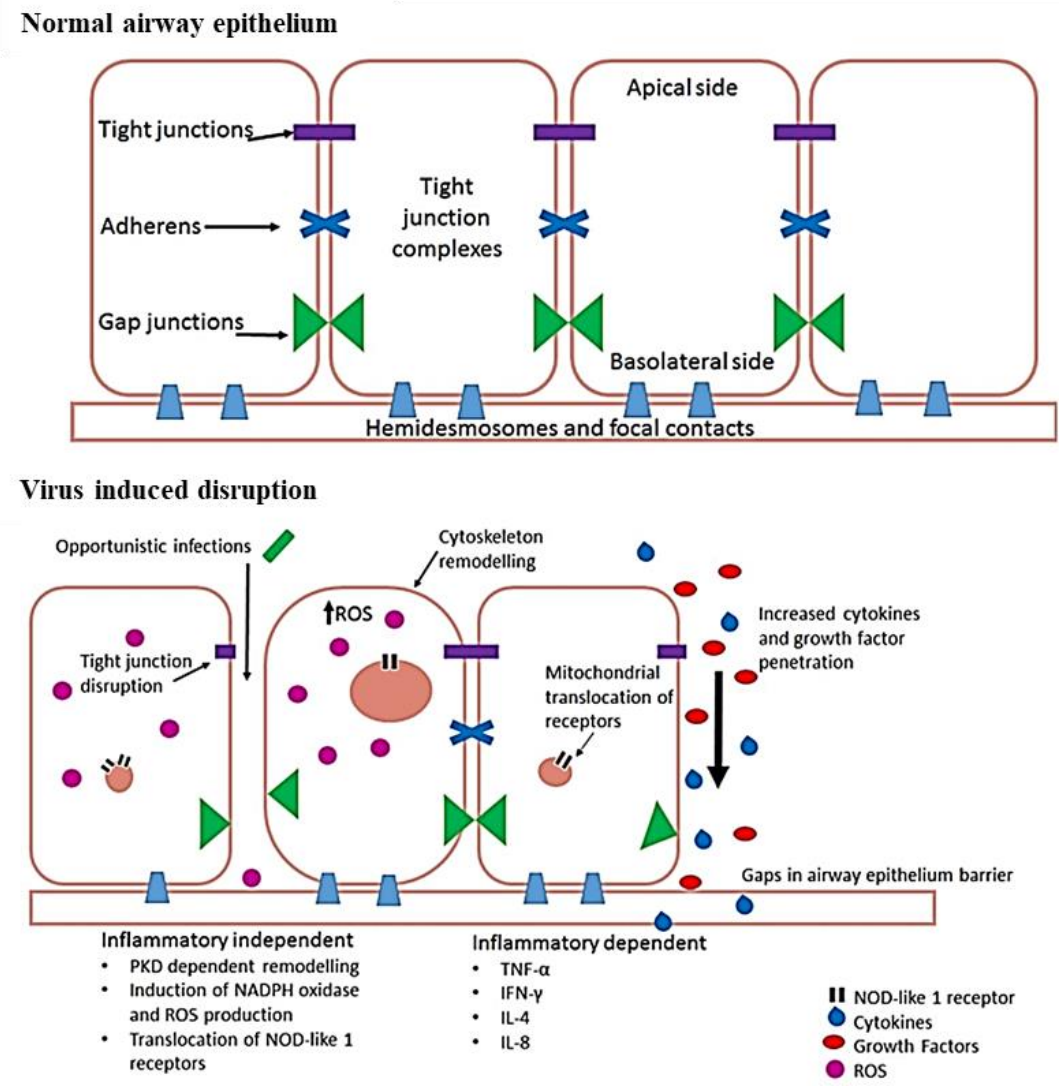

Figure 5.2 Normal airway epithelium before and after virus-induced barrier disruption. IL, interleukin; IFN, interferon; TNF, tumor necrosis factor (adapted from [2])

Once infected, the airway barrier can be disrupted inflammatory-independently and/or dependently. On one hand, viruses can generate oxidative stress independent of both viral replication and inflammatory-related signaling for NAD(P)H activities. This may lead to cytoskeletal remodeling and loss the barrier integrity. On the other hand, viral replication in cells causes the release of inflammatory factors such as TNFα, IFNγ, IL-4 and IL-8, which may heavily damage the barrier through the tight junction dysregulation mediated by matrix metalloproteinase and cytoskeleton remodeling. In particular, cytoskeletal remodeling mediated by protein kinase D results in loss of the adjoining contacts of the cells, allowing

cytokines, growth factors, immune cells and further viral particles to go inside the deep tissue layers for further damages.

5.2 SARS-CoV-2: Virus-host interaction

Figure 5.3 is a picture of SARS-CoV-2 (left) and a transmission electron micrograph of infected tissue of a patient during the pandemic (right). Morphologically, it is spherical and 80-120 nm in diameter, with a number of spikes on its surface and a positive-sense single-stranded RNA inside [3, 4]. This virus is made of four structural proteins, i.e., S (spike), E (envelope), M (membrane), and N (nucleocapsid) proteins [5]. The S, E, and M proteins together create the viral envelope; while the N protein holds the RNA genome.

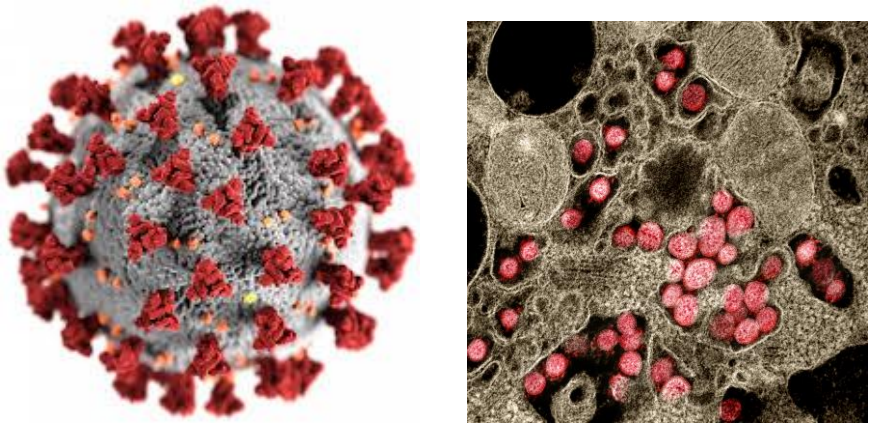

Figure 5.3 Left: SARS-CoV-2 virion, Grey: lipid envelope; Yellow: envelope proteins (E); Orange: membrane proteins (M), and Red: spike proteins (S). Right: Transmission electron micrograph of infected tissue of a patient, Red: SARS-CoV-2 virions [4].

The spike protein is a glycoprotein of 23 nm in length and 7 nm in diameter. The receptor-binding domain (RBD) of S-protein is responsible for the virus-host cell coupling [6], using angiotensin-converting enzyme 2 (ACE2) as receptor which is located on the cell membrane. Figure 5.4 shows the two subunits of S-protein, S1 and S2, and a cartoon representation of the pre- to post-fusion transition of the S-protein. Here, S1 is used to catalyze the viral attachment and S2 for the fusion of viral with the cellular membrane, helping viral endocytosis [7].

Once fused into the cell, an endosome forms around the virion and a host cysteine protease then comes to cleave it. Then, the virion releases its RNA to produce copies of the virus's proteins by using the cell's machinery. After assembling and budding into the lumen of the intermediate compartment of endoplasmic reticulum (ER) and Golgi, virions are released from the cell through exocytosis (Figure 5.5). During the viral replication, some virulence factors

are produced which promote the shedding of new virions from the host and impedes immune response, some others are released to trigger inflammatory responses and cell death.

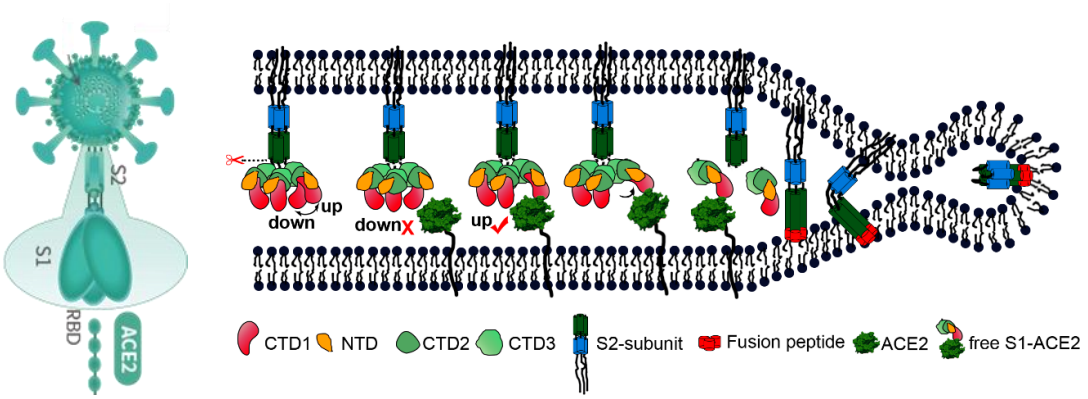

Figure 5.4 Left: Spike protein showing its RBD to ACE2 acceptor. Right: A cartoon representation showing the pre- to post-fusion transition of the S protein [7].

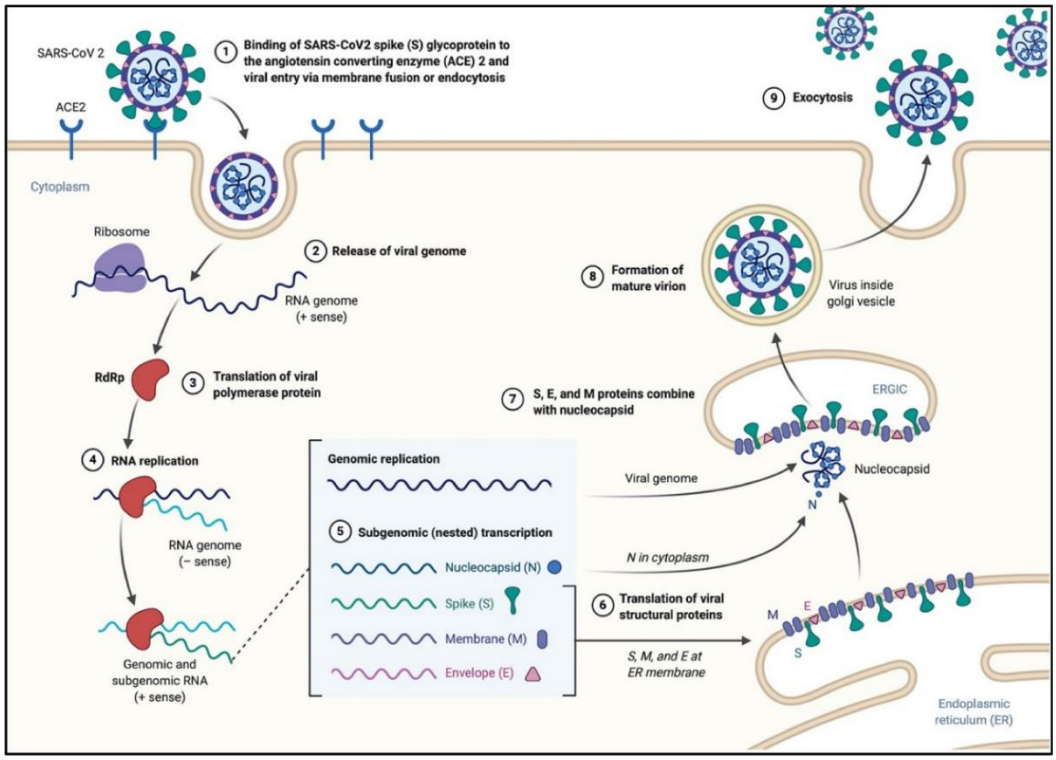

Figure 5.5 Replication of SARS-CoV-2 in a host cell. The S protein binds to an ACE2 receptor and enters the cell through an endosomal pathway. Once inside, the viral RNA is unveiled in the cytoplasm to produce necessary ingredients for new virus assembly and release from the cell through exocytosis [8].

.

5.3 ACE2 and renin-angiotensin system

The pathology of SARS-CoV-2 is related to damage of lung epithelium and disorders of the immune system such as cytokine storm and impaired antigen-presenting. It should also be related to imbalanced regulation of the renin-angiotensin system (RAS). This is because of the central role of ACE2, which is normally used for hydrolytic catalysis of angiotensin II (Ang-II), a vasoconstrictor peptide, into angiotensin (1–7), a vasodilator peptide. Since the infection may cause ACE2 downregulation, it gives rise to a toxic overaccumulation of Ang-II and thus affects harmfully the ACE2 rich organs, including lungs, heart, esophagus, kidneys, bladder, and ileum [9, 10].

RAS is an endocrine system involved in the regulation of blood pressure and electrolyte balance in the human body (Figure 5.6). Angiotensinogen is produced by the liver and converted to angiotensin I (Ang-I) by renin which itself is released by the kidney. Ang-I can then be converted to Ang-II by angiotensin-converting enzyme (ACE) or Angiotensin 1-9 (Ang 1-9) by ACE2. Ang-II can be further converted to Ang (1-7) by ACE2. Ang II coupled to angiotensin type 1 receptor (AT1R) plays opposite roles that Ang (1-7) coupled to MAS receptor (MASR), one is pro-inflammatory (AT1R related) and another anti-inflammatory (MASR related). Therefore, the downregulation of ACE2 leads to an imbalance in cellular regulation and the pro-inflammation pathway becomes dominant. Depending on the individual, such an imbalance may pose serious pathological problems. Figure 5.6 also shows possible intervention for such an imbalance. For example, angiotensin receptor blockers (ARBs) would decrease the effect of AT1R activation while ACE inhibitors (ACEi) would decrease the Ang I to Ang II conversion rate.

5.4 Effect of S-protein

Based on the above analysis, S-proteins alone should also have significant pathology effects by triggering ACE2 downregulation. If the spike protein is significantly excessive in molar with respect to the viral particles, the spike mediated the ACE2 down regulation will be dominant and the imbalance is RAS will also be important. Since RAS is related to human blood pressure and other key physiological parameters, ACE2 downregulation will further reduce human immunity and thus enhance the infection.

Previously, it has been shown that the reduction of ACE2 in mice could be induced not only by a viral infection but also by recombinant S-protein. The mice pre-treated with this spike

protein did not show significant pathology but if these animals were acid instilled, the spike protein pre-treatment leads to increased severity of the lung damage [11].

The objective of the present study is to evaluate the effect of S-proteins on hiPSC derived alveolar epithelium and the counteraction induced by AT1R blockers. In the following, we will first present the monitoring method and then show the results of our preliminary measurements.

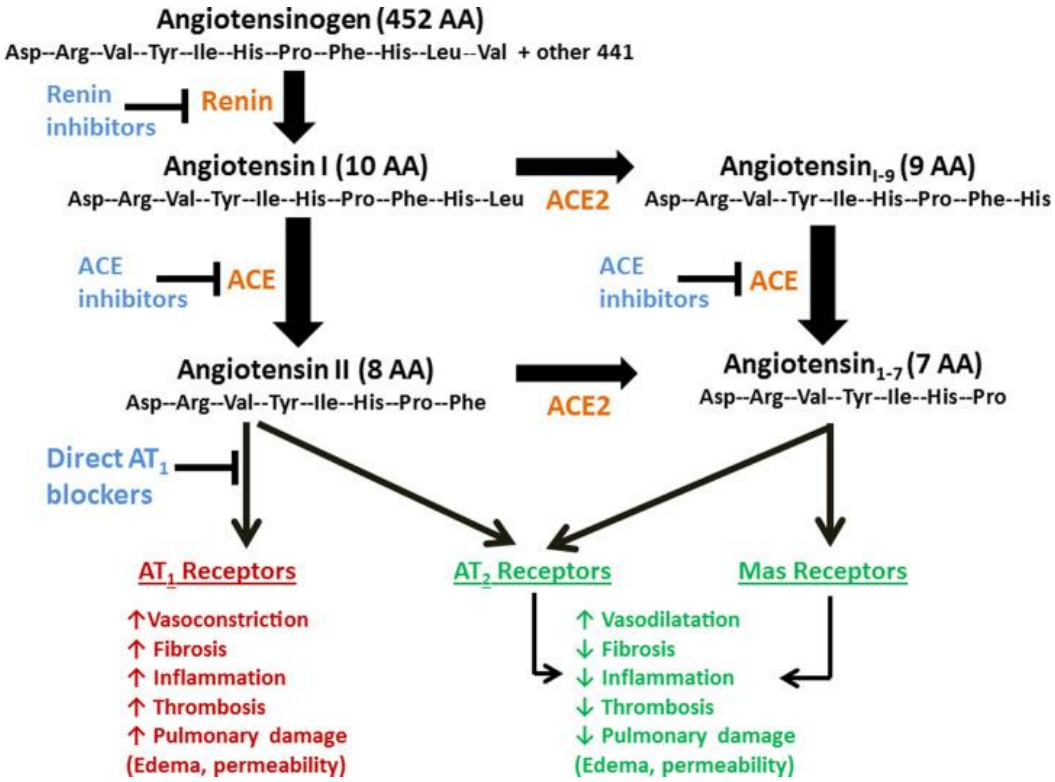

Figure 5.6 Counter-regulatory effects of angiotensin (1-7) on angiotensin II. Angiotensinogen produced by the liver is converted to angiotensin I (Ang-I) by renin released by kidney. Ang-I can then be converted to Ang-II by ACE or Angiotensin 1-9 (Ang 1-9) by ACE2. Ang-II can be further converted to Ang (1-7) by ACE2. Here, Ang-II coupled to angiotensin type 1 receptor (AT1R) plays opposite roles that Ang (1-7) coupled to MAS receptor (MASR), one is pro-inflammatory (AT1R related) and another anti-inflammatory (MASR related) [12].

5.5 ROS monitoring

ROS, including superoxide anions, hydrogen peroxide, and hydroxyl radicals, are constantly produced in cells, due to the one-electron reduction of molecular oxygen [13, 14]. In general, the production of ROS is tightly regulated by the scavenging system of ROS for which antioxidant enzymes may neutralize ROS by reversing one-electron reaction. Oxidative stress

caused by the imbalance between the excessive formation of ROS and insufficiency of antioxidant defenses may damage proteins, lipids and nucleotides. For this reason. Many pathologies such as age-dependent disorders, cancer, cardiovascular, inflammatory and neurodegenerative diseases are related to oxidative stress.

Previous studies [15-17] have shown that Ang-II can stimulate the intracellular ROS formation by AT1R activation. This means that ROS can also be correlated to ACE2, spike proteins and AT1R blockers (Figure 5.7).

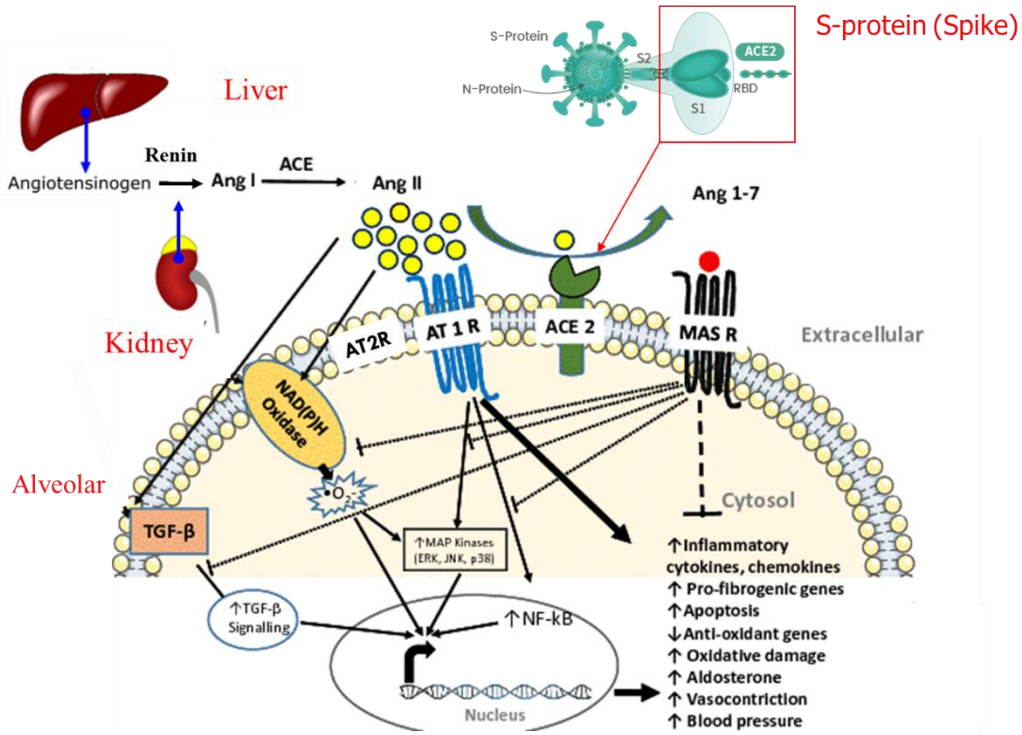

Figure 5.7 Renin-angiotensin system and effect of Ang-II, ACE2 and S-protein on AT1R and MASR activation (adapted from [18]).

To measure the intracellular level of ROS, oxidized fluorescent probes can be used. These probes are non-fluorescent esterified compounds, which can diffuse through the cell membrane and become fluorescent upon oxidation in cytoplasm. We have chosen 2',7'-dichlorofluorescein diacetate (DCFDA, Sigma) for the direct measurement of intracellular redox states.

Briefly, organoids-dissociated cells were replated (seeding density 3×10^4 cells/cm^2) on a culture patch with ABM in the replating medium (see chapter 4). After 2 days submerged culture and 5 days ALI culture, cells were washed one time with PBS and then incubated in a replating medium with 1 µg/mL S-protein for 24 h, followed by another treatment with 50 ng/mL Ang II (Sigma, France) for 3 h. For comparison, a sample was also treated in a replating

medium with 10 µM Losartan (Sigma, France) for 45 min, after S-protein and before Ang-II treatment. Here, Losartan is a well-known Ang-II receptor antagonist and widely used for hypertension treatment. A high dose of Losartan was considered which may totally block the AT1R activation.

The ROS labeling was done by incubating the cells in a replating medium with 10 µM DCFDA for 30 min at 37°C without light perturbation. Then, the cells were washed with PBS 3 times and then placed in fresh PBS. The ROS dependent fluorescence images were recorded with a Live-Cell Imaging System (MuviCyte™, PerkinElmer) using a 20X objective. Figure 5.8 shows bright field and ROS fluorescent microphotographs of the S-protein/Ang-II treated alveolar microtissue samples without (upper row) or with (lower row) passage with 10 µM Losartan for 45 min. As expected, the fluorescence intensity of the sample is lower than that without Losartan treatment, due to the reduced AT1R activation.

We have also recorded the variation of the fluorescence intensity of different samples as a function of time but found that the averaged fluorescence intensity of the sample varied irregularly during the first period and then increased slowly. A more systematic study is required to more clearly understand these variations and more generally the ROS monitoring.

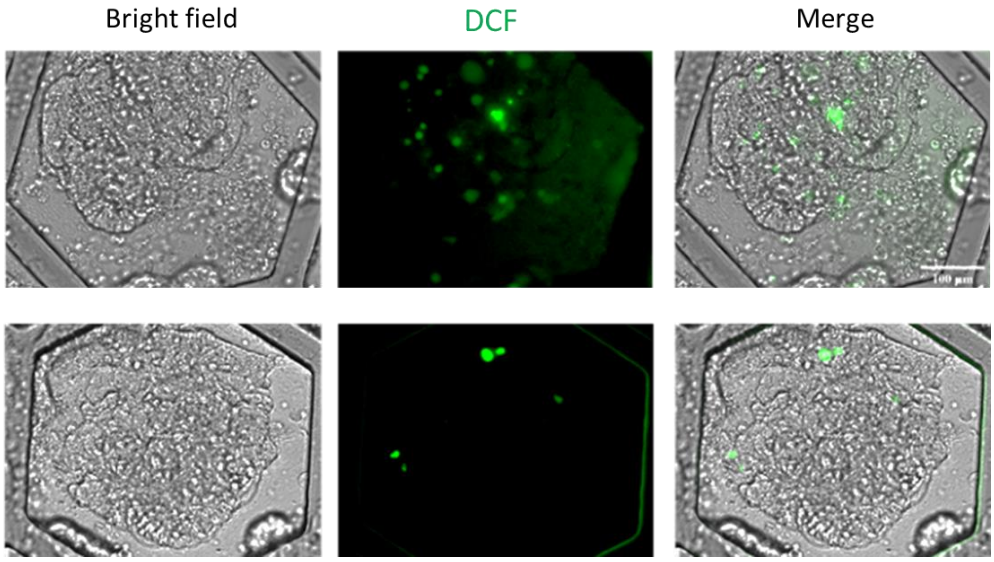

Figure 5.8. Bright-field and ROS fluorescent microphotograph of alveolar microtissues on ABM. Upper row: after incubation with 1 µg/mL spike proteins for 24 h and then with 50 ng/ml Ang-II for 3h. Lower row: after incubation with 1 µg/mL spike proteins for 24 h, 10 µM Losartan for 45 min, and 50 ng/ml Ang-II for 3h. These images were taken after 10 µM DCFDA treatment for 30 min and PBS washing.

5.6 Response of iPSC derived cardiomyocytes

Although the renin-angiotensin system is an endocrine system, heart and several other tissues contain and/or synthesize components of the system such as Ang-II to regulate/modulate tissue function [19]. For example, Ang II has an important role in cardiac and vascular pathology associated with hypertension, coronary heart disease, myocarditis, and congestive heart failure, in addition to effects on volume and electrolyte homeostasis [20]. Currently, a variety of drugs are used for inhibition of ACE or AT1R in order to counterbalance the effects in the renin-angiotensin system in a similar way as described above.

In chapter 3, we have described the development of a system for automatic control of hiPSC differentiation of cardiomyocytes (CM) and demonstrated the reliability of a simple protocol to generate functional cardiac tissue constructs. This differentiation protocol has been repeatedly used in the ENS laboratory and the resulted hiPSC-CM could also be used for the preliminary studies of the responses to spike proteins of SARS-Cov-2 [21]. Here, the hiPSC-CM cultivated for three months have been incubated with spike proteins at 1 µM concentration for 0.5, 9, and 20 h, showing no significant change in morphology and beating profile (Figure 5.9). The observation led us to suggest that in the absence of circulating Ang-II the effect of spike is not significant during a short period and that the local production of Ang-II is limited.

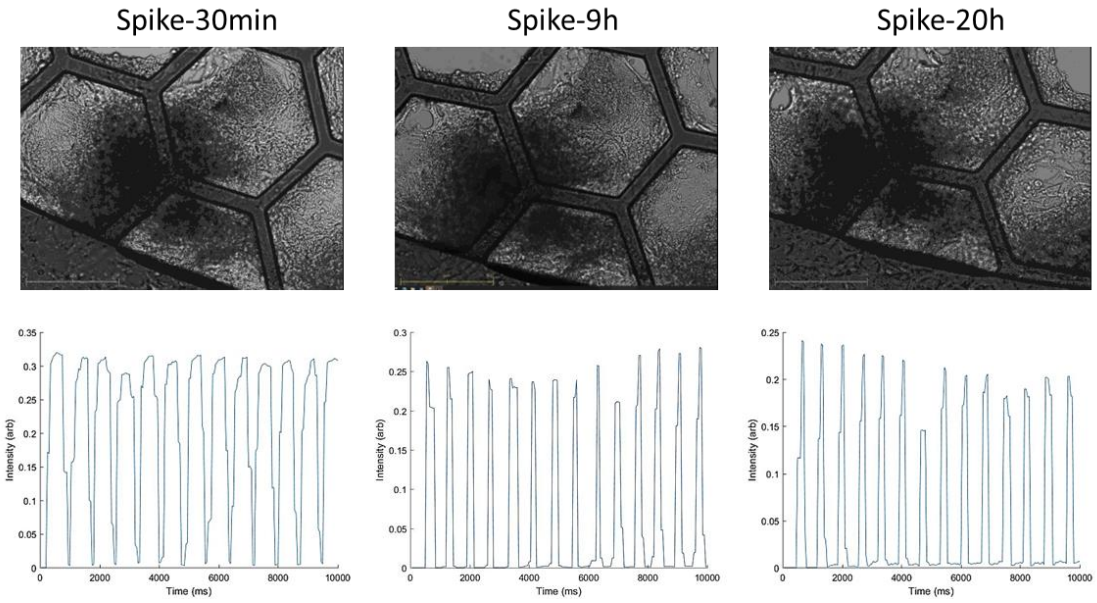

Figure 5.9 Bright field images and beating profiles of hiPSC derived cardiomyocytes after incubation with spike proteins for 0.5, 9 and 20 h.

After incubation for 20 h with the spike proteins, 100 ng/mL Ang-II was added. The bright field images and beating profiles recorded/analyzed at 0.5, 10 and 22 h are displayed in figure 5.10, showing clear toxicity effect of the spike proteins, since the spike proteins treated hiPSC-CMs underwent apoptosis and cessation of beating after 22 h. Similar effects have also been observed with a longer period of incubation with SARS-Cov-2 without circulating Ang-II [22, 23]. Although both SARS-Cov-2 and its spike protein are able to cause apoptosis and cessation of beating of hiPSC-CMs, the underlying mechanisms might be different.

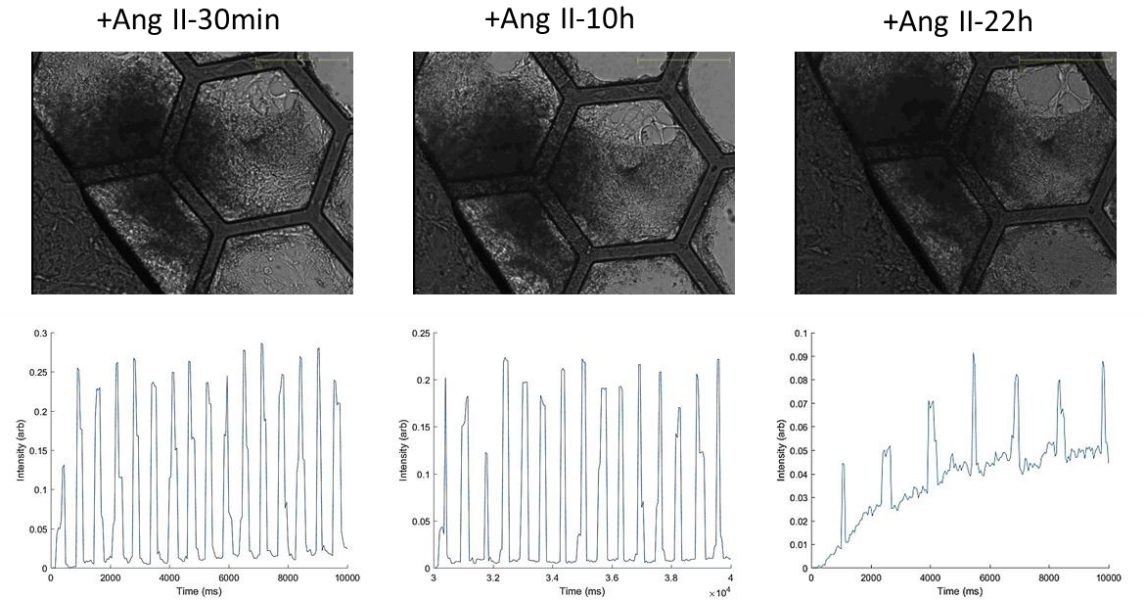

Figure 5.10 Bright-field images and beating profiles of hiPSC derived cardiomyocytes after incubation with spike proteins for 20 h and Ang-II for 0.5, 10, and 22 h.

We have to mention that in both alveolar and cardiac cases sufficient dosages of spike proteins and Ang-II have been used to generate strong cytotoxic effects. Indeed, Ang II can efficiently via AT1R activates the NF-κB protein complex, which is a "rapid-acting" primary transcription factor and first responder of harmful cellular stimuli, such as ROS, cytokines, virus, etc. Ang-II can induce activation of NF-κB signaling pathway promoting inflammation, which is often associated to the cellular necrosis, as well as apoptosis and fibrosis. More systematic studies have to be developed to understanding the underlying mechanisms.

5.7 Discussion

Basic research on virus-host interaction is essential to understand the pathophysiology of infection and identify the best drug candidates. Models that can faithfully recapitulate the immune environment and reproduce the viral life cycle of SARS-CoV-2 are urgently requested.

Primary human alveolar cells are expensive and do not proliferate indefinitely. Several infinitely proliferating cell lines, such as Caco-2, Calu-3, HEK293T, and Huh7 have been all used in SARS-CoV-2 infection experiments [24]. These cells do not accurately recapitulate human physiological conditions and usually generate low titer of SARS-CoV-2. Another cell line, Vero E6 isolated from the kidney epithelial cells of an African green monkey is now widely used for its high titer of viral particles and high coupling efficiency with the virus. This cell line is also limited and cannot be used to construct in-vitro models involving immune cells.

Recently, various organoids are derived from hiPSCs or primary cells. These organoids are generally composed of multiple cell types and reflecting somehow the local organization of human organs. Organoids can also be self-replicated so that they might be suitable for drug screening and disease modeling. The drawback of organoids is that they are generally immature and limited in size and functions. They cannot reproduce the systemic symptoms associated with whole-body responses to viral infection. Animal models are suited to avoid this problem but their immune systems are significantly different from human one. Moreover; our immune system is highly personal, age and environment-dependent. Only in-vitro approach is reliable from a long-term point of view.

In practice, the first step in in-vitro modeling is perhaps achieving a complete immune microenvironment constituted of both tissue constructs and immune cells. In the present context of the SARS-CoV-2 outbreak, the severe symptoms and high mortality are mainly due to inappropriate responses by the innate immune system such as cytokine storm, impair interferon responses, and suppress antigen presentation on both MHC class I and class II. Therefore, understanding and mimicking innate immune responses to SARS-CoV-2 will improve our understanding of pathogenesis, virus clearance, and contribute toward a vaccine and immunotherapeutic design and evaluation. The most important components of innate immunity include interferons and cytokines, pattern recognition receptors, neutrophils, NK cells macrophages and dendritic cells. Based on the existing protocols and the systematic integration of tissue and immune cells, one should be able to establish a general framework toward rapid development.

5.8 Conclusion

We have shown that the hiPSCs derived alveoli and cardiomyocytes could be used to study the toxicity of the spike proteins. Due to safety reasons, we were not able to work on the virus but the established methods are applicable to SAR-CoV-2 investigations. We also succeeded

in hiPSC differentiation to endothelial cells, hematopoietic stem cells, as well as megakaryocytes and macrophages. This would allow us to propose a more sophisticated in vitro model for the study of virus-host interaction. For example, alveolar and endothelial cells can be co-cultivated on two sides of an artificial basement membrane and macrophages can be introduced on alveolar side for in vitro modeling of innate immunological processes involving neutrophils and natural killer cells as well as dendritic cells all derived from the same hiPSCs. Finally, a multi-organ tissue system can be worked out, all derived from the same source of hiPSCs reprogrammed from cells of either healthy donors or patients. Clearly, there is a long way to go in this direction. The present work can be considered the first step to achieve the above ambitious goals.

References

[1] Ware, L and M Matthay (2012). "The acute respiratory distress syndrome." New England Journal of Medicine **332**(8): 27-37.

[2] Atkinson, SK, et al. (2016). "How does rhinovirus cause the common cold cough?" Bmj Open Respiratory Research **3**(1).

[3] Viruses, CSGotICoTo "The species Severe acute respiratory syndrome-related coronavirus: classifying 2019-nCoV and naming it SARS-CoV-2." NPG Open Access **5**(4).

[4] Cohen, J (2020). "Wuhan seafood market may not be source of novel virus spreading globally." Science.

[5] https//en.wikipedia.org/wiki/Severe_acute_respiratory_syndrome_coronavirus_2

[6] Wrapp, D, et al. (2020). "Cryo-EM structure of the 2019-nCoV spike in the prefusion conformation." Science **367**(6483): 1260-1263.

[7] Song, W, et al. (2018). "Cryo-EM structure of the SARS coronavirus spike glycoprotein in complex with its host cell receptor ACE2." PLoS pathogens **14**(8): e1007236.

[8] Alanagreh, La, et al. (2020). "The human coronavirus disease COVID-19: its origin, characteristics, and insights into potential drugs and its mechanisms." Pathogens **9**(5): 331.

[9] Li, M-Y, et al. (2020). "Expression of the SARS-CoV-2 cell receptor gene ACE2 in a wide variety of human tissues." Infectious diseases of poverty **9**: 1-7.

[10] Gheblawi, M, et al. (2020). "Angiotensin-converting enzyme 2: SARS-CoV-2 receptor and regulator of the renin-angiotensin system: celebrating the 20th anniversary of the discovery of ACE2." Circulation research **126**(10): 1456-1474.

[11] Kuba, K, et al. (2005). "A crucial role of angiotensin converting enzyme 2 (ACE2) in SARS coronavirus–induced lung injury." Nature medicine **11**(8): 875-879.

[12] Verdecchia, P, et al. (2020). "The pivotal link between ACE2 deficiency and SARS-CoV-2 infection." European journal of internal medicine.

[13] Bigarella, CL, et al. (2014). "Stem cells and the impact of ROS signaling." Development **141**(22): 4206-4218.

[14] Finkel, T and NJ Holbrook (2000). "Oxidants, oxidative stress and the biology of ageing." nature **408**(6809): 239-247.

[15] Sachse, A and G Wolf (2007). "Angiotensin II–induced reactive oxygen species and the kidney." Journal of the American Society of Nephrology **18**(9): 2439-2446.

[16] Pendergrass, KD, et al. (2009). "The Angiotensin II–AT1 Receptor stimulates reactive oxygen species within the cell nucleus." Biochemical and biophysical research communications **384**(2): 149-154.

[17] Su, Q, et al. (2017). "Renin-angiotensin system acting on reactive oxygen species in paraventricular nucleus induces sympathetic activation via AT1R/PKCγ/Rac1 pathway in salt-induced hypertension." Scientific reports **7**(1): 1-13.

[18] Padda, RS, et al. (2015). "Angiotensin-(1-7): a novel peptide to treat hypertension and nephropathy in diabetes?" Journal of diabetes & metabolism **6**(10).

[19] Dostal, DE and KM Baker (1999). "The cardiac renin-angiotensin system: conceptual, or a regulator of cardiac function?" Circulation research **85**(7): 643-650.

[20] Keidar, S, et al. (2007). "ACE2 of the heart: from angiotensin I to angiotensin (1–7)." Cardiovascular research **73**(3): 463-469.

[21] Huang, XC, HE, Y et al. In preparation.

[22] Sharma, A, et al. (2020). "Human iPSC-derived cardiomyocytes are susceptible to SARS-CoV-2 infection." Cell Reports Medicine **1**(4): 100052.

[23] Marchiano, S, et al. (2020). "SARS-CoV-2 infects human pluripotent stem cell-derived cardiomyocytes, impairing electrical and mechanical function." BioRxiv.

[24] Takayama, K (2020). "In vitro and animal models for SARS-CoV-2 research." Trends in pharmacological sciences **41**(8): 513-517.

Chapter 6
Conclusion and perspectives

Conclusion and perspectives

This thesis work aimed at new culture devices and systems for advanced stem cell research and alveolar tissue modeling. These include fabrication of ultrathin artificial basement membrane, development of automatic culture and differentiation system, and validation of the devices and systems with human induced pluripotent stem cells (hiPSCs) for virus-host interaction studies.

We firstly adopted a culture patch technique to realize the ultrathin artificial basement membrane, which recapitulates to a large extent the biochemical and biophysical characteristics of the natural basement membrane. By using conventional photolithography and electrospinning techniques, a culture patch made of a monolayer of crosslinked gelatin nanofibers on a honeycomb microframe could be obtained and then used as a backbone for the deposition of a protein mixture of collagen type IV and laminin. The thickness of the resulting protein layer is in the order of 100 nm and it is made of 100% of natural BM materials on which much improved epithelial cell layers could be obtained. This device is compatible with the conventional culture using dishes, multiwell plates and flasks as well as microfluidic devices for organ-on-a-chip applications. Subsequently, various accessories were created, including mounting devices for homogenous seeding, TEER measurement, multi-patch culture, rotational microbioreactor, etc. Besides, a cage device was designed and realized which allowed us to create an array of homogenous spheroids or organoids assays, all caged in patch devices.

We secondly developed an automatic culture system for multi-source based hiPSCs differentiation and long-term maturation of hiPSCs derived cells. This system is composed of a unit for culture medium distribution, a unit for incubation and a central unit for process control. This system has been used for perfusion-diffusion cell culture by fast renewing of the culture medium. Both results of numerical simulation and cell proliferation suggested an improved exchange of the cell nutrients and metabolites. This system was later used for a cardiac differentiation from hiPSCs, which demonstrated the reliability of the system for multi-source control during automatic hiPSC processing. In addition, this system has been used for the long-term maturation of hiPSC derived neurons and neural networks. In general, both multi-source and long-term processing is time-consuming, laborious, and monotone. Our system overcomes these inconveniences and makes the whole work simple without human intervention. Upon these successes, several hiPSC differentiation protocols have been tested, including those

towards alveolar, airways, and endothelial cells as well as hematopoietic stem cells and their derivatives.

We thirdly established a robust fabrication procedure to produce functional alveolar cells. This procedure began with hiPSCs induction and differentiation in a dish and in a gel layer in order to form well-defined organoids made of both alveolar type 1 (AT1) and type 2 (AT2) cells. These organoids could then be freezed and defreezed for routine uses. By dissociating and replating them on an ultrathin artificial basement membrane culture, epithelial alveolar layers could be obtained. Cells in both alveolar organoids and alveolar expressed AT1 and AT2 markers as well as ACE2 markers, thus demonstrating the hiPSCs derived cells are suitable candidates for in vitro modeling. TEER measurements confirmed the importance of artificial basement membrane in tissue layer formation. From a long-term perspective, we were much interested in co-culture or tri-culture of alveolar tissues and other cells and particular immune cells derived from the same origin of hiPSCs, because they have all human cell-specific receptors and inherent immune tolerance. This would largely improve the current approaches and by considering a high degree of recapitulation of human tissues, organs, and systems including appropriate immune cells and ultimately the sophisticated immunity of the human body. With the help of automatic culture system, ultrathin artificial basement membrane, microfluidics, a new perspective can make the difference in regenerative medicine, drug discovery, and immunological studies.

Finally, we have been working on virus-host interaction by using hiPSC derived alveolar and cardiac cells. In the actual context of the worldwide outbreak of SARS-CoV-2, we initiated a preliminary study with the S-protein of SARS-CoV-2, which should be also applicable for the in-vitro modeling viral infections. To begin with, we measured ROS level related fluorescence image intensity of alveolar samples infected by S-proteins. The physiological aspects and in particular the virus-host interaction of SARS-CoV-2 were described. The importance of the ACE2 receptor and the renin-angiotensin system were discussed. In addition, the toxicity of the S-proteins could be studied by observation apoptosis and cessation of beating of cardiac tissue constructs. Based on the results of this preliminary study, more systematic investigations are expected to understand the underlying mechanisms of the S-protein toxicity.

Due to time-limitation, many issues could not be dealt with and many questions remain to be answered. During the last period, several new types of organoids, tissue layers and immune cells could be worked out in the laboratory using hiPSCs of the same origin, including endothelial cells, megakaryocytes, hematopoietic stem cells, macrophages, etc. Studies of

hiPSCs to several other types of cells, including neutrophils, natural killer cells, hepatocytes, kidney, and intestinal cells, are underway.

In this regard, the work presented in this thesis can be considered as a brick for the construction of advanced in-vitro models as well as multi-organ tissue systems. So far, we are very close to an alveolar-capillary co-culture model, in which hiPSCs were derived to both alveolar cells and capillary endothelial cells. Adjacent co-culture has been tested on two sides of an ultrathin basement membrane, confirming the feasibility of this approach but further quality improvement is expected. If successful, macrophages, neutrophils and natural killer cells will be introduced to model the innate immunity of the system. To further adapt this system to adaptive immunity studies, hiPSCs derived dendritic cells, T and B cells can be introduced. Using cells all derived from the same source of hiPSCs reprogrammed from cells of either healthy donors or patients, multi-organ tissue systems can be created. This gives an ambitious blueprint and we still have a long way to go.

In this thesis work, we have been working on several aspects of a highly interdisciplinary project, including cell culture and differentiation, numerical simulation, microdevice fabrication, and automatic system development. This approach is challenging but also has plenty of possibilities to create new devices and new systems. For example, new models could be created such as shown in the appendix of the thesis. Altogether, we achieved an important step in creating a reliable and useful alveolar model for future studies.

Appendix

Appendix

The main objective of this PhD work is to develop a reliable method for hiPSC differentiation towards alveolar tissue manufacturing and to study their responses to the S-proteins of coronavirus SARS-CoV-2. In addition, we also worked out several new types of devices or new protocols which are closely related to our main objectives, as described below.

1. Fabrication of cage devices for spheroid handling (Appendix A)

This work has been initiated to explore the potential of our patch technology for in-vitro cancer studies. We firstly fabricated honeycomb microframes with large hole sizes and large thicknesses to increase the size of tumor spheroids which can be formed in each of the honeycomb compartments. Then, we treated the nanofiber layer with agarose as an anti-adhesion agent to promote spheroid formation. Finally, we added a cover layer with a patterned mesh to prevent the escape of the formed spheroids. Afterward, single cells are seeded into each of the compartments through the large holes of the mesh. Once formed, the size of the tumor spheroids becomes larger than the size of the mesh so that tumors are caged in the honeycomb compartments.

As can be understood, the spheroids generally have limited attachment to the substrate which means that without the cover mesh layer or the cage structure, the spheroids can easily escape their confinement space. Therefore, the cage confinement is reliable and unique for the retention of the spheroids. The fabrication of the device is straightforward due to the bench processes. The fabricated devices as well as the formed tumor spheroids are robust and simple to use. For example, they can be easily inserted into a microfluidic device for a variety of assays under stimulation or drug treatment. They can also be used for implantation assays, knowing that not on tumor spheroids but also other types of cell aggregation or organoids can also be formed in a similar manner. We believe that this type of device will be useful for both fundamental research and advanced applications.

2. Fabrication of ultrathin artificial basement membrane (Appendix B)

As discussed in the introduction, the basement membrane plays a crucial role in epithelial and endothelial layer formation. It serves as physical barriers for large molecules and species but allows selectively small molecules. In order to recapitulate the most important properties of the basement membrane, we have used the type IV collagen and laminin, the two main proteins of the natural basement membrane, for the formation of our artificial basement

membrane. We also used a scale-down fabrication strategy to achieve an ultrathin membrane formation by patterning a thin layer into a honeycomb microframe and electrospinning a monolayer of gelatin nanofibers. Here, the microframe allows easy handling while the monolayer of nanofibers after crosslinking serves as a backbone for the formation of the ultrathin membrane of collagen-laminin in the porous area of the nanofibers.

In appendix C, the fabrication processes of the artificial basement membrane were detailed. The performance of the fabricated artificial basement membrane has also been studied using MDCK cells (not shown here), which demonstrated the advantage of this approach in terms of the cell polarity, the tight junction formation, homogeneity, and the long-term retention of the epithelial cell layer. The results presented in this work (Chapter 4 & 5) on alveolar and alveolar/endothelial formation further confirm the importance of the basement membrane in tissue engineering.

3. Effect of periodic deformation on cells cultured on nanofibers (Appendix C)

The periodic deformation of the alveolus is due to the aspiration of the lung. To model it, we used a microfluidic device for the integration of alveolar tissue and generation of a periodic deformation of the tissue. Once inserted, the alveolar tissue serves as a barrier to separate the upper and lower chamber of the device, one for the air circulation and another for the culture medium flow. By using a high precision pressure regulator, the air pressure in the upper chamber can be modulated which resulted in the desired periodic deformation of the alveolar tissue. Although this model has to be largely improved, it allowed us to demonstrate the effect of a periodic deformation on cells cultured on a monolayer of nanofibers. Indeed; under a static culture condition, cells seeded on a nanofiber layer are significantly affected by the morphology of the fiber layer which may not be homogeneously distributed. The periodic deformation of the fiber layer allowed a re-setting of the cell-substrate attachment and the cell-cell coupling. Our results demonstrated that the alveolar layer can be improved after being subjected to such a periodic deformation. More generally speaking, the periodic deformation of alveolus should have similar effects on the alveolar integrity, in addition to the physiological modulation of the blood circulation, blood, and alveolar basement membrane, etc. More systematic studies are expected in this direction.

4. Bioreactor for hiPSC differentiation of immune cells (Appendix D)

The outbreak of new coronavirus SARS-CoV-2 has generated huge impacts on many aspects of our society and our daily life. To deal with, clinicians have hardly worked to identify

the clinic features of the disease and to find better care solutions. Pathologists have tried every effort to understand the disease based on various assays. Despite these tremendous efforts, significant challenges remain, partially due to the lack of precise in-vitro models involving both human tissues and human immune cells of the same origin. Since human pluripotent stem cells can be differentiated into the two cell categories, it might be relevant to develop a precise in-vitro model for the SARS-CoV-2 studies. As demonstrated in this thesis work, we already achieved fabrication of alveolar tissue constructs and we should also be able to generate immune cells from the same hiPSCs and then develop a model for virus-host interaction involving immune cells.

In principle, all immune cells can be generated from hematopoietic stem cells, providing an appropriate culture environment and stimulations. We thus firstly designed a new type of micro bioreactor, which is dedicated to patch culture device, for hiPSC differentiation into hematopoietic stem cells. We then tried to obtain functional macrophages. These are described in Appendix D.

Appendix A
Fabrication of micro-cage devices for spheroid handling

Microelectronic Engineering 225 (2020) 111256

Contents lists available at ScienceDirect

Microelectronic Engineering

journal homepage: www.elsevier.com/locate/mee

Research paper

Fabrication of micro-cages and caged tumor spheroids for microfluidic chip-based assays

Yong He[a], Boxin Huang[a], Elrade Rofaani[a], Jie Hu[a], Yuanhui Liu[a], Gabriele Pitingolo[a], Li Wang[b], Jian Shi[b], Carole Aimé[a], Yong Chen[a,*]

[a] PASTEUR, Département de chimie, École normale supérieure, PSL University, Sorbonne Université, CNRS, 75005 Paris, France
[b] MesoBioTech, 231 Rue Saint-Honoré, 75001 Paris, France

ARTICLE INFO

Keywords:
Tumor spheroid
Microfluidics
Cage device

ABSTRACT

We developed a simple method to fabricate micro-cages and caged tumor spheroids for microfluidic chip-based assays. The micro-cage device consists of an array of honeycomb compartments with a monolayer of cross-linked and agarose-coated gelatin nanofibers at the bottom and a mesh of 200 μm hole-size on the top. U87-MG single cells were dispersed through the mesh and resulted tumor spheroids confined in each of the cage compartment after incubation. As expected, the tumor spheroids are one-by-one distributed in each of the compartment with the same size and they grew inside the compartments. The final size of the spheroid was limited by both diffusion and confinement. If the height of the cage is small, the nanofiber layer underneath tumors could be deflected due to mechanic stress of growing tumors. If the height of the cage is large, tumors grew freely without stress but their size was limited by diffusion. In both cases, tumors tended to remain in spherical shape. To illustrate the robustness of the approach, the tumor caged device was reversibly integrated into a microfluidic chip for drug test. Our results show that under tangent flow conditions, combretastatin A-4 had a clear effect on tumor disassembling.

1. Introduction

Despite decades of intensive research, cancer remains one of the worldwide leading causes of mortality and more important efforts are expected, including both *in-vivo* and *in-vitro* assays [1–5]. In this regard, robustly producing and handling of tumor spheroids using cancer cell lines, dissociated cancer cell and cutting tumor samples are necessary for detailed analysis. Previously, Hanging-Drop method [6,7] and Liquid-Overlay method [8–11] were widely used for spheroid formation. These methods are simple, but the resulted spheroids have to be transferred to another culture platform. Rotating bioreactor [12,13] and magnetic levitation [14,15] are also frequently used to increase the production yield but the fabricated spheroids generally lack the size uniformity. More recently, patterned micro-well arrays [16–18] were used to improve the uniformity of the tumor spheroids but the applications of these methods are limited since they are too simple to take into account the complexity of the tumor niche, which is a specific microenvironment where tumors are formed and regulated.

To overcome the above limitations, we developed a cage method which allows not only the formation of uniform tumor spheroids but also the integration of the fabricated spheroids into a microfluidic device for different assays. Our cage device is in the form of a patch with honeycomb frame sandwiched by a monolayer of agarose coated nanofibers and a mesh of relatively large openings. Both frame and mesh were defined by UV-lithography and soft-lithography and the nanofibers were produced by electrospinning, in a similar way of culture patch fabrication [19–21]. Single tumor cells could be dispersed through the mesh holes into each of the honeycomb compartments. Upon incubation, cells aggregated to form single spheroids in each of the compartments (Fig. 1). Since the size of the spheroids is generally larger than that of the mesh holes, they could be efficiently caged, allowing robust handling and manipulation. While both mesh and nanofiber monolayer are highly permeable and the patch can be quasi suspended in the culture medium, the spheroid growth conditions should be better than other culture platforms. We thus demonstrate the formation of uniform tumor spheroids and their integration into a microfluidic chip. Interestingly, we observed a significant deflection of the fiber layer due to mechanical forces of the growing spheroids. We also performed a preliminary drug test under both conventional and microfluidic culture conditions. Other types of stresses such as hypoxia could also be applied and the cage device could operate with other devices such as microfilters [22], therefore holding high potential of

* Corresponding author.
E-mail address: yong.chen@ens.fr (Y. Chen).

https://doi.org/10.1016/j.mee.2020.111256
Received 21 October 2019; Received in revised form 12 February 2020; Accepted 13 February 2020
Available online 14 February 2020

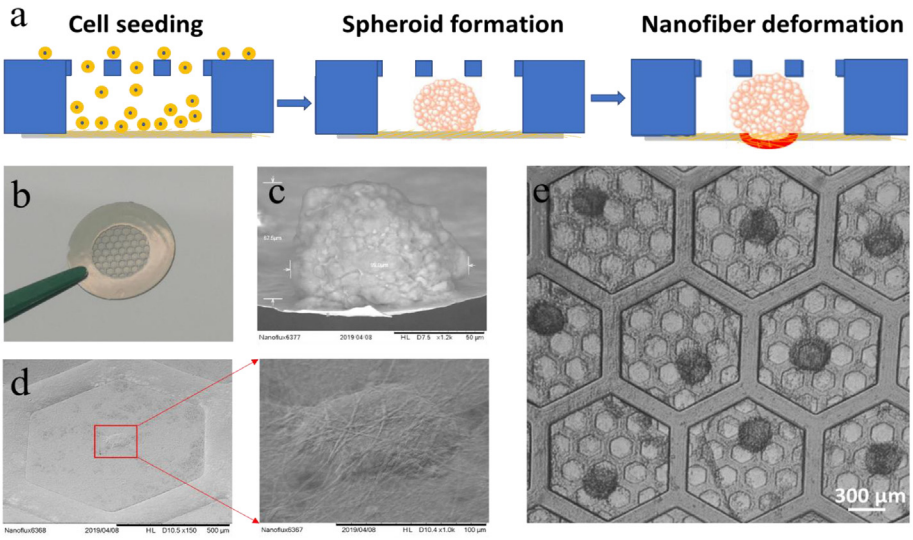

Fig. 1. (a) Schematic of a cage, caged tumor spheroid formation, and tumor growth induced deformation of the underneath nanofiber monolayer; (b) Photograph of a cage device; (c-d) Scanning electron microscopy image of a caged tumor spheroid and tumor growth induced deflection of the nanofiber monolayer; (e) Microphotograph of caged tumor spheroids in each of the honeycomb compartments.

this approach.

2. Materials and methods

2.1. Fabrication of micro-cage device

The cage device was fabricated by photolithography, soft-lithography and electrospinning. Firstly, a double layer SU-8 mold was fabricated by photolithography. The mesh layer was patterned on a silicon wafer using a 50 μm thick SU-8 negative photoresist (Fig. 2a). Then, the honeycomb frame of height in the range of 200 to 300 μm was directly patterned on the mesh layer (Fig. 2b). This double layer SU-8 mold was then exposed in trimethylchlorosilane (TMCS, Sigma, France) vapor during 10 min for anti-sticking surface treatment. Afterward, a mixture of PDMS (GE RTV 615) pre-polymer and its cross-linker at ratio of 10:1 was casted on the SU-8 mold (Fig. 2c). After curing at 75 °C for 2 h, the PDMS layer was peeled off and treated with TMCS anti-sticking agent. Secondly, the replicated PDMS structure was placed on a glass plate and a solution of polyethylene glycol diacrylate (PEGDA Mw = 250, Sigma) mixed with 1 *v*/v% Irgacure 2959 (Ciba Specialty Chemicals, France) was injected in the free space of the PDMS-glass assembly, followed by UV exposure for 2 min (Fig. 2d and e). Thirdly, a monolayer of gelatin nanofibers was electrospun and cross-linked on the opposite side of the mesh. This has been done by using a similar fabrication protocol of our previous work [19,21]. Briefly, the electrospinning was performed with a gelatin solution of 10 wt% gelatin powder (G2625, Sigma) in DI water, ethyl acetate, and acetic acid at a volume ratio of 10: 14: 21. The ejection of the gelatin solution through a needle (23-gauge) to the collector (cage) was controlled with at a speed of 0.2 ml/h, a distance of 10 cm and bias voltage was 11 kV, respectively (Fig. 2f). The sample was then dried overnight in a desiccator and the gelatin nanofibers was soaked in an ethanol solution containing 2 M N-hydroxysuccinimide (NHS, Sigma) and 0.2 M 1ethyl-3-(3-dimethylaminopropyl)carbodiimide hydrochloride(EDC, Sigma) for 4 h. The sample was then washed three times in ethanol and dried in a vacuum overnight. Finally, the nanofiber layer was treated with a solution of agarose (Fisher Scientific, France) 0.2 *w*/*v*% in DI water and the cage device was dehydrated in oven at 60 °C for 2 h.

2.2. Cell culture

U87-MG cells (human glioblastoma cells) were grown in T75-flask

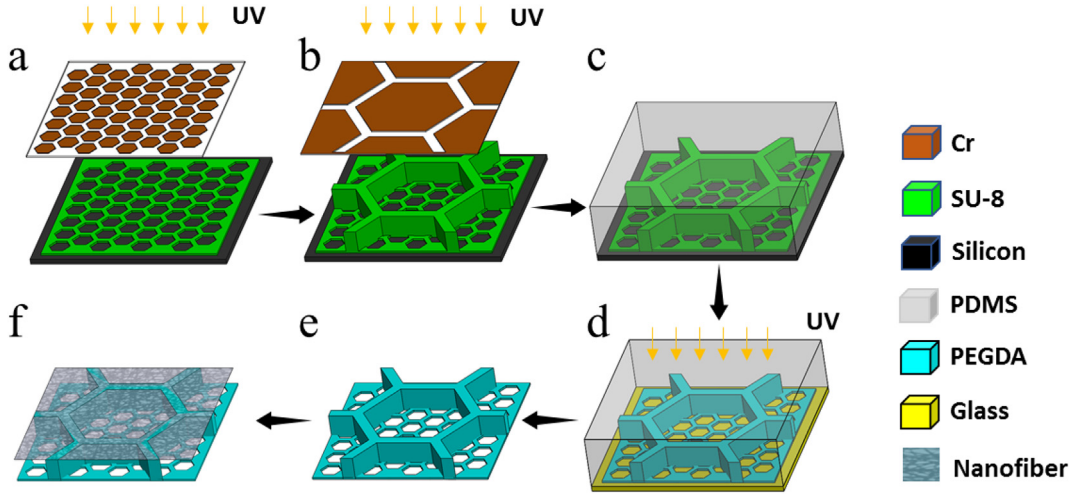

Fig. 2. Schematic diagram of the fabrication process of the cage device: (a) Cage layer patterning of the mold by UV lithography and SU8 resist on a silicon wafer; (b) Microframe patterning of the mold by UV lithography and another SU8 resist layer; (c) Replication of the mold pattern into PDMS by soft lithography; (d) Secondary replica of the mold patterning by micro-aspiration assisted UV curing of PEGDA; (e) Microframe with mesh structures released from glass substrate; (f) Electrospinning, crosslinking and agarose coating of the gelatin nanofiber layer.

inside an incubator of 37 °C and 5% CO_2. The culture medium was Dulbecco's Modified Eagle Medium (DMEM) supplemented with 10% fetal bovine serum and 1% penicillin-streptomycin. The cells were passaged using TrypLE express enzyme when they reached 80–90% confluency. The cells were resuspended in complete DMEM medium and dispersed at density 1.5×10^5 cells per device in the cage through the mesh. Then, the device was placed in the culture dish for incubation under conventional culture conditions for up to 10 days and the medium was exchanged each two days. Prior to cell seeding, the cage devices were sterilized in 70% ethanol with exposure to UV during 30 min and equilibrated in complete culture medium for 1 h.

2.3. SEM observation

Caged tumor spheroids were fixed in PBS containing 4% formaldehyde for 15 min. Then, they were rinsed twice with PBS buffer, and merged in 30% ethanol (in DI water) for 30 min. Afterward, the samples were dehydrated in a graded series of ethanol solutions with concentrations of 50%, 70%, 80%, 90%, 95%, and 100%, respectively, and in each for 10 min. Before observation, a 2 nm thick gold layer was deposited on the samples by sputtering. The images were captured with a SEM machine (Hitachi TM3030) operated at 15 kV.

2.4. Microfluidic culture

After incubation for 3 days, the device with caged tumor spheroids was reversibly integrated into a microfluidic chip (MesoBioTech, France) and a tangent flow was applied at a flow rate of 0.1 ml/h in the mesh side using a syringe pump. After incubation for another 3 days, the chip was dismounted and the cage device was placed in a 35 mm dish with complete culture medium for further observation.

2.5. Drug test and live/dead assay

The cage device with tumor spheroids was placed in another culture medium containing 1 μM anti-cancer drug Combretastatin A4 (CA4) [23]. After incubation for 24 h, disassembling of the tumor spheroids were observed and live/dead assay was performed with PBS containing 4 μM Calcein AM (Invitrogen, L3224) and 5 μM propidium iodide (Sigma-Aldrich, P4170) solution, respectively. After incubation for 30 min, the cage device was rinsed twice with fresh PBS to remove any residual staining molecules and kept in PBS for observation. Finally, fluorescence images were recorded with an inverted fluorescence microscope (Axio Observer Z1, Zeiss).

3. Results and discussion

3.1. Cage device

The fabrication process of the cage device is straightforward by using different lithography methods, including UV lithography, soft lithography and micro-aspiration assisted lithography. To study the tumor growth in different size of space, different height 200 (H200), 250 (H250), 300 (H300) μm of cage devices were fabricated as shown in Fig. 3a-3c. Fig. 3d and e shows respectively the top-view of a microframe with honeycomb compartments with 200 μm mesh size and a 1.2 μm thick agarose layer with gelatin nanofibers backbone on another side of the frame. Thus, single cells could be introduced on the agarose layer through the mesh and then gave rise to the formation of caged tumor spheroids.

3.2. Caged tumor spheroids

Fig. 4a shows the tumor spheroids in the cages of different height at day 1, 4, 5, 6. Cell aggregation and spheroid formation could be observed at day 2. At day 6 after cell seeding, caged spheroids were fixed and dehydrated for SEM observation. Despite the decreased spheroid volume after dehydration, remarkably, we observed an important nanofiber deflection underneath of the tumor spheroids as shown in Fig. 1c and d. Considering the fact that the final tumor size (about 220 μm) is comparable to the height of the cage (200 μm), the tumor spheroids trended to keep their spheroid shape by deflecting the nanofiber layer without flattening. In addition, uniform formation of tumor spheroid in each large honeycomb can be seen in Fig. 1e.

Fig. 4b shows clearly that the tumor size increased until day 4 and started to decrease at day 5. This is probably due to the change from single cells to cell aggregations and the strong effect of cell-cell interaction. It is also interestingly to note that the tumor size increased when they were in a larger height of cage device. However, the final size always remained stable in all three heights of cage devices, due probably to the limitation of device height because spheroid size in H200 and H250 cage devices both exceeded the cage height. Besides, there could be not enough nutrition diffusion in center area of the spheroids, preventing cell proliferation. The above experiments have been repeated for five times, showing the same results.

3.3. Microfluidic integration

The tumor spheroids formed in the cage were stable and could be easily handled and subjected to different stimuli. The cage device was taken out from the dish at day 3 and was integrated into a microfluidic culture device, for another 3 days diffusive culture, as shown in Fig. 5a and b. The culture medium flowed in the space outside the cage and passed by the honeycomb mesh side at a flow rate of 0.1 ml/h. Fig. 4c shows dead/live image of tumor spheroid cultured in a cage device under cis-flow or diffusive culture conditions, showing the feasibility of culturing them under flow conditions. Clearly, the tumor spheroid could be maintained with few dead cells, and large variety of perturbation can thus be applied.

3.4. Anti-cancer drug effects

In order to investigate the drug effect on the spheroids formed in cage devices, combretastatin A4 (CA4) was used for anti-cancer study at day 6. This drug binds much better to the colchicine site on tubulin to inhibit polymerization and further prevent cell division, thus it is highly cytotoxic to a variety of human cancer cells. As expected, the caged spheroids taken out from a culture dish at day 6 were then immersed for 2 days in 1 μM CA4 supplemented culture medium and showed a clear disassembling effect, as shown in Fig. 6. The live/dead images showed that there were more dead cells in center area of smaller spheroids, while less in larger spheroids, also due to the drug permeability to the center core, especially in larger height of cage devices. Therefore, these images clearly demonstrated the drug resistance of larger spheroids and strong cancer cell-cell interaction.

Finally, we would like to mention that the deflection of the fiber layer due to the growing tumor spheroid might be used to study the mechanical properties of the tumor. Previously, Stylianopoulos et al. have addressed this issue and found that evolution of stress and growth rate both depend strongly on the mechanical interactions with the surrounding host tissue [24,25]. They suggested that the solid stress on tumor growth involved not only the inhibitory effect of stress on cancer cell proliferation and the induction of apoptosis, but also the resistance of the surrounding tissue to tumor expansion. By studying the mechanic interaction of stem cell colonies with a 3D patterned elastomeric substrate, a contractile force of the order of 1 mN was deduced. In the present case, the solid stress causing the deflection of the fiber layer can be estimated by considering an edge-clamped thin disk. Based on the theory of plates and shells [26], the pressure Δp on the disk is given by

$$\Delta p = \frac{16Eh^3}{3(1-\nu^2)R^4}\left(\delta + 0.488\frac{\delta^3}{h^2}\right)$$

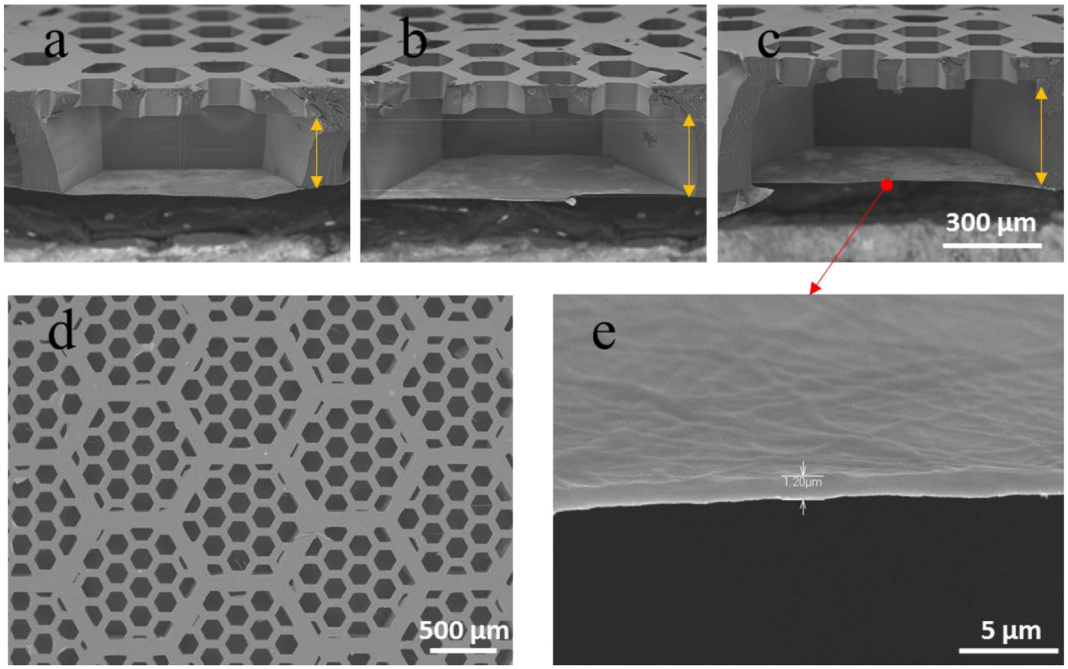

Fig. 3. Scanning electron microscopy images of the fabricated cages: Sideview of the cages with height 200 μm (a, H200), 250 μm (b, H250) and 300 μm (c, H300), respectively; (d) Top-view of the mesh of hole-size 200 μm (d) and agarose coating nanofibers (e).

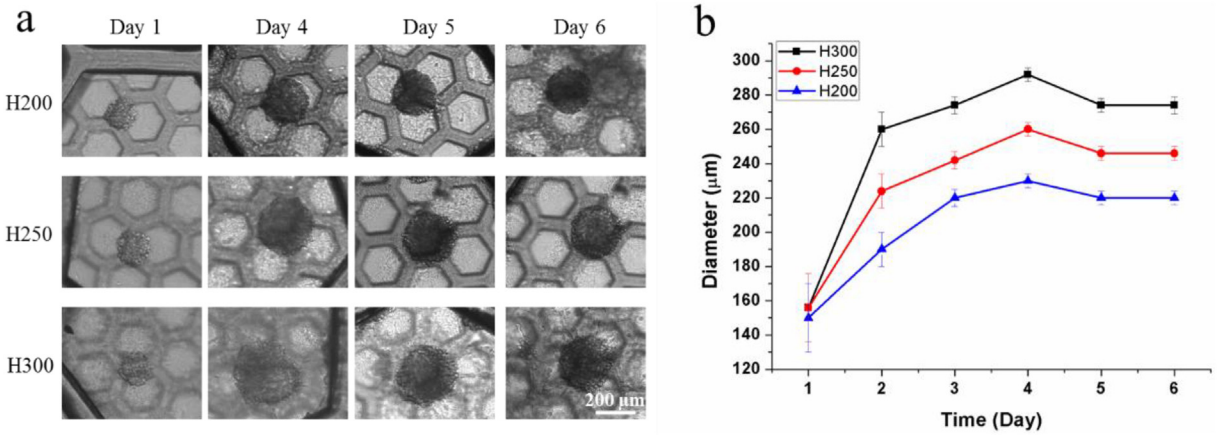

Fig. 4. Cage height and incubation time dependences of the caged tumor spheroids: (a) Microphotograph of tumor spheroids in H200, H250 and H300 cages at day 1, 4, 5, 6; (b) Size variation of the spheroids in different cages up to 6 days.

where h and R and the thickness and radius of the disk, E and v are the Young's module and Poisson ratio of disk material, δ is the deflection of the disk center point. Assuming a disk of 0.1 μm thickness and 50 μm radius with a Young module of 10 MPa and a Poison ratio $<$ 0.3, a pressure of ~3.4 kPa is obtained, which is in the range of previous findings [25]. More detailed analyses are needed for quantitative assessments.

4. Conclusions

We have developed a fabricated method to produce caged tumor spheroids. This cage device is robust and easy to use. Uniform tumor spheroids could be generated in the cages by single cell seeding and static culture. If the height of the cage is too small, the underneath fibers were deflected due to mechanical stress of the growing tumors. If the height of the case is too large, tumors grew freely and their size was limited by diffusion. The caged tumor spheroids were also integrated in a microfluidic chip and they could be cultivated under tangent flow conditions but dissembled after drug introduction. More systematic studies will be carried out by considering other types of stress such as hypoxia, ischemia, compression, *etc.* and isolation of the released cells [22], thereby faciliating *in-vitro* cancer modeling.

Credit author statement

Y.H. and B.X. performed the device preparation and cell culture experiments, L.W. and J.S. manufactured the plastic device and microfluidic accessories, E.R., J.H., Y.L, G.P. and C.A. aided in device making and cell culturing, Y.C. were involved in planning and supervision of the work. All authors discussed the results and commented on the manuscript.

Declaration of Competing Interest

None.

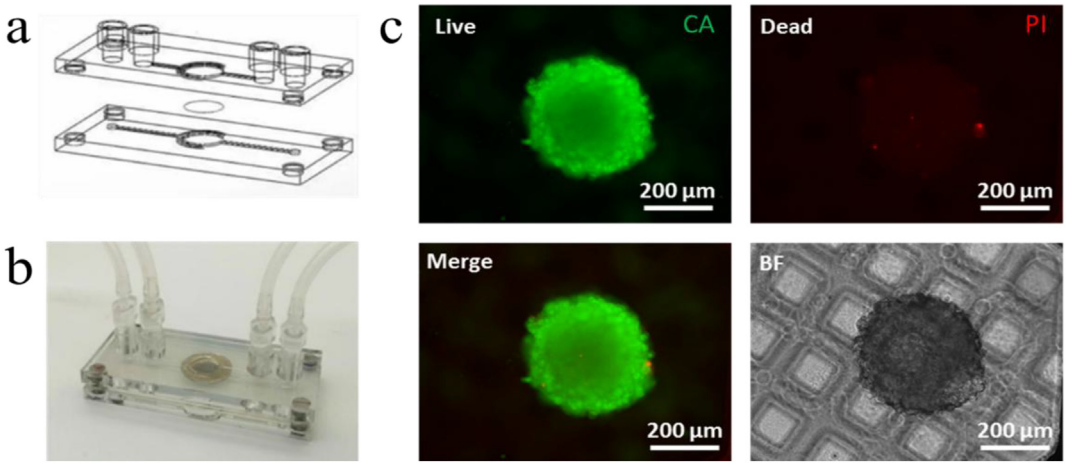

Fig. 5. Schematic (a) and photograph (b) of a microfluidic chip for the cage device integration; (c) Live/dead fluorescence images of tumor spheroids after incubation for 3 days in a H200 cage device.

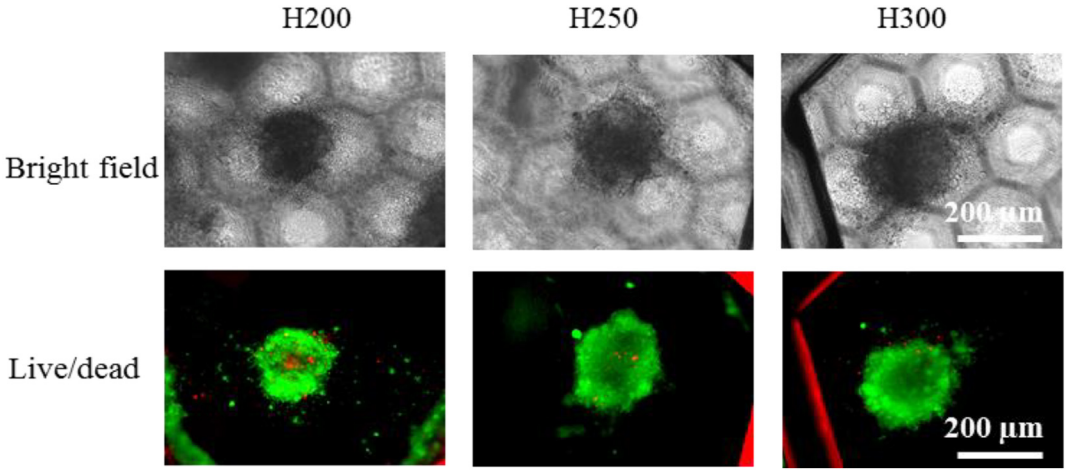

Fig. 6. Bright field and live/dead fluorescence images of tumor spheroids confined in H200, H250 and H300 cages after days in CA4 supplemented medium (day 6-day 8).

Acknowledgements

This work was supported by Agence de Recherche Nationale under contract ANR-17-CE09-0017 (AlveolusMimics), European Commission Cost Action BIONECA (CA 16122), DIM ELICIT program of Ile-de-France, and PSL Valorization through Pre-maturation project. Yong He is grateful to the China Scholarship Council for grant of his PhD studies.

References

[1] F. Bray, J. Ferlay, I. Soerjomataram, R.L. Siegel, L.A. Torre, A. Jemal, Global cancer statistics 2018: GLOBOCAN estimates of incidence and mortality worldwide for 36 cancers in 185 countries, CA Cancer J. Clin. 68 (6) (2018) 394–424.

[2] G.B.O.D.C. Collaboration, Global, regional, and national cancer incidence, mortality, years of life lost, years lived with disability, and disability-adjusted life-years for 29 cancer groups, 1990 to 2016: a systematic analysis for the global burden of disease study, JAMA Oncology 4 (11) (2018) 1553–1568.

[3] T. Rodrigues, B. Kundu, J. Silva-Correia, S.C. Kundu, J.M. Oliveira, R.L. Reis, V.M. Correlo, Emerging tumor spheroids technologies for 3D in vitro cancer modeling, Pharmacology therapeutics 184 (2018) 201–211.

[4] M.E. Katt, A.L. Placone, A.D. Wong, Z.S. Xu, P.C. Searson, In vitro tumor models: advantages, disadvantages, variables, and selecting the right platform, Front. Bioeng. Biotechnol. 4 (2016) 12.

[5] E.C. Costa, A.F. Moreira, D. de Melo-Diogo, V.M. Gaspar, M.P. Carvalho, I.J. Correia, 3D tumor spheroids: an overview on the tools and techniques used for their analysis, Biotechnol. Adv. 34 (8) (2016) 1427–1441.

[6] Y.-C. Tung, A.Y. Hsiao, S.G. Allen, Y.-s. Torisawa, M. Ho, S. Takayama, High-throughput 3D spheroid culture and drug testing using a 384 hanging drop array, Analyst 136 (3) (2011) 473–478.

[7] R. Foty, A simple hanging drop cell culture protocol for generation of 3D spheroids, JoVE (51) (2011) e2720.

[8] T.-M. Achilli, J. Meyer, J.R. Morgan, Advances in the formation, use and understanding of multi-cellular spheroids, Expert. Opin. Biol. Ther. 12 (10) (2012) 1347–1360.

[9] D. Loessner, K.S. Stok, M.P. Lutolf, D.W. Hutmacher, J.A. Clements, S.C. Rizzi, Bioengineered 3D platform to explore cell–ECM interactions and drug resistance of epithelial ovarian cancer cells, Biomaterials 31 (32) (2010) 8494–8506.

[10] F. Ozawa, K. Ino, T. Arai, J. Ramón-Azcón, Y. Takahashi, H. Shiku, T. Matsue, Alginate gel microwell arrays using electrodeposition for three-dimensional cell culture, Lab Chip 13 (15) (2013) 3128–3135.

[11] Y.-s. Torisawa, A. Takagi, Y. Nashimoto, T. Yasukawa, H. Shiku, T. Matsue, A multicellular spheroid array to realize spheroid formation, culture, and viability assay on a chip, Biomaterials 28 (3) (2007) 559–566.

[12] I. Martin, D. Wendt, M. Heberer, The role of bioreactors in tissue engineering, Trends Biotechnol. 22 (2) (2004) 80–86.

[13] R.Z. Lin, H.Y. Chang, Recent advances in three-dimensional multicellular spheroid culture for biomedical research, Biotechnol. J.: Healthcare Nutr. Technol. 3 (9–10) (2008) 1172–1184.

[14] G.R. Souza, J.R. Molina, R.M. Raphael, M.G. Ozawa, D.J. Stark, C.S. Levin, L.F. Bronk, J.S. Ananta, J. Mandelin, M.-M. Georgescu, Three-dimensional tissue culture based on magnetic cell levitation, Nat. Nanotechnol. 5 (4) (2010) 291.

[15] W.L. Haisler, D.M. Timm, J.A. Gage, H. Tseng, T. Killian, G.R. Souza, Three-dimensional cell culturing by magnetic levitation, Nat. Protoc. 8 (10) (2013) 1940.

[16] J.M. Karp, J. Yeh, G. Eng, J. Fukuda, J. Blumling, K.-Y. Suh, J. Cheng, A. Mahdavi, J. Borenstein, R. Langer, Controlling size, shape and homogeneity of embryoid bodies using poly (ethylene glycol) microwells, Lab Chip 7 (6) (2007) 786–794.

[17] Y. Tang, J. Liu, Y. Chen, Agarose multi-wells for tumour spheroid formation and anti-cancer drug test, Microelectron. Eng. 158 (2016) 41–45.

[18] F. Mirab, Y.J. Kang, S. Majd, Preparation and characterization of size-controlled glioma spheroids using agarose hydrogel microwells, PLoS One 14 (1) (2019) e0211078.

[19] Y. Tang, L. Liu, J. Li, L. Yu, L. Wang, J. Shi, Y. Chen, Induction and differentiation of human induced pluripotent stem cells into functional cardiomyocytes on a compartmented monolayer of gelatin nanofibers, Nanoscale 8 (30) (2016) 14530–14540.
[20] Y. Tang, F.P.U. Severino, F. Iseppon, V. Torre, Y. Chen, Patch method for culture of primary hippocampal neurons, Microelectron. Eng. 175 (2017) 61–66.
[21] Y. Tang, L. Liu, J. Li, L. Yu, F.P.U. Severino, L. Wang, J. Shi, X. Tu, V. Torre, Y. Chen, Effective motor neuron differentiation of hiPSCs on a patch made of crosslinked monolayer gelatin nanofibers, J. Mater. Chem. B 4 (19) (2016) 3305–3312.
[22] Y. Tang, J. Shi, S. Li, L. Wang, Y.E. Cayre, Y. Chen, Microfluidic device with integrated microfilter of conical-shaped holes for high efficiency and high purity capture of circulating tumor cells, Sci. Rep. 4 (2014) 6052.
[23] G.C. Tron, T. Pirali, G. Sorba, F. Pagliai, S. Busacca, A.A. Genazzani, Medicinal chemistry of combretastatin A4: present and future directions, J. Med. Chem. 49 (11) (2006) 3033–3044.
[24] C. Voutouri, F. Mpekris, P. Papageorgis, A.D. Odysseos, T. Stylianopoulos, Role of constitutive behavior and tumor-host mechanical interactions in the state of stress and growth of solid tumors, PloS one, Front. Oncol. 9 (8) (2014) e104717.
[25] M. Kalli, T. Stylianopoulos, Defining the role of solid stress and matrix stiffness in cancer cell proliferation and metastasis, Front. Oncol. 8 (2018) 55.
[26] S.P. Timoshenko, S. Woinowsky-Krieger, Theory of plates and shells, McGraw-hill1959.

Appendix B
Fabrication of ultrathin artificial basement membrane

Microelectronic Engineering 232 (2020) 111407

Contents lists available at ScienceDirect

Microelectronic Engineering

journal homepage: www.elsevier.com/locate/mee

Research paper

Fabrication of ultrathin artificial basement membrane for epithelial cell culture

Elrade Rofaani[a,b], Juan Peng[a], Li Wang[c], Yong He[a], Boxin Huang[a], Yong Chen[a,*]

[a] PASTEUR, Département de chimie, École normale supérieure, PSL University, Sorbonne Université, CNRS, 75005 Paris, France
[b] The Agency for Assessment and Application of Technology, 10340 Jakarta, Indonesia
[c] MesoBioTech, 231 Rue Saint-Honoré, 75001 Paris, France

ARTICLE INFO

Keywords:
Basement membrane
monolayer nanofibers
epithelial culture

ABSTRACT

Basement membranes are essential for epithelial and endothelial tissue organization. To mimic them, we developed a fabrication method to produce ultrathin membrane of collagen IV and laminin. A honeycomb microframe of thickness 50 μm and compartment-size 400 μm was firstly patterned in polyethylene glycol diacrylate (PEGDA) by using lithography and vacuum assisted UV curing techniques. Then, a monolayer of gelatin nanofibers was electrospun and crosslinked on the microframe to form a secondary structure, a fiber mesh with much smaller pore sizes, in each of the honeycomb compartments. Finally, a collagen IV-laminin gel layer was deposited and dehydrated, leading to the formation of ultrathin membrane over a large area with a nanofiber backbone. Such an artificial basement membrane is mechanically stable and fully bio-compatible. It is also semi-permeable which can slow down considerably the diffusion of large size molecules. More importantly, it can be used to improve the monolayer formation of epithelial cells. Thus, this culture device recapitulates the biological basement membrane, permits the epithelial tissue formation, and allows mimicking a sophisticated cellular microenvironment.

1. Introduction

Basement membranes (BMs) are sheet-like extracellular matrix (ECM) on which epithelial or endothelial cells stay and organize [1–7]. These sheet-like structures are generally made of collagen IV, laminin, nidogen, and heparan sulfate proteoglycans with a thickness less than 100 nm. While collagen IV and laminin form two independent polymeric networks, other BM proteins make them associated and stable. BMs promote the formation of epithelial and endothelial layers via specific cell adhesion molecules and sulfated glycolipids, which are a priori organ and tissue dependent but share the common ground of being ultrathin and filtration barrier with selective molecular permeability. Although the importance of BMs has long been recognized, only a limited number of investigations have been reported to mimic such a structure [8–10]. Hozumi et al. conjugated laminin-derived peptide to chitosan matrices to mimic the basement membrane but the produced peptide-chitosan was only used for surface treatment of the culture plates [8]. Rossi et al. used electrospinning technique to produce polyester meshes with specific peptide sequences, which allowed co-culture of skin cells [9]. Similarly, Nishiguchi et al. used a mixture of polyester and polyethylene glycols to produce electrospun nanofibers for a bipolar cultured alveolar-capillary barrier model [10]. More generally, natural ECM proteins and synthetic polymers could be used to produce 2D and 3D matrices for cell culture studies but most of the proposed structures did not take into account the sheet-like morphology of nature BMs [11–13]. In particular, the plastic or elastomer membranes widely used are inherently inappropriate for BM mimicking since they are with large through holes, not thin enough, and cannot be homogeneous for the supported cell layers [14–17]. In this regard, a sheet-like scaffold made of continuous collagen IV-laminin ultrathin film is highly desired for most of the BM functions.

Here, we report on a fabrication strategy to achieve such an artificial basement membrane (ABM). We firstly patterned a polymer honeycomb frame of 50 μm thickness and 400 μm hole-sizes and then electrospun on it a monolayer of gelatin nanofibers with pores of much smaller sizes [18,19]. After crosslinking and different from our previous studies, a solution of collagen IV and laminin mixture was pipetted on the frame-nanofiber assembly. After dehydration, a stable collagen IV-laminin membrane of thickness in the order of 100 nm could be obtained with a porous fiber backbone. The formation of such ultrathin membranes of large surface should be difficult, and we believe that this hierarchical structure is relevant and applicable to BM related studies.

* Corresponding author.
E-mail address: yong.chen@ens.psl.eu (Y. Chen).

https://doi.org/10.1016/j.mee.2020.111407
Received 3 July 2020; Received in revised form 24 July 2020; Accepted 26 July 2020
Available online 29 July 2020

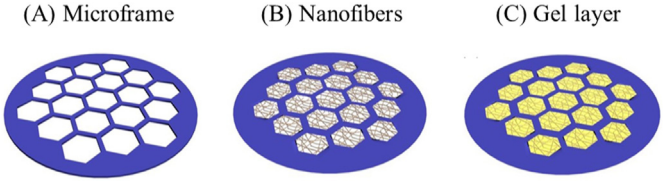

Fig. 1. Schematic of the fabrication steps of ultrathin artificial basement membrane (ABM): (A) Patterning of honeycomb microframe, (B) Electrospinning of monolayer of nanofibers, (C) Deposition of ultrathin film of collagen IV-laminin.

For simplicity, only two major components, i.e., collagen IV and laminin, were used, without taking into account the composition of specific tissue or organ. We will describe the fabrication detail and show the preliminary characterization results of the proposed ABMs, which clearly demonstrated the advantage of using ABMs for the monolayer formation of epithelial cells.

2. Materials and methods

2.1. Fabrication of ABMs

We followed the same fabrication process of our previous work to obtain a patch form of culture device made of honeycomb microframe and monolayer of gelatin nanofibers [18,19]. In addition, we deposited a gel solution of collagen IV and laminin mixture on the frame-fiber system, which became ultrathin membrane after dehydration (Fig. 1). Briefly, a honeycomb structure of 400-μm hole size, 50-μm linewidth and 50-μm thickness was defined in a SU-8 photoresist (Microchem, France) by photolithography. This pattern was sequentially replicated into polydimethylsiloxane (PDMS, Eleco-EFD, France) by casting and then from PDMS to polyethylene glycol diacrylate (PEGDA) by vacuum assisted UV-curing. Afterwards, the frame replica was coated by 10 nm Au and gelatin nanofibers were electrospun. Here, 10 wt% gelatin (#61890, Sigma-Aldrich, France) was dissolved in a mixed solution of acetic acid, ethyl acetate (#270989, Sigma-Aldrich, France) and DI water at a volume ratio of 21:14:10. The nanofibers were deposited at distance 10 cm and voltage 11 kV for 3 and 5 min, controlled with a high voltage supply (Heinzinger, Germany), a syringe-pump (#78-9100B, Kd Scientific, USA) at a feeding rate of 0.2 mL/h. After electrospinning, gelatin nanofibers were dried in a desiccator overnight and cross-linked in a 0.2 M mixture of 1-ethyl-3-(3-dimethylaminopropyl) carbodiimide hydrochloride (EDC) (#6383, Sigma-Aldrich, France) and N-hydroxysuccinimide (NHS) (#130672, Sigma-Aldrich, France) in ethanol for 4 h. After crosslinking, samples were rinsed with 99.5% ethanol three times and dried in vacuum overnight to remove the remaining chemicals.

The above fabricated frame-nanofiber system was used as support for the final deposition of ABM materials. A 50 μL solution composed of 0.05% or 0.1% (*w/v*) collagen IV (#C7521, Sigma-Aldrich, France) in water containing 0.1 M acetic acid and 2% (*v/v*) laminin (#L2020, Sigma-Aldrich, France) was pipetted on the frame-nanofiber system. After dehydration at 37 °C for 3–5 h, a continuous film of collagen IV-laminin mixture could be obtained and its morphology analysis was performed with a tabletop scanning electron microscopy (SEM, TM-3030, Hitachi, Japan).

2.2. Permeability test

Molecular diffusion across an ABM was studied using 70 kDa Rhodamine B isothiocyanate-dextran (RITC) (#R9379, Sigma-Aldrich, France) at a concentration of 250 μg/mL in a mixture of 50% Minimum Essential Medium (MEM) (#10370–021, Gibco, France) and 50% Dulbecco's Phosphate Buffer Saline (DPBS) (#14190–094, Gibco, France). For comparison, measurements were performed with a patch without gel layer deposition and a Geltrex (#1413202, Gibco, France) coated patch. They were all mounted in a homemade transwell support (Boyden chamber) and placed in a 6 well plate (#734–2323, VWR, France). 0.5 mL buffer with RITC and 2.0 mL buffer without RITC were injected separated in the apical and basal sides of the chamber. After diffusion for 24 h, 300 μL solution were taken from the basal side of each well. 100 μL of the solution was placed in a 96 well plate (#353072, Falcon-Corning, USA) in triplicate and the fluorescence intensity of the samples was measured at λ_{exc}: 530/25 nm and λ_{ems}: 645/40 nm using fluorescence plate reader (Synergy HT, BioTek with Gen™ software). Then, the percentage of diffused molecules was deduced by

$$Diffusion\ (\%) = \frac{IV_{apical}}{I_0 V_{basal}} \times 100\% \quad (1)$$

where I_0 (I) and V_{apical} (V_{basal}) are the fluorescence intensity (arbitrary unit) and the volume of the initial (final) solution in apical (basal) side of the membrane.

2.3. Cell seeding and culture

Before cell seeding, ABMs were sterilized in ethanol for 15 min then washed in DPBS, dried under ultraviolet light for 30 min. Alveolar epithelial type II A549 cells (#86012804, Sigma-Aldrich, France) were cultured in DMEM/F-12 with glutamax supplement (#10565018, Gibco, France) containing 10% fetal bovine serum (#16000044, FBS, Gibco, France) and 1% penicillin/streptomycin (#15140122, Gibco, France) at 37 °C with 5% CO_2. The Boyden chamber inserted with patch was used as air–liquid interface cell culture model and placed in 6 well plate. Firstly, cells were seeded in the top compartment of Boyden chamber at a density of 2×10^5 cells per patch and incubated for 3 days. Then, the culture medium was replaced by a base medium of DMEM/F-12 with glutamax supplement containing 4% FBS, 1% penicillin/streptomycin, and 250 nM dexamethasone (#D4902, Sigma-Aldrich, France). After one day culture, the medium in the top compartment was removed, leaving the apical surface of the cells exposed to air (in an atmosphere of 5% CO_2 at 37 °C). Afterwards, the culture was continued and the medium in the low compartment was changed every two days for up to 17 days. Here, the culture medium with a lower FBS concentration and 250 nM dexamethasone was used for long-term culture.

2.4. Immunostaining observation

Cells were rinsed with DPBS and fixed with 4% paraformaldehyde (#P6148, Sigma-Aldrich, France) for 15 min. Samples were permeabilized with 0.5% Triton X-100 (#HFH10, Thermofisher, France) for 10 min and saturated with DPBS supplemented with 0.1% Triton X-100 and 3% BSA (#A9056, Sigma-Aldrich, France) for 2 h at room temperature. Afterwards, staining was performed with primary antibodies for overnight at 4 °C, which followed by incubation with fluorescent second antibodies for 2 h. The primary antibody Alexa fluor 488-conjugated anti-collagen IV (#53–9871-82, Invitrogen, France) and anti-laminin (#PA1–16730, Invitrogen, France) were used for staining ABM, while unconjugated antibody ZO-1 (#40–2200, Invitrogen, France) and E-cadherin (#14–3249-80, Invitrogen, France) were followed by the secondary antibody Alexa Fluor 488 and 647 (#A-11008 and #A-31573, Invitrogen, France) were used for staining of A549 cells. Finally, nucleus was stained with DAPI (#62247, Invitrogen, France) for 30 min at room temperature. Samples were observed with a confocal microscope (LSM 710, Zeiss, France). Images were collected as TIF files and analyzed with software ImageJ.

3. Results and discussion

In general, an ultrathin membrane with uniform biochemical properties is physiologically more relevant than thicker membranes

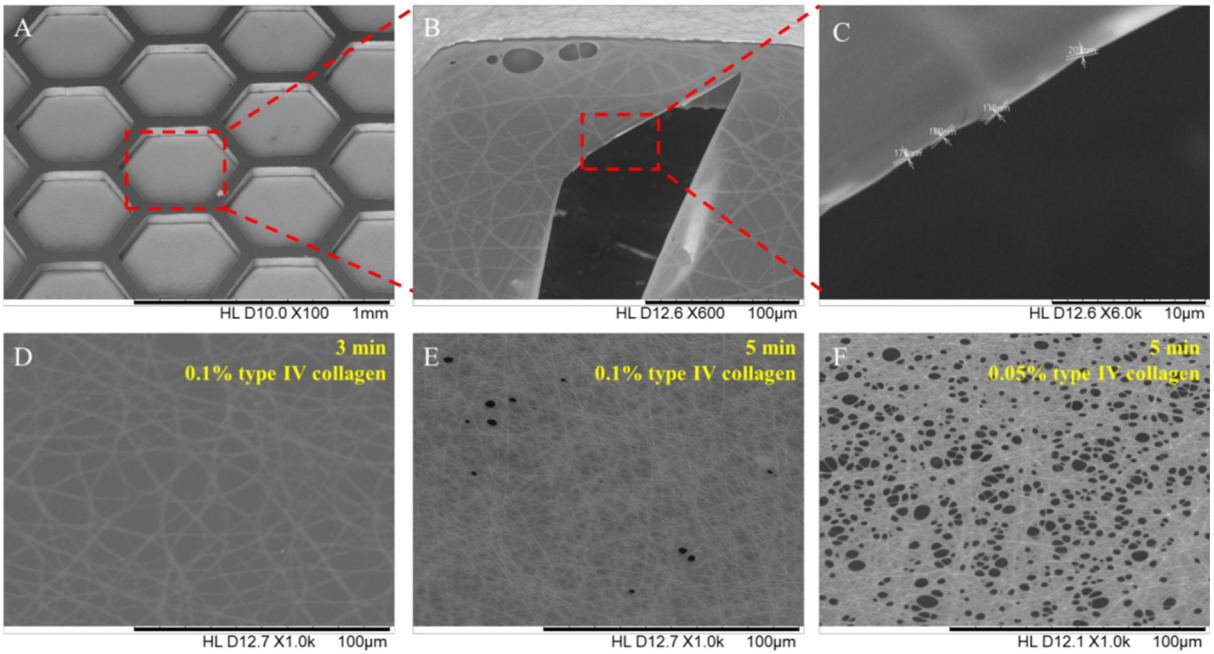

Fig. 2. Scanning electron microscope images of the fabricated devices. (A) Overview showing a homogenous gel layer (membrane of collagen IV-laminin) supported by a mesh of monolayer nanofibers (backbone) and honeycomb microframe. (B, C) Detailed view of the sample showing the fibers and the membrane. (D, E) Comparison of two samples obtained by 3 and 5 min nanofiber electrospinning and deposition-dehydration of a gel with 0.1% collagen IV-laminin. (F) Sample obtained by 5 min electrospinning and deposition-dehydration of a gel of 0.05% concentration. The red dot squares indicate the zoom areas. Scale bar was shown under each image. (For interpretation of the references to colour in this figure legend, the reader is referred to the web version of this article.)

with through holes for epithelial and endothelial cell culture. However, it is hardly conceivable to produce a bio-membrane of thickness in the order of 100 nm over a large area (a few mm^2). To overcome this difficulty, we adopted a hierarchic device design by embedding a nanofiber backbone inside the membrane and using a honeycomb microframe as carrier of an ultrathin membrane. We firstly created a large pore-sized PEGDA microframe. Then, we deposited on it a monolayer of crosslinked gelatin nanofibers with a high porosity. Typically, the fiber diameter is in the range of 100 to 500 nm [18], the pore size is in the order of a few μm, and the contact angle of the fiber layer is about 45°. With such a mesh structure, thin gel layers of collagen IV-laminin can be easily formed in the porous areas of the fibers. After dehydration, the thickness of the gel layer became smaller and the fiber-gel assembly was self-organized, giving rise to an ultrathin membrane with a fiber mesh backbone. Since this membrane is made of BM specific proteins, it is naturally bio-compatible. As expected, the fabricated membrane is mechanically stable and easy to use. Also, the developed fabrication method is straightforward and applicable to large scale manufacturing.

Fig. 2 shows scanning electron microscope (SEM) images of fabricated membranes. As expected, the monolayer of nanofibers looked like a backbone to support the ultrathin membrane in the open areas of PEGDA microframe (Fig. 2A). From these SEM images, the pore sizes of the fibers can be determined. Statistically, the area of the pores varied in the range of 5 to 50 (10) μm^2 for the fibers produced by 3 (5) min electrospinning, corresponding a porosity of 62% (50%) respectively. With a gel of 0.1% collagen IV-laminin, the thickness of membrane after dehydration can be as small as 166.5 ± 35.5 nm (Fig. 2C, n = 3). Note that with the same gel concentration, such an ultrathin membrane can be more easily broken in large pores obtained by 3 min electrospinning (Fig. 2B). Decreasing the pore size by, for example, 5 min electrospinning resulted in a more stable membrane. Similarly, a smaller gel concentration (from 0.1% to 0.05%) did not allow the formation of a continuous thin membrane (Fig. 2F). Clearly, the thickness of the membrane is gel concentration dependent and 0.1% gel concentration results in the most successful ABM for 5 min electrospun nanofibers.

To elucidate the tradeoff between the pore size and the membrane thickness, we consider a gel layer embedded in a pore of radius R and thickness h. The surface energy of the gel layer $E_s = 2\gamma\pi R2$, the contact energy of the gel anchoring the mesh $E_a = 2\gamma' \pi hR$, where γ and γ′ are respectively the energy density of air-gel and gel-solid. For the formation of a stable gel layer, $E_s < E_a$, i.e., $R < \left(\frac{\gamma'}{\gamma}\right)h$. This means that the pore size has to be limited in order to have a small membrane thickness.

To evaluate the quality of the deposition of the collagen and laminin, immunofluorescence images were taken after anti-collagen (green) and anti-laminin (red) staining (Fig. 3). As expected, on the contrary to the patch without gel deposition, the fabricated ABMs showed both homogenous green and red fluorescence over the whole active areas, indicating excellent coverage of the collagen IV and laminin in the pore areas.

The fabricated ABMs have also been used for permeability test. Fig. 4 shows the percentage of diffusion of molecule RITC 70 kDa across a patch without gel treatment, an ABM and a Geltrex coated patch for 24 h. As can be seen, the patch was highly permeable to RITC 70 kDa molecules because of the high porosity of the monolayer nanofibers. In contrast, only about 20% of RITC 70 kDa molecules could be diffused through ABM and Geltrex coated patches, suggesting a limited permeability of the membrane.

To demonstrate the feasibility of monolayer formation of epithelial cells, A549 cells were cultured on ABMs. It is known that the primary function of BMs is to hold epithelial cells through substrate adhesion molecules and to promote the formation of epithelial layer with junctional proteins like tight junction (TJ) proteins. Both BM and TJ are necessary to maintain cell layer integrity and both play roles of protective and functional barriers. More specifically, continous tight junctions are necessary as a boundary between the apical and basolateral cell surface domains to regulate molecule diffusion along the paracellular pathway [20]. Our results showed that A549 cells on both ABM and patch exhibited continuous ZO-1 and E-cadherin expressions at the cell borders for more than two weeks and that the expression level of ZO-1 and E-cadherin proteins increased with time (Fig. 5). However, the expression of ZO-1 and E-cadherin of the cells on ABM

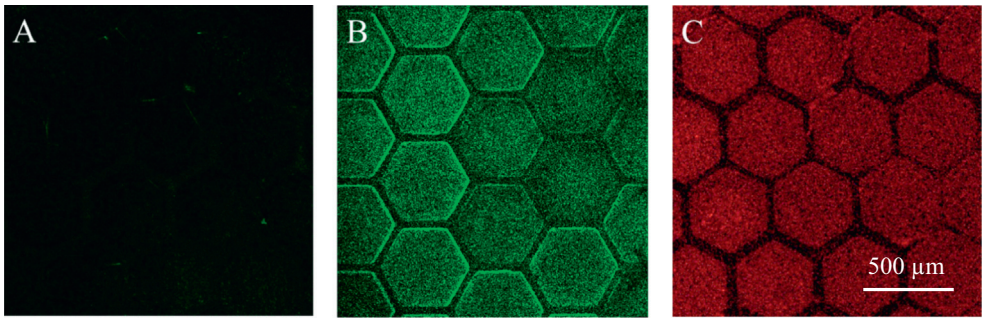

Fig. 3. Immunostaining fluorescence images of the membrane structure before (A) and after (B, C) deposition of ultrathin ABM. Immunostaining of collagen IV in green and laminin in red. (For interpretation of the references to colour in this figure legend, the reader is referred to the web version of this article.)

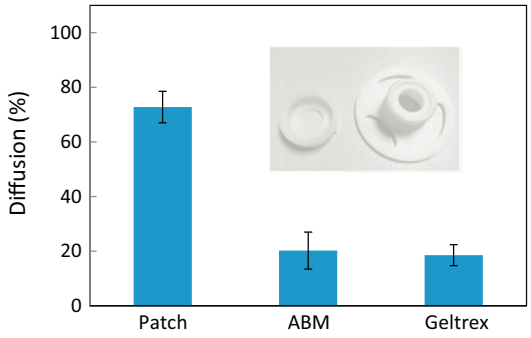

Fig. 4. Permeability of 70 kDa Rhodamine B isothiocyanate-dextran (RITC) across a membrane for 24 h. Patch: without gel deposition, ABM: patch with a gel layer of collagen IV-laminin, Geltrex: patch after deposition with a commercial gel. Values are means ± s.e.m. In insert: the homemade transwell-like device used for this experiment.

was more pronounced and more homogenous than on patch. Here, ZO-1 is one of tight junction-associated proteins, located at the plasma membrane in the apical junctional region, while E-cadherin is a cell-cell adhesion molecule, located on the lateral plasma membrane slightly below the tight junction. Therefore, our results suggest that ABM enhances the formation of tight junctions. Clearly, at day 9 ZO-1 and E-cadherin of the cells on ABM appeared more clearly than on patch. At day 17, they formed a more complete network on ABM than on patch. Finally, the vertical section (*XZ*) images clearly show a polarity of cells on ABM, which could not be observed with other types of BM mimics [17] and further, suggests the advantage of ABM. This can also be seen from the vertical section (*XZ*) image of cells on patch at day 17, where two cell layers appeared due to absence of BM proteins. A549 cells were derived from lung cancer and are often used as models of alveolar Type II pulmonary epithelium. Our results showed that monolayer of A549 cells could be achieved and sustained on ABM but not on patch. This means that ABM, like natural BM, plays important roles to the homeostasis of epithelial layer by dynamic regulation of cell-BM interaction, cell migration and cell division through a variety of signaling and cytoskeleton regulation events. More investigations are expected to understand these events with ABMs.

Previously, culture patches without collagen IV-laminin treatment could be used as substrates for differentiation of human induced pluripotent stem cells toward cardiomyocytes [18] and neurons [21] as well as primary neuron cells [22] and fibroblasts [23]. In such cases, collagen IV-laminin treatment would not be necessary since these cells were not epithelial. In general, the use of ABM as substrate should be relevant for epithelial and endothelial culture and tissue modeling where cell polarity and TJs are primarily important.

4. Conclusion

We proposed a three-level fabrication strategy to mimic natural

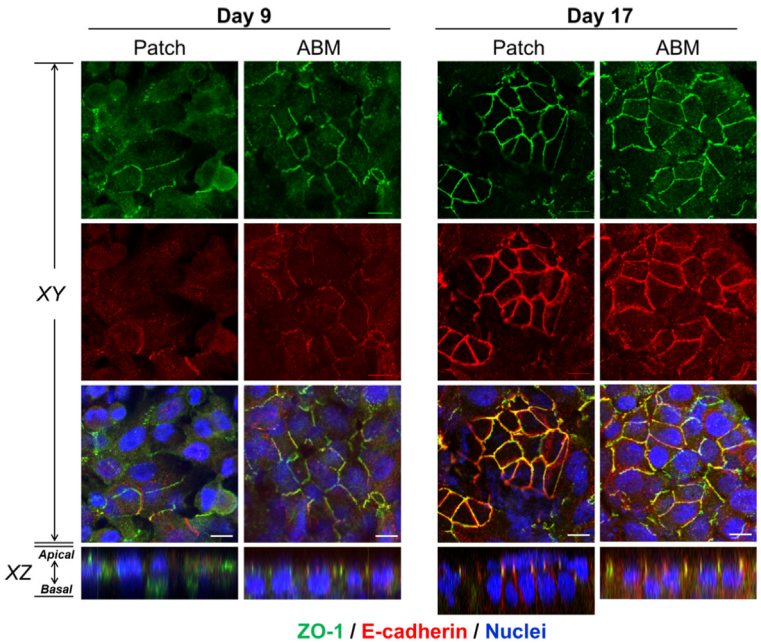

Fig. 5. Confocal immunofluorescence images of A549 cells cultured on a patch and an ultrathin ABM for 9 and 17 days. ZO-1 was stained in green, E-cadherin in red and nucleus in blue. Single confocal sections of monolayer were shown (*XY*). Images of vertical sections were presented downside (*XZ*). The scale bar represents 10 µm. (For interpretation of the references to colour in this figure legend, the reader is referred to the web version of this article.)

BMs. The first-level structure, i.e., the honeycomb microframe, is handleable and compatible to conventional culture. The second-level structure, i.e., the monolayer of crosslinked gelatin nanofibers, serves as backbone to handle an ultrathin membrane. Finally, the ultrathin membrane made of collagen IV-laminin mixture acts as functional ABM. Altogether, the hierarchic structure is mechanically stable and easy to use. Our results showed that 0.1% gel concentration of collagen IV-laminin mixture was appropriate to form ultrathin films of thickness in the order of 100 nm in the porous areas of electrospun nanofibers. In addition, such a fabrication strategy is straightforward for the formation of ultrathin membrane with other materials. The permeability of the membrane has been studied with 70 kDa RITC, showing characteristic diffusion behavior. The fabricated membrane has also been used to improve the monolayer formation of epithelial cells. We believe that such an ultrathin ABM should be more appropriate for tissue and organ-on-a-chip studies comparing to the commonly used plastic or elastomeric membranes.

Credit author statement

E.R and J.W. performed the device preparation, characterization, cell culture experiments, L.W, Y.H. and B.X aided in device making and cell culturing, Y.C. was involved in planning and data analyses. All authors discussed the results and commented on the manuscript.

Aknowledgment

This work was supported by the Agence Nationale de la Recherche under contract No ANR-17-CE09-0017 (AlveolusMimics), DIM ELICIT program from Région Ile-de-France, and PSL Valorization through Prematuration project. ER was granted by Indonesia Endowment Fund for Education, Ministry of Finance of The Republic of Indonesia (LPDP).

Declaration of Competing Interest

None.

References

[1] G.W. Laurie, C.P. Leblond, What is known of the production of basement membrane components, J. Histochem. Cytochem. 31 (1983) 159–163, https://doi.org/10.1177/31.1A_SUPPL.6186721 no. 1 A.
[2] M. Paulson, Basement membrane proteins: Structure, assembly, and cellular interactions, Crit. Rev. Biochem. Mol. Biol. 27 (1–2) (1992) 93–127, https://doi.org/10.3109/10409239209082560.
[3] V.S. LeBleu, B. MacDonald, R. Kalluri, Structure and function of basement membranes, Exp. Biol. Med. 232 (9) (2007) 1121–1129, https://doi.org/10.3181/0703-MR-72.
[4] P.D. Yurchenco, Basement membranes: Cell scaffoldings and signaling platforms, Cold Spring Harb. Perspect. Biol. 3 (2) (2011) 1–27, https://doi.org/10.1101/cshperspect.a004911.
[5] A. Pozzi, P.D. Yurchenco, R.V. Iozzo, The nature and biology of basement membranes, Matrix Biol. 57–58 (2017) 1–11, https://doi.org/10.1016/j.matbio.2016.12.009.
[6] R.P. Mecham, Cell Biology of Extracellular Matrix, vol. 69, Springer, US, 1992 no. 6.
[7] M.S. Thomsen, L.J. Routhe, T. Moos, The vascular basement membrane in the healthy and pathological brain, J. Cereb. Blood Flow Metab. 37 (10) (2017) 3300–3317, https://doi.org/10.1177/0271678X17722436.
[8] K. Hozumi, J. Kumai, Y. Yamada, M. Nomizu, Active peptide-conjugated chitosan matrices as an artificial basement membrane, Polymers (Basel). 7 (2) (2015) 281–297, https://doi.org/10.3390/polym7020281.
[9] A. Rossi, L. Wistlich, K.H. Heffels, H. Walles, J. Groll, Isotropic versus bipolar functionalized biomimetic artificial basement membranes and their evaluation in long-term human cell co-culture, Adv. Healthc. Mater. 5 (15) (2016) 1939–1948, https://doi.org/10.1002/adhm.201600224.
[10] A. Nishiguchi, S. Singh, M. Wessling, C.J. Kirkpatrick, M. Möller, Basement membrane mimics of biofunctionalized nanofibers for a bipolar-cultured human primary alveolar-capillary barrier model, Biomacromolecules 18 (3) (2017) 719–727, https://doi.org/10.1021/acs.biomac.6b01509.
[11] E.S. Place, N.D. Evans, M.M. Stevens, Complexity in biomaterials for tissue engineering, Nat. Mater. 8 (6) (2009) 457–470, https://doi.org/10.1038/nmat2441.
[12] F.J. O'Brien, Biomaterials & scaffolds for tissue engineering, Mater. Today 14 (3) (2011) 88–95, https://doi.org/10.1016/S1369-7021(11)70058-X.
[13] R. Cruz-Acuña, A.J. García, Synthetic hydrogels mimicking basement membrane matrices to promote cell-matrix interactions, Matrix Biol. 57–58 (2017) 324–333, https://doi.org/10.1016/j.matbio.2016.06.002.
[14] D. Huh, B.D. Matthews, A. Mammoto, M. Montoya-Zavala, H. Yuan Hsin, D.E. Ingber, Reconstituting organ-level lung functions on a chip, Science (80-.). 328 (5986) (2010) 1662–1668, https://doi.org/10.1126/science.1188302.
[15] A.O. Stucki, et al., A lung-on-a-chip array with an integrated bio-inspired respiration mechanism, Lab Chip 15 (5) (2015) 1302–1310, https://doi.org/10.1039/c4lc01252f.
[16] K.H. Benam, et al., Small airway-on-a-chip enables analysis of human lung inflammation and drug responses in vitro, Nat. Methods 13 (2) (2016) 151–157, https://doi.org/10.1038/nmeth.3697.
[17] N. Higuita-Castro, et al., Using a novel microfabricated model of the alveolar-capillary barrier to investigate the effect of matrix structure on atelectrauma, Sci. Rep. 7 (1) (2017) 1–13, https://doi.org/10.1038/s41598-017-12,044-9.
[18] Y. Tang, et al., Induction and differentiation of human induced pluripotent stem cells into functional cardiomyocytes on a compartmented monolayer of gelatin nanofibers, Nanoscale 8 (30) (2016) 14530–14,540, https://doi.org/10.1039/c6nr04545f.
[19] J.S.Y. Chen, Y.D. Tang, L. Wang, Cell culture device, Patent, WO 2017/005927A, Jan 12, (2017).
[20] M. Hirsch, W. Noske, The tight junction: structure and function, Micron 24 (3) (1993) 325–352, https://doi.org/10.1016/0968-4328(93)90057-8.
[21] Y. Tang, et al., Effective motor neuron differentiation of hiPSCs on a patch made of crosslinked monolayer gelatin nanofibers, J. Mater. Chem. B 4 (19) (2016) 3305–3312, https://doi.org/10.1039/c6tb00351f.
[22] Y. Tang, F.P. Ulloa Severino, F. Iseppon, V. Torre, Y. Chen, Patch method for culture of primary hippocampal neurons, Microelectron. Eng. 175 (2017) 61–66, https://doi.org/10.1016/j.mee.2017.01.012.
[23] B. Wang, et al., Fabrication of spaced monolayers of electrospun nanofibers for three-dimensional cell infiltration and proliferation, Microelectron. Eng. vol. 198, (2018) 73–77, https://doi.org/10.1016/j.mee.2018.07.005 no. March.

Appendix C
Effect of periodic deformation on alveolar cell layer on nanofibers

Received: 18 February 2020 | Revised: 9 April 2020 | Accepted: 13 June 2020

DOI: 10.1002/bit.27458

ARTICLE

BIOTECHNOLOGY AND BIOENGINEERING WILEY

Alveolar mimics with periodic strain and its effect on the cell layer formation

Milad Radiom[1] | Yong He[2] | Juan Peng-Wang[2] | Armelle Baeza-Squiban[3] | Jean-François Berret[1] | Yong Chen[2]

[1]Laboratoire Matière et Systèmes Complexes, CNRS UMR 7057, Université Paris Diderot Paris-VII, Paris, France

[2]Département de Chimie, Sorbonne Universités–UPMC Univ Paris 06, CNRS UMR 8640, Pasteur, École Normale Supérieure–PSL Research University, Paris, France

[3]Unité de Biologie Fonctionnelle et Adaptative, CNRS UMR 8251, Université Paris Diderot Paris-VII, Paris, France

Correspondence
Milad Radiom, Laboratoire Matière et Systèmes Complexes, CNRS UMR 7057, Université Paris Diderot Paris-VII, Bâtiment Condorcet, 10 rue Alice Domon et Léonie Duquet, F-75205 Paris, France.
Email: milad.radiom@u-paris.fr

Yong Chen, Département de Chimie, Sorbonne Universités–UPMC Univ Paris 06, CNRS UMR 8640, Pasteur, École Normale Supérieure–PSL Research University, 24 rue Lhomond, F-75005 Paris, France.
Email: yong.chen@ens.psl.eu

Abstract

We report on the development of a new model of alveolar air–tissue interface on a chip. The model consists of an array of suspended hexagonal monolayers of gelatin nanofibers supported by microframes and a microfluidic device for the patch integration. The suspended monolayers are deformed to a central displacement of 40–80 μm at the air–liquid interface by application of air pressure in the range of 200–1,000 Pa. With respect to the diameter of the monolayers, that is, 500 μm, this displacement corresponds to a linear strain of 2–10% in agreement with the physiological strain range in the lung alveoli. The culture of A549 cells on the monolayers for an incubation time of 1–3 days showed viability in the model. We exerted a periodic strain of 5% at a frequency of 0.2 Hz for 1 hr to the cells. We found that the cells were strongly coupled to the nanofibers, but the strain reduced the coupling and induced remodeling of the actin cytoskeleton, which led to a better tissue formation. Our model can serve as a versatile tool in lung investigations such as in inhalation toxicology and therapy.

KEYWORDS

alveolar air–tissue interface, alveolus mimic, gelatin nanofibers, lung-on-a-chip, physiological strain

1 | INTRODUCTION

Alveolar air sacs are the soft membrane-like tissues at the distal ends of the lungs where gas exchange between atmosphere and blood occurs. The number of air sacs is in the range of 300–400 million in adult lungs which covers an appreciable surface area of about 70 m^2 (Robert, 2000; Weibel, 2015). The air sacs have been shown to have irregular morphologies (Perlman & Bhattacharya, 2007), but on the average to be hexagonal with a diameter of about 200 μm (Fung, 1988). The local epithelium is mainly composed of type I (AETI) and type II (AETII) cells which are respectively squamous and cuboidal in morphology and are respectively responsible for gas exchange and for the secretion of lung surfactant fluid into the alveolar lumen (Desai, Brownfield, & Krasnow, 2014; Dunsmore & Rannels, 1996; Fehrenbach, 2001; Maina & West, 2005; Weibel, 2015). AETI cells are connected to capillary endothelial cells via an extracellular matrix (ECM) which is composed of basement membranes and interstitial space. The ECM has a thickness of about a few hundred nanometers (Dunsmore & Rannels, 1996; Maina & West, 2005; Townsley, 2012; Weibel, 2015). The composition of the basement membranes is mainly of collagen IV bundles and elastin fibers (Dunsmore & Rannels, 1996; Maina & West, 2005; Townsley, 2012). A thin ECM is required for efficient diffusion of the gas, solutes, and proteins across the tissue, and to accommodate tissue expansion during breathing. The secreted lung surfactant fluid facilitates the latter by lowering the air–liquid surface tension to about 10–25 mN/m. From a mechanical point of view, alveoli are the most susceptible tissue in the lungs: They are deformed to a linear strain of 4–12% during normal and deep breathing (Fredberg & Kamm, 2006; Guenat & Berthiaume, 2018; Roan & Waters, 2011; Waters, Roan, & Navajas, 2012).

From about three decades ago, several in vitro models of alveoli were developed which offer cheap, accessible, easy-to-handle, and reliable alternatives to animal models and are used to investigate cell

differentiation, surfactant secretion, and tissue injury induced by mechanical strain among other investigations (Bilek, Dee, & Gaver, 2003; Chess, Toia, & Finkelstein, 2000; Hermanns et al., 2009; Higuita-Castro, Mihai, Hansford, & Ghadiali, 2014; Jacob & Gaver, 2012; Kamotani et al., 2008; Sanchez-Esteban et al., 2001; Scott, Yang, Stanik, & Anderson, 1993; Trepat et al., 2004; Tschumperlin & Margulies, 1998; Vlahakis, Schroeder, Limper, & Hubmayr, 1999). The use of animal models is unethical and there is a significant social momentum to replace, reduce, and refine them. Over the last decade, microfabrication techniques, such as photolithography and 3D bioprinting have been used to develop advanced devices for improved in vitro modeling by considering topographic cues, shear stress, pressure and deformation, epithelial and endothelial coculture, among others (Campillo et al., 2016; Douville et al., 2011; Higuita-Castro et al., 2017; Huh et al., 2007; Jain et al., 2018; Nalayanda et al., 2009). One model consisted of two overlapping microchannels separated by a microporous polydimethylsiloxane (PDMS) membrane, and used cyclic vacuum to induce uniaxial stretching in the membrane (Huh et al., 2010). This model was used to replicate inflammatory response to tumor necrosis, neutrophil chemotaxis, and phagocytosis of bacteria. The same model was later used to replicate pulmonary edema (Huh et al., 2012). Another model incorporated a bio-inspired microdiaphragm in a microfluidic chip to induce 3D deformations in a microporous PDMS membrane (A. O. Stucki et al., 2015, J. D. Stucki et al., 2018). These developments are motivated by the need for modeling lung diseases, accelerating the screening of new drugs, and investigating the toxicity of engineered nanomaterials (Park, Georgescu, & Huh, 2019; Tenenbaum-Katan, Artzy-Schnirman, Fishler, Korin, & Sznitman, 2018).

Current in vitro models generally use cell culture substrates that are made out of biocompatible polymers or elastomers such as PDMS, polyethylene terephthalate, and polyester. Among others, PDMS is more common because it is simple to process, and it has a relatively low elastic modulus leading to its deformability. Nevertheless, PDMS has some shortcomings, for example, it has a high tendency for adsorption of biomarker proteins and drugs which is associated to its hydrophobicity (Boxshall et al., 2006; van Meer et al., 2017), and it does not have the fibrous structure and the biochemical properties of the ECM which are known to direct cell differentiation, migration, and other activities (Frantz, Stewart, & Weaver, 2010; Zhou et al., 2018). To circumvent some of these issues, recently cell culture substrates made out of collagen and elastin were developed and were shown to have a reduced adsorption affinity for biomarkers as compared with PDMS (Zamprogno et al., 2019). Nevertheless, the drop-casted collagen–elastin solutions formed relatively thick layers, 5–10 μm, as compared with alveolar ECM (Dunsmore & Rannels, 1996; Maina & West, 2005; Weibel, 2015; Zamprogno et al., 2019).

In the present work, we use an array of suspended monolayers of gelatin nanofibers for replicating the alveolar air–tissue interface. The monolayers are designed to have a hexagonal or honeycomb geometry to closely imitate the average shape of the alveolar air sacs (Fung, 1988; Perlman & Bhattacharya, 2007). The use of gelatin is for its biocompatibility and its derivation from collagen which is the most abundant protein in the basement membrane (Dunsmore & Rannels, 1996; Maina & West, 2005; Townsley, 2012). The resulting monolayers have a high porosity which is desirable for a minimal exogenous material contact with the cells, and a maximal exposure to the culture medium (Liu et al., 2014; Tang, Liu, Li, Yu, Severino, et al., 2016; Tang, Liu, Li, Yu, Wang, et al., 2016; Tang, Ulloa Severino, Iseppon, Torre, & Chen, 2017). The suspended monolayers have a thickness <1 μm and a relatively low elastic modulus affording their deformability at the air–liquid interface. We use this property to mimic the breathing dynamics of alveoli by applying air pressure of relatively low values. Human lung epithelial A549 cells originally isolated from a lung tumor (Lieber, Smith, Szakal, Nelson-Rees, & Todaro, 1976) were cultured on the monolayers and exposed to mechanical strain at biologically relevant rates. This cell line is a common model of lung alveolar tissue in in vitro investigations (Douville et al., 2011; Higuita-Castro et al., 2014; Huh et al., 2010; Kamotani et al., 2008; Trepat et al., 2004; Vlahakis et al., 1999), and is used here to show the functionality of our alveolar mimics model.

2 | MATERIALS AND METHODS

2.1 | Culture patch

Fabrication of the culture patch is similar to the previous ones and is schematically shown in Figure 1a–j (Tang, Liu, Li, Yu, Severino, et al., 2016; Tang, Liu, Li, Yu, Wang, et al., 2016). A silicon wafer is coated with Dry Film resist (DF1100; Engineered Materials Systems) to a thickness of 200 μm using a rolling coater at 100°C (Figure 1a). A chromium (Cr) mask with honeycomb pattern (μPG101; Heidelberg Instruments) together with UV exposure is then used to create a honeycomb pattern onto the Dry Film layer (Figure 1b). On top of the exposed Dry Film layer, a new layer of Dry Film is added to a thickness of 100 μm (Figure 1c). This time, a second Cr mask together with UV exposure is used to pattern an outer ring onto the layer (Figure 1d). Development in cyclohexanone results in the removal of uncured Dry Film areas (Figure 1e). The resulting positive mold has a thickness of 200 μm in the central honeycomb area and 300 μm in the outer ring. The resulting mold is initially treated with antisticking trimethylchlorosilane by exposure to its vapors for 20 min. Afterward, PDMS (Sylgard 184, monomer to curing agent ratio 10:1) is poured on top of the mold (Figure 1f). PDMS is cured for 2 hr at 70°C resulting in a PDMS stamp (Figure 1g). The PDMS stamp is then adhered to a glass slide using plasma activation and vacuum. The gap between PDMS stamp and glass is then filled with OrmoStamp (Micro Resist Technology, Germany; Figure 1h) and UV-cured for 2 min (Figure 1i). The result is a microframe with an array of 87 honeycomb cells (Figure 1j). Each honeycomb has a diameter equal to 500 μm and a pitch distance of 200 μm (Figure 2a). In the next step, the frame is coated with a thin layer of gold (15 nm) using sputter deposition (Emitech K675X) before electrospinning. A gelatin solution containing 10% by weight gelatin (porcine skin; Sigma-Aldrich) in

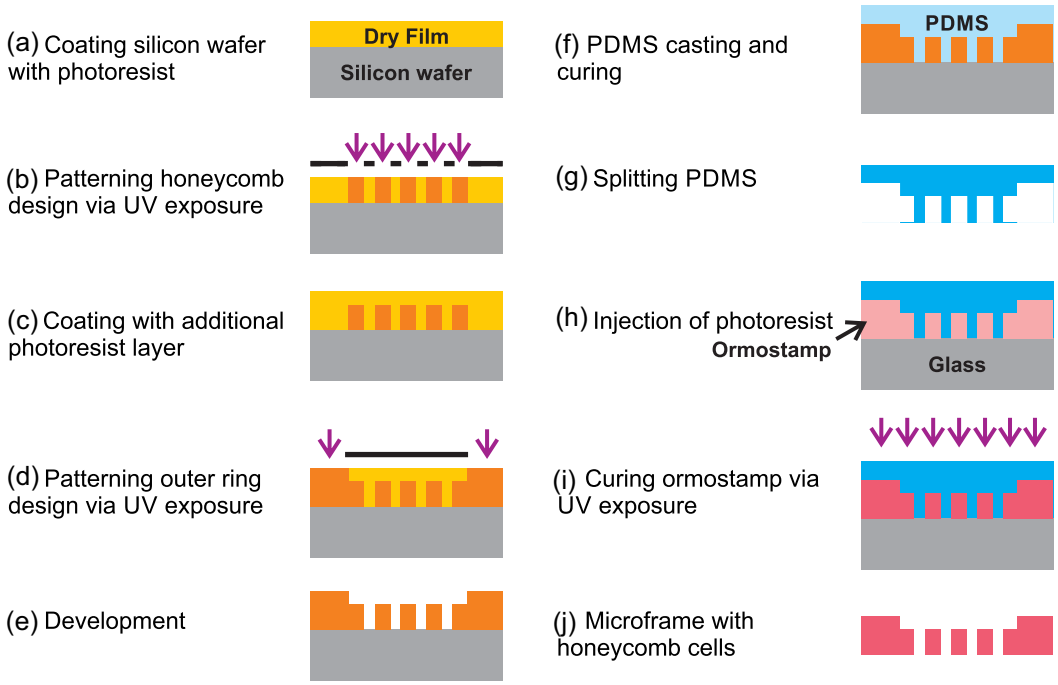

FIGURE 1 Schematic of fabrication steps of honeycomb microframe (a–j) before electrospinning of the gelatin nanofibers. PDMS, polydimethylsiloxane [Color figure can be viewed at wileyonlinelibrary.com]

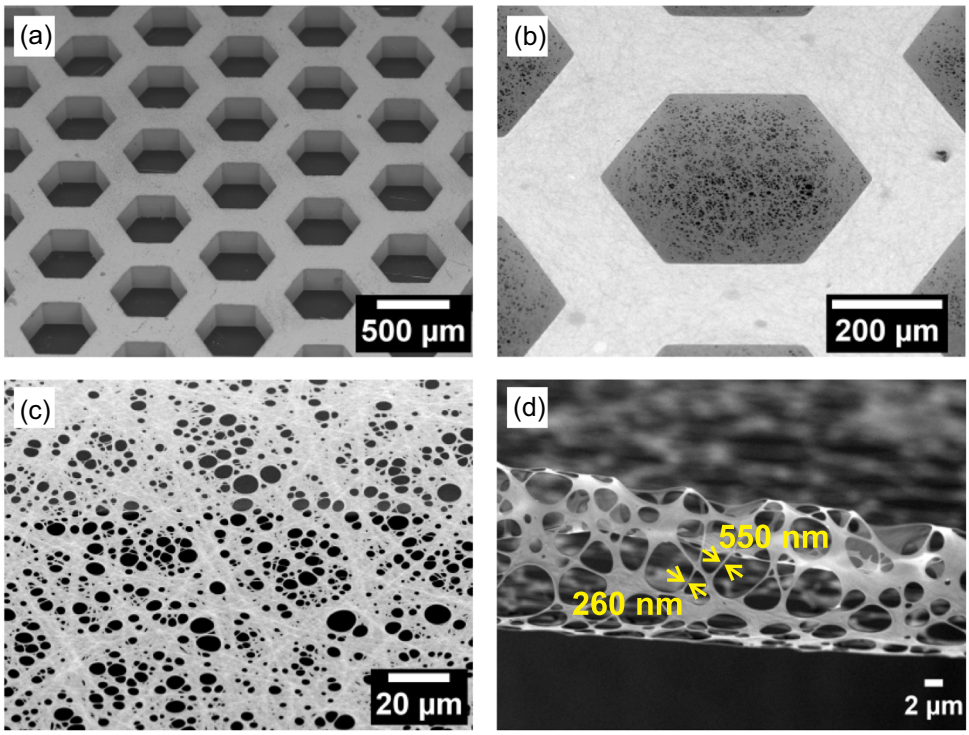

FIGURE 2 (a) Scanning electron microscopy (SEM) image of a culture patch consisting of 87 honeycomb microframes with 500-µm cell size and 200-µm band width. In the picture, 24 microframes are visible. The thickness of the microframes is 200 µm. (b) SEM image of a suspended monolayer of gelatin nanofibers after electrospinning and crosslinking over a honeycomb microframe. (c) SEM image of the microporous structure of a gelatin nanofiber monolayer showing the distribution of pore sizes in the range of 1–10 µm. (d) SEM image from a cut through a gelatin nanofiber monolayer showing the thickness of the monolayer in the range of 100–500 nm. Except for (c), all images were taken at an angle of 75° [Color figure can be viewed at wileyonlinelibrary.com]

a mixture of acetic acid (840 µl), ethyl acetate (560 µl), and milli-Q water (400 µl) is prepared. During electrospinning, a high voltage (11 kV) is applied to a metal syringe needle while it is placed vertically above the microframe at a distance of 10 cm. A bias is applied to an aluminum foil that is in contact with the microframe from underneath. During electrospinning, the gelatin solution is ejected at a rate of 0.2 ml/hr for 4 min. In the next step, electrospinned gelatin nanofibers are dried overnight in a desiccator and then crosslinked in a solution that contains 0.38 g *N*-(3-dimethylaminopropyl)-*N*′-ethylcarbodiimide hydrochloride (Sigma-Aldrich) and 0.23 g *N*-hydroxysuccinimide (Sigma-Aldrich) in absolute ethanol to a total volume of 10 ml. After 4 hr of reaction at 4°C, the culture patches are washed three times in absolute ethanol and allowed to dry overnight in a desiccator. The electrospinning and crosslinking steps result in 87 suspended monolayers of gelatin nanofibers on the apical side of the microframe. Figure 2b shows one suspended monolayer. Each monolayer is hexagonal with a diameter of 500 µm.

2.2 | Monolayer deformation

After fabrication, the patch, with or without A549 cells, is integrated into a microfluidic chip (MesoBioTech) which accommodates airflow from apical channels and medium flow from basal channels. To apply air pressure, the outlet of the air channel is blocked. An air pump is then used to build up air pressure behind an airflow controller (FC-HP1; MesoBioTech), which is then used to regulate and apply air pressure in a sinusoidal wave. The wave function is generated by programming in a dedicated software of the FC-HP1 controller. The maximum pressure is adjusted, and the minimum pressure is set to be the atmospheric pressure. The period of the wave function is set to be 5 s (0.2 Hz) in accordance with the normal breathing rate (Waters et al., 2012). Medium flow is controlled via a syringe pump and a flow rate of 0.1–1 ml/hr is established in the basal channels. During operation, the suspended monolayers of gelatin are at the air–liquid interface. By application of air pressure, the monolayers are strained, and their displacements recorded using an inverted optical microscope (Axio Observer.Z1; Zeiss) and a ×10 objective lens in phase-contrast mode.

2.3 | Cell culture

Adenocarcinoma A549 cells were obtained from the American Type Culture Collection (ATCC). The cells were grown in T25-flasks in Dulbecco's modified Eagle's medium supplemented with 10% fetal bovine serum (FBS) and 1% penicillin–streptomycin (PS) inside an incubator with humidified atmosphere (37°C, 5% CO_2 air). When the cells reached about 80–90% confluency they were passaged using TrypLE express enzyme.

Before cell seeding, the culture patch was cleaned in 70% ethanol and exposed to UV for 30 min. On the culture patch, the cells were seeded at a density of 6.0×10^5 cells/ml (3.0×10^5 cells per patch). A fresh culture medium was replaced 2 hr later and then the culture medium was changed every 2 days. The cells were cultured for 1–3 days in the submersed state in the incubator (37°C, 5% CO_2 air). The culture patch with cells was then mounted in the microfluidic chip and brought to the microscope stage for observations during mechanical strain tests. During these tests, the cells were maintained in the air–liquid interface. After the tests, the culture patch was removed from the chip for the next procedure or analysis, for example, Live–dead assay, or put in a Petri dish with fresh culture medium for analysis 24 hr later. DMEM, FBS, PS, and TrypLE were all from Gibco brand.

2.4 | Live–dead assay

The culture patch was placed in a Petri dish. Cells were incubated with 4 µM calcein AM (Invitrogen) and 5 µM propidium iodide (Sigma-Aldrich) in Dulbecco's phosphate-buffered saline (DPBS) for live and dead cell staining, respectively. After 30 min of incubation (37°C, 5% CO_2 air), the cells were rinsed with fresh DPBS two times to remove any residual staining molecules. The fluorescence was measured with an inverted fluorescence microscope (Axio Observer.Z1) using a ×10 objective lens. These measurements were repeated on at least two different occasions and on five different cell-cultured monolayers for 1-day and 3-day cultures.

2.5 | Immunostaining assay

The culture patch was placed in a Petri dish. Cells were rinsed with DPBS and fixed with 4% paraformaldehyde for 15 min at 4°C. They were then permeabilized using 0.5% Triton X-100 for 10 min, and then saturated with DPBS supplemented with 0.1% Triton X-100 and 3% bovine serum albumin for 2 hr at room temperature. Afterward, the cells were stained with fluorescent antibodies, namely Alexa Fluor 488-conjugated phalloidin (20 µl/ml, A12379; Life Technologies) to label the actin filaments (F-actin), and 4′,6-diamidino-2-phenylindole (DAPI) to label the nuclei. Samples were observed using a Zeiss confocal microscope (LSM 710; Zeiss) and ×20 and ×40 objectives. These measurements were repeated on at least two different occasions and on three different cell-cultured monolayers for 1-day and 3-day cultures.

2.6 | Modeling

The displacement–pressure response of the gelatin nanofiber monolayers is interpreted in terms of the displacement of a clamped circular plate under uniform pressure. To evaluate the response, the displacement profile of the plate is initially presumed. In the theory that is adapted in this study, the profile has the following expression (Y. Zhang, 2016):

$$w = w_0\left(1 - \frac{r^2}{a^2}\right)^2, \quad (1)$$

where w is the axisymmetric displacement of the plate, that is, $w = w(r)$, w_0 the displacement at the center of the plate, r the radial distance from the center of the plate, and a its radius. Solution to the governing equations of plate bending under uniform pressure gives the following displacement–pressure expression (Y. Zhang, 2016):

$$\frac{Pa^4}{64D} = \left[1 + \frac{3}{4}\left(\frac{a}{t}\right)^2(1-\upsilon^2)\frac{\sigma_0}{E}\right]w_0 + (0.4118 + 0.25\,\upsilon - 0.16088\,\upsilon^2)\frac{w_0^3}{t^2}, \quad (2)$$

where D is the bending modulus:

$$D = \frac{Et^3}{12\,(1-\upsilon^2)}, \quad (3)$$

P the pressure, E the elastic modulus, υ the Poisson's ratio, and t the plate thickness. We note that other models are available in the literature and may be used in our data analysis; a list is provided in Y. Zhang (2016). However, the differences between these model estimations are not significant in the calculations of the mechanical properties of PDMS and gelatin nanofiber monolayers that we present in the section below (Y. Zhang, 2016).

3 | RESULTS AND DISCUSSION

3.1 | Gelatin nanofiber membrane

As mentioned before, the fabrication protocol of the culture patch is similar to the previous ones (Tang, Liu, Li, Yu, Severino, et al., 2016; Tang, Liu, Li, Yu, Wang, et al., 2016); however, in this study, we changed the material used in making of the honeycomb microframes. In particular, we found that microframes made out of poly(ethylene glycol) diacrylate (PEGDA) swelled in contact with culture medium and changed shape during mechanical strain testing. This situation generally resulted in the liquid leaking into the air channels of the microfluidic device. Unlike PEGDA, when OrmoStamp (Micro Resist Technology, Germany) was used, the microframes were robust and did not change shape. Thereby, our experiments were performed with microframes made out of OrmoStamp. OrmoStamp is a photoresist resin that forms structures with glass-like properties after UV curing. We note that changing the material of the microframe from PEGDA to OrmoStamp did not affect the process of electrospinning and crosslinking and the general characteristics of the gelatin nanofiber monolayers remained the same (Tang, Liu, Li, Yu, Severino, et al., 2016; Tang, Liu, Li, Yu, Wang, et al., 2016). Moreover, as we found no loss of viability in our cell experiments with OrmoStamp, this material appears to be compatible with A549 cells as detailed below.

Figure 2a shows an array of honeycomb microframes after fabrication via lithography. On the basal side of the microframes we electrospinned and then crosslinked a layer of gelatin nanofibers. Before electrospinning, the microframes were coated with a thin layer of gold that set the potential for driving the polymer solution to the microframe during electrospinning. An example of the resulting gelatin nanofiber monolayer is shown in Figure 2b. This protocol results in an array of suspended monolayers of gelatin nanofibers on the apical side of the microframes. The choice of a honeycomb shape is motivated by the estimated average morphology of the alveoli. Alveolar fields were imaged using confocal microscopy and were shown to consist of irregular morphologies (Perlman & Bhattacharya, 2007); however, the average shape may well be estimated as a hexagon (Fung, 1988). After fabrication, the suspended monolayers have a diameter of 500 μm closely related to the size of alveoli (Robert, 2000; Weibel, 2015). The diameter of an inscribed circle is thereby 433 μm and is used later for the estimations of the elastic moduli and the radial and tangential strains following Equation (2).

The process of electrospinning and crosslinking results in the formation of a microporous monolayer as shown in Figure 2c. The porosity is higher in the center of the monolayer whereby the pore sizes are also larger. The porosity decreases gradually with proximity to the microframe walls. The pore sizes were generally in the range of 1–10 μm and the porosity was higher than 50%. As a measure of control, we discarded any patch in which the pore size exceeded 20 μm in any of the 87 gelatin nanofiber monolayers in one culture patch. We cut a few patches to measure the thickness of the monolayer. Interestingly, we found that after cutting the monolayer folds on itself. This behavior shows a pre-stress state in the gelatin nanofibers induced during crosslinking. After being cut, the stress is released, and the monolayer folds on itself. To measure the thickness, we set the angle of scanning electron microscope camera to 75° and measured thickness values in the range of 100–500 nm as shown in Figure 2d. The thickness of the monolayer is thereby in the range of the thickness of the alveolar ECM. Moreover, the monolayer microporous and fibrous structure resembles the ECM structure (Dunsmore & Rannels, 1996; Maina & West, 2005; Townsley, 2012; Weibel, 2015). As gelatin is derived from collagen, the resulting substrate has in addition an ECM-like chemical composition (Dunsmore & Rannels, 1996; Maina & West, 2005; Townsley, 2012; Weibel, 2015). These characteristics offer advantages to PDMS-based models. Additional images of the gelatin monolayers, distribution of pore sizes, and monolayer thickness are provided in Supporting Information Data S1.

3.2 | Biomimetic strain

A culture patch was integrated into a microfluidic chip with basolateral and apical channels which were used respectively for medium flow and air pressure. In the experiments with bare culture patch, that is, with no cell seeding, water was used as the medium. After filling the basolateral channels with water, the monolayers were at the air–liquid interface. The application of air pressure, in this case, resulted in the deformation of the monolayers. This setup is shown schematically in Figure 3. During these tests, five monolayers were randomly selected and for each monolayer, the displacement of the center w_0 was recorded. After the removal of pressure, we ascertained that the monolayers returned to their initial undeformed state.

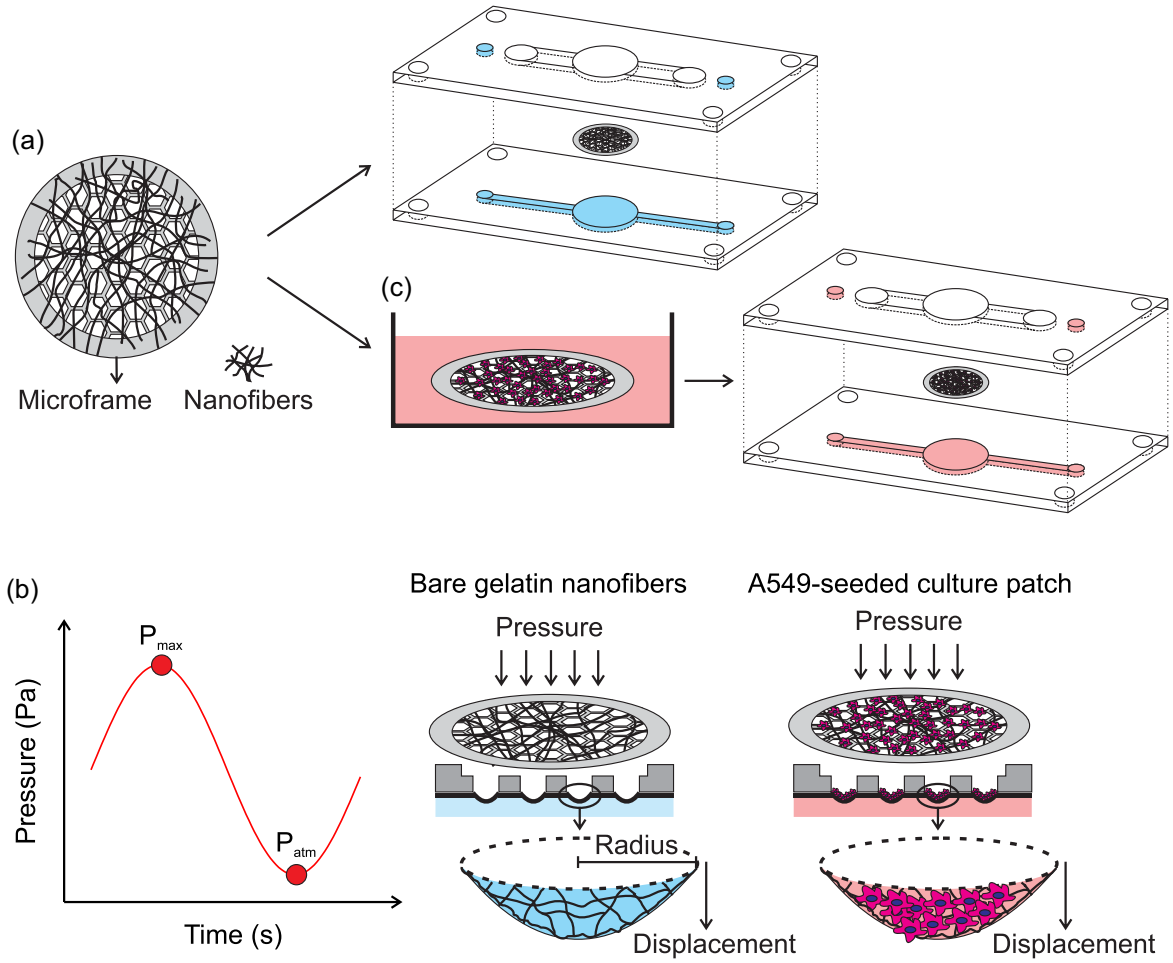

FIGURE 3 (a) A culture patch consists of honeycomb microframes and suspended monolayers of gelatin nanofibers. The culture patch with or without cells can be reversibly integrated into a microfluidic chip for characterization and evaluation of alveolus mimic functionality. The chip accommodates air pressure from apical channels and liquid flow from basal channels. Water (blue) and culture medium (pink) are used in the experiments with bare patch and cell-cultured patch, respectively. (b) Sinusoidal air pressure wave results in the displacement of individual gelatin nanofiber monolayers or cell-cultured monolayers [Color figure can be viewed at wileyonlinelibrary.com]

Figure 4 shows the displacement of the gelatin nanofiber monolayers as a function of the maximum of the applied air pressure. Each data point is an average of central displacement from five different monolayers and the error bars are the standard deviations. The differences in the displacement responses of individual monolayers at each pressure, that is, the extent of standard deviations, may be associated with differences in the density of the nanofibers in the monolayers as well as thickness. However, these variations may be estimated to be minute considering that electrospinning is a random deposition process and may be improved if the fibers were deposited uniformly, for example, by rotating the microframe during electrospinning. Nevertheless, from the standard deviation values, we found that the monolayers vary by only about 10% or less from the average response which we consider to be insignificant. The resolution in the pressure measurements was estimated to be about 100 Pa; this value is added as an error bar to the data points. We find that it is generally possible to exert pressures up to about 1,000 Pa and induce displacements as large as 100 μm.

The displacement of the monolayer at the air–liquid interface results from an interplay between the applied air pressure, the elasticity of the monolayer, and the liquid surface tension. In our measurements, we obtained an overall displacement which is precisely a cooperative displacement of the monolayer and the air–liquid interface. The displacement of the air–liquid interface may be calculated from Laplace's equation (Israelachvili, 2011):

$$P = \gamma\left(\frac{1}{R_1} + \frac{1}{R_2}\right), \tag{4}$$

where γ is the liquid surface tension equal to 72.8 mN/m for water and R_1 and R_2 are the two orthogonal or principal radii of curvature. In our geometry, $R_1 = R_2$. Using chord theorem, Equation (4) simplifies to:

$$P = \frac{4\gamma w_0}{a^2 + w_0^2}. \tag{5}$$

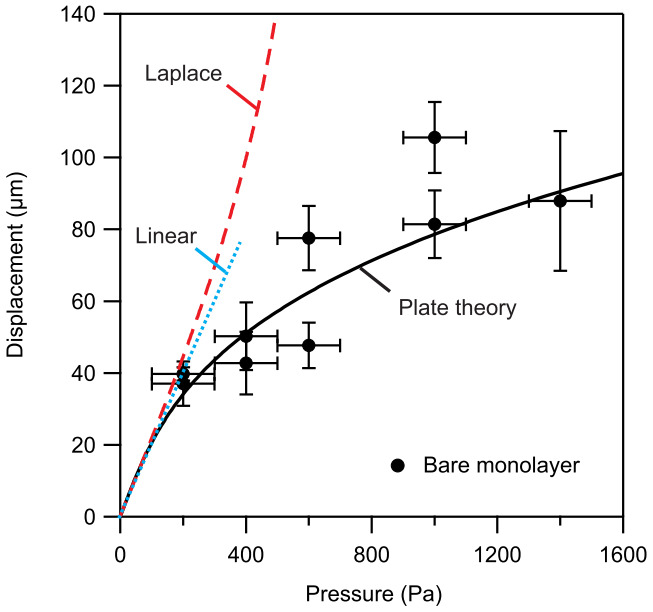

FIGURE 4 Displacement–pressure response of gelatin nanofiber monolayer together with fit to plate theory Equation (2). The best fit values are the elastic modulus $E = 4.0 \pm 1.0$ MPa and the residual stress $\sigma_0 = 0.2 \pm 0.1$ MPa, while the Poisson's ratio is set to 0.5. The linear response approximation for low values of applied pressure is also depicted (blue dotted line). Displacement–pressure response of air–liquid interface is calculated from Laplace's equation (5) and is depicted for comparison (red broken line). Error bars on *y* axis are standard deviations of recorded displacements from five different suspended gelatin monolayers. Error bars on *x* axis are errors of pressure measurement estimated to be about 100 Pa [Color figure can be viewed at wileyonlinelibrary.com]

In Figure 4 we show that the overall displacement is smaller than the prediction of Laplace's equation. This difference reveals the effect of gelatin nanofibers in stiffening the interface. We performed control experiments with honeycomb microframes that did not have the gelatin monolayers and observed that beyond a pressure of about 400 Pa the air broke into the liquid channel. This observation shows that the air–liquid interface becomes unstable at pressures higher than 400 Pa. Addition of gelatin nanofiber monolayers to the air–liquid interface stabilizes the interface whereby pressures more than 1,000 Pa may be applied. Although the values of the interface displacement become smaller, it is explained below that the resulting strains in the monolayers are in the range of the physiological alveolar strain.

Figure 4 further shows that the displacement of the monolayer increases with pressure but deviates from a linear dependence. In the theory of plate deformation, this departure is associated with a transition from bending-dominant displacement to stretching-dominant displacement (Wan & Lim, 1998; Wan, Guo, & Dillard, 2003; Y. Zhang, 2016), and is found to occur early in our applied pressure range. The displacement values as a function of pressure were fit to Equation (2) as shown in the figure. The fit parameters are the elastic modulus and the residual surface stress for which we obtained respectively $E = 4.0 \pm 1.0$ MPa and $\sigma_0 = 0.2 \pm 0.1$ MPa. We did not fit for the Poisson's ratio and instead assumed $\upsilon = 0.5$. The elastic moduli of wet gelatin scaffolds and membranes have been measured in the past using methods such as stress–strain mechanical testing and found them to be in the range of 1–4 MPa in agreement with our measured value (Higuita-Castro et al., 2017; Kim et al., 2009; S. Zhang et al., 2009). We note that the measured value for the elastic modulus of gelatin monolayer shows that the monolayer is compliant (e.g., as compared with PDMS). However, the elastic modulus of gelatin monolayer is still very high as compared with the elastic modulus of lung tissue which has been measured to be in the range of a few kilopascals (Polio et al., 2018; Roan & Waters, 2011).

An important conclusion from this part is that the suspended gelatin monolayers at the air–liquid interface can act like membranes with a well-defined displacement–pressure response. For example, similar experiments were performed with PDMS membrane in the same microfluidic chip. The PDMS membranes had a diameter equal to 9 mm and thicknesses in the range of 50–400 μm. A sinusoidal air pressure wave was applied to the apical side of the membranes while water flowed through the basal channels. Air pressure resulted in the displacement of the PDMS membrane, for which we recorded the value at the center. As PDMS is transparent, we used a marker to color the center of the membrane to ease its visualization in the microscope. We found that displacement increases with pressure but deviates from a linear dependence which is again associated with stretching-dominant displacement (Wan & Lim, 1998; Wan et al., 2003; Y. Zhang, 2016). Fits to the displacement values using Equation (2) resulted in elastic moduli in the range of 3–7 MPa in agreement with the reported values in literature (Qian et al., 2016; Thangawng, Ruoff, Swartz, & Glucksberg, 2007). Experiments with PDMS membranes are presented in Supporting Information Data S2.

The evolution of displacement with pressure that we obtained with gelatin monolayers at the air–liquid interface as shown in Figure 4 has a similar qualitative behavior to PDMS membranes (Figure S3). This similarity corroborates that the mechanical response of the microporous monolayer is akin to a membrane making the monolayers structurally, that is, ECM-like, and mechanically, that is, membrane-like, relevant for alveolus mimic investigations as shown below.

We now come back to the discussion of mechanical strain as a result of the monolayer displacement. In Supporting Information Data S3 we provide a full mechanical characterization based on Equation (2). The equations for radial and tangential strains are also provided. From the calculations, one obtains that the maximum of the radial and tangential strains are $e_{r,\,max} = 0.7 \times (w_0/a)^2$ and $e_{t,\,max} = 0.6 \times (w_0/a)^2$, respectively. However, these maxima do not occur in the same radial position. In particular, the radial strain is maximum at a distance $r = 0.6a$ closer to the periphery, while the tangential strain is maximum at the center. Applying these relations, we find a maximum strain value in the range of 2–10% from the displacement–pressure response of the monolayers shown in Figure 4 which is in good agreement with the physiological range of alveolar strain, 4–12% (Fredberg & Kamm, 2006; Guenat & Berthiaume, 2018; Roan & Waters, 2011; Waters et al., 2012).

3.3 | Alveolus mimic model

The gelatin nanofiber monolayers were then used as substrates for the culture of A549 cells. This cell line is commonly used in in vitro investigations of lung alveoli as related with technical developments of microfluidic devices, as well as modeling cell responses (Douville et al., 2011; Higuita-Castro et al., 2014; Huh et al., 2010; Kamotani et al., 2008; Trepat et al., 2004; Vlahakis et al., 1999). The cells were seeded at a density of 3.0×10^5 cells per patch and were found to start adhering to gelatin nanofibers within an hour after seeding. A culture of 1 day generally resulted in a cell layer with about 50% confluency and a distribution of both extended and round morphologies. After 3 days, most cells adhered well to the gelatin nanofibers and the confluency was more than 90%. Comparing with the growth on a Petri dish, we found a similar growth rate with a duplication time of about 1 day in good agreement with ATCC. Examples of cell culture of gelatin monolayers are presented in Supporting Information Data S4.

Thereafter, cell-cultured patches were integrated into the microfluidic chip for the application of air pressure and mechanical strain as depicted schematically in Figure 3. Air pressure wave was applied from the apical side and the flow of culture medium was established in the basal channels. Recording cell layer displacement was similar to the bare gelatin monolayers, however, the presence of the cell layer made the visualizations easier.

Figure 5a shows a series of light microscopy images where the displacements of a cell-cultured gelatin monolayer are shown. One observes that from the initial relaxed position (i), where the central displacement $w_0 = 0$ μm at the atmospheric pressure, the entire surface of the cell-cultured monolayer deforms by increasing air pressure. At a pressure of about half of the maximum, the center of the monolayer is displaced by 35 μm (position ii) while at the maximum pressure of 400 Pa the center of the monolayer is at its full-depth displacement which is measured to be 70 μm (position iii). In Supporting Information Data S5, we show that the variation in the transmitted light intensity between the center of the monolayer and its corners correlates linearly with the central displacement. We use the linear relation to calibrate the displacement of the entire surface area of the monolayer. Figure 5b shows the displacement of the monolayer along its diameter at similar positions i to iii.

The displacement profiles shown in Figure 5b may then be interpreted in terms of the radial displacement profile of Equation (1). As shown in the figure, there is a good agreement between the experimental profiles and the model validating the use of Equation (2) in fitting our data. More importantly, the theory may be used to estimate the extent of radial and tangential strains during the experiments which we will discuss below.

Several cell-cultured patches were then investigated for their displacement–pressure responses. For each culture patch, we measured the displacements of five different cell-cultured monolayers at different locations on the culture patch and report an average value with a standard deviation in Figure 5c. The extent of standard deviation has the same argument as mentioned earlier in the case of bare gelatin monolayers. However, with cells, there is an additional complexity due to the use of culture medium with low surface tension which facilitates occasional formation of small bubbles in the channels. These bubbles may interfere with the displacement of the monolayer and increase the extent of variations in the measured displacements. Nevertheless, we find that for a pressure range of 400–1,000 Pa, the cell layer is displaced in the range of 20–100 μm. In Figure 5c, we also plotted the fitted curve to the displacement–pressure response of bare monolayers from Figure 4. Comparison of the experimental displacement–pressure response of cell-cultured monolayers with the response of monolayers

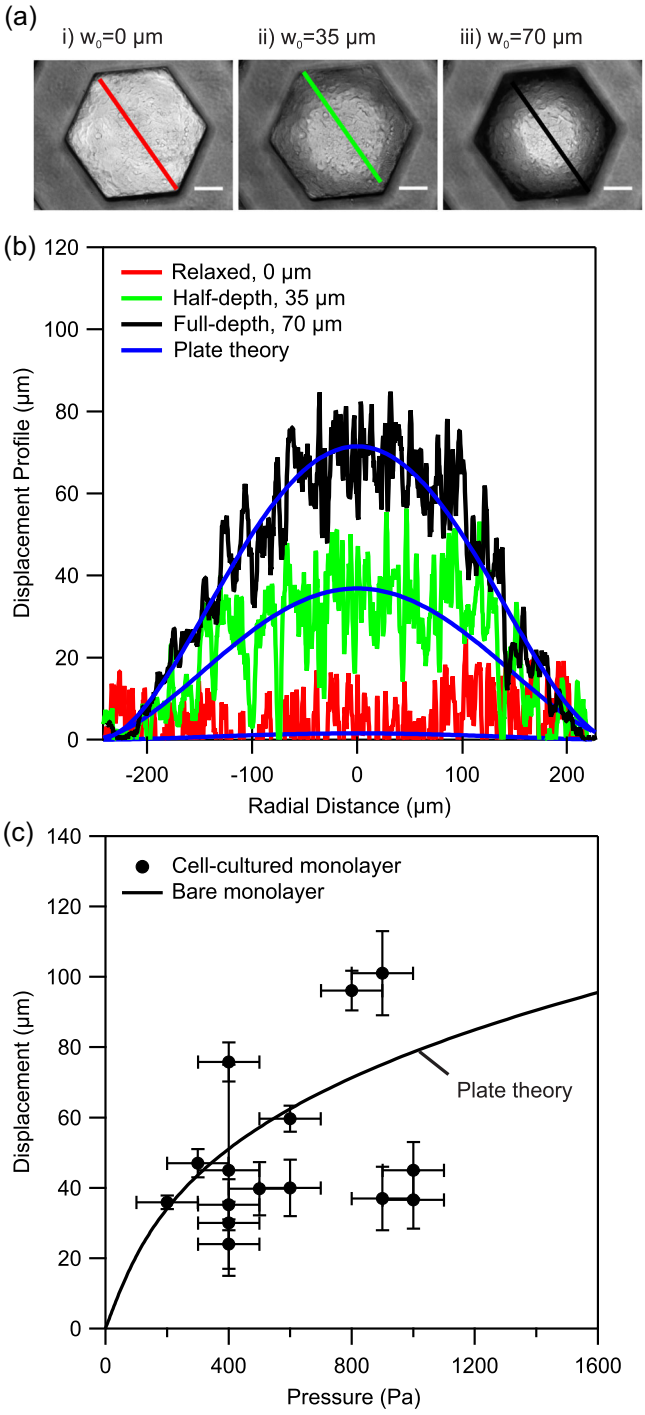

without cells shows similarity in the range of displacements as a function of pressure between the two cases. This observation shows that the added cell layer did not significantly alter the elasticity of the monolayer. We attribute this observation to a much higher compliance (i.e., less stiff character) of the cell layer as compared with the gelatin monolayer (He, Chen, Sun, & Zheng, 2012). In particular, the elastic modulus of single cells and cell monolayers have been measured to be in the range of a few kilopascals using atomic force microscopy nanoindentation technique and stress–strain mechanical tests (Brückner & Janshoff, 2015; Harris et al., 2012; Roan, Wilhelm, & Waters, 2015). The stiffness of the cell monolayer is thereby much smaller than the stiffness of the gelatin monolayer for which we measured a value of elasticity equal to 4 MPa. Thereby, the combination of the two layers has an elastic modulus that is similar to the elastic modulus of gelatin monolayer. This finding is similar to those reported in the past with silicon membranes and the culture of AETII rat cells (Tschumperlin & Margulies, 1998). This characteristic of the gelatin monolayer is akin to ECM that is also responsible for the mechanical integrity and stability of the alveolar tissue during breathing extensions (Dunsmore & Rannels, 1996; Maina & West, 2005; Waters et al., 2012; Weibel, 2015).

We now come back to the discussion of the effect of mechanical strain on the cells as a result of the monolayer displacement. The equations for radial and tangential strains were shown earlier. Applying these relations, we find a maximum strain value in the range of 1–11% from the displacement–pressure response of cell-cultured monolayers shown in Figure 5. This range is again in good agreement with the physiological range of alveolar strain, 4–12% (Fredberg & Kamm, 2006; Guenat & Berthiaume, 2018; Roan & Waters, 2011; Waters et al., 2012). We discuss cell viability and morphology in the following sections.

3.4 | Cell viability

Several culture patches were tested for evaluating cell viability after the mechanical strain tests. These patches were deformed to a strain of about 5% at a frequency of 0.2 Hz for a duration of 1 hr. Immediately after the tests (denoted by 0 hr), the patches were stained with markers of live and dead cells, calcein AM, and propidium iodide, respectively, and observed with fluorescence microscopy. Figure 6a shows examples of these measurements. The green emission originates from cellular enzymatic activity with calcein and is a signature of live cells. We found a significant number of live cells on the gelatin monolayers after the strain tests. The effect of the strain is still not significant after 24 hr, where again a significant green emission is collected from the same patch. Limited number of red emissions is associated with propidium iodide diffusing inside a permeable membrane and signifies a low number of dead cells. We quantified the total number of cells by summing up the total number of live and dead cells and expressed the cell viability in terms of the percentage of the live cells. Figure 6b,c shows that no significant reduction in cell viability was found upon the application of mechanical strain and, in particular, in comparison with parallel measurements with cells that did not experience any strain. The results persist in cultures of 1 day and 3 days. A slight increase in the intensity of the reflected green light at the periphery of the monolayer in Figure 6a is not related with the mechanical strain and is seen with static patches as well. A higher number of cells in the periphery may be related with the smaller pore sizes in this part of the monolayer which provides a larger number of adhesion sites for the cells. This effect may result in cell migration or higher proliferation in the periphery.

The results of Figure 6 are in agreement with a previous work which showed that mechanical strain had no effect on the proliferation and viability of A549 cells at higher strain values than used here (Vlahakis et al., 1999). It was otherwise shown that mechanical strain may increase the proliferation of the adenocarcinoma alveolar H441 cells (Chess et al., 2000), and the primary human alveolar epithelial cells (Stucki et al., 2015). Slightly increased viability after the mechanical strain was also observed with primary human bronchial cells (J. D. Stucki et al., 2018). Measurements with AETII cells from rat models showed that seeding density and incubation time may have an effect on cell death during mechanical strain tests (Tschumperlin & Margulies, 1998). In particular, cell death was found to be the least when the seeding density was the highest, an effect that was associated with increased cell–cell contacts (Tschumperlin & Margulies, 1998). Increasing strain level to higher than the physiological range is otherwise shown to result in tissue injury and cell death (Hammerschmidt, Kuhn, Grasenack, Gessner, & Wirtz, 2004; Tschumperlin, Oswari, & Margulies, 2000). Substantial injuries are reported in models of air-way reopening in which shear stresses from moving droplets are applied to the cells (Bilek et al., 2003; Douville et al., 2011; Higuita-Castro et al., 2014, 2017). From our results, we conclude that a physiological strain of 5% has no effect on the viability of A549 cells. This result further shows the applicability of our model in replicating the environment of alveolar cells.

FIGURE 5 (a) Light microscopy images of a cell-cultured gelatin monolayer at different displacement levels. Position "i" is the initial relaxed state at the atmospheric pressure, position "ii" the half-depth displacement equal to 35 μm, and position "iii" the full-depth displacement equal to 70 μm at the maximum of the applied air pressure equal to 400 Pa in this experiment. (b) The displacement profile of the cell-cultured gelatin monolayer obtained from the variations in the light intensity from the center to the edge of the monolayer after calibration (Supporting Information Data S5). The displacement profile shows a good agreement with the theoretical profile of Equation (1). (c) Displacement–pressure response of several cell-cultured gelatin monolayers. Solid line is the reproduced displacement–pressure response of bare gelatin monolayer obtained from the fit to data in Figure 4. Error bars on *y* axis are the standard deviation of recorded displacements from five different cell-cultured monolayers. Error bars on *x* axis are errors of pressure measurement estimated to be about 100 Pa. In total, seven cell-cultured patches were investigated [Color figure can be viewed at wileyonlinelibrary.com]

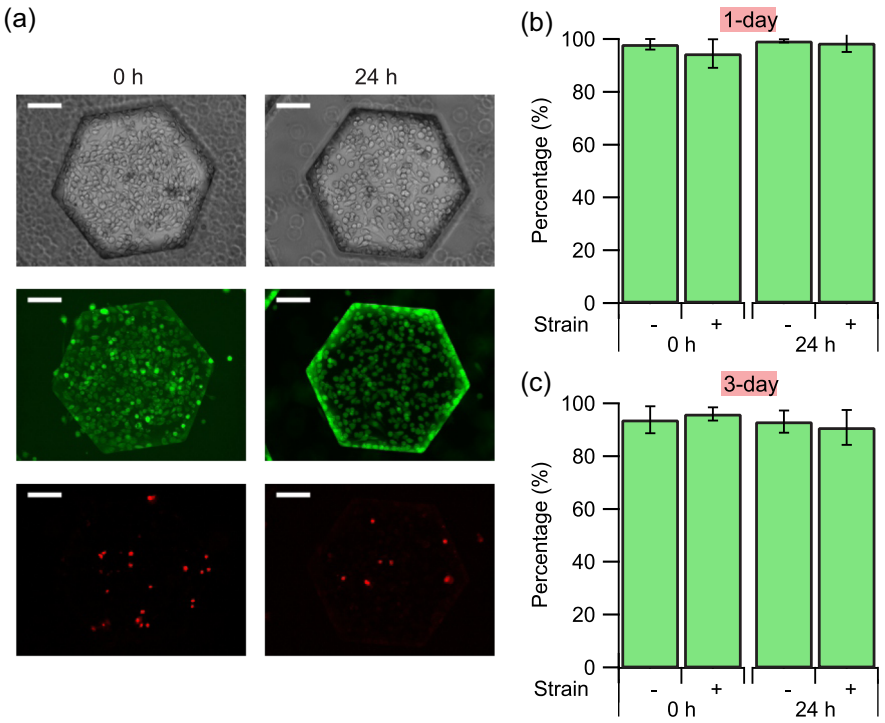

FIGURE 6 (a) Cell viability assay using calcein to mark live cells (green) and propidium iodide to mark dead cells (red) immediately after the strain test denoted by 0 hr and after incubation for 24 hr. The top images are phase-contrast images of the cells followed by green and red fluorescence emission images showing the distribution of the live and the dead cells, respectively. Scale bar = 100 μm. Deduced percentages of viable cells at Day 1 (b) and Day 3 (c), with and without application of a periodic strain of 5% at a frequency of 0.2 Hz for a duration of 1 hr. Values are expressed as mean ± standard error of the mean. These measurements were repeated on at least two different occasions and on five different cell-cultured monolayers for 1-day and 3-day cultures [Color figure can be viewed at wileyonlinelibrary.com]

3.5 | Cell morphology

Cell behaviors are sensitive to stiffness, morphology, and biochemical composition of the substrate. On a suspended monolayer of gelatin nanofibers, cells tend to explore adhesive contacts, resulting in cell membrane deformation and an increase in contact area with the nanofibers. If the cell density on the monolayer is high enough, cell–cell contacts become important at the expense of adhesion with the nanofibers (Dahlin, Kasper, & Mikos, 2011; Wu et al., 2011). When a periodic deformation is applied, the cell cytoskeleton is reorganized due to mechanotransduction. We investigated the effect of periodic strain on actin cytoskeleton rearrangement which is the most studied cytoskeleton element. We examined these effects by analyzing immunofluorescence images of A549 cells on the culture patch after incubation for 1 and 3 days and applying a periodic strain of about 5% at a frequency of 0.2 Hz. The strain level was chosen to be in the range of alveolar strain during normal breathing and the applied frequency to match the normal breathing rate (Fredberg & Kamm, 2006; Guenat & Berthiaume, 2018; Roan & Waters, 2011; Waters et al., 2012). Pressure application continued for a period of 1 hr which has been shown to prevent tissue damage at similar strain levels (Tschumperlin & Margulies, 1998; Tschumperlin et al., 2000). Similar test conditions have been used in modeling nanoparticle interactions with lung alveoli, mechanical ventilation-induced alveolar tissue injury, as well as obstructive sleep apnea (Campillo et al., 2016; Davidovich et al., 2013; Huh et al., 2010). After the strain tests, the cells were immediately fixed and stained with phalloidin and DAPI to mark actin filaments in green and nuclei in blue, respectively.

Figure 7 shows the effect of strain on the cell layer formation. The immunostaining images were acquired with cells on gelatin monolayers after 3 days of incubation without the application of mechanical strain as shown in Figure 7a. In parallel, images were obtained with cells after 3 days of incubation and after application of strain as shown in Figure 7b. Few of the image sections were selected for the close comparison of in-plan and out-plan cell distributions. Images marked $Z = 0$ indicate top layers (out-plan), the ones labeled $Z = +3$ μm or +6 μm show the main layers (in-plan), and the other sections labeled $Z = +10$ μm represent bottom layers corresponding to cell–nanofiber contact (out-plan). The parallel examination shows that without the strain step, the cell distribution was not homogenous on the gelatin monolayer and some cells went out of the main plan. On the contrary, the strain step resulted in a monolayer of cells in the whole honeycomb compartment, indicating that the periodic strain may release the cells from their original anchor points with the nanofibers resulting in a more homogenous redistribution which indicates the formation of a tighter cell layer.

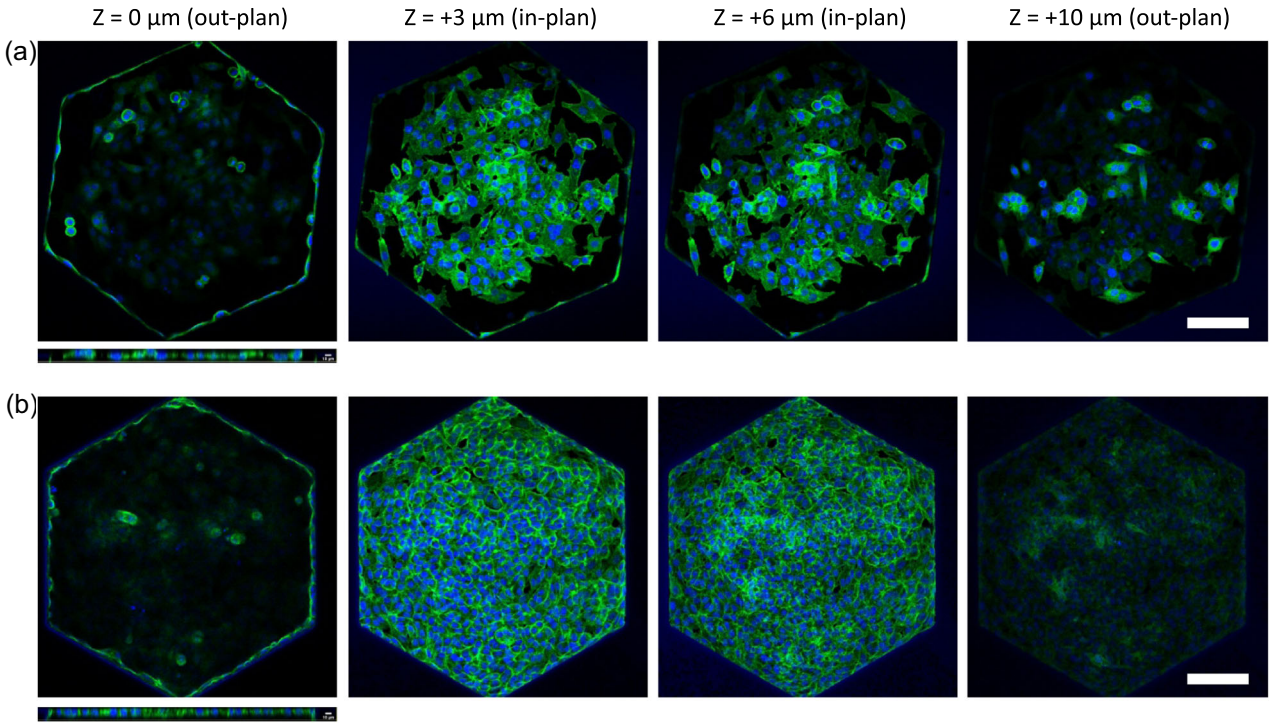

FIGURE 7 Selected sections of immunostaining confocal images of cells on culture patch after incubation for 4 days: (a) without mechanical strain, and (b) with a periodic strain (level 5% at a frequency of 0.2 Hz for a duration of 1 hr) at Day 3. F-actin was stained with Alexa Fluor 488-conjugated phalloidin (green) and nuclei with DAPI (blue). DAPI, 4′,6-diamidino-2-phenylindole. Scale bar = 100 µm [Color figure can be viewed at wileyonlinelibrary.com]

Figure 8a shows examples of the confocal images of the cells found at the center and the peripheral parts of the monolayers. The images were taken at different height levels, and in this figure, "bottom" corresponds to cell–nanofiber contact and "maximum" to maximum intensity projection of pixel value. Selected areas from "bottom" images are enlarged and shown to the left of these images. The enlarged areas are marked with dashed line squares. In Supporting Information Data S6, additional images are shown at the level of the nuclei which is about 5 µm above the cell–nanofiber contact and denoted by "middle," and at a location that is 12 µm above the contact and denoted by "top."

Cells that did not experience any strain after 1 day of culture displayed a number of green fluorescence accumulations in the form of spots in all cell areas. These spots are visible in cell–nanofiber contact-level images and are marked with yellow arrows in Figure 8a. The formation of these accumulations indicates a nonhomogeneous distribution of actin filaments (F-actin) at the cell–nanofiber contact level. Due also to a strong cell–nanofiber contact, cells generally display a non-rounded morphology which is more clearly visible in the nuclei-level images shown in Figure S6. Cells of 1-day culture that experienced strain show a reduced number of F-actin spots particularly for the cells located in the central parts of the monolayer where the strain is the highest. Additionally, these cells show a more rounded morphology after the strain application which is visible in both the central and the peripheral parts of the monolayer. Several of these observations are persistent in cells of 3-day culture. For example, these cells also show F-actin accumulations and they also form a non-rounded morphology. However, the cell morphology change after the mechanical strain is less obvious with these cells which is also related to the cell–cell contacts.

Figure 8b shows the effect of strain on the percentage of cells with clear F-actin accumulations in the cell areas inspected at the level of cell–nanofiber contact. Application of strain is found to reduce the number of clear F-actin accumulations in cells of 1-day as well as 3-day cultures. The effect is found to be significant in both the central and peripheral parts of the gelatin monolayer, although more cells with clear F-actin accumulations are generally found in the central part than the peripheral part. The latter effect is associated with denser fibrous parts in the periphery. Clear F-actin spots also became less visible with incubation time which is associated with effects from increased cell–cell contacts with a longer incubation.

Figure 8c shows the effect of strain on cell morphology. We express cell morphology in terms of a roundness parameter, which is defined by $4A/\pi d^2$, where A is the cell area and d the length of the major axis. We find that with cell cultures of 1 day, the cell morphology is largely influenced by the nanofibers' network due to the effect of contact guidance. For example, a periodic deformation of the network at a physiological strain level of 5% is sufficient for remodeling the cytoskeleton and to make the cells more rounded. With high cell number on the monolayer, the cell–cell interactions become important and reduce the influence of the underlying mobile network on changing the cell

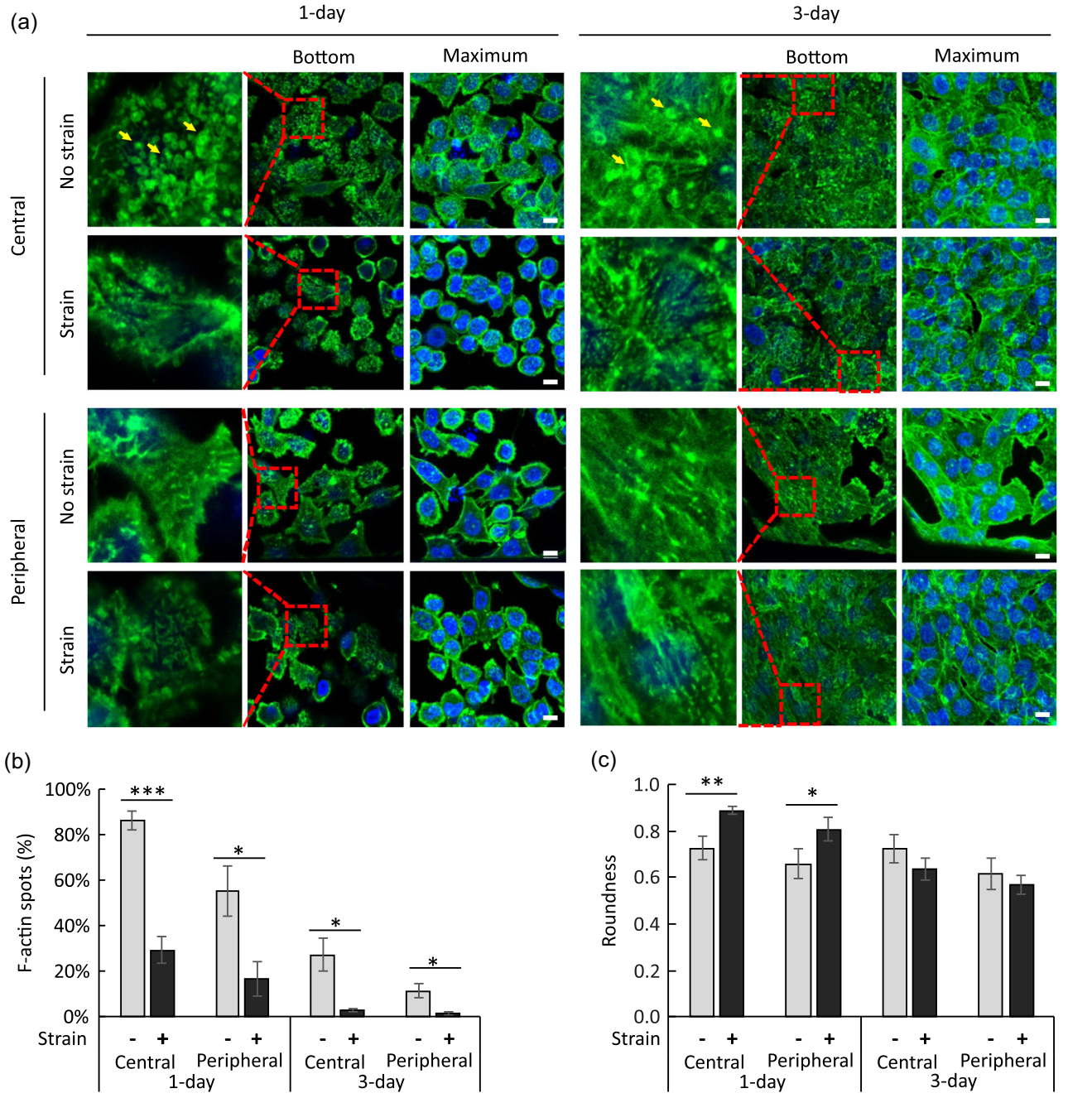

FIGURE 8 (a) Confocal images of immunostained cells on culture patches after 1 day and 3 days of culture in static condition and with a periodic strain of 5% at a frequency of 0.2 Hz for a duration of 1 hr. Images were taken from the cells in the central and the peripheral parts of the gelatin monolayers. Single confocal sections from the cell–nanofiber contact level ("bottom") and maximum intensity projections of z-stacks ("maximum") are shown. Dashed line squares on "bottom" images show selected areas which are enlarged and shown to the left. Yellow arrows point at green fluorescence accumulations which are observable in the enlarged areas. F-actin was stained with Alexa Fluor 488-conjugated phalloidin (green) and nuclei with DAPI (blue). Scale bars = 10 μm. (b) Deduced percentage of cells with clear F-actin accumulations in the cell areas at the cell–nanofiber contact level at Day 1 and Day 3 in static condition and with strain (5%, 0.2 Hz, 1 hr). (c) Deduced cell roundness at Day 1 and Day 3 in static condition and with strain (5%, 0.2 Hz, 1 hr). The measurements were repeated on at least two different occasions and on three different cell-cultured monolayers for 1-day and 3-day cultures. Values are expressed as mean ± standard error of the mean. DAPI, 4′,6-diamidino-2-phenylindole. *$p < .05$; **$p < .001$; ***$p < .0001$ (Student's t test) [Color figure can be viewed at wileyonlinelibrary.com]

morphology. Although strong cell–nanofiber adhesion prohibits cell movements, periodic deformation helps the cells to move and to form a homogeneous epithelial layer in the central and peripheral parts of the monolayer. The result is that the cells appear to be less rounded after the strain step in 3-day cultures which is evident from a decrease in roundness parameter of the cells. These results corroborate previous observations of good adhesion between gelatin nanofibers and other cells such as human pluripotent stem cells, motor neuron cells, primary

hippocampal neurons and cardiomyocytes (Liu et al., 2014; Tang, Liu, Li, Yu, Severino, et al., 2016; Tang, Liu, Li, Yu, Wang, et al., 2016; Tang et al., 2017), and extends the applicability of gelatin nanofiber monolayers to alveolar cells.

4 | CONCLUSIONS

We have demonstrated that suspended monolayers of gelatin nanofibers could be used as membrane-like substrates for alveolar cell culture and periodic deformation to mimic the alveolar air–tissue interface. Comparing with the more conventional approaches using PDMS membrane, this technique is advantageous: Gelatin is derived from collagen, the monolayer has a microporous structure providing the possibility of the air–liquid interface culture and minimal material contact with the cells, the monolayer has a relatively low elastic modulus resulting in its strain modulation in a physiological range. A549 culture on the monolayers showed viability after periodic strain of 5% at 0.2 Hz for 1 hr for cultures of 1-day and 3-days. Our results showed that the strain can efficiently remodel the actin cytoskeleton of the cells in the cell–nanofiber contact positions by reducing the number of anchoring points leading to a better tissue formation. The methods and tools developed herein are applicable to diverse lung studies, for example, inhalation toxicology and therapy.

ACKNOWLEDGMENTS

Maria Sarkis, Oliver Brookes, and Elrade Rofaani are thanked for fruitful discussions. Ayako Yamada is thanked for help during the fabrication of honeycomb microframe. Agence Nationale de la Recherche (ANR) is gratefully acknowledged for their financial support of this study through ANR-17-CE09-0017 (AlveolusMimics).

CONFLICT OF INTERESTS

The authors declare that there are no conflict of interests.

ORCID

Milad Radiom http://orcid.org/0000-0002-6339-9288
Juan Peng-Wang https://orcid.org/0000-0002-8407-9793
Armelle Baeza-Squiban https://orcid.org/0000-0003-2403-8823
Jean-François Berret https://orcid.org/0000-0001-5458-8653
Yong Chen https://orcid.org/0000-0002-2903-8753

REFERENCES

Bilek, A. M., Dee, K. C., & Gaver, D. P., 3rd. (2003). Mechanisms of surface-tension-induced epithelial cell damage in a model of pulmonary airway reopening. *Journal of Applied Physiology*, *94*(2), 770–783. https://doi.org/10.1152/japplphysiol.00764.2002

Boxshall, K., Wu, M.-H., Cui, Z., Cui, Z., Watts, J. F., & Baker, M. A. (2006). Simple surface treatments to modify protein adsorption and cell attachment properties within a poly(dimethylsiloxane) microbioreactor. *Surface and Interface Analysis*, *38*(4), 198–201. https://doi.org/10.1002/sia.2274

Brückner, B. R., & Janshoff, A. (2015). Elastic properties of epithelial cells probed by atomic force microscopy. *Biochimica et Biophysica Acta*, *1853*(11), 3075–3082. https://doi.org/10.1016/j.bbamcr.2015.07.010

Campillo, N., Jorba, I., Schaedel, L., Casals, B., Gozal, D., Farre, R., … Navajas, D. (2016). A novel chip for cyclic stretch and intermittent hypoxia cell exposures mimicking obstructive sleep apnea. *Frontiers in Physiology*, *7*, 319. https://doi.org/10.3389/fphys.2016.00319

Chess, P. R., Toia, L., & Finkelstein, J. N. (2000). Mechanical strain-induced proliferation and signaling in pulmonary epithelial H441 cells. *American Journal of Physiology*, *279*(1), L43–L51. https://doi.org/10.1152/ajplung.2000.279.1.L43

Dahlin, R. L., Kasper, F. K., & Mikos, A. G. (2011). Polymeric nanofibers in tissue engineering. *Tissue Engineering*, *17*(5), 349–364. https://doi.org/10.1089/ten.TEB.2011.0238

Davidovich, N., DiPaolo, B. C., Lawrence, G. G., Chhour, P., Yehya, N., & Margulies, S. S. (2013). Cyclic stretch-induced oxidative stress increases pulmonary alveolar epithelial permeability. *American Journal of Respiratory Cell and Molecular Biology*, *49*(1), 156–164. https://doi.org/10.1165/rcmb.2012-0252OC

Desai, T. J., Brownfield, D. G., & Krasnow, M. A. (2014). Alveolar progenitor and stem cells in lung development, renewal and cancer. *Nature*, *507*, 190–194. https://doi.org/10.1038/nature12930.

Douville, N. J., Zamankhan, P., Tung, Y. C., Li, R., Vaughan, B. L., Tai, C. F., … Takayama, S. (2011). Combination of fluid and solid mechanical stresses contribute to cell death and detachment in a microfluidic alveolar model. *Lab on a Chip*, *11*(4), 609–619. https://doi.org/10.1039/c0lc00251h

Dunsmore, S. E., & Rannels, D. E. (1996). Extracellular matrix biology in the lung. *American Journal of Physiology*, *270*(1), L3–L27. https://doi.org/10.1152/ajplung.1996.270.1.L3

Fehrenbach, H. (2001). Alveolar epithelial type II cell: Defender of the alveolus revisited. *Respiratory Research*, *2*(1), 33–46. https://doi.org/10.1186/rr36.

Frantz, C., Stewart, K. M., & Weaver, V. M. (2010). The extracellular matrix at a glance. *Journal of Cell Science*, *123*(Pt 24), 4195–4200. https://doi.org/10.1242/jcs.023820

Fredberg, J. J., & Kamm, R. D. (2006). Stress transmission in the lung: Pathways from organ to molecule. *Annual Review of Physiology*, *68*, 507–541. https://doi.org/10.1146/annurev.physiol.68.072304.114110

Fung, Y. C. (1988). A model of the lung structure and its validation. *Journal of Applied Physiology*, *64*(5), 2132–2141. https://doi.org/10.1152/jappl.1988.64.5.2132

Guenat, O. T., & Berthiaume, F. (2018). Incorporating mechanical strain in organs-on-a-chip: Lung and skin. *Biomicrofluidics*, *12*(4), 042207. https://doi.org/10.1063/1.5024895

Hammerschmidt, S., Kuhn, H., Grasenack, T., Gessner, C., & Wirtz, H. (2004). Apoptosis and necrosis induced by cyclic mechanical stretching in alveolar type II cells. *American Journal of Respiratory Cell and Molecular Biology*, *30*(3), 396–402. https://doi.org/10.1165/rcmb.2003-0136OC

Harris, A. R., Peter, L., Bellis, J., Baum, B., Kabla, A. J., & Charras, G. T. (2012). Characterizing the mechanics of cultured cell monolayers. *Proceedings of the National Academy of Sciences of the United States of America*, *109*(41), 16449–16454. https://doi.org/10.1073/pnas.1213301109

He, X.-T., Chen, Q., Sun, J.-Y., & Zheng, Z.-L. (2012). Large-deflection axisymmetric deformation of circular clamped plates with different moduli in tension and compression. *International Journal of Mechanical Sciences*, *62*, 103–110. https://doi.org/10.1016/j.ijmecsci.2012.06.003

Hermanns, M. I., Fuchs, S., Bock, M., Wenzel, K., Mayer, E., Kehe, K., … Kirkpatrick, C. J. (2009). Primary human coculture model of alveolo-capillary unit to study mechanisms of injury to peripheral lung. *Cell and Tissue Research*, *336*(1), 91–105. https://doi.org/10.1007/s00441-008-0750-1

Higuita-Castro, N., Mihai, C., Hansford, D. J., & Ghadiali, S. N. (2014). Influence of airway wall compliance on epithelial cell injury and adhesion during interfacial flows. *Journal of Applied Physiology*, *117*(11), 1231–1242. https://doi.org/10.1152/japplphysiol.00752.2013

Higuita-Castro, N., Nelson, M. T., Shukla, V., Agudelo-Garcia, P. A., Zhang, W., Duarte-Sanmiguel, S. M., … Ghadiali, S. N. (2017). Using a

novel microfabricated model of the alveolar-capillary barrier to investigate the effect of matrix structure on atelectrauma. *Scientific Reports*, *7*(1), 11623. https://doi.org/10.1038/s41598-017-12044-9

Huh, D., Fujioka, H., Tung, Y. C., Futai, N., Paine, R., 3rd, Grotberg, J. B., & Takayama, S. (2007). Acoustically detectable cellular-level lung injury induced by fluid mechanical stresses in microfluidic airway systems. *Proceedings of the National Academy of Sciences of the United States of America*, *104*(48), 18886–18891. https://doi.org/10.1073/pnas.0610868104

Huh, D., Leslie, D. C., Matthews, B. D., Fraser, J. P., Jurek, S., Hamilton, G. A., … Ingber, D. E. (2012). A human disease model of drug toxicity-induced pulmonary edema in a lung-on-a-chip microdevice. *Science Translational Medicine*, *4*(159), 159ra147. https://doi.org/10.1126/scitranslmed.3004249

Huh, D., Matthews, B. D., Mammoto, A., Montoya-Zavala, M., Hsin, H. Y., & Ingber, D. E. (2010). Reconstituting organ-level lung functions on a chip. *Science*, *328*(5986), 1662–1668. https://doi.org/10.1126/science.1188302

Israelachvili, J. N. (2011). *Intermolecular and surface forces* (3rd ed.). Boston: Academic Press.

Jacob, A. M., & Gaver, D. P., 3rd. (2012). Atelectrauma disrupts pulmonary epithelial barrier integrity and alters the distribution of tight junction proteins ZO-1 and claudin 4. *Journal of Applied Physiology*, *113*(9), 1377–1387. https://doi.org/10.1152/japplphysiol.01432.2011

Jain, A., Barrile, R., van der Meer, A. D., Mammoto, A., Mammoto, T., De Ceunynck, K., … Ingber, D. E. (2018). Primary human lung alveolus-on-a-chip model of intravascular thrombosis for assessment of therapeutics. *Clinical Pharmacology and Therapeutics*, *103*(2), 332–340. https://doi.org/10.1002/cpt.742

Kamotani, Y., Bersano-Begey, T., Kato, N., Tung, Y. C., Huh, D., Song, J. W., & Takayama, S. (2008). Individually programmable cell stretching microwell arrays actuated by a Braille display. *Biomaterials*, *29*(17), 2646–2655. https://doi.org/10.1016/j.biomaterials.2008.02.019

Kim, S. E., Heo, D. N., Lee, J. B., Kim, J. R., Park, S. H., Jeon, S. H., & Kwon, I. K. (2009). Electrospun gelatin/polyurethane blended nanofibers for wound healing. *Biomedical Materials*, *4*(4), 044106. https://doi.org/10.1088/1748-6041/4/4/044106

Lieber, M., Smith, B., Szakal, A., Nelson-Rees, W., & Todaro, G. (1976). A continuous tumor-cell line from a human lung carcinoma with properties of type II alveolar epithelial cells. *International Journal of Cancer*, *17*(1), 62–70. https://doi.org/10.1002/ijc.2910170110

Liu, L., Yoshioka, M., Nakajima, M., Ogasawara, A., Liu, J., Hasegawa, K., … Chen, Y. (2014). Nanofibrous gelatin substrates for long-term expansion of human pluripotent stem cells. *Biomaterials*, *35*(24), 6259–6267. https://doi.org/10.1016/j.biomaterials.2014.04.024

Maina, J. N., & West, J. B. (2005). Thin and strong! The bioengineering dilemma in the structural and functional design of the blood-gas barrier. *Physiological Reviews*, *85*(3), 811–844. https://doi.org/10.1152/physrev.00022.2004

Nalayanda, D. D., Puleo, C., Fulton, W. B., Sharpe, L. M., Wang, T. H., & Abdullah, F. (2009). An open-access microfluidic model for lung-specific functional studies at an air-liquid interface. *Biomedical Microdevices*, *11*(5), 1081–1089. https://doi.org/10.1007/s10544-009-9325-5

Park, S. E., Georgescu, A., & Huh, D. (2019). Organoids-on-a-chip. *Science*, *364*(6444), 960–965. https://doi.org/10.1126/science.aaw7894

Perlman, C. E., & Bhattacharya, J. (2007). Alveolar expansion imaged by optical sectioning microscopy. *Journal of Applied Physiology*, *103*(3), 1037–1044. https://doi.org/10.1152/japplphysiol.00160.2007

Polio, S. R., Kundu, A. N., Dougan, C. E., Birch, N. P., Aurian-Blajeni, D. E., Schiffman, J. D., … Peyton, S. R. (2018). Cross-platform mechanical characterization of lung tissue. *PLOS One*, *13*(10), e0204765. https://doi.org/10.1371/journal.pone.0204765

Qian, X., Zhang, W., Peng, C., Liu, X., Yu, Q., Ni, K., & Wang, X. (2016). Characterizing the deformation of the polydimethylsiloxane (PDMS) membrane for microfluidic system through image processing. *Micromachines*, *7*(5), 92. https://doi.org/10.3390/mi7050092

Roan, E., & Waters, C. M. (2011). What do we know about mechanical strain in lung alveoli? *American Journal of Physiology*, *301*(5), L625–L635. https://doi.org/10.1152/ajplung.00105.2011

Roan, E., Wilhelm, K. R., & Waters, C. M. (2015). Kymographic imaging of the elastic modulus of epithelial cells during the onset of migration. *Biophysical Journal*, *109*(10), 2051–2057. https://doi.org/10.1016/j.bpj.2015.10.005

Robert, H. N. (2000). *Lung surfactants: Basic science and clinical applications. Lung Biology in Health and Disease*, (Vol. 149). New York: Marcel Dekker Inc.

Sanchez-Esteban, J., Cicchiello, L. A., Wang, Y., Tsai, S. W., Williams, L. K., Torday, J. S., & Rubin, L. P. (2001). Mechanical stretch promotes alveolar epithelial type II cell differentiation. *Journal of Applied Physiology*, *91*(2), 589–595. https://doi.org/10.1152/jappl.2001.91.2.589

Scott, J. E., Yang, S. Y., Stanik, E., & Anderson, J. E. (1993). Influence of strain on [3H]thymidine incorporation, surfactant-related phospholipid synthesis, and cAMP levels in fetal type II alveolar cells. *American Journal of Respiratory Cell and Molecular Biology*, *8*(3), 258–265. https://doi.org/10.1165/ajrcmb/8.3.258

Stucki, A. O., Stucki, J. D., Hall, S. R. R., Felder, M., Mermoud, Y., Schmid, R. A., … Guenat, O. T. (2015). A lung-on-a-chip array with an integrated bio-inspired respiration mechanism. *Lab on a Chip*, *15*(5), 1302–1310. https://doi.org/10.1039/C4LC01252F

Stucki, J. D., Hobi, N., Galimov, A., Stucki, A. O., Schneider-Daum, N., Lehr, C.-M., … Guenat, O. T. (2018). Medium throughput breathing human primary cell alveolus-on-chip model. *Scientific Reports*, *8*(1), 14359. https://doi.org/10.1038/s41598-018-32523-x

Tang, Y., Liu, L., Li, J., Yu, L., Severino, F. P. U., Wang, L., … Chen, Y. (2016). Effective motor neuron differentiation of hiPSCs on a patch made of crosslinked monolayer gelatin nanofibers. *Journal of Materials Chemistry B*, *4*(19), 3305–3312. https://doi.org/10.1039/C6TB00351F

Tang, Y., Liu, L., Li, J., Yu, L., Wang, L., Shi, J., & Chen, Y. (2016). Induction and differentiation of human induced pluripotent stem cells into functional cardiomyocytes on a compartmented monolayer of gelatin nanofibers. *Nanoscale*, *8*(30), 14530–14540. https://doi.org/10.1039/C6NR04545F

Tang, Y., Ulloa Severino, F. P., Iseppon, F., Torre, V., & Chen, Y. (2017). Patch method for culture of primary hippocampal neurons. *Microelectronic Engineering*, *175*, 61–66. https://doi.org/10.1016/j.mee.2017.01.012

Tenenbaum-Katan, J., Artzy-Schnirman, A., Fishler, R., Korin, N., & Sznitman, J. (2018). Biomimetics of the pulmonary environment in vitro: A microfluidics perspective. *Biomicrofluidics*, *12*(4), 042209. https://doi.org/10.1063/1.5023034

Thangawng, A. L., Ruoff, R. S., Swartz, M. A., & Glucksberg, M. R. (2007). An ultra-thin PDMS membrane as a bio/micro–nano interface: Fabrication and characterization. *Biomedical Microdevices*, *9*(4), 587–595. https://doi.org/10.1007/s10544-007-9070-6

Townsley, M. I. (2012). Structure and composition of pulmonary arteries, capillaries, and veins. *Comprehensive Physiology*, *2*(1), 675–709. https://doi.org/10.1002/cphy.c100081

Trepat, X., Grabulosa, M., Puig, F., Maksym, G. N., Navajas, D., & Farre, R. (2004). Viscoelasticity of human alveolar epithelial cells subjected to stretch. *American Journal of Physiology*, *287*(5), L1025–L1034. https://doi.org/10.1152/ajplung.00077.2004

Tschumperlin, D. J., & Margulies, S. S. (1998). Equibiaxial deformation-induced injury of alveolar epithelial cells in vitro. *American Journal of Physiology*, *275*(6), L1173–L1183. https://doi.org/10.1152/ajplung.1998.275.6.L1173

Tschumperlin, D. J., Oswari, J., & Margulies, A. S. (2000). Deformation-induced injury of alveolar epithelial cells. Effect of frequency, duration, and amplitude. *American Journal of Respiratory and Critical Care Medicine*, *162*(2 Pt 1), 357–362. https://doi.org/10.1164/ajrccm.162.2.9807003

van Meer, B. J., de Vries, H., Firth, K. S. A., van Weerd, J., Tertoolen, L. G. J., Karperien, H. B. J., … Mummery, C. L. (2017). Small molecule absorption by PDMS in the context of drug response bioassays. *Biochemical and Biophysical Research Communications*, *482*(2), 323–328. https://doi.org/10.1016/j.bbrc.2016.11.062

Vlahakis, N. E., Schroeder, M. A., Limper, A. H., & Hubmayr, R. D. (1999). Stretch induces cytokine release by alveolar epithelial cells in vitro. *American Journal of Physiology*, *277*(1), L167–L173. https://doi.org/10.1152/ajplung.1999.277.1.L167

Wan, K.-T., Guo, S., & Dillard, D. A. (2003). A theoretical and numerical study of a thin clamped circular film under an external load in the presence of a tensile residual stress. *Thin Solid Films*, *425*(1), 150–162. https://doi.org/10.1016/S0040-6090(02)01103-3

Wan, K.-T., & Lim, S.-C. (1998). The bending to stretching transition of a pressurized blister test. *International Journal of Fracture*, *92*(4), 43–47. https://doi.org/10.1023/A:1007612016147

Waters, C. M., Roan, E., & Navajas, D. (2012). Mechanobiology in lung epithelial cells: Measurements, perturbations, and responses. *Comprehensive Physiology*, *2*(1), 1–29. https://doi.org/10.1002/cphy.c100090

Weibel, E. R. (2015). On the tricks alveolar epithelial cells play to make a good lung. *American Journal of Respiratory and Critical Care Medicine*, *191*(5), 504–513. https://doi.org/10.1164/rccm.201409-1663OE

Wu, S.-C., Chang, W.-H., Dong, G.-C., Chen, K.-Y., Chen, Y.-S., & Yao, C.-H. (2011). Cell adhesion and proliferation enhancement by gelatin nanofiber scaffolds. *Journal of Bioactive and Compatible Polymers*, *26*(6), 565–577. https://doi.org/10.1177/0883911511423563

Zamprogno, P., Wüthrich, S., Achenbach, S., Stucki, J. D., Hobi, N., Schneider-Daum, N., … Guenat, O. T. (2019). Second-generation lung-on-a-chip array with a stretchable biological membrane. *bioRxiv*, 608919. https://doi.org/10.1101/608919

Zhang, S., Huang, Y., Yang, X., Mei, F., Ma, Q., Chen, G., … Deng, X. (2009). Gelatin nanofibrous membrane fabricated by electrospinning of aqueous gelatin solution for guided tissue regeneration. *Journal of Biomedical Materials Research Part A*, *90A*(3), 671–679. https://doi.org/10.1002/jbm.a.32136

Zhang, Y. (2016). Large deflection of clamped circular plate and accuracy of its approximate analytical solutions. *Science China Physics, Mechanics & Astronomy*, *59*(2), 624602. https://doi.org/10.1007/s11433-015-5751-y

Zhou, Y., Horowitz, J. C., Naba, A., Ambalavanan, N., Atabai, K., Balestrini, J., … Thannickal, V. J. (2018). Extracellular matrix in lung development, homeostasis and disease. *Matrix Biology*, *73*, 77–104. https://doi.org/10.1016/j.matbio.2018.03.005

SUPPORTING INFORMATION

Additional supporting information may be found online in the Supporting Information section.

How to cite this article: Radiom M, He Y, Peng-Wang J, Baeza-Squiban A, Berret J-F, Chen Y. Alveolar mimics with periodic strain and its effect on the cell layer formation. *Biotechnology and Bioengineering*. 2020;117:2827–2841. https://doi.org/10.1002/bit.27458

Appendix D
Realization of a bioreactor for patch-based hiPSC differentiation

Realization of a bioreactor for patch-based hiPSC differentiation

The main objective of this PhD study is to develop an alveolar model which also involves immune cells such as macrophages. As all immune cells are derivatives of hematopoietic stem cells (HSCs), we developed a new type of bioreactor for on patch hiPSCs differentiation to hematopoietic stem cells. The derived HSCs are then used to differentiate them to macrophages, neutrophils, etc.

1. Bioreactor design

To be compatible with our culture patch, we designed a rotational bioreactor (Fig 1) in which several culture patches are inserted in a patch mounting device (disk) and the rotation is controlled with a microprocessor and a step motor. The culture medium can be pumped in the culture dish through an inlet and pumped out through an outlet, both controlled with the same processor.

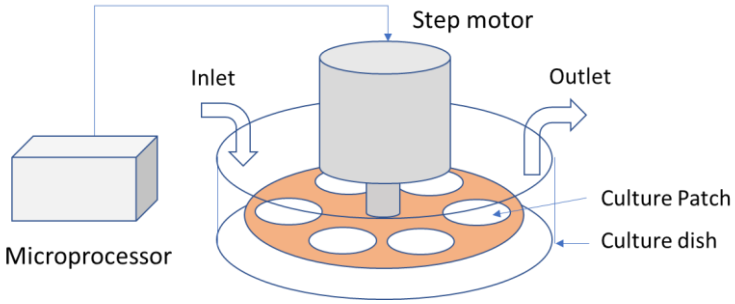

Figure 1. Schematic of a bioreactor for patch-based culture and differentiation.

As can be seen, this design is very simple but flexible and versatile for various applications. The operation of this system is easy but accurate since all steps, including rotation speed, operation time, disk position, and flow, are controlled with a microprocessor. When used for HSC production, the culture medium containing different differentiation can be pumped in and exchanged freely, which allows harvesting the produced HSCs in time. Depending on the rotation speed, the centrifugation force varies which can remove species of different sizes, mass and attachment. Besides, this system can be installed in an incubator equipped with a CCD camera, which allows real-time and in situ imaging.

Fig 2 shows the design of the patch mounting device, which consists of three layers, two in plastic and one in PDMS.

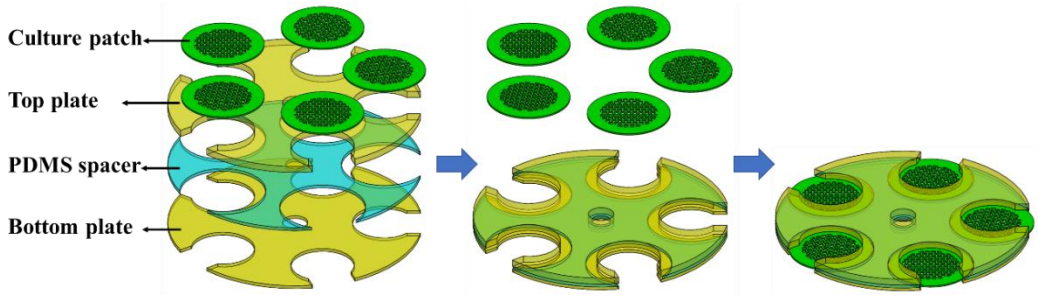

Figure 2. Schematic of a patch mounting device assembled with a top plate, a PDMS spacer and a bottom plate. Left: exploded; Middle: before patch mounting; Right: after patch mounting.

Using this device, we can integrate our culture patch into dynamic culture and control the shear force by adjusting the rotation speed. Meanwhile, the agitation produced by the rotation is more conducive to the diffusion of nutrients in the medium. Therefore, dynamic culture such as differentiation and collection of hematopoietic stem cells can be implemented on this device.

2. Numerical simulation

1) Establishment of simulation model

The software COMSOL Multiphysics, was used to simulate the flow rate and centrifugal effect in a tissue culture dish of 60 mm. Firstly, we simplified and established a 2D model pattern in the software, as shown in Fig 3. Then, we chose simulation modules “Rotating Machinery, Laminar flow” and “Particle Tracing for Fluid Flow” for numerical simulation based on the Finite-Element Method (FEM).

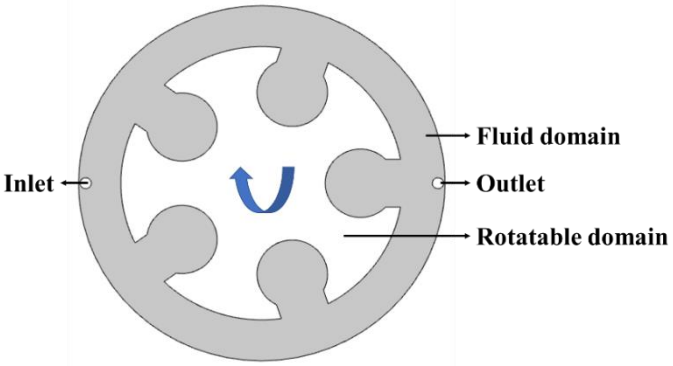

Figure 3. Geometry of the disk in culture dish for 2D modeling. White: plastic part of the plate; Gray: Free space filled by culture medium.

Numerical simulation has been performed with the fluid domain as shown in Fig 3 and water was used as the fluid because of its similar features to the culture medium. Before the simulation, we preset the whole timing to 20 s, the rotating speed to a constant 60 rpm, the inlet

flow rate to 0.02 m/s in the first 1 s and 0 m/s in the later 19 s by multiplying the function with 0.02 m/s (see Fig 4). The particle tracing is based on the velocity field of flow and was introduced from the same inlet.

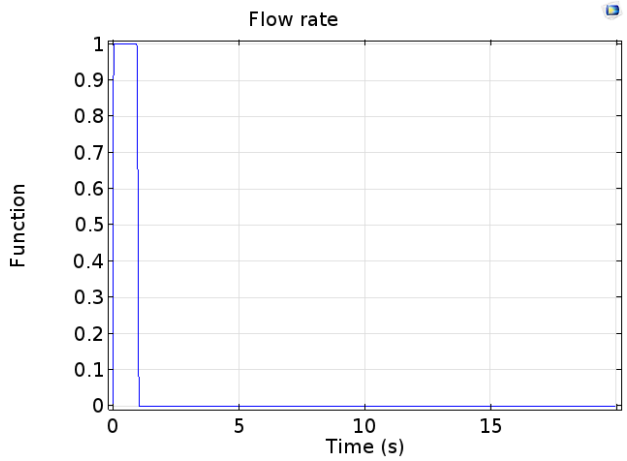

Figure 4. Calculated variation of flow rate as a function of time

2) Results of simulation

Fig 5 shows the change of the velocity in the dish during the rotation of the disk. It can be found that under a constant rotation, the velocity field can quickly reach an equilibrium state and show a uniform gradient decrease along the center to the outwards. In addition, there is also a velocity distribution in each hole which is used to hold the culture patch, showing smaller velocity near the center and larger near the "estuary". After 10s, the change of the flow field is not obvious, achieving a balanced and uniform distribution of flow velocity.

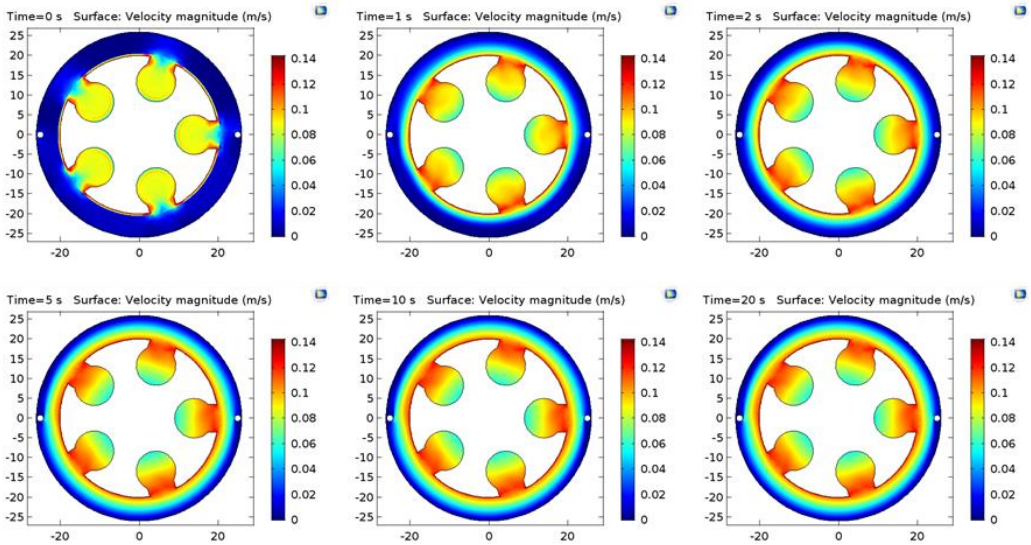

Figure 5. Velocity field at 0 s, 1 s, 2 s, 5 s, 10 s, 20 s

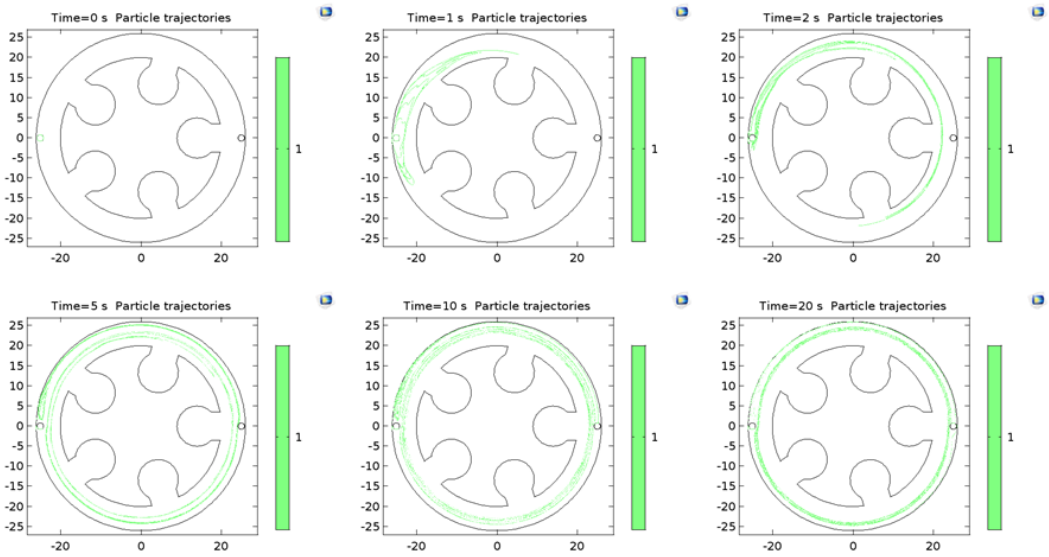

Figure 6. Particle distribution under the centrifugal force at 0 s, 1 s, 2 s, 5 s, 10 s, 20 s

Fig 6 shows a particle tracking method to simulate the particle distribution in the case of rotation. It can be found that in the case of the aforementioned flow field, the particles swim around the periphery due to the centrifugal force generated by the rotation. This method is very suitable for showing the efficacy of hematopoietic stem cell collection based on rotating. We also found that even in the same time, the flow velocity has reached equilibrium, but the particle distribution around the periphery still needs an extra 10s to achieve a stable drifting.

3) Fabrication of bioreactor

This bioreactor is composed of two plastic layers and one PDMS spacer. AutoCAD is used to design the pattern for fabrication. The plastic layers of 1mm thickness and 40 mm diameter were micro-milled on a G-code-driven CNC stage (Minetech, Japan). Then the PDMS spacer layer was cut by a cutting plotter (GRAPHTEC CE6000-40, Japan). Afterward, these three layers were assembled by a M3 screw made of nylon. Finally, the assembly was mounted on the rotating shaft of a motor, which is driven and controlled by Arduino programming. This prototype is shown in Fig 7. The motor was fixed on the dish cap separated by the support plate. In order to maintain the balance of the petri dish, we used a dish cap made of metal aluminum, which was pre-coated with a layer of anti-corrosion and non-toxic material. After testing, this bioreactor device can work under different rotational speeds (0 ~ 100 rpm) and volume of medium (~6 mL).

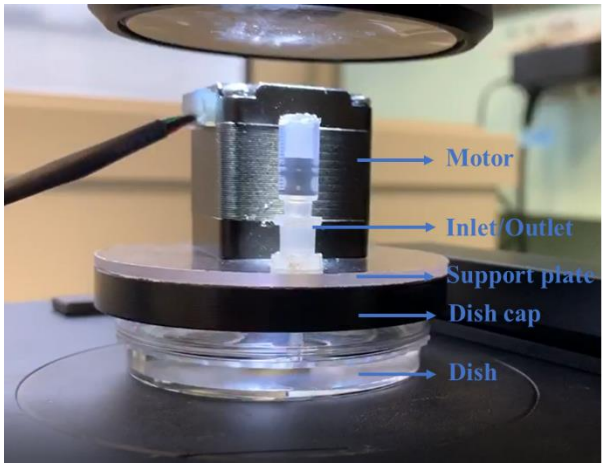

Figure 7. A bioreactor with a step motor, a support plate, a culture dish, one inlet, and one outlet on the stage of a microscope.

4) Conclusion

Based on the mechanical and fluid simulation, we designed and fabricated a rotational bioreactor. This is used for hiPSCs differentiation and HSCs collection. This device can also be used for other needs, such as shear-induced remodeling of cytoskeleton, spheroid formation with a caged device, etc. Finally, stack disks can be used in the same bioreactor, thereby providing a useful tool for large scale applications.

French summary
Résumé en français

Résumé en français

1. Introduction

Le poumon humain adulte est composé de millions de minuscules sacs (alvéoles) où les échanges gazeux ont lieu. La couche interne du sac, l'épithélium alvéolaire, est formée par deux types de cellules: le type 1 alvéolaire (AT1) et le type 2 alvéolaire (AT2). Elles adhèrent sur une couche de matrice extracellulaire spécifique, la membrane basale alvéolaire. L'ensemble des cellules alvéolaires et la membrane basale forment une barrière étanche qui sépare l'alvéole et les réseaux capillaires sanguins à l'extérieur du sac. On sait que les cellules AT1 couvrent 95% de la surface alvéolaire tandis que les cellules AT2 sécrètent un tensioactif pour recouvrir la couche interne du sac. Les cellules AT2 peuvent également générer des cellules AT1 pour réparer les alvéoles lésées. Il existe également des cellules immunitaires telles que les macrophages alvéolaires dans les sacs alvéolaires pour aider les alvéoles à fonctionner. De nombreuses maladies sont dues au dysfonctionnement des alvéoles à cause de l'infection, la pollution, le vieillissement, etc. Bien qu'un très grand nombre d'études soient réalisées, il n'existe que quelques modèles in vitro et aucun d'entre eux n'est capable de récapituler correctement les caractéristiques d'un alvéole humain en tenant compte, par exemple, de l'immunité des cellules constitutives et les propriétés de la membrane basale.

Le but de ce travail de thèse est de développer un modèle alvéolaire en différenciant les cellules souches pluripotentes induites humaines (hiPSCs) en cellules AT1 et AT2 et en les cultivant sur une membrane basale artificielle ultra-mince. Cette thèse était initialement prévue pour la fabrication de tissu alvéolaire mais l'épidémie du nouveau coronavirus SARS-CoV-2 est soudainement apparue, ce qui a obligé des travaux supplémentaires vers une étude immunologique impliquant à la fois une infection virale et un micro-environnement immunitaire.

Les hiPSCs sont obtenues par reprogrammation des cellules de tissu somatique. Ce sont des cellules souches de type embryonnaire capables de se renouveler pendant de nombreuses générations et de se différencier en différents types de cellules, y compris les cellules alvéolaires, endothéliales, et immunitaires. Cela permet de développer un modèle in vitro sophistiqué d'étudier l'interaction virus-cellule. Étant donné qu'ici le tissu alvéolaire et les cellules immunitaires sont tous deux dérivés de la même source des hiPSCs, ils sont intrinsèquement immun tolérants et immuno-compétents. Afin de récapituler la spécification de l'épithélium, des membranes basales artificielles ultra-minces sont réalisées en collagène de

type 4 et laminine. En outre, un système de culture automatique a été développé pour la différenciation des hiPSCs avec plusieurs types de milieu de culture ou la maturation des cellules différenciées à une longue période.

L'objectif de ce travail de thèse est de développer une méthode de différenciation automatique de hiPSCs vers un épithélium alvéolaire fonctionnel utilisable pour des études d'immunologie. La thèse est organisée en cinq chapitres, suivis d'une conclusion générale et de quatre annexes.

Le chapitre 2 présente des méthodes de fabrication et des techniques microfluidiques utilisées dans ce travail. La photolithographie, le moulage assisté par aspiration et l'électrofilage (électrospinning) qui sont nécessaires à la fabrication de dispositif de culture (patch) sont décrits. Un dispositif microfluidique pour l'intégration du patch ou d'un tissu est introduit. D'autres techniques de fabrication telles que le micro-fraisage et les traceurs de découpe qui sont utilisés comme accessoires pour la culture cellulaire et différenciation des hiPSCs sont également présentées.

Le chapitre 3 est consacré au développement d'un système de culture automatique pour la différenciation des hiPSCs. Ce système est composé d'une unité de distribution des milieux de culture, d'une unité d'incubation et d'une unité centrale de contrôle du processus. En utilisant un tel système, les cultures statiques et dynamiques sont comparées et la différenciation des hiPSCs en cardiomyocytes est étudiée pour montrer le potentiel du système pour différentes applications.

Le chapitre 4 se concentre sur la production d'épithélium alvéolaire par différenciation automatique des hiPSCs. Les organoïdes alvéolaires sont d'abord générés dans une couche de gel, qui peuvent être congelés, dégelés et dissociés en cellules uniques. Cela facilite grandement l'ensemble des processus d'ingénierie tissulaire puisque les organoïdes générés contiennent à la fois des cellules alvéolaires de type 1 et de type 2 et ils sont facilement utiles plus tard une fois produits. En replaçant les cellules dissociées sur un patch ou une membrane basale artificielle, l'épithélium alvéolaire peut être obtenu et étudié par des méthodes de caractérisations telles que la microscopie de fluorescence par marquage immunologique et la résistance électrique trans-épithéliale.

Le chapitre 5 décrit une étude préliminaire sur l'effet toxique de protéines S du nouveau coronavirus (SARS-Cov-2) aux cellules alvéolaires et les cardiomyocytes dérivées d'hiPSCs. On sait que l'infection du virus commence par le couple entre cette protéine virale et l'enzyme de conversion de l'angiotensine 2 (ACE2) exprimée sur la surface des cellules ciblées et que ce couple empêche la conversion de l'angiotensine 2 (Ang-II) en l'angiotensine 1-7 (Ang 1-7).

Or, Ang-II peut activer une voie de signalisation opposée de celle d'Ang (1-7), ce qui provoque un effet inflammatoire or toxique par le couple de protéine S et ACE2. Par mesure du niveau des espèces réactives oxydatives (ROS) dans les cellules alvéolaires ou le battement cardiaque en présence d'Ang II, nous devrions déterminer la toxicité des protéines S du SARS-Cov-2.

Le chapitre 6 est le résumé et la perspective de la thèse.

En annexe, plusieurs travaux liés à la thèse sont présentés, qui décrivent respectivement i) la fabrication de dispositifs à micro-cage pour la manipulation des sphéroïdes, ii) la fabrication de membrane basale artificielle ultra-fine, iii) l'effet de déformation périodique de la couche de nanofibres sur la cellule alvéolaire, et iv) la réalisation d'un bioréacteur spin-disque pour la différenciation des hiPSCs vers les cellules souches hématopoïétiques.

2. Différenciation automatique des cellules souches

1) Description du système

En tant que la première génération de plateforme du laboratoire, nous avons choisi de travailler avec un microcontrôleur ATmega 2560 monté sur une carte Arduino pour automatiser nos processus de culture et de différenciation (https://www.arduino.cc/). Les cartes Arduino sont disponibles dans le commerce et sont équipées de jeux de broches d'entrée / sortie (E / S) numériques et analogiques qui peuvent être interfacées avec les composants électroniques et pneumatiques ainsi que des circuits supplémentaires impliqués dans un système automatique. Les cartes fournissent également des interfaces de communication série vers un PC à l'aide d'un câble USB, ce qui permet de charger un programme avec une interface de programmation d'application simple.

Typiquement, cette plateforme se compose de trois parties: i) Unité de stockage, ii) Unité de contrôle, et iii) Unité de culture cellulaire. L'unité de stockage a été conçue pour maintenir les milieux de culture à basse température dans des tubes Falcon standard et pour les distribuer sur demande. Le capuchon de chaque tube a une entrée reliée à une vanne rotative et une sortie reliée à une autre vanne rotative. L'unité de culture cellulaire se compose de deux pompes péristaltiques, de deux tubes Falcon et d'une cellule de culture où une plaque métallique est placée au-dessus d'une boîte Pétri. L'unité de contrôle est basée sur une carte Arduino Mega 2560. Cette unité est également équipée de deux pompes péristaltiques, d'un clavier, d'un écran OLED, de ports de communication RS485, etc. Les pompes et les valves sont toutes contrôlées par le microcontrôleur. La connexion fluidique des trois unités est assurée par des tuyaux en silicone avec des connecteurs Luer standard.

Pendant la culture cellulaire, l'unité de stockage est maintenue à 4 °C dans un réfrigérateur et l'unité de culture cellulaire est placée dans un incubateur à 37 °C avec 5% de CO_2 humidifié. Lorsqu'un milieu de culture est sélectionné, les deux vannes rotatives sont commutées simultanément dans les positions où l'air filtré peut entrer dans le tube et le milieu peut être pompé. Le milieu est d'abord injecté dans le réservoir par une pompe. Lorsque le réservoir est rempli, le milieu est injecté dans la boîte de culture par une autre pompe pour l'incubation. Ensuite, le milieu est transporté dans le tube d'évacuation par une autre pompe.

Avant la culture cellulaire, les tuyaux et les connecteurs ont été stérilisés. Une culture cellulaire dynamique avec des cellules HeLa a été testée. En accord avec la simulation de fluide, nos résultats ont montré une différence remarquable sur la croissance de la population cellulaire, dû à la différence en renouvellement de milieu de culture et en évacuation de métabolites des cellules.

2) Différenciation automatisée des hiPSCs vers cellules cardiaques et neuronales

Pour évaluer les performances de la plateforme mise au point dans ce travail, nous avons testé deux protocoles connus vers les cardiomyocytes et les neurones.

Le protocole de différenciation cardiaque implique six types de milieux de culture et nécessite des remplacements de milieu réguliers chaque jours sur deux semaines. Avec notre technique de patch de culture, nous montrons la formation de colonies homogènes hiPSCs et le battement régulier des cardiomyocytes résultants. Nous avons ainsi démontré une plateforme automatisée et fiable pour les différenciations de multi-phases.

Nous avons également travaillé sur la différenciation des hiPSCs vers des réseaux de neurones fonctionnels, qui nécessite une maturation de longue période, de plusieurs semaines à plusieurs mois. Les résultats de nos expériences ont démontré la possibilité de contrôler cela de façon entièrement automatique. Il nous semble qu'un réseau de neurones formé par différenciation automatisée est plus performant par rapport à celui formé manuellement, probablement due aux différences en stabilité et en régularité des opérations de changement du milieu de culture pendant une période relativement longue.

Notons que cette plateforme est compatible non seulement avec les méthodes de culture conventionnels (boîte, flacon et plaque de multi-puits) mais aussi avec les dispositifs micro-fabriqués tels que les patches de culture et les dispositifs microfluidiques. Ainsi, cette plateforme que nous avons mise au point est polyvalente et applicable à une grande variété d' essais cellulaires.

3. Fabrication de constructions de tissu alvéolaire

1) Introduction

Les modèles alvéolaires in vitro précédents étaient principalement basés sur la lignée cellulaire immortalisée A549, qui était dérivée d'une tumeur pulmonaire pneumocystose de type II. Cette lignée cellulaire est souvent utilisée pour la modélisation du cancer, les dosages de médicaments anticancéreux et les études de transfection génique. Lorsqu'elles sont cultivées in vitro, les cellules peuvent croître en monocouche à la surface de la boîte de culture ou du ballon et peuvent devenir des cellules alvéolaires de type I après une culture de longue période. Cependant, il est inconvénient de les cultiver avec d'autres composants non tumoraux (stroma, vasculaires, inflammatoires). En plus, elles sont instables génétiquement lors du passage à long terme et de la croissance sélective des sous-populations.

Plus récemment, les hiPSCs ont été utilisées pour différencier les cellules alvéolaires et la formation de l'épithélium alvéolaire. Ces cellules expriment des marqueurs natifs de cellules alvéolaires du type 1 (AT1) et du type 2 (AT2), contenant respectivement une forme squameuse et des corps lamellaires. Étant donné que les cellules dérivées de hiPSCs sont plus cohérentes avec les cellules primaires et peuvent être dérivées de différents donneurs, elles ont montré des réponses distinctes en fonction de l'âge du patient, des antécédents génétiques et du type de source de tissu. En comparaison avec les cellules A549 qui répondent aux toxines différemment des cellules primaires et varient en phénotypes et fonctions dans différentes conditions de culture, les cellules alvéolaires dérivées de hiPSCs peuvent être plus stables. Cependant, la différenciation dirigée des hiPSCs en AT1 et AT2 nécessite généralement une culture à long terme, une méthode de différenciation automatique telle que présentée dans le chapitre précédent est souhaitable pour réduire la variation d'un lot à l'autre ainsi que les coûts de main-d'œuvre.

Notons que les hiPSCs sont aussi capable de se différencier pour générer des organoïdes alvéolaires Ces organoïdes sont généralement composés d'une variété de types de cellules et des principaux composants de la matrice extracellulaire (ECM), ce qui rend cette approche plausible pour les études in vitro des fonctions alvéolaires. Cependant, la formation d’une couche épithéliale alvéolaire reste toujours nécessaire non seulement pour l'exigence d'interfaces air-liquide et de déformation mécanique dans la modélisation pulmonaire, mais aussi pour les essais divers et variés à haut débit. Notre objectif est donc de réaliser ces couches alvéolaires à partir des hiPSCs en passant une étape de formation des organoïdes alvéolaires.

2) Constructions de tissu alvéolaire

Une fois que les organoïdes alvéolaires sont formés, nous les dissocions en cellules uniques et les cultivons sur une membrane basale artificielle. Après une période de maturation, une couche épithéliale alvéolaire est obtenue. En pratique, nous commençons par une génération de mésoderme à partir des hiPSCs puis la formation d'un intestin antérieur ventral-antérieur. Ensuite, des facteurs de différenciation sont introduits pour dériver les sphéroïdes en organoïdes progéniteurs alvéolaires.

Nous avons utilisé des membranes basales artificielles ultra-minces (ultra thin artificial basement membrane, uABMs) d'une épaisseur de l'ordre de 100 nm comme substrat de culture. Une fois que les cellules dissociées des organoïdes alvéolaires sont placées sur une uABM, elles sont cultivées dans un milieu de culture normale pendant deux jours. Après avoir monté l'uABM avec les cellules sur un dispositif, les cellules sont cultivées à l'interface air-liquide pendant 3 à 7 jours supplémentaires. Comme résultats, une couche épithéliale est formée avec l'expression des cellules alvéolaires de type I (AT1) et de type II (AT2), démontrés par des anticorps apparentés qui se lient à la podoplanine (PDPN) ou à l'aquaporine 5 (AQP5) (AT1), SFTPC (AT2), ACE2 (les deux). Des mesures TEER ont également été effectuées pendant et après la culture, confirmant une meilleure performance avec les uABMs.

Par ailleurs, nous avons démontré un multi-passage des organoïdes alvéolaires dans un cycle de 2 semaines. La cryoconservation et la décongélation de ces organoïdes ont été aussi mises en œuvre, assurant une production reproductible et fiable de la lignée organoïde alvéolaire. Pour appliquer cette technique aux études immunologiques, nous avons également vérifié et confirmé l'expression ACE2 des cellules alvéolaires dérivées. Dans l'ensemble, notre modèle d'épithélium est facilement utile pour une variété d'essais, tels que le dépistage de médicaments, l'infection virale, la co-culture avec des cellules endothéliales et des cellules immunitaires.

4. Réponse des cellules alvéolaires à la protéine S du SRAS-CoV-2

1) Introduction

La recherche fondamentale sur l'interaction virus-hôte est essentielle pour comprendre la physiopathologie de l'infection et identifier les meilleurs candidats de médicaments. Des modèles capables de récapituler fidèlement l'environnement immunitaire et de reproduire le cycle de vie viral du SRAS-CoV-2 sont demandés en urgence. Les cellules alvéolaires humaines primaires sont chères et ne prolifèrent pas indéfiniment. Plusieurs lignées cellulaires proliférant à l'infini, telles que Caco-2, Calu-3, HEK293T et Huh7 ont été utilisées dans des

expériences d'infection par le SRAS-CoV-2, qui ne récapitulent pas avec précision les conditions physiologiques humaines et génèrent généralement une faible réponse au SRAS-CoV-2. Une autre lignée cellulaire, Vero E6 isolée des cellules épithéliales rénales d'un singe vert africain est largement utilisée pour sa grande sensibilité et son efficacité de couplage élevée avec le virus. Mais, cette lignée cellulaire est également limitée et ne peut pas être utilisée pour construire des modèles in vitro impliquant des cellules immunitaires.

Récemment, des organoïdes dérivés des hiPSCs sont largement utilisés dans les études diverses et variées. L'inconvénient de ces organoïdes est qu'ils sont généralement immatures et limités en taille et en fonctions. Ils ne peuvent pas reproduire les symptômes systémiques associés aux réponses du corps entier à une infection virale. Les modèles animaux ont été adaptés pour éviter ce problème, mais leur système immunitaire est très différent de celui de l'homme. En outre, le système immunitaire humain est très personnel, dépendant de l'âge et de l'environnement. Pour une perspective à long terme, une approche in vitro en utilisant des tissues dérivées de hiPSCs devrait être plus fiable.

En pratique, la première étape de la modélisation in vitro est peut-être la réalisation d'un micro-environnement immunitaire complet constitué à la fois de constructions tissulaires et de cellules immunitaires. Dans le contexte actuel de l'épidémie de SRAS-CoV-2, les symptômes graves et la mortalité élevée sont principalement dus à des réponses inappropriées du système immunitaire inné telles que la tempête de cytokines, altèrent les réponses à l'interféron et suppriment la présentation de l'antigène à la fois sur les complexes majeurs d'histocompatibilité de classe I et de classe II (MHC-I et MHC-II). Par conséquent, comprendre et imiter les réponses immunitaires innées au SRAS-CoV-2 in-vitro devrait nous permettre d’améliorer notre compréhension de la pathogenèse et de contribuer à la conception et à l'évaluation d'un vaccin et d'une immunothérapie. Les composants les plus importants de l'immunité innée comprennent les interférons et les cytokines, les récepteurs de reconnaissance de formes, les macrophages, les neutrophiles, des cellules tueuses naturelles, et les cellules dendritiques. Sur la base des protocoles existants et de l'intégration systématique des tissus et des cellules immunitaires, on devrait être en mesure d'établir un cadre général vers un développement rapide de modèles envisagés.

Ainsi, nous avons d’abord ‘infecté’ les épithéliales alvéolaires que nous avons réalisé par les protéines S du SRAS-Cov-2. Les réponses cellulaires aux protéines S sont surveillées par imagerie et fluorescence reliée aux espèces réactives de l'oxygène (ROS) dans les cellules alvéolaires avec et sans traitement médicamenteux en présence d'angiotensine II.

2) Résultats et discussion

Pour mesurer le niveau de ROS cellulaire, des sondes fluorescentes oxydées sont utilisées. Ces sondes sont des composés estérifiés non fluorescents, qui peuvent diffuser à travers la membrane cellulaire et devenir fluorescents lors de l'oxydation dans le cytoplasme. Nous avons choisi le diacétate de 2 ', 7'-dichlorofluorescéine (DCFDA, Sigma) pour la mesure directe des états redox intracellulaires.

La variation de l'intensité de fluorescence de chaque échantillon a été analysé en examinant les images en champ claire et en fluorescence capturés automatiquement dans un incubateur normale (37°C et 5% CO_2). Il se trouve que l'intensité de fluorescence ainsi que le niveau de ROS dans les cellules alvéolaire augmente au fur à mesure près que tous à cause de la production constante des ROS, mais l'augmentation de cellules 'infectés' par les protéines S du SARS-Cov-2 semble plus rapide par celle sans infection. Il semble aussi que la présence de peptides angiotensine II (Ang-II) soit nécessaire puisque les cellules alvéolaires elles-même ne sont pas spécifiques pour la génération mais sont spécifiques pour la répondre. En effet, les récepteurs ACE2 (enzyme de conversion de l'angiotensine 2) sont largement exprimés par les cellules alvéolaires qui sont normalement utilisés pour convertir Ang-II à angiotensine-(1-7) (Ang-(1-7)). Du fait que Ang-II et Ang-(1-7) jouent des rôles opposés, l'un est pro-inflammatoire et l'autre anti-inflammatoire, le couplage des protéines S et ACES2 pose un problème d'activation excessive du récepteur type 1 de Ang-II (AT1R), ce qui est signifiant pour l'augmentation du niveau des ROS. Il semble aussi que Lorsatan, un médicament couronnement utilisé pour traiter les hypertensions, ait un effet antagonique puisqu'elle est un bloqueur de AT1R. Enfin, l'effet toxique de protéines S du SARS-Cov-2 a été aussi testé en utilisant les cardiomyocytes dérivées des hiPSCs. Nous avons observé un effet claire d'apoptoses cellulaire puisque nos cellules cardiaques ont cessé de se battre après l'incubation avec les protéines S et l'Ang-II.

Notons que ces observations sont préliminaires et que beaucoup restent à vérifier et à étudier plus systématiquement. Néanmoins, il nous semble que cette approche est exploitable en considérant l'importance des modèles in-vitro immunitaires.

5. Conclusion and perspectives

Ce travail de thèse visait de nouveaux dispositifs et systèmes de culture pour la recherche avancée sur les cellules souches et la modélisation des tissus alvéolaires. Celles-ci incluent la fabrication d'une membrane basale artificielle ultra-mince, le développement d'un système de

culture et de différenciation automatique, et la validation des dispositifs et des systèmes avec les hiSPCs pour les études préliminaires.

Nous avons tout d'abord développé un système de culture automatique pour la différenciation des hiPSCs impliquant plusieurs sources et la maturation à long terme des cellules dérivées de hiPSCs. Ce système est composé d'une unité de distribution du milieu de culture, d'une unité d'incubation et d'une unité centrale de contrôle de processus. Ce système a été utilisé pour la culture cellulaire par perfusion-diffusion par renouvellement rapide du milieu de culture. En accord avec nos expériences, les résultats numériques ont suggéré un échange amélioré des nutriments cellulaires et des métabolites. Ce système a ensuite été utilisé pour une différenciation cardiaque des hiPSCs, ce qui a démontré la fiabilité du système pour une distribution à multi-source automatique. De plus, ce système a été utilisé pour la maturation à long terme des neurones et des réseaux neuronaux dérivés de hiPSCs. En général, le contrôle de différenciation des hiPSCs est laborieux et monotone sur une longue période. Notre système surmonte ces inconvénients et simplifie l'ensemble du travail sans intervention humaine.

Nous avons ensuite établi une procédure de fabrication robuste pour produire des cellules alvéolaires fonctionnelles. Cette procédure a commencé par la fabrication des organoïdes alvéolaires. Ces organoïdes pourraient être congelés et dégelés pour des usages ultérieurs. En les dissociant et replantant sur une membrane basale artificielle ultra-mince, des couches alvéolaires épithéliales pourraient être obtenues. Comme souhaité, ces cellules expriment les protéines des alvéolaires AT1 et AT2 ainsi que ACE2. Les mesures TEER ont confirmé l'importance de la membrane basale artificielle dans la formation de la couche tissulaire. Pour une perspective à plus long terme, nous nous sommes intéressés à la co-culture ou à la tri-culture de ces alvéolaires avec d'autres types de cellules et des cellules immunitaires en particulier, toutes dérivées de la même source des hiPSCs, pour des raisons d'immuno-compatibilité et de immunocompétence. Cela devrait compléter les approches actuelles en considérant la nécessité de récapitulation immunitaire. Plus généralement, cette approche est basé sur un système de culture automatique, une membrane basale artificielle ultra-fine, une puce microfluidique d’intégration et une co-culture des cellules tissulaire et immunitaire, elle est aussi applicable pour la recherche et développement en médecine régénérative, découverte de médicaments et études immunologiques.

Ce travail de thèse est hautement interdisciplinaire. Plusieurs prototypes ont été réalisés tels que le système de culture automatique et le bioréacteur spin-disque. Plusieurs protocoles ont été évalués tels que la différenciation de cardiaques, de neurones et des alvéoles. Des résultats numériques ont été aussi produits par simulation au cas nécessaire. Enfin, le modèle alvéolaire

proposé a été appliqué à une étude préliminaire sur la réponse aux infections virales. Dans l'ensemble, nous avons franchi une étape importante dans la création d'un modèle alvéolaire fiable et utile pour les études futures.

Abbreviation list

2D	Two dimensional
3D	Three dimensional
AA	Ascorbic acid
ABM	Artificial Basement Membrane
ABS	Acrylonitrile butadiene styrene
ACE2	Angiotensin-converting enzyme 2
ACEi	ACE inhibitor
ADR	Adverse drug reaction
ALI	Air-liquid interface
AM	Alveolar macrophage
Ang I	Angiotensin I
Ang II	Angiotensin II
ARBs	Angiotensin II receptor blockers
ASC	Adult stem cell
AT1	Alveolar epithelial type I cell
AT2	Alveolar epithelial type II cell
ATRA	All-trans-retinoic acid
BDGF	Brain-derived neurotrophic factor
BSA	Bovine serum albumin
CAD	Computer-aided design
CNC	Computer numerical control
CNS	Central nervous system
COC	Cyclic lefin copolymer
COPD	Chronic obstructive pulmonary disease
CVD	Chemical vapor deposition
DAPI	4’-6-diamidino-2-phenylindole
dcAMP	dibutyryl cyclic adenosine monophosphate
DCFDA	2’,7’-dichlorofluorescein diacetate
DMSO	Dimethyl sulfoxide
DSM	Dorsomorphin dihydrochloride
EB	Embryonic body

ECM	Extracellular matrix
EDC	1-ethyl-3-(3-dimethylaminopropyl) carbodiimide hydrochloride
EDTA	Ethylenediaminetetraacetic acid
ER	Endoplasmic reticulum
ESC	Embryonic stem cell
FBS	Fetal bovine serum
FDM	Fused deposition modeling
FEM	Finite-Element Method
GDNF	Glial cell-derived neurotrophic factor
HSC	Hematopoietic stem cell
iBMX	3-isobutyl-1-methylxanthine
IL	Interleukin
iPSC	Induced pluripotent stem cell
KGF	Keratinocyte Growth Factor
MEA	Micro electrode array
MEM/NEAA	Minimum essential medium/non-essential amino acid
NHS	N-hydroxysuccinimide
NK	Natural killer
NPC	Neuron progenitor cell
PAF	Platelet-activating factor
PBS	Phosphate-buffered saline
PC	Polycarbonate
PCL	Polycaprolactone
PCR	Polymerase chain reaction
PDL	Poly-D-lysine
PDMS	Polydimethylsiloxane
PDPN	Podoplanin
PE	Polyethylene
PEG	Poly(ethylene glycol)
PEGDA	Poly(ethylene glycol) diacrylate
PLA	Poly(lactic acid)
PLGA	Poly(lactic-co-glycolic acid)
PMMA	Poly(methyl methacrylate)
PP	Polypropylene

PS	Penicillin-Streptomycin
PS	Polystyrene
PTFE	Polytetrafluoroethylene
RAS	Renin-angiotensin system
RBD	Receptor binding domain
RIE	Reactive-ion etching
ROS	Reactive oxygen species
SFD	Serum-free differentiation
SFTPC	Surfactant protein C
SL	Stereolithography
TEER	Transepithelial electrical resistance
TMCS	Trimethylchlorosilane
TNF	Tumor necrosis factor
ZO-1	Zonula occludens-1
µPG	Micropattern generator

Publication list

1. **He, Y.**, Huang, B., Rofaani, E., Hu, J., Liu, Y., Pitingolo, G., & Chen, Y. (2020). Fabrication of micro-cages and caged tumor spheroids for microfluidic chip-based assays. Microelectronic Engineering, 225, 111256.
2. Pitingolo, G., **He, Y.**, Huang, B., Wang, L., Shi, J., & Chen, Y. (2020). An automatic cell culture platform for differentiation of human induced pluripotent stem cells. Microelectronic Engineering, 111371. (Pitingolo, G. and He, Y., contributed equally to this paper)
3. Radiom, M., **He, Y.**, Peng-Wang, J., Baeza-Squiban, A., Berret, J. F., & Chen, Y. (2020). Alveolar mimics with periodic strain and its effect on the cell layer formation. Biotechnology and Bioengineering, 117(9), 2827-2841.
4. Huang, B., **He, Y.**, Wang, L., Shi, J., Hu, J., Rofaani, E., ... & Chen, Y. (2020). Microfluidic channel with embedded monolayer nanofibers for cell culture and co-culture. Microelectronic Engineering, 225, 111235.
5. Rofaani, E., Peng, J., Wang, L., **He, Y.**, Huang, B., & Chen, Y. (2020). Fabrication of ultrathin artificial basement membrane for epithelial cell culture. Microelectronic Engineering, 232, 111407.

RÉSUMÉ

L'objectif de ce travail est de développer un modèle alvéolaire basé sur une membrane basale artificielle ultramince (ABM) et un système automatique de contrôle de la différenciation des cellules souches pluripotentes induites par l'homme (hiPSC). L'ABM a été réalisé par dépôt de gel de collagène de type IV et de laminine sur un réseau de monocouche de nanofibres de gélatine à haute porosité. Des organoïdes alvéolaires pourraient être générés, gelés et dégelés pour des utilisations de routine. Des tissus alvéolaires ont été obtenus en dissociant les organoïdes alvéolaires en cellules uniques et en les cultivant sur un ABM dans des conditions d'interface air-liquide. Ils ont ensuite été caractérisés par des mesures de la résistance électrique transépithéliale, démontrant la faisabilité du modèle. Le système automatique développé a également été utilisé pour la différenciation des hiPSCs en cardiomyocytes et en neurones. Enfin, les tissus alvéolaires et les cardiomyocytes dérivés de hiPSC ont été utilisés pour des études préliminaires des réponses cellulaires à la protéine S de Covid-19, montrant une toxicité remarquable qui mérite une étude très approfondie.

MOTS CLÉS

Cellules souches, organoïdes, modèle alvéolaire, dispositifs

ABSTRACT

The objective of this work is to develop an alveolar model based on an ultrathin artificial basement membrane (ABM) and an automatic system for the control of differentiation of human-induced pluripotent stem cells (hiPSCs). The ABM was achieved by gel deposition of type IV collagen and laminin on a high porosity backbone of monolayer of gelatin nanofibers. Alveolar organoids could be generated, freezed and defreezed for routine uses. Alveolar tissue constructs were fabricated by disassociating alveolar organoids into single cells and culturing them on an ABM under air-liquid interface conditions. They were then characterized by transepithelial electrical resistance monitoring, demonstrating the reliability of the model. The developed automatic system has also been used for hiPSC differentiation into cardiomyocytes and neurons. Finally, the hiPSC derived alveolar tissues and cardiomyocytes were used for preliminary studies of the cellular responses to the S-protein of Covid-19, showing remarkable toxicity which deserves further investigations.

KEYWORDS

Stem cells, organoids, alveolar model, microdevices